School of Engineering and Mathematical Sciences
CITY UNIVERSITY LONDON

Implementation of the Finite Difference Time Domain Algorithm for the Analysis of Terahertz Waves

Christos Markides

A thesis submitted for the Degree of Doctor of Philosophy in Information Engineering.

Supervisors:

Professor B.M.A. Rahman

Dr. Christos Themistos

July, 2014

Contents

List of Figures

Acknowledgements

I, Christos Markides, grant powers of discretion to the University Librarian to allow this thesis to be copied in whole or in part without further reference to me. This permission covers only single copies made for study purposes, subject to normal conditions of acknowledgement.

Christos Markides

July, 2014

Abstract

The aim of this report is to present results related to the application of the Finite Difference Time Domain (FDTD) method for the study of various devices at terahertz frequencies. The FDTD method has emerged as one of the most widely used numerical analysis methods used for electromagnetic simulations. The FDTD method can be used to solve numerous types of problems ranging from modelling the behaviour of microwave circuits, waveguides, and photonics to simulating terahertz devices and plasmas.

In this study the FDTD approach is derived from first principles (finite differences) and explicit equations are shown based on Maxwell's equations. Furthermore, absorbing boundary conditions (ABCs) are discussed for the FDTD method. The algorithm is tested against a range of problems to ensure its validity and accuracy. The FDTD method is then applied for the numerical analysis of a range of devices at terahertz frequencies. The numerical results obtained from the application of the FDTD method to examine a microstrip circuit with filter loading and a Multi-mode Interference (MMI) coupler at terahertz frequencies are discussed in detail. Moreover, the results of the application of the FDTD method for the calculation of the dispersion characteristics of plasmonic waveguides are also presented.

Finally, a summary of the work carried out is presented and an outline is given for future research which can be carried out by using the FDTD method for the study of terahertz frequency devices.

List of Symbols and Abbreviations

Symbol / Abbreviation	Explanation
1D	One-dimensional
2D	Two-dimensional
3D	Three-dimensional
ABC	Absorbing boundary condition
ADE	Auxiliary differential equation
ADI	Alternating-direction explicit
Au	Gold
B	Magnetic flux density
C	Capacitance
c	Speed of light in vacuum
CFL	Courant-Friedrichs-Lewy
CPML	Complex frequency shift PML
D	Electric flux density
DFT	Discrete Fourier transform
E	Electric field
FDTD	Finite-Difference Time-Domain
FETD	Finite Element Time Domain
FFT	Fast Fourier transform
FSS	Frequency selective surface
FWHM	Full-width half-maximum
FWHP	Full-width half-power
GaAs	Gallium Arsenide
GPL	General Public Licence
H	Magnetic field
I	Current
J	Electric current intensity
k	wavenumber
L	Inductance
LD	Lorentz - Drude
M	Magnetic current density
MMI	Multi-mode interference

Symbol / Abbreviation	Explanation
MoM	Method of moments
MPI	Message Passing Interface
N_λ	Number of cells per wavelength
NDE	Non-destructive evaluation
OPTL	Optically pumped lasers
PDE	Partial differential equation
PEC	Perfect electric conductor
PLRC	Piecewise recursive convolution
PMC	Perfect magnetic conductor
PS	Polystyrene
QCL	Quantum-cascade lasers
R	Resistance
RC	Recursive convolution
PML	Perfectly matched layer
RAM	Random access memory
S	Courant-Friedrichs-Lewy factor
SP	Surface plasmon
SPM	Surface plasmon mode
SPP	Surface plasmon polariton
t	Time
TE	Transverse electric
TE_z	Transverse electric relative to the z direction (only H_z, E_x, and E_y are present)
TEM	Transverse electromagnetic
TFMS	Thin-film microstrip lines
TF/SF	Total-field scattered-field
TM	Transverse magnetic
TM_z	Transverse magnetic relative to the z direction (only E_z, H_x, and H_y are present)
UPML	Uniaxial PML
Δt	Time increment
$\Delta x, \Delta y, \Delta z$	Space increment
ε	Electric permittivity
λ	Wavelength
μ	Magnetic permeability
σ	Electric conductivity
ω	Angular frequency

List of Publications

The work in this thesis is, in part, based on the following publications:

[1] C. Themistos, C. Markides, B.M.A. Rahman, K.T.V. Grattan, "Characterization of microstrips for THz waves", *IEEE EDSSC*, Bangkok, 2012.

[2] B. M. A. Rahman, K. T. Grattan C. Themistos, C. Markides, "Design Optimization of Low-loss Waveguides and Devices for THz Systems," in *International Conference on Fibre Optics and Photonics*, p. M1A.1, Chennai, India, 2012.

[3] C. Markides, C. Themistos, H. Tanvir, B. M. A. Rahman, K. T. V. Grattan, "Multimode Interference 3 dB Splitters in Hollow Core Metallic Waveguides for Low-Loss THz Wave Transmission," *Selected Topics in Quantum Electronics, IEEE Journal of*, vol.19, no.1, pp.8500606, Jan.-Feb. 2013.

[4] C. Themistos, K. Kalli, M. Komodromos, C. Markides, A. Quadir ; B. M. Azizur Rahman, K. T. V. Grattan, "Low-loss multimode interference couplers for terahertz waves," *Proc. SPIE 8426, Microstructured and Specialty Optical Fibres*, 84260X, Brussels, June , 2012.

[5] B. M. a. Rahman, M. Uthman, A. Quadir, N. Kejalakshmy, C. Markides, and C. Themistos, "Low-loss waveguides and devices for compact THz systems," *Proc. SPIE 8716, Terahertz Physics, Devices, and Systems VII: Advanced Applications in Industry and Defense*, pp. 87160R-87160R-8, Maryland, USA 2013.

[6] B. M. A. Rahman, C. Themistos, H. Tanvir, M. Uthman, A. Quadir, and C. Markides, "Low-loss waveguides for THz guidance and devices," *Proc. SPIE 8624, Terahertz, RF, Millimeter, and Submillimeter-Wave Technology and Applications VI*, pp. 862414-862414-6, California, USA, 2013.

[7] C. Markides, C. Viphavakit, C. Themistos, M. Komodromos, K. Kalli, A. Quadir, A. Rahman, "Dispersion characteristics of plasmonic waveguides for THz waves", *Proc. SPIE, Modelling and Numerical Analysis*, Prague, April 2013.

[8] B. M. A. Rahman, C. Themistos, A. Quadir, M. Uthman, C. Markides, H. Tanvir and K. T. V. Grattan, "Design Optimization of Low-loss Waveguides and Devices for THz Systems", *Infrared and Optoelectronics: Materials and Devices*, Chicago, 2012.

[9] C. Themistos, A. Quadir, C. Markides, H. Tanvir, B. M. A. Rahman, "Rigorous characterization of surface plasmonic waveguides and guided-wave devices for THz systems", *Int. Conf. on Metamaterials, Photonic Crystals and Plasmonics*, UAE, 2013.

[10] B. M. A. Rahman, C. Markides, M. Uthman, A. Quadir, N. Kejalakshmy, and C. Themistos, "Characterization of low-loss waveguides and devices for terahertz radiation", *Optical Engineering: Special Section Paper Terahertz Physics and Applications*, vol. 53(3), pp. 031210-031210, 2014

Chapter 1

Introduction

In recent years extensive research has been carried out in the terahertz portion of the electromagnetic spectrum, which is loosely defined as the frequencies from 300 GHz to 30 THz (wavelengths from 1 mm to 10 μm). Traditionally terahertz science and technology has been applied in space spectroscopy, examining far-infrared radiation, molecular spectroscopy and in the diagnostics of plasma [1]. Today terahertz science and technology is applied to many more sectors, given the recent advancements and innovations in photonics and nanotechnology. The unique properties of this frequency domain have resulted in terahertz technology emerging as a state-of-the-art research field, thus gaining popular interest. In September, 2011 the IEEE launched the inaugural edition of the *IEEE Transactions on Terahertz Science and Technology* as a means to bridge to gap between microwaves and visible light, with topics and technologies that encompass terahertz techniques and applications [2].

The rapid growth in terahertz technology and science is closely linked with the continual advances of high-frequency electronics and cutting edge technology in semiconductors and superconductor logic circuits also operating at higher frequencies. In particular terahertz technology is growing rapidly in a wide range of independent fields from terahertz sources and detectors to application specific systems [3].

In terms of terahertz sources, there have been three major approaches in the field. For the past few decades optical generation of terahertz radiation using lasers has been the dominant approach. Primarily femtosecond lasers are used for terahertz Time Domain Spectroscopy (TDS), whereas for Frequency Domain Spectroscopy (FDS) other types of lasers are used [4]. Another approach is based on the recently developed terahertz Quantum Cascade Laser (QCL). The development of terahertz QCL has witnessed remarkable progress recently. The third approach which is well established at low frequencies employs solid-state electronic devices for generating terahertz radiation [5].

Progress in terahertz applications depends on the transmission properties of terahertz sources, the penetration of terahertz radiation through dielectric materials and the high sensitivity of terahertz sensors. The unique properties of terahertz radiation and spectroscopic sensing have led to new fields of interest and significant advances in astrophysics and atmospheric science, biological and medical sciences, security screening and illicit material detection, homeland security, non-destructive evaluation (NDE), information and communications technology (ICT), and ultrafast spectroscopy. Terahertz radiation exhibits good balance between good resolution and penetration as well as good selectivity (fingerprint) in many materials [1]. Based on the above, two distinct categories emerge from terahertz technology applications: sensing and communications.

Moreover terahertz TDS and Frequency Domain Spectroscopy (FDS) combined with advanced analytical technological methods that are applicable to various materials have been employed in biological, medical and pharmaceutical applications, security, information and communication technology, earth and space exploration, as well as semiconductor and other industrial applications [4]. In terms of medical and pharmaceutical applications, terahertz technology has been used for tissue identification, and detecting disease [6] and terahertz TDS has been applied to observe many materials including biomolecules, cancer tissue, DNA (single stranded), proteins and bacteria with far greater detail than infrared spectroscopy [7, 8]. It has also been reported that several studies have been carried out on the diagnosis of cancer using terahertz TDS [9].

In the field of Information and Communication Technologies (ICT) the development speed in terms of computation and memory size is unprecedented. Over a period of more than forty years, processor speed and memory size are doubling roughly every 18 months, according to Moore's Law [10]. Experts believe that this development will continue in the next decade, but this demands radical changes in architecture and software. In the next two decades, diminishing transistor-speed scaling and practical energy limits create new challenges for continued performance scaling. As a result, the frequency of operations will increase slowly, with energy the key limiter of performance, forcing designs to use large-scale parallelism, heterogeneous cores, and accelerators to achieve performance and energy efficiency [11]. Recently, there has been an increasing interest in the application of terahertz waves to broadband wireless communications. The demand for higher data rates and seamless connection of fibre optic (wired) and wireless communication networks in terms of modulation and data rates has led to the development of terahertz wireless communications based on photonics technologies [12]. Also in telecommunication networks the first integrated photonic devices that were deployed during the past decade and the fibre-linked optical communication is growing at unprecedented rates, realizing data rates greater than terabit per second. High-performance wireless networks could be implemented with the breakthrough and the development circuits based on terahertz technology that could enable wireless communication at speeds nearing 40 Gigabits using sub-THz waves [13]. In terms of the development of various circuits for ICT, recent studies have reported integrated quantum circuits operating at a frequency of 1 THz [14]. Furthermore, the transport of THz pulses on the surface of metal wires with negligible dispersion and low attenuation has also been reported [15].

Terahertz wave generation and detection is a key element in ICT to realize faster, mobile, robust, and relatively inexpensive systems. In order to achieve even greater system functionality and cost as well as bringing the economics of Moore's Law to photonic and terahertz components and devices, the need for more accurate models describing the behaviour of electromagnetic fields in novel optical devices is required. For this purpose computer modelling and simulation of the complex electromagnetic fields in devices and components is used. Computer

modelling and simulation is based on analytical and numerical methods that are formulated based on the governing Maxwell's equations. Furthermore, numerical simulations provide a framework for feasibility studies and design optimization of devices thus reducing fabrication costs and saving time.

The behaviour of electromagnetic structures can be modelled using numerical modelling techniques. These techniques can be classified into analytical methods and numerical methods. With analytical methods, a solution is obtained by solving the basic electromagnetic equations, thus minimising the final computation time. However, it is often applicable to much simpler structures only. On the other hand numerical methods are computational schemes or models that can be applied to a spectrum of problems by modifying the basic model to fit the problem. Numerical methods provide the advantage of solving a problem in a finite sequence of arithmetic and logical operations. In contrast with analytical methods, numerical methods lack the analytical investigation of the problem and fail to describe the physical mechanisms that are taking place. Furthermore semi-analytical methods could be used to find a solution to a simplified problem with certain acceptable approximations based on analytical approaches [16].

Due to the complex nature of modern optical devices, the use of analytical methods has been restricted to modelling only simple structures. Instead, existing and improved numerical methods and techniques are receiving wider attention for modelling of practical optical components and devices. Numerical methods are often applicable to a wide range of problems, thus offering approximate solutions to Maxwell's equations with good accuracy. These methods are often flexible and robust and in most cases a particular method is preferred depending on the media or the structure under consideration. However, these advantages do not come without a cost, specifically with long computational times and memory requirements. Numerical methods are divided into two distinct categories: time and frequency domain.

Frequency domain numerical methods solve Maxwell's equations for a specific frequency. These numerical methods produce accurate and stable results in simulating complicated structures and they have proved robust over the years. However, they are not suitable for simulating devices where it is desirable to analyse the characteristics of a device over a broad range of frequencies. Incorporating the material and device nonlinearities in frequency domain numerical methods still poses a significant problem. The most widely used frequency domain numerical methods are the Method of Moments (MoM) [17, 18], the Finite Element Method (FEM) [19, 20], and the Beam Propagation Method (BPM) [21, 22]. A wide range of commercial software packages are available that offer a wide range of tools to simulate devices using one or more frequency domain methods. Some of the most popular packages in the scientific community are FEM based COMSOL Multiphysics [23] and Ansoft HFSS [24], and MoM based FEKO, for radiation and coupling analysis [25].

Time domain numerical analysis methods solve Maxwell's equations over time. These allow the simulation of devices and obtain results using Fast or Discrete Fourier Transforms (FFT/DFT) over a wide range of frequencies. The most well known time domain methods include the Finite Element Time Domain Method (FETD) [26], the Finite Difference Time Domain (FDTD) method [27, 28], the Transmission Line Modelling method (TLM) [27, 28], and the Time Domain Integral Equation (TDIE) [29] techniques. Similarly, some of the most popular commercial software packages that employ time domain numerical analysis include Lumerical FDTD Solutions [30], Remcom XFdtd [31], and Optiwave OptiFDTD [32]. Moreover, some well-known open source FDTD software under the General Public Licence (GPL) licence are the Massachusetts Institute of Technology Electromagnetic Equation Propagation (MEEP) [33], Angora: a free FDTD electromagnetic simulation package with full parallelizability based on the Message Passing Interface (MPI) developed by the Biomedical Engineering Department of Northwestern University [34], and California Institute of Technology 3D FDTD – pFDTD for single core CPU [35].

1.1 Finite Element Method

The Finite Element Method (FEM) is a numerical technique for solving a wide variety of engineering problems. The Finite Element Method could be used to solve Maxwell's differential equations based on the formulation of a problem.

In the FEM formulation, the domain of interest is divided into discrete elements, otherwise called finite elements, often triangular, which is the principal characteristic of the method. Each element is can have different properties in terms of its relative conductivity and relative permittivity, thus making the dielectric material lossy, anisotropic, or nonlinear.

This method provides an approximation to a continuous physical problem in which the approximation of physical fields on finite elements provides good precision; hence by increasing the number of elements, so do the numbers of discrete variables, thus the solution approaches a continuous domain of computation. Variations in the formulation of this method have been reported for both optical and microwave problems [36]. The FEM has become a powerful computational tool for studying complicated problems with the introduction of various improvements to the formulation, such as the development of methods to suppress or eliminate spurious [37] and nonphysical solutions [38].

The FEM with the aid of perturbation techniques has been used to determine the complex propagation characteristics of surface-plasmon modes that are supported by metal-dielectric interfaces. Symmetrical and nonsymmetrical three-layer optical waveguides incorporating a thin metal layer can be studied, and the variations of the effective index and the attenuation constant with metal thicknesses have been presented for both the short-range and long-range modes [39].

Although the FEM has been used as to solve Maxwell's equations in terms of the eigenvalue problems, it has also been extended for the analysis of various shaped optical integrated circuits to include time-domain propagation yielding to the Finite Element Time Domain (FETD) method [40].

1.2 Beam Propagation Method

One of the most popular methods based on simplified wave equations is the Beam Propagation Method (BPM). This type of field propagation was initially used for underwater acoustic and seismology research [21]. The BPM is a frequency-domain approach and it is widely used for the simulation of integrated photonic devices. The BPM originally solved the paraxial wave equation under the scalar approximation, providing a spectral propagation algorithm for an arbitrary incident beam propagating in a medium of slowly-varying refractive index.

The BPM was first formulated by Feit and Fleck using the Fast Fourier Transform for optical problems [41]. Today the BPM is used to investigate linear and nonlinear phenomena in lightwave propagation in various materials based on the Helmholtz Equation. The BPM yields the response of a given device to an external optical signal. Then analysis of the results can be used to obtain information about the modal properties of that device.

The BPM can be used for a layout of devices that are not described by a quantitative theory and it can influence the technological problems on the operation of components. Furthermore it can also be used for solving problems with theories and approximations using computers as CAD to gain insight on the behaviour of a special device.

The BPM has been studied and developed extensively. It has been extended to include one-, two- and three-dimensional problem solving using a full vectorial approach [42]. Due to its numerical efficiency and versatility, the finite element method has been used to extend the full vectorial BPM formulation to the full vector finite-element BPM (FE-BPM) formulation [43]. A new method was also introduced based on the vector finite-element formulation of the beam propagation method combined with the imaginary distance propagation technique [44] to obtain modes. The BPM was also extended to a new method called time-domain reflective beam propagation method (TD-RBPM) again for the analysis of optical pulse propagation and reflection in waveguide structures with multiple discontinuities [45]. Moreover, the BPM has been extended to the bidirectional

BPM formulation to allow the analysis of strong reflections in waveguiding structures [46]. The bidirectional BPM can simulate the wave propagation for optical discontinuity problems, as well as the junction between two different optical waveguide structures. The iterative bidirectional BPM can also be used for the analysis of the reflectivity of coated optical fibres [47].

Recently an alternating direction implicit (ADI), scheme for the wide-angle finite-difference beam propagation method (FD-BPM) based on the wide angled Pade multistep method has been proposed [48].

1.3 Finite Difference Time Domain Method

Kane Yee published the first paper in May 1966 to describe Maxwell's equations in the equivalent set of finite difference equations, thus showing the discretisation of space and time [28]. This has lead to further investigation of time-varying media and also formed the basis of the Finite Difference Time Domain method. Yee's approach applies simple, second order accurate central-difference approximations for the space and time derivatives of the electric and magnetic fields directly to the respective differential operators of the curl equations. The algorithm proposed by Yee solves for both electric and magnetic fields using the coupled Maxwell's equations instead of solving individual components (electric or magnetic) with a wave equation, which is similar to the combined-field integral equation of the Method of Moments. Thus creating a more robust solution and a straightforward manner in which the electric and magnetic properties of the material can be modelled.

The Finite Difference Time Domain Method will be presented in greater detail in the following chapter to include the explicit equations, stability factors, incident wave conditions and absorbing boundary conditions. Furthermore, results will be presented later on for different electromagnetic problems solved using the FDTD method.

1.4 Organisation of this Thesis

The aim of this thesis is to present the results of the application of the FDTD method as a numerical analysis tool for modelling various devices such as microstrips, multimode-interference couplers (MMI), low-loss waveguides, and the study of surface plasmons in low-loss waveguide at terahertz frequencies.

Chapter 1 reports on the progress in terahertz science and technology. The chapter outlines the growth in terahertz techniques and applications in recent years, in terms of terahertz sources, wave generation and transmission, as well as sensing applications. Moreover, widely used numerical methods for modelling electromagnetic structures, both in frequency and time domain, are presented and briefly discussed.

In this thesis, Chapter 2 introduces the theory of Finite Difference approximation and the FDTD method based on Yee's algorithm. The chapter provides an overview of Maxwell's equations and how finite differences are used to solve Maxwell's equations. The basic theory on the finite-differences is outlined and applied to the one-dimensional wave equation and the Finite-Difference Time Domain method equations are presented. Finally absorbing boundary conditions are discussed and explicit equations are outlined for terminating the computational domain.

Chapter 3 presents the application of the FDTD method on a variety of devices. Numerical results are presented in order to emphasize the general applicability of the method to a variety of problems. This also serves as a test of the application implemented in MATLAB to a wide range of structures from the lower frequency spectrum up to terahertz frequency applications. The findings are then compared with results found in the literature.

In Chapter 4, the performance of microstrip circuits and microstrip transmission lines is presented. A rigorous investigation of microstrip circuits at terahertz frequencies is demonstrated with specific interest in the effect of the deposition of polysterene film along the metal surface of the device thus

controlling the position of the resonant frequency using the FDTD method, whereas the FEM is used for modal analysis of the device [49]. The modelling of such structures can be applied in developing terahertz band-stop filters and in sensing applications.

Chapter 5 introduces a low-loss multimode interference coupler for terahertz waves [50, 51]. The FDTD method is used to model a novel design of a low-loss hollow-core polystyrene coated waveguide operating as a multimode interference-based half-power (3dB) splitter for THz frequencies. The FDTD method has been utilized to demonstrate the optical field evolution along the direction of propagation both in time and space.

Chapter 6 investigates the nature of plasmonic waveguides and the numerical dispersion artefacts using the FDTD method for numerical analysis [52]. A rectangular low-loss plasmonic waveguide at terahertz frequencies is presented. The FDTD method is used to simulate and calculate the numerical dispersion of a low-loss polystyrene coated rectangular waveguide at terahertz frequencies, by varying the width of the source (spot size) and the structural properties of the waveguide.

Finally, Chapter 7 concludes this work with a summary of the main ideas introduced and an outline of future research that could be carried out.

References

[1]   P. H. Siegel, "Terahertz technology," *Microwave Theory and Techniques, IEEE Transactions on,* vol. 50, no. 3, pp. 910-928, 2002.

[2]   P. H. Siegel, "Inaugural Editorial," *Terahertz Science and Technology, IEEE Transactions on,* vol. 1, no. 1, pp. 1-4, 2011.

[3]   W. L. Chan, J. Deibel, and D. M. Mittleman, "Imaging with terahertz radiation," *Reports on Progress in Physics,* vol. 70, p. 1325, 2007.

[4]   M. Tonouchi, "Cutting-edge terahertz technology," *Nature Photonics,* vol. 1, pp. 97-105, 2007.

[5]   I. Hosako, N. Sekine, M. Patrashin, S. Saito, K. Fukunaga, Y. Kasai, P. Baron, T. Seta, J. Mendrok, S. Ochiai, and H. Yasuda, "At the dawn of a new era in Terahertz technology," *Proceedings of the IEEE,* vol. 95, no. 8, pp. 1611-1623, 2007.

[6]   P. H. Siegel, "Terahertz technology in biology and medicine," *Microwave Symposium Digest, 2004 IEEE MTT-S International,* vol. 3, pp. 1575-1578, USA, 2004.

[7]   M. Nagel, P. Haring Bolivar, M. Brucherseifer, H. Kurz, A. Bosserhoff, and R. Buttner, "Integrated THz technology for label-free genetic diagnostics," *Applied Physics Letters,* vol. 80, pp. 154-156, 2002.

[8]   J. Cunningham, C. Wood, A. G. Davies, I. Hunter, E. H. Linfield, and H. E. Beere, "Terahertz frequency range band-stop filters," *Applied Physics Letters,* vol. 86, pp. 213503-213503-3, 2005.

[9]   B. Fischer, M. Hoffmann, H. Helm, R. Wilk, F. Rutz, T. Kleine-Ostmann, M. Koch, and P. Jepsen, "Terahertz time-domain spectroscopy and imaging of artificial RNA," *Optics Express,* vol. 13, pp. 5205-5215, 2005.

[10]   G. E. Moore, "Cramming more components onto integrated circuits," *Proceedings of the IEEE,* vol. 86, pp. 82-85, 1998.

[11]   S. Borkar and A. A. Chien, "The future of microprocessors," *Communications of the ACM,* vol. 54, pp. 67-77, 2011.

[12]   T. Nagatsuma, S. Horiguchi, Y. Minamikata, Y. Yoshimizu, S. Hisatake, S. Kuwano, N. Yoshimoto, J. Terada, and H. Takahashi, "Terahertz wireless communications based on photonics technologies," *Optics Express,* vol. 21, pp. 23736-23747, 2013.

[13]   A. Hirata, R. Yamaguchi, T. Kosugi, H. Takahashi, K. Murata, T. Nagatsuma, N. Kukutsu, Y. Kado, N. Iai, S. Okabe, S. Kimura, H. Ikegawa, H. Nishikawa, T. Nakayama, and T. Inada, "10-Gbit/s wireless link using InP HEMT MMICs for generating 120-GHz-band millimeter-wave signal," *Microwave Theory and Techniques, IEEE Transactions on,* vol. 57, pp. 1102-1109, 2009.

[14]   T. Akiyama, N. Georgiev, T. Mozume, H. Yoshida, A. V. Gopal, and O. Wada, "1.55-μm picosecond all-optical switching by using intersubband absorption in InGaAs-AlAs-AlAsSb coupled quantum wells," *Photonics Technology Letters, IEEE,* vol. 14, pp. 495-497, 2002.

[15]   K. Wang and D. M. Mittleman, "Metal wires for terahertz wave guiding," *Nature,* vol. 432, pp. 376-379, 2004.

[16]   A. Canova, A. Manzin, and M. Tartaglia, "Evaluation of different analytical and semi-analytical methods for the design of ELF magnetic

field shields," *Industry Applications, IEEE Transactions on,* vol. 38, pp. 788-796, 2002.

[17]   K. Do-Hoon, R. J. Burkholder, and P. H. Pathak, "Efficient method of moments formulation for large PEC scattering problems using asymptotic phasefront extraction (APE)," *Antennas and Propagation, IEEE Transactions on,* vol. 49, pp. 583-591, 2001.

[18]   R. F. Harrington, *Field Computation by Moment Methods,* 1st ed., Wiley-IEEE Press, 1993.

[19]   A. J. Davies, *The Finite Element Method: An Introduction with Partial Differential Equations,* 2nd ed., New York: Oxford University Press, 2011.

[20]   O. C. Zienkiewicz, R. L. Taylor, and J. Z. Zhu, *The Finite Element Method: Its Basis and Fundamentals,* 6th ed., Burlington: Elsevier ButterHeinem, 2005.

[21]   R. März, *Integrated Optics: Design and Modeling.* Boston: Artech House, 1995.

[22]   J. VanRoey, J. van derDonk, and P. E. Lagasse, "Beam-propagation method: analysis and assessment," *Optical Society of America, Journal of,* vol. 71, pp. 803-810, 1981.

[23]   Comsol, "Multiphysics," Available: http://www.comsol.com/.

[24]   Ansoft, "HFSS: 3D Full-Wave electromagnetic Field Simulation," Available: http://www.ansoft.com.

[25]   Feko: Available: http://www.feko.info.

[26]   W. Man-Fai, O. Picon, and V. Fouad Hanna, "A finite element method based on Whitney forms to solve Maxwell equations in the time domain," *Magnetics, IEEE Transactions on,* vol. 31, pp. 1618-1621, 1995.

[27]   A. Taflove and S. C. Hagness, *Computational Electrodynamics: The Finite-Difference Time-Domain Method,* 3rd ed., Artech House Publishers, 2005.

[28]   K. S. Yee, "Numerical solution of initial boundary value problem involving Maxwell's equations in isotropic media," *IEEE Trans. Antennas Propagat.,* vol. 14, pp. 302-307, 1966.

[29]   S. M. Rao and T. K. Sarkar, "Numerical solution of time domain integral equations for arbitrarily shaped conductor/dielectric composite bodies," *Antennas and Propagation, IEEE Transactions on,* vol. 50, pp. 1831-1837, 2002.

[30]   Lumerical, "FDTD Solutions," Available: http://www.lumerical.com.

[31]   REMCOM, "XFdtd," Available: http://www.remcom.com.

[32]   Optiwave, "OptiFDTD," Available: http://www.optiwave.com.

[33]   A. Oskooi and S. G. Johnson, "MEEP," Massachusetts Institute of Technology, Available: http://ab-initio.mit.edu/wiki/index.php/Meep.

[34]   I. R. Capoglu, "Angora: A free finite-difference time-domain (FDTD) electromagnetic simulation package," Northwestern University, Available: http://www.angorafdtd.org/.

[35]   S.-H. Kim, "3D FDTD - pFDTD," California Institute of Technology, Available: http://www.its.caltech.edu/~seheon/FDTD.html.

[36]   B. M. A. Rahman and J. B. Davies, "Finite-Element Analysis of Optical and Microwave Waveguide Problems," *Microwave Theory and Techniques, IEEE Transactions on,* vol. 32, pp. 20-28, 1984.

[37] B. M. A. Rahman and J. B. Davies, "Penalty Function Improvement of Waveguide Solution by Finite Elements," *Microwave Theory and Techniques, IEEE Transactions on*, vol. 32, pp. 922-928, 1984.

[38] M. Koshiba, K. Hayata, and M. Suzuki, "Finite-element method analysis of microwave and optical waveguides - trends in countermeasures to spurious solutions," *Electronics and Communications in Japan (Part II: Electronics)*, vol. 70, pp. 96-108, 1987.

[39] C. Themistos, B. M. A. Rahman, and K. T. V. Grattan, "Finite-element analysis of surface-plasmon modes for lossy optical waveguides by the use of perturbation techniques," *Applied Optics*, vol. 34, pp. 7695-7701, 1995.

[40] T. Van and A. Wood, "A time-domain finite element method for Helmholtz equations," *Computational Physics, Journal of*, vol. 183, pp. 486-507, 2002.

[41] M. D. Feit and J. J. A. Fleck, "Computation of mode properties in optical fiber waveguides by a propagating beam method," *Applied Optics*, vol. 19, pp. 1154-1164, 1980.

[42] M. Z. Delgado-Leon and H. E. Hernandez-Figueroa, "A new 3D vectorial beam propagation method for optical waveguides," *Microwave and Optoelectronics Conference, 1997. 'Linking to the Next Century'. Proceedings., 1997 SBMO/IEEE MTT-S International*, pp. 554-557, vol.2., 1997.

[43] S. S. A. Obayya, B. M. A. Rahman, and H. A. El-Mikati, "New full-vectorial numerically efficient propagation algorithm based on the finite element method," *Lightwave Technology, Journal of*, vol. 18, pp. 409-415, 2000.

[44] S. S. A. Obayya, B. M. A. Rahman, K. T. V. Grattan, and H. A. El-Mikati, "Full vectorial finite-element-based imaginary distance beam propagation solution of complex modes in optical waveguides," *Lightwave Technology, Journal of*, vol. 20, pp. 1054-1060, 2002.

[45] F. Ning-Ning and H. Wei-Ping, "Time-domain reflective beam propagation method," *Quantum Electronics, IEEE Journal of*, vol. 40, pp. 778-783, 2004.

[46] P. Kaczmarski and P. E. Lagasse, "Bidirectional beam propagation method," *Electronics Letters*, vol. 24, pp. 675-676, 1988.

[47] S. S. A. Obayya, *Computational Photonics*, West Sussex: Wiley, 2011.

[48] E. V. Bekker, P. Sewell, T. M. Benson, and A. Vukovic, "Wide-Angle Alternating-Direction Implicit Finite-Difference Beam Propagation Method," *Lightwave Technology, Journal of*, vol. 27, pp. 2595-2604, 2009.

[49] C. Themistos, C. Markides, B. M. A. Rahman, and K. T. V. Grattan, "Characterization of microstrips for THz waves," in *Electron Devices and Solid State Circuit (EDSSC), 2012 IEEE International Conference on*, pp. 1-4, Bangok, Thailand, 2012.

[50] C. Markides, C. Themistos, H. Tanvir, B. M. A. Rahman, and K. T. V. Grattan, "Multimode Interference 3dB splitters in hollow core metallic waveguides for low loss THz wave transmission," *Selected Topics in Quantum Electronics, IEEE Journal of*, vol. 19, no. 1, p. 8500606, 2012.

[51] C. Themistos, K. Kalli, M. Komodromos, C. Markides, A. Quadir, B. M. A. Rahman, and K. T. V. Grattan, "Low-loss multimode interference

couplers for terahertz waves," in *Proc. SPIE Microstructured and Specialty Optical Fibres*, pp. 84260X-84260X, Brussels, 2012.

[52]   C. Markides, C. Viphavakit, C. Themistos, M. Komodromos, K. Kalli, A. Quadir, and B. M. A. Rahman, "Dispersion characteristics of plasmonic waveguides for THz waves," in *Proc. SPIE Optics and Optoelectronics*, Prague, 2013.

Chapter 2

Finite Difference Time Domain Method

The four main categories of numerical methods used in computational electromagnetics are differential equation, integral equation methods, mode matching, and numerical methods based on asymptotic approximations. The Finite-Difference Time-Domain (FDTD) Method is based on the approximation of derivatives by finite differences. Essentially the algorithm divides the problem geometry into a spatial grid where electric and magnetic fields are placed at discrete positions in space, and Maxwell's equations are solved in time at discrete time instances. This can be implemented by applying finite-difference approximations to the time and space derivatives appearing in Maxwell's equations, thus constructing a time marching algorithm that simulates the progression of the fields in time [1]. In the following sections the theory of the finite differences method is outlined.

2.1 Finite-Differences Approximation and Numerical Differentiation

The definition of the derivative of a continuous function $f(x)$ sampled at discrete points can be expressed as

$$f'(x) = \lim_{\Delta x \to 0} \frac{f(x + \Delta x) - f(x)}{\Delta x} \qquad (2.1)$$

Given that Δx is a small non-zero finite value, then the derivative of the function $f(x)$ can be approximated to

$$f'(x) \approx \frac{f(x+\Delta x) - f(x)}{\Delta x} \qquad (2.2)$$

Equation (2.2) is called the *forward difference* formula and is used to evaluate $f'(x)$ between the forward point $f(x+\Delta x)$ and the current point $f(x)$, where the prime identifies the first derivative.

Similarly by using the backward point $f(x-\Delta x)$ the *backward difference* formula can be obtained, such that

$$f'(x) \approx \frac{f(x) - f(x-\Delta x)}{\Delta x} \qquad (2.3)$$

Finally by combining equations (2.2) and (2.3) a formula can be obtained for approximating $f'(x)$ by averaging the forward and backward difference formulae.

$$f'(x) \approx \frac{f(x+\Delta x) - f(x-\Delta x)}{2\Delta x} \qquad (2.4)$$

Equation (2.4) is called the *central difference* formula due to the averaging scheme employed.

In finite differences a Taylor's expansion of a function $u(x,t_n)$ about the space point x_i to the space point $x_i + \Delta x$, keeping time fixed at t_n yields:

$$u(x_i + \Delta x)\Big|_{t_n} = u\Big|_{x_i,t_n} + \Delta x \cdot \frac{\partial u}{\partial x}\Big|_{x_i,t_n} + \frac{(\Delta x)^2}{2} \cdot \frac{\partial^2 u}{\partial x^2}\Big|_{x_i,t_n} + \frac{(\Delta x)^3}{6} \cdot \frac{\partial^3 u}{\partial x^3}\Big|_{x_i,t_n}$$
$$+ \frac{(\Delta x)^4}{24} \cdot \frac{\partial^4 u}{\partial x^4}\Big|_{\xi_i,t_n} \qquad (2.5)$$

where the last term is the error term and ξ_1 is a point in space located between x_i and $x_i + \Delta x$. Similarly consider the Taylor's expansion about the space point x_i to the space point $x_i - \Delta x$:

$$u(x_i - \Delta x)\Big|_{t_n} = u\Big|_{x_i,t_n} - \Delta x \cdot \frac{\partial u}{\partial x}\Big|_{x_i,t_n} + \frac{(\Delta x)^2}{2} \cdot \frac{\partial^2 u}{\partial x^2}\Big|_{x_i,t_n} - \frac{(\Delta x)^3}{6} \cdot \frac{\partial^3 u}{\partial x^3}\Big|_{x_i,t_n}$$
$$+ \frac{(\Delta x)^4}{24} \cdot \frac{\partial^4 u}{\partial x^4}\Big|_{\xi_2,t_n} \quad (2.6)$$

where the last term is the error term and ξ_2 is a point in space located between x_i and $x_i - \Delta x$. Now, using the mean value theorem and adding equations (2.5) and (2.6) yields

$$u(x_i + \Delta x)\Big|_{t_n} + u(x_i - \Delta x)\Big|_{t_n} = 2 \cdot u\Big|_{x_i,t_n} + (\Delta x)^2 \cdot \frac{\partial^2 u}{\partial x^2}\Big|_{x_i,t_n} + \frac{(\Delta x)^4}{12} \cdot \frac{\partial^4 u}{\partial x^4}\Big|_{\xi_3,t_n} \quad (2.7)$$

where the last term is the error term and ξ_3 is a point in space located between $x_i - \Delta x$ and $x_i + \Delta x$. Rearranging equation (2.7) results in

$$\frac{\partial^2 u}{\partial x^2}\Big|_{x_i,t_n} = \left[\frac{u(x_i + \Delta x) - 2 \cdot u(x_i) + u(x_i - \Delta x)}{(\Delta x)^2} \right]_{t_n} + O\Big[(\Delta x)^2\Big] \quad (2.8)$$

where $O\Big[(\Delta x)^2\Big]$ is a notation for the remainder term, which approaches to zero as the square of the space increment Δx. Equation (2.8) is commonly referred to as a second-order accurate, central difference approximation to second partial space derivative of u. Thus, the latest value of the function u is obtained by

$$u_i^{n+1} \cong (c\Delta t)^2 \left[\frac{u_{i+1}^n - 2 \cdot u_i^n + u_{i-1}^n}{(\Delta x)^2} \right] + 2 \cdot u_i^n - u_i^{n-1} \quad (2.9)$$

where the subscript i denotes the space position, with Δx space increment, and the superscript n is the time observation point, with Δt time step. In terms of all subsequent finite-differences expressions, the notation u_i^n denotes a field quantity calculated at the space point $x_i = i\Delta x$ and at time point $t_n = n\Delta t$. Applying the same principle in equation (2.4) the derivative $f'(x)$ can be expressed as

$$f'(x) = \frac{f(x+\Delta x) - f(x-\Delta x)}{2\Delta x} + O\left[(\Delta x)^2\right] \qquad (2.10)$$

Based on the second-order accurate formula (2.10) the error introduced is proportional to square of the sampling rate. Hence, if the sampling period is decreased by half, the error is reduced by a factor of four.

Consider a function $f(x) = \sin(x) \cdot e^{-0.4x}$ illustrated in Figure 2.1, where the exact first-order derivative is given by $f'(x) = \cos(x) \cdot e^{-0.4x} - 0.4 \cdot \sin(x) \cdot e^{-0.4x}$. The function is sampled at $\Delta x = \pi/5$, and approximate derivatives are calculated based on the forward, backward and central difference formulae plotted in Figure 2.2. Moreover, the approximate derivatives and error are calculated also for a sampling period of $\Delta x = \pi/10$. The results are illustrated in the following figures:
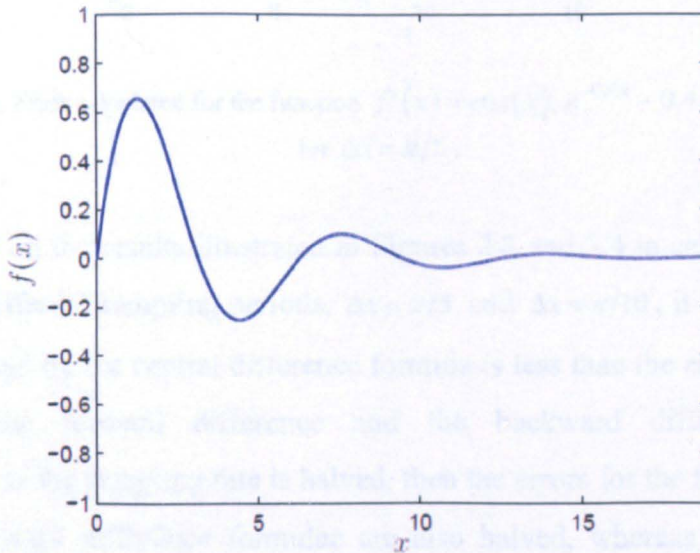
Figure 2.1. Output of the function $f(x) = \sin(x)e^{-0.4x}$.
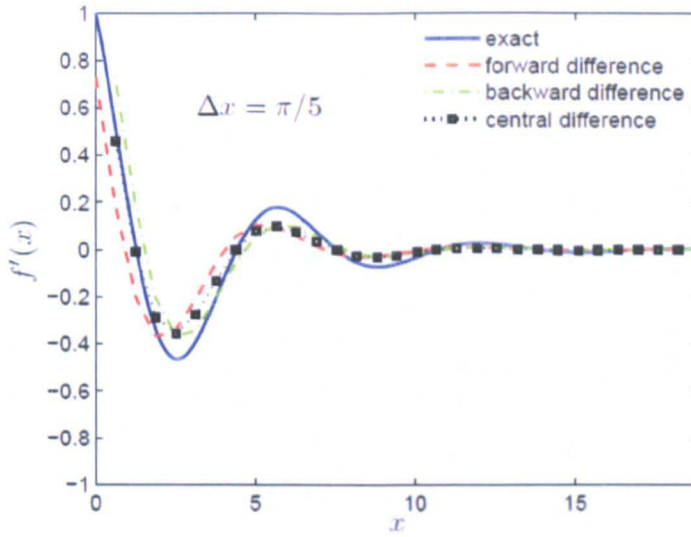
Figure 2.2. Finite differences for the function $f'(x) = \cos(x) \cdot e^{-0.4x} - 0.4 \cdot \sin(x) \cdot e^{-0.4x}$.
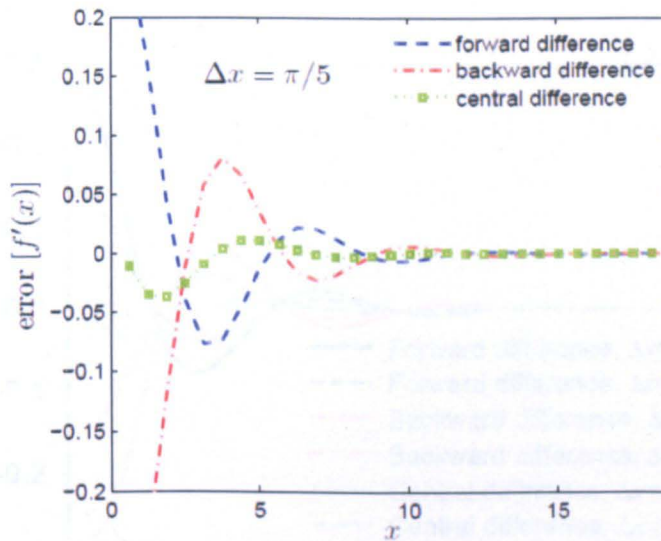
Figure 2.3. Error calculated for the function $f'(x) = \cos(x) \cdot e^{-0.4x} - 0.4 \cdot \sin(x) \cdot e^{-0.4x}$
for $\Delta x = \pi/5$.

Based on the results illustrated in Figures 2.3 and 2.4 in calculating the error for the two different sampling periods, $\Delta x = \pi/5$ and $\Delta x = \pi/10$, it is evident that the error introduced by the central difference formula is less than the error introduced by calculating the forward difference and the backward difference formulae. Furthermore, as the sampling rate is halved, then the errors for the forward difference and the backward difference formulae are also halved, whereas the error for the central difference is reduced by a factor of four. The errors for the two sampling rates for each of the three finite difference formulae are plotted in Figure 2.5
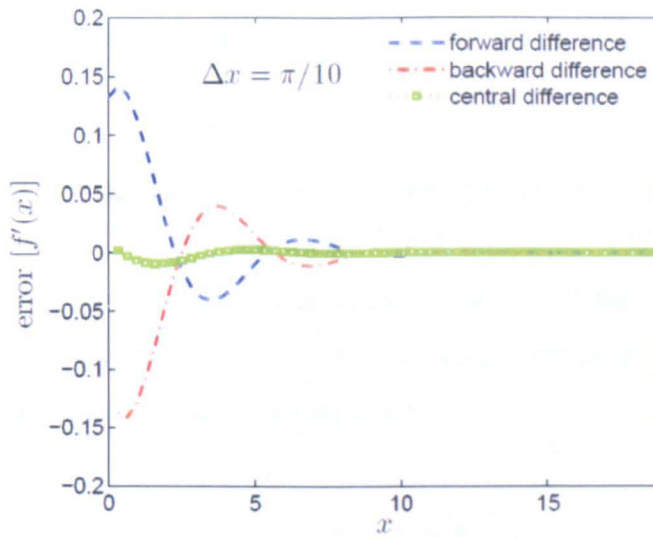
Figure 2.4. Error calculated for the function $f'(x) = \cos(x) \cdot e^{-0.4x} - 0.4 \cdot \sin(x) \cdot e^{-0.4x}$ for $\Delta x = \pi/10$.
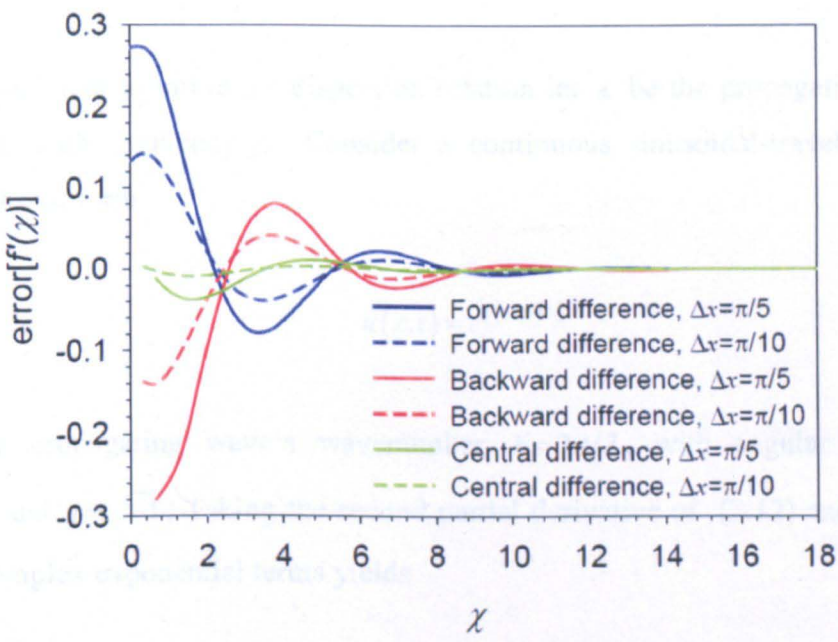
Figure 2.5. Finite differences formulae error calculated for $\Delta x = \pi/5$ and $\Delta x = \pi/10$ sampling rates.

2.2 Finite-Differences Approximation of the Scalar Wave Equation

Finite differences are applied to obtain a basic partial differential equation that describes wave motion of the one-dimensional numerical FDTD solutions. The results obtained here are to show the numerical stability of the solutions as well to identify numerical dispersion and numerical phase artifacts [2]. Consider the following one-dimensional scalar wave equation

$$\frac{\partial^2 u}{\partial t^2} = c^2 \cdot \frac{\partial^2 u}{\partial x^2} \qquad (2.11)$$

where c is the speed of light in free space and $u = u(x,t)$.

In order to examine the dispersion relation let λ be the propagating wave's wavelength with frequency f. Consider a continuous sinusoidal-travelling wave given in phasor form

$$u(x,t) = e^{j(\omega t - kx)} \qquad (2.12)$$

where the propagating wave's wavenumber $k = 2\pi/\lambda$, with angular frequency $\omega = 2\pi f$, and $j = \sqrt{-1}$. Taking the second partial derivative of (2.12) and factoring out any complex exponential terms yields

$$-\omega^2 = c^2 \cdot \left(-k^2\right)$$
$$\omega^2 = c^2 \cdot k^2 \quad \rightarrow \quad k = \pm\omega/c \qquad (2.13)$$

where the signs indicate the wave propagation in the $+x$-direction or $-x$-direction.

The wave phase velocity is defined as

$$v_p = \frac{\omega}{k} = \pm c \qquad (2.14)$$

indicating that it is a constant, regardless of the frequency. Furthermore by considering the angular frequency to be a function of the wavenumber $\omega = \omega(k)$ and differentiating based on the following equation

$$v_g = \frac{d\omega}{dk} \qquad (2.15)$$

yields the group velocity,

$$v_g = \frac{d\omega}{dk} = \frac{2c^2 k}{2\omega} = \frac{c^2}{\omega} \cdot \left(\pm \frac{\omega}{c} \right) = \pm c \qquad (2.16)$$

showing that the group velocity in this case is a constant $\pm c$, and independent of the frequency for dispersionless propagating waves with constant phase velocity.

The general solution for the numerical dispersion relation given (2.12) and taking into account that $\tilde{k} = \tilde{k}_{real} + j\tilde{k}_{imag}$ be the possibly complex-valued wavenumber results in

$$u_i^n = e^{j(\omega t - kx)} = e^{j\left[\omega n\Delta t - \left(\tilde{k}_{real} + j\tilde{k}_{imag}\right)i\Delta x\right]} = e^{\tilde{k}_{imag} \cdot i \cdot \Delta x} \cdot e^{j\left(\omega n\Delta t - \tilde{k}_{real}\, i\Delta x\right)} \qquad (2.17)$$

where $j = \sqrt{-1}$ and i refers the position in space. By evaluating (2.17) we can examine the grid space resolution based on three different cases. In this first case the equation is evaluated for very fine sampling in time and space $(\Delta t \to 0, \Delta x \to 0)$. In the second case the equation is evaluated based on the *magic time-step* where $(c\Delta t = \Delta x)$, and finally the equation is tested for a dispersive wave propagation. In all three cases, the real wavenumbers are evaluated and the numerical phase velocities are calculated in terms of c.

The numerical travelling wave equation of (2.17) can now be substituted into the finite differences equation (2.9). After factoring out the exponential terms, and grouping the space and time terms, Euler's identity is applied to the complex exponentials [2]. This leads to the equation of the general dispersion artefact where the wavenumber $\tilde{k}$ is given by

$$\tilde{k} = \frac{1}{\Delta x}\cos^{-1}\left\{1+\left(\frac{\Delta x}{c\Delta t}\right)^2 \cdot \left[\cos(\omega\Delta t)-1\right]\right\} \qquad (2.18)$$

Given the above evaluations the results indicate that the grid space resolution directly impacts the numerical phase velocity. Based on [3] let the stability or the Courant-Friedrichs-Lewy (CFL) factor be

$$S = \frac{c\Delta t}{\Delta x} \qquad (2.19)$$

Let the grid sampling resolution in space cells per free-space wavelength be

$$N_\lambda = \frac{\lambda_0}{\Delta x} \qquad (2.20)$$

Now based on the classic definition of the phase velocity for the continuous-wave equation (2.14) the numerical phase velocity for the real-numerical-wavenumber domain is given by

$$\tilde{v}_p = \frac{\omega}{\tilde{k}_{real}} \qquad (2.21)$$

The following figure illustrates the numerical phase velocity normalised to the speed of light and the attenuation constant normalised to Δx versus the grid sampling density in points per free-space wavelength for a Courant stability factor of $S = 0.5$ and $S = 1/\sqrt{2}$.
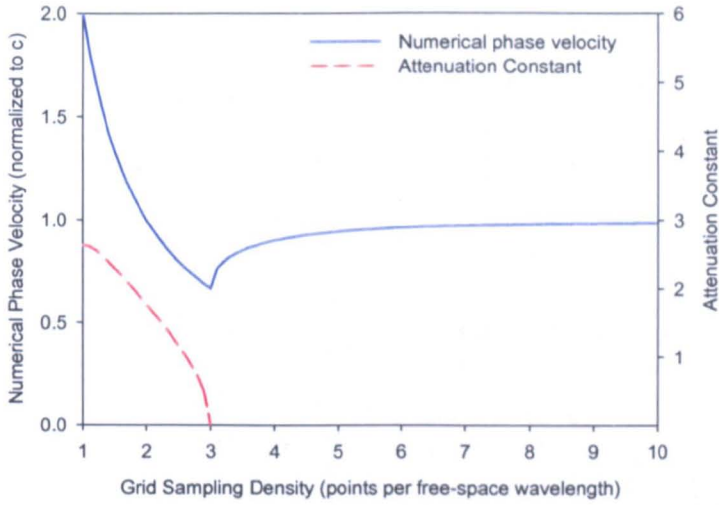
Figure 2.6. Numerical phase velocity $\widetilde{v}_p/c$ and attenuation constant per grid cell $a\Delta x$ for $S = 0.5$.
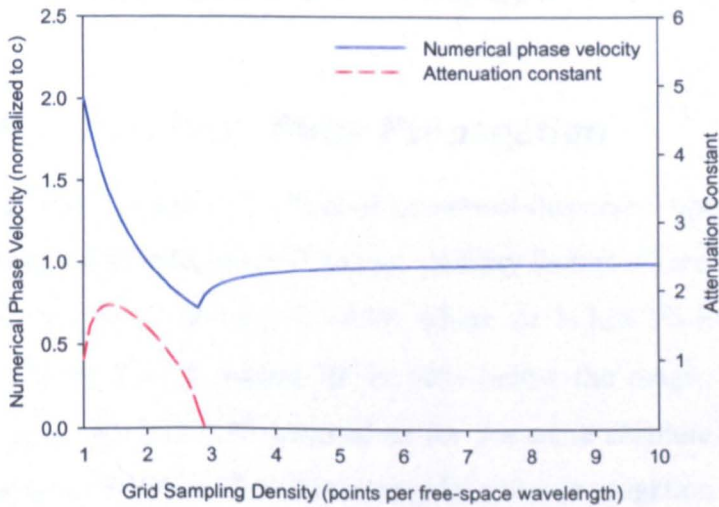
Figure 2.7. Numerical phase velocity $\widetilde{v}_p/c$ and attenuation constant per grid cell $a\Delta x$ for $S = 1/\sqrt{2}$.

Given the results illustrated in Figures 2.6 and 2.7, it appears that initially the numerical phase velocity exceeds c for $N_\lambda < 2$ and reaches its maximum for $N_\lambda = 1$. Moreover it appears that evanescent wave modes are propagating at superluminal speed, but are rapidly attenuated.

In Figure 2.8 below, the percentage error of the numerical phase velocity relative to the free-space speed of light using a grid sampling density $N_\lambda \le 3$.
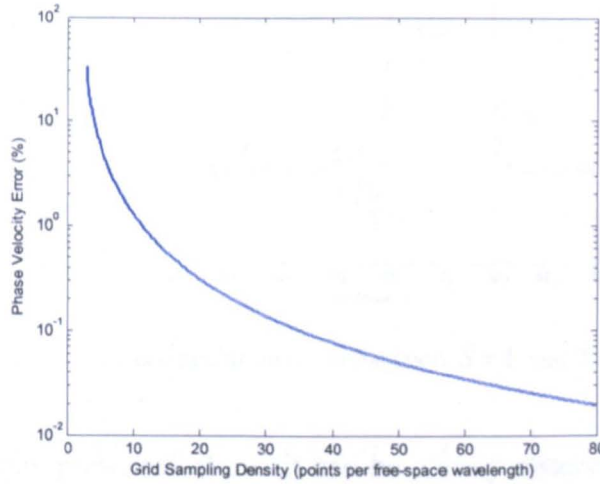
Figure 2.8. The percentage error in the numerical phase velocity relative to the free-speed of light, for $3 \le N_\lambda \le 80$ and $S = 0.5$.

2.3 Numerical Results of Pulse Propagation

The following graphs illustrate the effect of numerical dispersion upon a rectangular pulse in free-space for three different Courant stability factors where $S = 1$ and Δt is set to the magic time step $c\Delta t = \Delta x$, $S = 0.99$, where Δt is just 1% below the magic time-step, and finally $S = 0.5$ where Δt is 50% below the magic time-step. The snapshots in Figures 2.9 and 2.10 were taken for the same absolute time step ($n = 160$) for comparison, for a 40-cell-wide rectangular pulse propagation in free space.
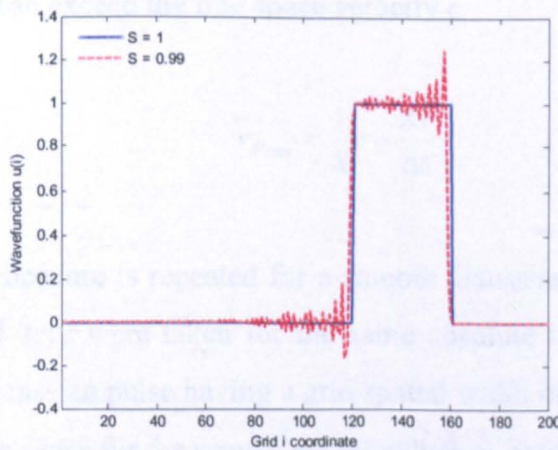
Figure 2.9. Rectangular pulse propagation for $S = 1$ and $S = 0.99$.

25
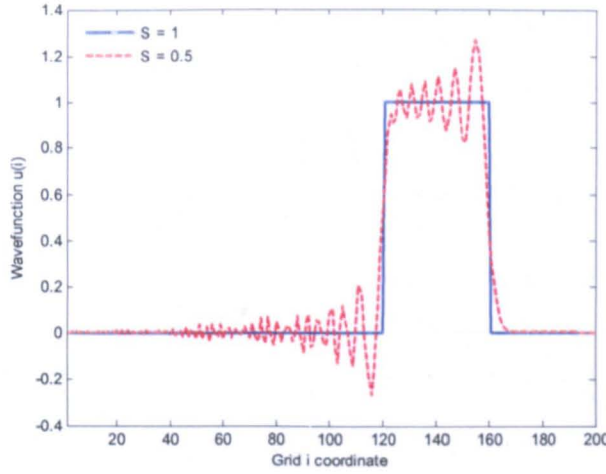
Figure 2.10. Rectangular pulse propagation $S = 1$ and $S = 0.5$.

In the graphs presented above it can be clearly observed that for a courant factor of $S = 1$ the rectangular pulse is preserved. This is due to fact that the time-step discontinuities of the propagating pulse are modelled perfectly. In this case, this is expected since for $S = 1$, the numerical phase velocity is $\tilde{v}_p \equiv c$. In Figure 2.9, for $S = 0.99$ when Δt is just 1% below the magic time-step, the time-step discontinuities generate a "ringing" effect at the leading and trailing edges of the pulse. This represents a time-retarded propagation due to the time-step discontinuities, as the numerical phase velocity is now $\tilde{v}_p < c$. Furthermore, in Figure 2.10, although the "ringing" effect is significantly greater for $S = 0.5$ when Δt is just 50% below the magic time-step, a weak superluminal response also appears propagating just ahead of the leading edge as the numerical phase velocity is $\tilde{v}_p > c$. This is justified through the dispersion theory described earlier, where the maximum possible phase velocity in the grid can exceed the free space velocity c

$$\tilde{v}_{P_{max}} = \frac{1}{S}c = \frac{\Delta x}{\Delta t} \tag{2.22}$$

The same procedure is repeated for a smooth Gaussian pulse. The snapshots in Figures 2.11 and 2.12 were taken for the same absolute time step ($n = 160$) for comparison, for a Gaussian pulse having a grid spatial width of 40 grid cells between the $1/e$ points in free space for the same Courant values as before.

26
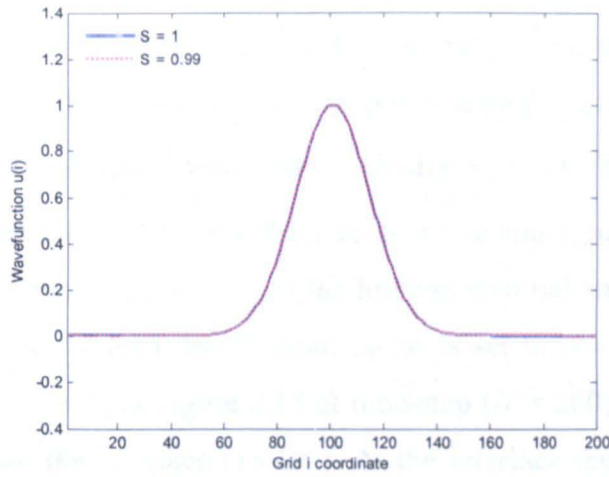
Figure 2.11. Gaussian pulse propagation for $S = 1$ and $S = 0.99$.
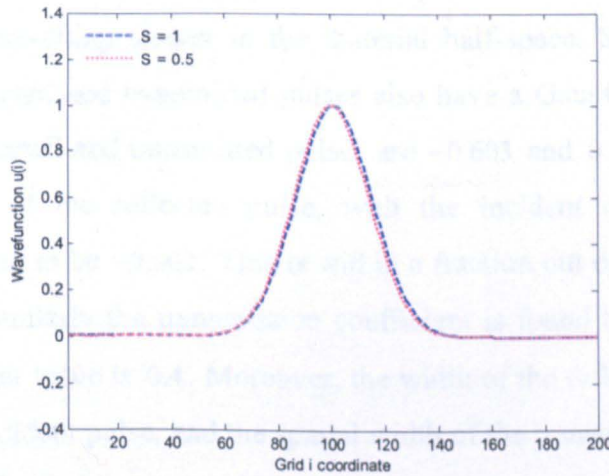
Figure 2.12. Gaussian pulse propagation for $S = 1$ and $S = 0.5$.

In Figures 2.11 and 2.12, it is evident that the Gaussian pulse undergoes significantly less distortion than the rectangular pulse. In fact in Figure 2.11, the pulse for $S = 0.99$ shows almost no significant difference relative to the propagation of the pulse for $S = 1$. Similarly, in Figure 2.12 for $S = 0.5$, the Gaussian pulse propagation shows only a slight retardation relative to $S = 1$. All these phenomena are due to the fact that the entire spectrum of wavelengths propagating is properly evaluated and well resolved within the grid's sampling process. This shows that the Gaussian pulse is preserved while propagating within the grid.

The effect of simply modifying the Courant number to model phase-velocity discontinuity is shown in the next figure. A Gaussian pulse with unit amplitude and spatial width of 40 grid cells between the $1/e$ points is propagating from free space to a lossless material half-space with phase velocity $v_p = c/4$. This is simulated by setting the Courant factor $S = 1$ for the free space region (grid coordinate $i = 1$ to $i = 139$) with refractive index $n = 1$. For the lossless material half-space region (grid coordinate $i = 140$ to $i = 200$), the Courant factor is set to $S = 0.25$ equivalent to a refractive index of $n = 4$. In Figure 2.13 at time-step ($N = 260$), the Gaussian pulse has already reached the interface ($i = 139$). At the interface the Gaussian pulse has experienced partial reflection and transmission. In the material half-space where $n = 4$, the wavelength is $\lambda_g = \lambda/4$, and the phase velocity is $v_g = v_p/4$, this also causes the pulse to be travelling slower in the material half-space. Since the material is lossless, the reflected and transmitted pulses also have a Gaussian shape. The peak values of the reflected and transmitted pulses are -0.603 and 0.399 respectively. By taking the ratio of the reflected pulse, with the incident pulse, the reflection coefficient is found to be -0.603. This is within a fraction out of the exact analytical value of -0.6. Similarly the transmission coefficient is found to be 0.399, whereas the exact analytical value is 0.4. Moreover, the width of the reflected pulse is almost identical to the incident pulse, and the spatial width of the transmitted pulse is almost $1/4$ the width of the incident pulse. This proves that the numerical model can be used to obtain the scattering parameters of different structures modelled.
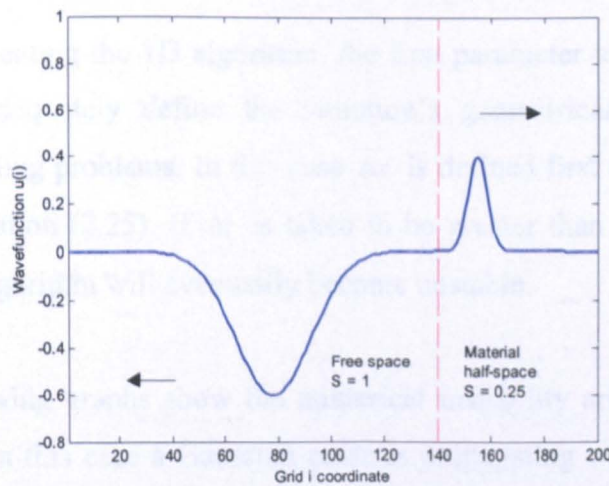
Figure 2.13. Reflection and transmission of a Gaussian pulse propagating from free space to a material half-space having $v_p = c/4$.

The results for the 1D propagation of the wave in Figure 2.13 are also related to the Fresnel transmission and reflection coefficients [4], where the reflection (r) and transmission (t) coefficient are given by

$$r = \frac{E_r}{E_i} = \frac{n_i \cos(\theta_i) - n_t \cos(\theta_t)}{n_i \cos(\theta_i) + n_t \cos(\theta_t)} \qquad (2.23)$$

$$t = \frac{E_t}{E_i} = \frac{2n_i \cos(\theta_i)}{n_i \cos(\theta_i) - n_t \cos(\theta_t)} \qquad (2.24)$$

where the subscripts i, r, and t denote the incident, reflected and transmitted components, E is the electric field, n is the index of refraction, and θ is the angle of incidence. Given the equations (2.23) and (2.24), for the 1D case, for a wave approaching the interface between the two regions described earlier, where $n_i = 1$ and $n_t = 4$ (material half-space) with $0°$ degrees angle of incidence, the transmission and reflection coefficients are equal to -0.6 and 0.4 respectively.

So far, examples of numerical stability involving the Courant factor $S \leq 1$ have been analysed. Based on the numerical propagation velocity equation (2.21) and the Courant stability factor (2.19), in defining the 1D scalar wave equation algorithm there is a limit on the relationship [3] between Δt and Δx given by

$$S = \frac{c \Delta t}{\Delta x} \leq 1 \quad \Rightarrow \quad \Delta t \leq \frac{\Delta x}{c} \qquad (2.25)$$

In implementing the 1D algorithm, the first parameter to be specified in the program is to adequately define the structure's geometrical details for wave-interaction modelling problems. In this case Δx is defined first and Δt is calculated based on the equation (2.25). If Δt is taken to be greater than the limit defined in (2.25), then the algorithm will eventually become unstable.

The following graphs show the numerical instability arising from choosing values of $S > 1$. In this case a Gaussian pulse is propagating within a uniform grid with a temporal width $40\Delta t$ between its $1/e$ points over 220 time-steps. The Courant stability factor is chosen to be $S = 1.0005$ and various snapshots of the wavefunction

$u(i)$ are taken at certain time steps. The trailing edge of the Gaussian pulse is quickly distorted due to the noise resulting from the numerical instability.
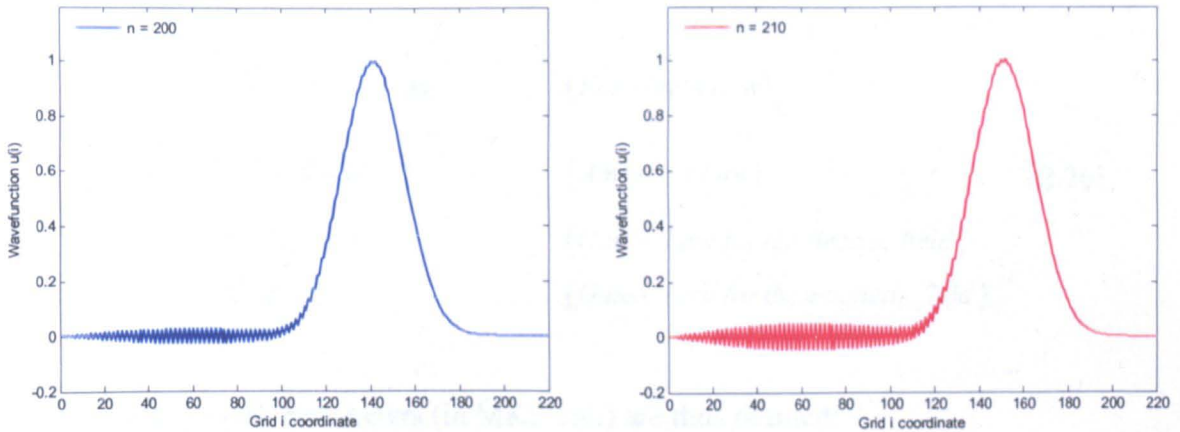
(a) Gaussian pulse at time-step $n = 200$ (b) Gaussian pulse at time-step $n = 220$

Figure 2.14. Comparison of a Gaussian pulse propagation with $S = 1.0005$.

Up to this point, examples of the numerical examples of the finite-difference time-domain method have been considered. The one dimensional wave equation has been solved using finite-differences and examined in terms of numerical stability, numerical dispersion and numerical phase velocity. Over the next sections Maxwell's equations are introduced and the FDTD method is presented.

The foundation of the FDTD electromagnetic analysis originated from Kane Yee's 1966 [1] algorithm, where a set of finite-difference equations for the time-dependent Maxwell's equations were presented. Yee's algorithm employs the second-order accurate to represent in discrete form, both in space and time, the differential and integral forms of Maxwell's equations. The FDTD method divides the three-dimensional geometry into cells to form a grid. A unit cell of this grid is called a Yee cell.

2.4 Maxwell's Equations

The time-dependent Maxwell's equations in differential form are presented as the starting point of the FDTD algorithm

$$\frac{\partial \vec{B}}{\partial t} = -\nabla \times \vec{E} - \vec{M} \qquad (Faraday's\ Law)$$

$$\frac{\partial \vec{D}}{\partial t} = \nabla \times \vec{H} - \vec{J} \qquad (Ampere's\ Law) \qquad (2.26)$$

$$\nabla \cdot \vec{D} = \rho_e \qquad (Gauss'\ Law\ for\ the\ electric\ field)$$

$$\nabla \cdot \vec{B} = 0 \qquad (Gauss'\ Law\ for\ the\ magnetic\ field)$$

where the following parameters (in MKS unit) are thus defined:

$\vec{E}$: electric field (volts/meter)

$\vec{D}$: electric flux density $(\text{coulombs/meter}^2)$

$\vec{H}$: magnetic field (amperes/meter)

$\vec{B}$: magnetic flux density (webers/meter^2)

$\vec{J}$: electric current density (amperes/meter^2)

$\vec{M}$: equivalent magnetic current density (volts/meter^2)

ρ_e : electric charge density $(\text{coulombs/meter}^3)$

For linear, isotropic, nondispersive materials the following relations using simple proportions hold

$$\vec{D} = \varepsilon \cdot \vec{E} = \varepsilon_r \varepsilon_0 \cdot \vec{E}$$
$$\vec{B} = \mu \cdot \vec{H} = \mu_r \mu_0 \cdot \vec{H} \qquad (2.27)$$

where

ε : electric permitivity (farads/meter)

ε_r : relative permittivity (dimensionless scalar)

ε_0 :   free-space permitivity $\left(8.854 \times 10^{-12} \text{ farads/meter}\right)$

μ :   magnetic permeability (henrys/meter)

μ_r :   relative permeability (dimensionless scalar)

μ_0 :   free-space permeability $\left(4\pi \times 10^{-7} \text{ henrys/meter}\right)$

Taking into consideration that the electric current density is the sum of the conduction current density and the impressed current density (acting as independent source), and the magnetic field density is the sum of the magnetic current density and the impressed magnetic source yields

$$\vec{J} = \vec{J}_{source} + \sigma \vec{E}$$
$$\overline{M} = \overline{M}_{source} + \sigma^* \overline{H} \tag{2.28}$$

where

σ :   electric conductivity (siemens/meter)

σ^* :   equivalent magnetic loss (ohms/meter)

Finally, by substituting (2.27) and (2.28) into equation (2.26) Maxwell's curl equations can be expressed as

$$\frac{\partial \overline{H}}{\partial t} = -\frac{1}{\mu} \nabla \times \vec{E} - \frac{1}{\mu}\left(\overline{M}_{source} + \sigma^* \overline{H}\right) \tag{2.29}$$

$$\frac{\partial \overline{E}}{\partial t} = -\frac{1}{\varepsilon} \nabla \times \overline{H} - \frac{1}{\varepsilon}\left(\vec{J}_{source} + \sigma \vec{E}\right) \tag{2.30}$$

The vector components of the curl operators in the equations can be represented with the following six scalar equations in Cartesian coordinates (x, y, z):

$$\frac{\partial H_x}{\partial t} = \frac{1}{\mu}\left[\frac{\partial E_y}{\partial z} - \frac{\partial E_z}{\partial y} - \left(M_{source_x} + \sigma^* H_x\right)\right] \tag{2.31}$$

$$\frac{\partial H_y}{\partial t} = \frac{1}{\mu}\left[\frac{\partial E_z}{\partial x} - \frac{\partial E_x}{\partial z} - \left(M_{source_y} + \sigma^* H_y\right)\right] \qquad (2.32)$$

$$\frac{\partial H_z}{\partial t} = \frac{1}{\mu}\left[\frac{\partial E_x}{\partial y} - \frac{\partial E_y}{\partial x} - \left(M_{source_z} + \sigma^* H_z\right)\right] \qquad (2.33)$$

$$\frac{\partial E_x}{\partial t} = \frac{1}{\varepsilon}\left[\frac{\partial H_z}{\partial y} - \frac{\partial H_y}{\partial z} - \left(J_{source_x} + \sigma E_x\right)\right] \qquad (2.34)$$

$$\frac{\partial E_y}{\partial t} = \frac{1}{\varepsilon}\left[\frac{\partial H_x}{\partial z} - \frac{\partial H_z}{\partial x} - \left(J_{source_y} + \sigma E_y\right)\right] \qquad (2.35)$$

$$\frac{\partial E_z}{\partial t} = \frac{1}{\varepsilon}\left[\frac{\partial H_y}{\partial x} - \frac{\partial H_x}{\partial y} - \left(J_{source_z} + \sigma E_z\right)\right] \qquad (2.36)$$

The six coupled partial differential equations (2.31) – (2.36) form a system that can be used as a basis for the FDTD algorithm for electromagnetic wave interactions with objects in three-dimensional space.

2.5 FDTD Algorithm

Yee's algorithm uses Maxwell's curl equations to solve for both the electric and magnetic field in space and time. The $\vec{E}$ and $\vec{H}$ fields are arranged such that every $\vec{E}$ electric field vector is surrounded by four circulating $\vec{H}$ magnetic field vectors. Similarly, if the neighbouring cells are added to the figure, every $\vec{H}$ magnetic field vector is surrounded by four circulating $\vec{E}$ components. The arrangement of the field vector components are illustrated in Figure 2.15 below.

Yee's algorithm centres its $\vec{E}$ and $\vec{H}$ components in a three-dimensional space so that electric and magnetic field components are interleaved in space to permit a natural satisfaction of tangential field continuity conditions at media interfaces. The algorithm evaluates $\vec{E}$ and $\vec{H}$ components at alternate half-time steps. This means that all of the $\vec{E}$ computations in the modelled space are completed and stored in memory for a particular time point using previously computed $\vec{H}$ data. The positions of the various $\vec{E}$ field components are in the middle of the edges, where each $\vec{E}$ field component is surrounded by four $\vec{H}$ field vector components.
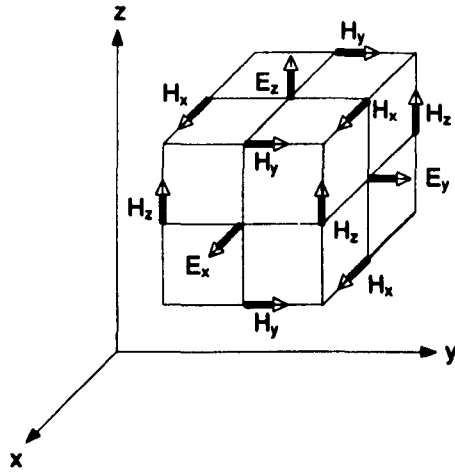
Figure 2.15. A three-dimensional arrangement of field components on a Yee cell.

Yee's leapfrog algorithm solves for all of the $\vec{E}$ components at a given time-step based on $\vec{H}$ data that has been previously computed and stored in memory. Then the magnetic field is computed at the next time-step using the $\vec{E}$ data just computed. The process is repeated until the time-stepping is concluded. The following figure illustrates the space-time steps for a one-dimensional-wave propagation, thus showing the half space-step and half time-step for the space and time derivatives. The magnetic and electric fields are zero everywhere in the grid as an initial condition.
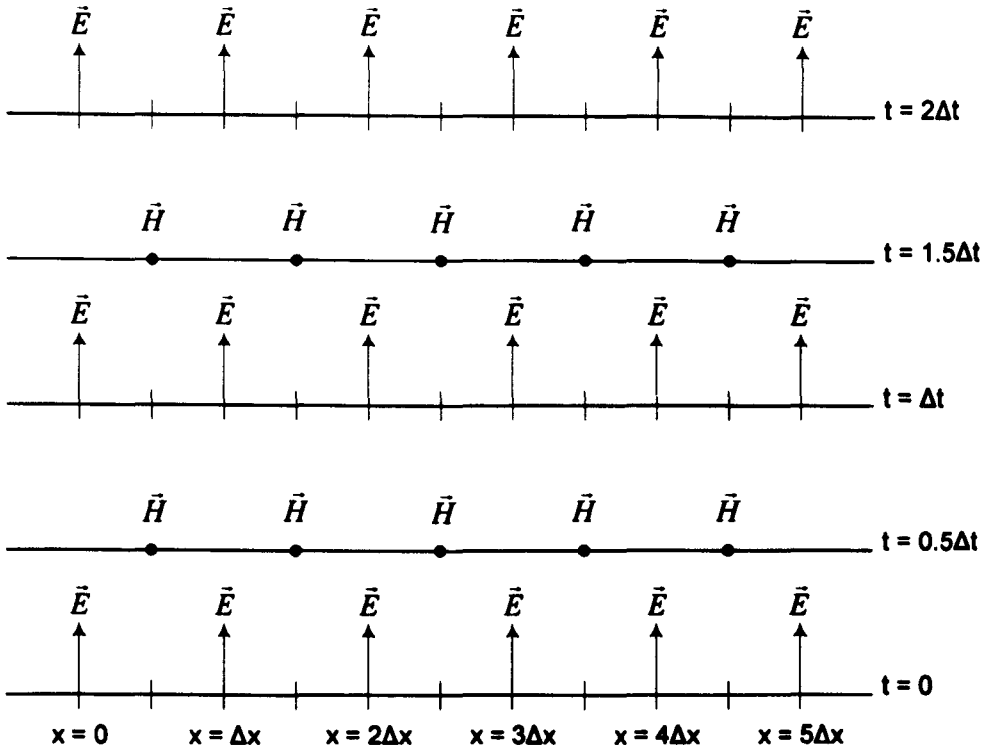
Figure 2.16. Space-time diagram for the one-dimensional wave propagation.

As the algorithm runs, at each time-step the system of the electric and magnetic field vector components are updated based on the system of equations, which is fully explicit. In this case, there is no need to solve a system of linear equations and the required computer memory and time is proportional to the size of the computational domain, which is based on the size of the structure under consideration. The computational domain is the space under consideration where the simulation will be performed.

The following notation for finite-differences is introduced for points and functions in space and time using a rectangular lattice

$$(i,j,k) = (i\Delta x, j\Delta y, k\Delta z) \qquad (2.37)$$

$$u(i\Delta x, j\Delta y, k\Delta z, n\Delta t) = u_{i,j,k}^{n} \qquad (2.38)$$

where Δx, Δy, Δz are the respective space increments in the x, y, and z directions, and i, j, and k are integers. Furthermore Δt is the time increment and n is an integer.

35

Finally, the six equations ((2.31) – (2.36)) presented in section 2.4 can be solved using finite differences to construct the FDTD vector equations. Before the time-stepping algorithm begins, the general updating equations are defined and stored. The updating coefficients are given by the following set of equations

Updating Coefficients – E-Field Component Location (i,j,k)

$$C_a\big|_{i,j,k} = \left(1 - \frac{\sigma_{i,j,k} \cdot \Delta t}{2 \cdot \varepsilon_{i,j,k}}\right) \bigg/ \left(1 + \frac{\sigma_{i,j,k} \cdot \Delta t}{2 \cdot \varepsilon_{i,j,k}}\right) \qquad (2.39)$$

$$C_{b_1}\big|_{i,j,k} = \left(\frac{\Delta t}{\varepsilon_{i,j,k} \cdot \Delta x}\right) \bigg/ \left(1 + \frac{\sigma_{i,j,k} \cdot \Delta t}{2 \cdot \varepsilon_{i,j,k}}\right) \qquad (2.40)$$

$$C_{b_2}\big|_{i,j,k} = \left(\frac{\Delta t}{\varepsilon_{i,j,k} \cdot \Delta y}\right) \bigg/ \left(1 + \frac{\sigma_{i,j,k} \cdot \Delta t}{2 \cdot \varepsilon_{i,j,k}}\right) \qquad (2.41)$$

Updating Coefficients – H-Field Component Location (i,j,k)

$$D_a\big|_{i,j,k} = \left(1 - \frac{\sigma^*_{i,j,k} \cdot \Delta t}{2 \cdot \mu_{i,j,k}}\right) \bigg/ \left(1 + \frac{\sigma^*_{i,j,k} \cdot \Delta t}{2 \cdot \mu_{i,j,k}}\right) \qquad (2.42)$$

$$D_{b_1}\big|_{i,j,k} = \left(\frac{\Delta t}{\mu_{i,j,k} \cdot \Delta x}\right) \bigg/ \left(1 + \frac{\sigma^*_{i,j,k} \cdot \Delta t}{2 \cdot \mu_{i,j,k}}\right) \qquad (2.43)$$

$$D_{b_2}\big|_{i,j,k} = \left(\frac{\Delta t}{\mu_{i,j,k} \cdot \Delta y}\right) \bigg/ \left(1 + \frac{\sigma^*_{i,j,k} \cdot \Delta t}{2 \cdot \mu_{i,j,k}}\right) \qquad (2.44)$$

where the subscripts denote the two possible lattice increments used for the finite-differences in each field vector component calculation. In the case of a cubic lattice then $\Delta x = \Delta y = \Delta z$ and $\Delta_1 = \Delta_2 = \Delta$, thus $C_{b_1} = C_{b_2}$ and $D_{b_1} = D_{b_2}$. The updating coefficients are used for calculating the electric and magnetic field vector equations for regions having continuous variation of material properties with spatial position.

The finite-difference expressions can now be expressed for space region with a finite number of objects with distinct electrical properties as

$m = \text{MEDIA}_{E_x|_{i,j+1/2,k+1/2}}$

$$E_x\big|_{i,j+1/2,k+1/2}^{n+1/2} = C_a(m) \cdot E_x\big|_{i,j+1/2,k+1/2}^{n+1/2} + C_b(m) \cdot \Big[H_z\big|_{i,j+1,k+1/2}^{n} - \tag{2.45}$$

$$H_z\big|_{i,j,k+1/2}^{n} + H_y\big|_{i,j+1/2,k}^{n} - H_y\big|_{i,j+1/2,k+1}^{n} - J_{source_x}\big|_{i,j+1/2,k+1/2}^{n} \cdot \Delta \Big]$$

$m = \text{MEDIA}_{E_y|_{i-1/2,j+1,k+1/2}}$

$$E_y\big|_{i-1/2,j+1,k+1/2}^{n+1/2} = C_a(m) \cdot E_y\big|_{i-1/2,j+1,k+1/2}^{n-1/2} + C_b(m) \cdot \Big[H_x\big|_{i-1/2,j+1,k+1}^{n} - \tag{2.46}$$

$$H_x\big|_{i-1/2,j+1,k}^{n} + H_z\big|_{i-1,j+1,k+1/2}^{n} - H_z\big|_{i,j+1/2,k+1}^{n} - J_{source_y}\big|_{i-1/2,j+1,k+1/2}^{n} \cdot \Delta \Big]$$

$m = \text{MEDIA}_{E_z|_{i-1/2,j+1/2,k+1}}$

$$E_z\big|_{i-1/2,j+1/2,k+1}^{n+1/2} = C_a(m) \cdot E_z\big|_{i-1/2,j+1/2,k+1}^{n-1/2} + C_b(m) \cdot \Big[H_y\big|_{i,j+1/2,k+1}^{n} - \tag{2.47}$$

$$H_y\big|_{i-1,j+1/2,k+1}^{n} + H_x\big|_{i-1/2,j,k+1}^{n} - H_x\big|_{i-1/2,j+1,k+1}^{n} - J_{source_z}\big|_{i-1/2,j+1/2,k+1}^{n} \cdot \Delta \Big]$$

$m = \text{MEDIA}_{H_x|_{i-1/2,j+1/2,k+1}}$

$$H_x\big|_{i-1/2,j+1,k+1}^{n+1} = D_a(m) \cdot H_x\big|_{i-1/2,j+1,k+1}^{n} + D_b(m) \cdot \Big[E_y\big|_{i-1/2,j+1/2,k+3/2}^{n+1/2} - \tag{2.48}$$

$$E_y\big|_{i-1/2,j+1,k+1/2}^{n+1/2} + E_z\big|_{i-1/2,j+3/2,k+1}^{n+1/2} - E_z\big|_{i-1/2,j+3/2,k+1}^{n+1/2} - M_{source_x}\big|_{i-1/2,j+1,k+1}^{n+1/2} \cdot \Delta \Big]$$

$m = \text{MEDIA}_{H_y|_{i-1/2,j+1,k+1}}$

$$H_y\big|_{i,j+1/2,k+1}^{n+1} = D_a(m) \cdot H_y\big|_{i,j+1/2,k+1}^{n} + D_b(m) \cdot \Big[E_z\big|_{i+1/2,j+1/2,k+1}^{n+1/2} - \tag{2.49}$$

$$E_z\big|_{i-1/2,j+1/2,k+1}^{n+1/2} + E_x\big|_{i,j+1/2,k+1/2}^{n+1/2} - E_x\big|_{i,j+1/2,k+3/2}^{n+1/2} - M_{source_y}\big|_{i,j+1/2,k+1}^{n+1/2} \cdot \Delta \Big]$$

$m = \text{MEDIA}_{H_z|_{i,j+1,k+1/2}}$

$$H_z\big|_{i,j+1,k+1/2}^{n+1} = D_a(m) \cdot H_z\big|_{i,j+1,k+1/2}^{n} + D_b(m) \cdot \Big[E_x\big|_{i,j+3/2,k+1/2}^{n+1/2} - \tag{2.50}$$

$$E_x\big|_{i,j+1/2,k+1/2}^{n+1/2} + E_y\big|_{i-1/2,j+1,k+1/2}^{n+1/2} - E_y\big|_{i+1/2,j+1,k+1/2}^{n+1/2} - M_{source_z}\big|_{i,j+1,k+1/2}^{n+1/2} \cdot \Delta \Big]$$

where $\text{MEDIA}(i,j,k)$ is an integer array for each field of vector components.

It is now possible to construct the time-marching algorithm for the FDTD method using the updating equations given in (2.45) – (2.50). The following diagram illustrates explicitly the FDTD procedure. The FDTD algorithm iterations will continue until the stopping criteria defined at the beginning of the algorithm are met.
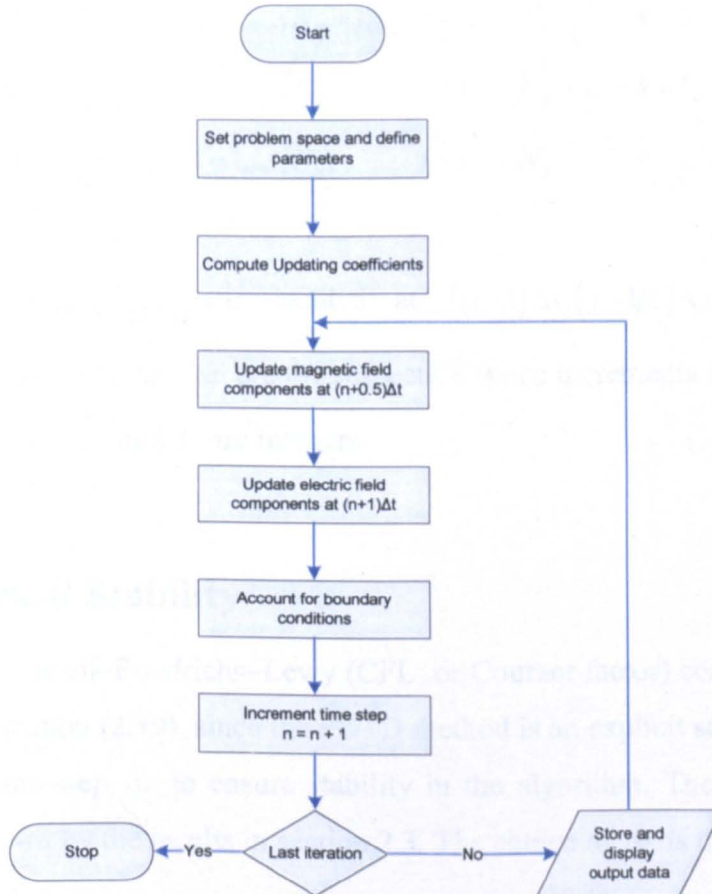
Figure 2.17. The FDTD explicit algorithm.

The first step in the algorithm is to define the problem parameters, such as the FDTD domain space – including the objects and material types, sources and boundary conditions. Next the coefficients are calculated based on the material type of the objects and the FDTD domain space. The algorithm continues by iterating and in each step the magnetic field components are calculated, then the electric field components. Finally the boundary conditions are applied to the FDTD domain space and the data can be stored at each time step or displayed.

Given the algorithm in Figure 2.17 and the updating equations of the FDTD method, for one three-dimensional Yee cell the following indexing scheme is used and applied to calculate all the necessary coefficients and fields

$$E_x\Big|_{i+1/2,j,k}^n, \qquad i=1,\ldots,N_x, \qquad j=1,\ldots,N_y+1, \qquad k=1,\ldots,N_z+1$$

$$E_y\Big|_{i,j+1/2,k}^n, \qquad i=1,\ldots,N_x+1, \qquad j=1,\ldots,N_y, \qquad k=1,\ldots,N_z+1$$

$$E_x\Big|_{i,j,k+1/2}^n, \qquad i=1,\ldots,N_x+1, \qquad j=1,\ldots,N_y+1, \qquad k=1,\ldots,N_z$$

$$H_x\Big|_{i,j+1/2,k+1/2}^{n-1/2}, \quad i=1,\ldots,N_x+1, \qquad j=1,\ldots,N_y, \qquad k=1,\ldots,N_z$$

$$H_y\Big|_{i+1/2,j,k+1/2}^{n-1/2}, \quad i=1,\ldots,N_x, \qquad j=1,\ldots,N_y+1, \qquad k=1,\ldots,N_z$$

$$H_z\Big|_{i+1/2,j+1/2,k}^{n-1/2}, \quad i=1,\ldots,N_x, \qquad j=1,\ldots,N_y, \qquad k=1,\ldots,N_z+1$$

For example $H_x\Big|_{i,j+1/2,k+1/2}^{n-1/2}$ is located at $\big((i-1)\Delta x,(j-1/2)\Delta y,(k-1/2)\Delta z\big)$ at $t=(n-1/2)\Delta t$, and Δx, Δy, Δz are the respective space increments in the x, y, and z directions, and i, j, and k are integers.

2.6 Numerical Stability

Although the Courant–Friedrichs–Lewy (CFL or Courant factor) condition has been presented in equation (2.19), since the FDTD method is an explicit scheme, there is a limit on the time step Δt to ensure stability in the algorithm. The choice of S is essential as shown by the results in section 2.3. The choice of Δt is thus given by

$$\Delta t < \frac{1}{c\sqrt{\dfrac{1}{(\Delta x)^2}+\dfrac{1}{(\Delta y)^2}+\dfrac{1}{(\Delta z)^2}}} \qquad (2.51)$$

where c is the wave propagation speed.

Hence the Courant factor from equation (2.19) is thus defined as

$$S = c\cdot\Delta t\sqrt{\dfrac{1}{(\Delta x)^2}+\dfrac{1}{(\Delta y)^2}+\dfrac{1}{(\Delta z)^2}} \qquad (2.52)$$

and the stability condition as

$$S < 1 \qquad (2.53)$$

2.7 Source Waveforms

In a FDTD simulation, sources are necessary components as they introduce electromagnetic wave excitations in the FDTD lattice for modelling various problems. Sources are divided into various classes and, depending on the type of problem to be simulated, the appropriate type of source is selected to model the physics of an electromagnetic wave.

In terms of lumped elements, two classes of sources can be found, *active* and *passive*. Active sources are voltage and current sources, whereas passive sources are resistors, inductors, and capacitors. Voltage and current sources without internal resistance are considered *hard sources*. Voltage and current sources, resistors, inductors, capacitors, and diodes are considered common lumped elements of circuit components.

Other classes of compact electromagnetic wave sources considered are the hard sourced $\bar{E}$ and $\bar{H}$ fields in one- and two-dimensional grids, $\bar{J}$ and $\bar{M}$ current sources in two- and three-dimensional space, the total-field/scattered field formulation (TF-SF) in one-, two-, and three-dimensional lattices and finally common waveguide sources.

In FDTD a wide range of sources might be selected to model a specific problem. Some common types of waveforms are Gaussian, sinusoidal, cosine modulated Gaussian or simply a unit step. Each waveform type has parameters representing its specific characteristics.

For example a Gaussian waveform can be written as a function of time as

$$f(t) = e^{-\frac{(t-t_0)^2}{\tau^2}} \qquad (2.54)$$

where τ determines the width of the Gaussian pulse and t_0 the time shift. A Gaussian pulse with a cosine function with frequency f_c can be expressed as

$$g(t) = \cos(\omega_c \cdot t) \cdot e^{-\frac{t^2}{\tau^2}} \qquad (2.55)$$

where $\omega_c = 2\pi f_c$.

The properties of the material to be modelled are specified for each cell prior to running the simulation. The material could be free-space, metal or dielectric or perfect electric conductors (PEC). With the material properties and the grid established, a source is specified. There are a number of sources that could be used to introduce a FDTD lattice to electromagnetic wave excitation in order to model engineering problems [5]. Once the source has been specified, the propagation of the wave is modelled based on the time-stepping algorithm. At each time-step the finite-difference set of equations are updated, which correspond to Maxwell's curl equations. As the wave propagates, phenomena such as induction of surface currents, scattering, penetration through apertures and cavity excitation are modelled with each time-step [6].

2.8 Absorbing Boundary Conditions

With the FDTD approach to solve electromagnetic field problems, a basic consideration is that most problems are considered to be open, that is the computational domain of the computed field is ideally unbounded. Based on this consideration the computer cannot store an unlimited amount of computed data, thus the field computation domain must be limited. However the computation zone must be large enough to include the structure of interest and a suitable boundary condition that the workspace can be terminated. The outer boundary conditions suitable to simulate the extension of the computational zone to infinity are called radiation conditions, lattice of truncation, or more commonly absorbing boundary conditions (ABC). Absorbing boundary conditions were introduced by Mur as a method of limiting the domain in which the field is computed [42, 43].

Boundary conditions have been essential in the study and simulation of electromagnetic field problems because they are used to truncate the computational domain near the target, while accurately simulating an infinite surface model. Soon after the introduction of ABCs another method was introduced to solve boundary problems. This method was called the on-surface radiation condition (OSRC) [7]. The OSRC method uses a radiation boundary operator directly on the surface of the target to reduce the frequency-domain integral equation for the scattered field to either an integration of known quantities or a second-order differential equation. This method could be used in both finite-differences and finite-element methods [8], and it is based on the optimisation of the mode-annihilating radiation boundary operators.

Although ABCs and the OSRC method provide effective reflection coefficients, the need for high-accuracy simulations required higher orders-of-magnitude performance. This is achieved with Berenger's introduction of a novel absorbing boundary condition for the FDTD in two- and three-dimensional meshes. Berenger proposed a novel technique called "perfectly matched layer (PML) for the absorption of electromagnetic waves" [9]. This technique is based on the use of an absorbing layer designed to absorb without the reflection of electromagnetic components, according to Berenger. Numerical results based on the PML technique have shown that the technique introduces a new degree of freedom in specifying loss and impedance, regardless of the angle of incidence of the wave, as well as the fact that it presents a good balance in terms of effectiveness and computational resources [10].

Berenger's PML signalled the beginning of several variations of ABCs and the extension to include other classes of problem. The technique was then extended to include the three-dimensional case [11]. For the FDTD method the Unaxial PML (UPML) technique based on Maxwell's equations, presented the same characteristics as Berenger's PML, but it was also more computationally efficient. Finally it could be extended to nonorthogonal and unstructured grid techniques [12]. The technique was generalised further to include complex frequency shifted tensor (CFS) for general media [13].

2.9 Definition of the PML Medium

The PML technique is based on the use of an absorbing layer with absorption characteristics and without reflection of electromagnetic waves. The layer surrounding the computational domain can absorb in theory any kind of electromagnetic wave travelling towards the boundaries without any reflection effects. The PML "matches" the propagating wave in order to cancel any reflection effects.

The finite-differences system of equations presented earlier in Section 2.5 can be reduced to the two-dimensional *transverse-magnetic mode with respect to z* (TM_z) and *transverse-electric mode with respect to z* (TE_z) cases. For the TM_z case, the sets of (E_z, H_x, H_y) field vector components are required, assuming that all partial derivatives with respect to z are equal to zero. Similarly, for the TE_z case, the sets of (H_z, E_x, E_y) field vector components are required. The two modes, TM_z and TE_z are completely decoupled from each other.

In Cartesian coordinates for the two-dimensional TM_z case the updating equations are obtained by

$$\varepsilon_0 \frac{\partial E_{zx}}{\partial t} + \sigma_x E_{zx} = \frac{\partial E_y}{\partial x} \tag{2.56}$$

$$\varepsilon_0 \frac{\partial E_{zy}}{\partial t} + \sigma_y E_{zy} = -\frac{\partial H_x}{\partial y} \tag{2.57}$$

$$\mu_0 \frac{\partial H_x}{\partial t} + \sigma_y^* H_x = \frac{\partial \left(E_{zx} - E_{zy} \right)}{\partial y} \tag{2.58}$$

$$\mu_0 \frac{\partial H_y}{\partial t} + \sigma_x^* H_y = \frac{\partial \left(E_{zx} + E_{zy} \right)}{\partial x} \tag{2.59}$$

where σ is the electric conductivity of the medium and σ^* is the equivalent magnetic loss. Here the double subscript denotes that the field vector component is split into two additive subcomponents, such that

$$E_{zx} = E_z + E_x \qquad (2.60)$$

$$E_{zy} = E_z + E_y \qquad (2.61)$$

The structure of a two-dimensional FDTD employing Berenger's PML Absorbing Boundary Conditions is presented in the figure below.
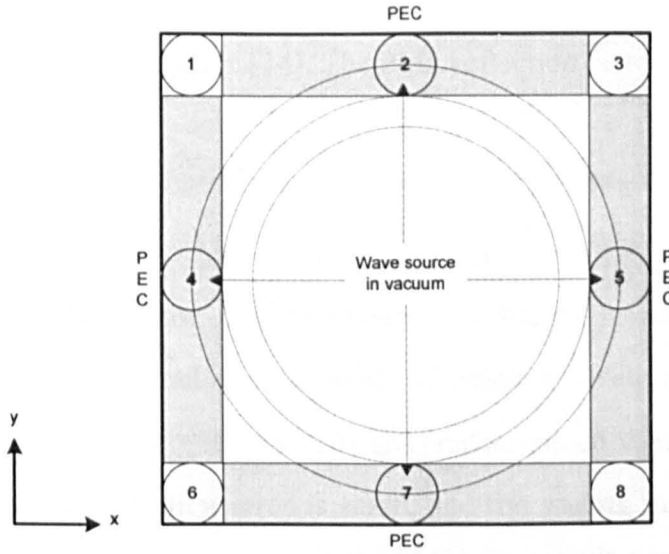
Figure 2.18. Structure of a two-dimensional FDTD grid with PMLs (grey area).

Based on Figure 2.18, the eight regions and the PML defined in each region are as follows:

1. $\mathrm{PML}\left(\sigma_{x1}, \sigma_{x1}^*, \sigma_{y2}, \sigma_{y2}^*\right)$

2. $\mathrm{PML}\left(0, 0, \sigma_{y2}, \sigma_{y2}^*\right)$

3. $\mathrm{PML}\left(\sigma_{x2}, \sigma_{x2}^*, \sigma_{y2}, \sigma_{y2}^*\right)$

4. $\mathrm{PML}\left(\sigma_{x1}, \sigma_{x1}^*, 0, 0\right)$

5. $\mathrm{PML}\left(\sigma_{x2}, \sigma_{x2}^*, 0, 0\right)$

6. $\mathrm{PML}\left(\sigma_{x1}, \sigma_{x1}^*, \sigma_{y1}, \sigma_{y1}^*\right)$

7. $\mathrm{PML}\left(0, 0, \sigma_{y1}, \sigma_{y1}^*\right)$

8. $\mathrm{PML}\left(\sigma_{x2}, \sigma_{x2}^*, \sigma_{y1}, \sigma_{y1}^*\right)$

With any discrete representation, numerical artefacts arise due to the finite spatial sampling of the FDTD discrete representation of Maxwell's equations. In this case if the PML technique is implemented as a discrete step discontinuity of the electric permittivity and magnetic permeability in the FDTD computational space, then significant wave reflections are observed at the PML surface. To reduce this error a reflection factor has been introduced so that the conductivity $\sigma_{x,0}$ increases at the surface of the PML as given in [14]. The PML reflection factor is given by

$$R(\theta) = e^{-2\eta\sigma_{x,0}\Delta\left(g^{d/\Delta}-1\right)\cos\theta/\ln g} \tag{2.62}$$

where g is a scaling factor, d is the thickness of the PML medium, Δ is the space increment, $\eta_1 = \sqrt{\mu_1/\varepsilon_1}$ and θ is the angle of incidence relative to the wave-directed surface normal. Usually g, d, and $R(0)$ are predetermined values, in order to ensure that the initial discretization error is small, and the scaling factor g determines the rate of increase of conductivity within the PML. As a result equation (2.62) becomes

$$\sigma_{x,0} = -\frac{\ln\left[R(0)\right]\ln(g)}{2\eta\Delta\left(g^{d/\Delta}-1\right)} \tag{2.63}$$

where for a 10-cell-thick PML, $R(0) = 1 \times 10^{-16}$, and $2 \le g \le 3$ has been found optimal for many FDTD simulations [2].

Berenger presented an improved PML, called the split PML where the thickness of the PML layer is reduced and a theoretical bound has been introduced to the PML thickness [14].

2.10 Uniaxial PML Implementation

In the implementation of Uniaxial PML (UPML), a two-step procedure is employed to update the components of $\vec{E}$ and $\vec{H}$ as presented in [2]. The first step is to obtain new values for the updating coefficient components and then using these values to calculate the new values of the electric and magnetic fields in the PML. For the electric field the D_x update coefficient is given by

$$
D_x\big|_{i+1/2,j,k}^{n+1} = \left(\frac{2\cdot\varepsilon\cdot\kappa_y - \sigma_y\Delta t}{2\cdot\varepsilon\cdot\kappa_y + \sigma_y\Delta t}\right)\cdot D_x\big|_{i+1/2,j,k}^{n} + \left(\frac{2\cdot\varepsilon\cdot\Delta t}{2\cdot\varepsilon\cdot\kappa_y + \sigma_y\Delta t}\right)\cdot
$$
$$
\left(\frac{H_z\big|_{i+1/2,j+1/2,k}^{n+1/2} - H_z\big|_{i+1/2,j-1/2,k}^{n+1/2}}{\Delta y} - \frac{H_y\big|_{i+1/2,j+1/2,k}^{n+1/2} - H_y\big|_{i+1/2,j-1/2,k-1/2}^{n+1/2}}{\Delta z}\right)
$$

(2.64)

The time-expression for the E_x is thus given by

$$
E_x\big|_{i+1/2,j,k}^{n+1} = \left(\frac{2\cdot\varepsilon\cdot\kappa_z - \sigma_z\Delta t}{2\cdot\varepsilon\cdot\kappa_z + \sigma_z\Delta t}\right)\cdot E_x\big|_{i+1/2,j,k}^{n} + \left(\frac{1}{\varepsilon\cdot(2\cdot\varepsilon\cdot\kappa_z + \sigma_z\Delta t)}\right)\cdot
$$
$$
\left[(2\cdot\varepsilon\cdot\kappa_x + \sigma_x\Delta t)\cdot D_x\big|_{i+1/2,j,k}^{n+1} - (2\cdot\varepsilon\cdot\kappa_x + \sigma_x\Delta t)\cdot D_x\big|_{i+1/2,j,k}^{n}\right]
$$

(2.65)

The update for the B_x coefficient is given by

$$
B_x\big|_{i,j+1/2,k+1/2}^{n+3/2} = \left(\frac{2\cdot\varepsilon\cdot\kappa_y - \sigma_y\Delta t}{2\cdot\varepsilon\cdot\kappa_y + \sigma_y\Delta t}\right)\cdot B_x\big|_{i,j+1/2,k+1/2}^{n+1/2} + \left(\frac{2\cdot\varepsilon\cdot\Delta t}{2\cdot\varepsilon\cdot\kappa_y + \sigma_y\Delta t}\right)\cdot
$$
$$
\left(\frac{E_z\big|_{i,j+1,k+1/2}^{n+1} - E_z\big|_{i,j,k+1/2}^{n+1}}{\Delta y} - \frac{E_y\big|_{i,j+1/2,k+1}^{n+1} - E_y\big|_{i,j+1/2,k}^{n+1}}{\Delta z}\right)
$$

(2.66)

The updating of the H_x component based on the above formulation is

$$H_x\big|_{i,j+1/2,k+1/2}^{n+3/2} = \left(\frac{2\cdot\varepsilon\cdot\kappa_z - \sigma_z\Delta t}{2\cdot\varepsilon\cdot\kappa_z + \sigma_z\Delta t}\right)\cdot H_x\big|_{i,j+1/2,k+1/2}^{n+1/2}$$

$$+ \left(\frac{1}{\mu\cdot(2\cdot\varepsilon\cdot\kappa_z + \sigma_z\Delta t)}\right)\cdot \qquad\qquad (2.67)$$

$$\left[(2\cdot\varepsilon\cdot\kappa_x + \sigma_x\Delta t)\cdot B_x\big|_{i,j+1/2,k+1/2}^{n+3/2} - (2\cdot\varepsilon\cdot\kappa_x + \sigma_x\Delta t)\cdot B_x\big|_{i,j+1/2,k+1/2}^{n+1/2}\right]$$

Similarly the updating equations can be formulated for both the updating coefficients and the electric and magnetic fields based on the updating equations of (2.45) – (2.50).

The PML concept has contributed significantly in the study of electromagnetic problems using the FDTD method. The PML theory has expanded to cover a wide range of computational models and thus far it has provided an efficient and robust method of applying boundary conditions.

2.11 Convolutional PML Implementation

Since its initial appearance, Berenger's PML technique has been dominant in the FDTD method for using ABCs as well as simulating the extension to infinity of the computational space. Although the PML formulation has been a robust and efficient technique in terminating the FDTD computational lattice, it suffers from absorbing evanescent waves. In this case the PML must be placed at a sufficient distance from the object, thus allowing evanescent waves to decay and making the computational space sufficiently larger [15]. A new causal form of the PML has been introduced in [16], referred to as the complex frequency shift (CFS) PML. A novel implementation of this new form of the PML based on the stretched coordinate formulation and a recursive convolution is referred to as Convolutional PML (CPML) [17]. Furthermore, it has been reported to be highly effective in absorbing evanescent waves and signals of long-time signature. One of the most significant advantages of the method is that the formulation is independent of the material medium and the

formulation remains unchanged when simulating lossy, dispersive, anisotropic, or non-linear structures.

The discrete form of the CPML method equations can be found in [13]. The updating equations for the CPML method as given in [18] take the form of

$$
\begin{aligned}
E_x\big|_{i,j+1/2,k+1/2}^{n+1/2} &= C_a(m) \cdot E_x\big|_{i,j+1/2,k+1/2}^{n+1/2} \\
&+ (1/\kappa_{ey}) \cdot C_{b_1}(m) \cdot \left[H_z\big|_{i,j+1,k+1/2}^{n} - H_z\big|_{i,j,k+1/2}^{n} \right] \\
&+ (1/\kappa_{ez}) \cdot C_{b2}(m) \cdot \left[H_y\big|_{i,j+1/2,k}^{n} - H_y\big|_{i,j+1/2,k+1}^{n} \right] \\
&+ \left[\Delta \cdot C_{b_1}(m) \cdot \psi_{exy}\big|^{n+1/2} + \Delta \cdot C_{b_2}(m) \cdot \psi_{exz}\big|^{n+1/2} \right]
\end{aligned}
\tag{2.68}
$$

where ψ_{exy}, ψ_{exz} are the CPML terms derived from the discrete convolution method and the subscripts indicate that the term is updating E_x and is associated with the derivative of the magnetic field term with respect to y. The CPML parameters have to be calculated in each iteration in the FDTD loop, thus

$$
\psi_{exy}\big|^{n+1/2} = b_{ey} \cdot \psi_{exy}\big|^{n-1/2} + \alpha_{ey} \left[H_z\big|_{i,j+1,k+1/2}^{n} - H_z\big|_{i,j,k+1/2}^{n} \right] \tag{2.69}
$$

where

$$
\begin{aligned}
b_{ey} &= e^{-\left(\frac{\sigma_{pey}}{\kappa_{ey}} + a_{pey}\right)\frac{\Delta_t}{\varepsilon_0}}, \quad \text{and} \\
\alpha_{ey} &= \frac{\sigma_{pey}}{\Delta \cdot \left(\sigma_{pey} \cdot \kappa_{ey} + a_{ey} \cdot \kappa_{ey}^2\right)} \cdot (b_{ey} - 1)
\end{aligned}
\tag{2.70}
$$

as σ_{pey}, κ_{ey} and α_{ey} are CPML parameters for each of the respective regions of the CPML as defined in the FDTD computational domain.

Given the updating equations in (2.68) and (2.69) the auxiliary CPML parameters and coefficients have to be calculated in the FDTD loop. In this case the FDTD algorithm is thus modified such that it first calculates the magnetic fields based on the equations given earlier in this chapter, and afterwards the auxiliary parameters of the CPML are calculated based on their previous values (stored in memory) and the current values of the electric fields. This will update the magnetic

field with the effect of the CPML in the regions enclosed with CPML ABCs. The next step is to calculate the electric fields based on the traditional equations given earlier, and then the auxiliary parameters of the CPML are calculated based on their previous values and new values of the magnetic field. The new values of the electric field and the previously calculated values of the magnetic field can now be used to update all fields in all CPML regions of the FDTD computational domain. The FDTD explicit algorithm including CPML ABCs is illustrated in Figure 2.19.
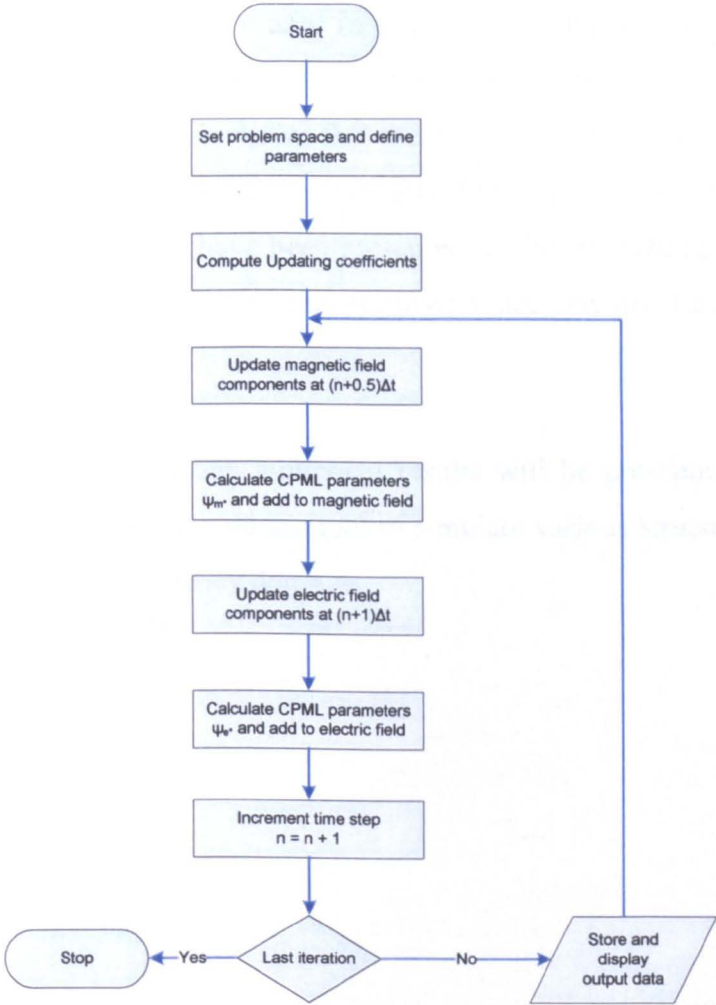
Figure 2.19. The FDTD algorithm including the CPML steps.

The key parameters of the CPML are σ_{max}, which is the maximum conductivity of the conductivity profile, n_{pml} is the order of the polynomial scaling, κ_{min} is the complex stretching variables of the modifed definition of the terminating medium, as presented in [19], and α_{min} and α_{max} are the scaling parameters of the inner domain and the CPML interface set to reduce the reflection error of evanescent

49

modes. The choice of parameters and the thickness of the CPML layer in terms of number of cells determine the performance of the method and several parametric studies can be found in the published works [13, 17, 20].

2.12 Summary

In this chapter, Maxwell's equations have been presented and the finite-differences approximation method has been applied to obtain discrete spatially and time-varying equations. These equations can be used in order to implement a computer program using the FDTD method. To deal with numerical dispersion the Courant factor has been introduced and it has been shown that there is a limit that has to be satisfied in order to obtain a numerically stable solution. Finally, two absorbing boundary conditions (PML and CPML) have been presented for the FDTD method in order to terminate the computational domain and simulate space and structures extending to infinity.

In the following chapters numerical results will be presented by using the FDTD method as a numerical analysis tool to simulate various structures and obtain results in both time and frequency domains.

References

[1]   K. S. Yee, "Numerical solution of initial boundary value problem involving Maxwell's equations in isotropic media," *Antennas and Propagation, IEEE Transactions on,* vol. 14, pp. 302-307, 1966.

[2]   A. Taflove and S. C. Hagness, *Computational Electrodynamics: The Finite-Difference Time-Domain Method,* 3 ed.: Artech House Publishers, 2005.

[3]   J. B. Schneider and C. L. Wagner, "FDTD dispersion revisited: faster-than-light propagation," *Microwave and Guided Wave Letters, IEEE,* vol. 9, pp. 54-56, 1999.

[4]   K. J. Willis, J. B. Schneider, and S. C. Hagness, "Amplified total internal reflection: theory, analysis, and demonstration ofexistence via FDTD," *Optics Express,* vol. 16, pp. 1903-1914, 2008.

[5]   C. L. Wagner and J. B. Schneider, "Divergent fields, charge, and capacitance in FDTD simulations," *Microwave Theory and Techniques, IEEE Transactions on,* vol. 46, pp. 2131-2136, 1998.

[6]   K. Umashankar and A. Taflove, "A novel method to analyze Electromagnetic scattering of complex objects," *Electromagnetic Compatibility, IEEE Transactions on,* vol. EMC-24, pp. 397-405, 1982.

[7]   G. Kriegsmann, A. Taflove, and K. Umashankar, "A new formulation of electromagnetic wave scattering using an on-surface radiation boundary condition approach," *Antennas and Propagation, IEEE Transactions on,* vol. 35, pp. 153-161, 1987.

[8]   T. G. Moore, J. G. Blaschak, A. Taflove, and G. A. Kriegsmann, "Theory and application of radiation boundary operators," *Antennas and Propagation, IEEE Transactions on,* vol. 36, pp. 1797-1812, 1988.

[9]   J.-P. Berenger, "A perfectly matched layer for the absorption of electromagnetic waves," *J. Comput. Phys.,* vol. 114, pp. 185-200, 1994.

[10]   D. S. Katz, E. T. Thiele, and A. Taflove, "Validation and extension to three dimensions of the Berenger PML absorbing boundary condition for FD-TD meshes," *Microwave and Guided Wave Letters, IEEE,* vol. 4, pp. 268-270, 1994.

[11]   J.-P. Berenger, "Three-dimensional perfectly matched layer for the absorption of electromagnetic waves," *Computational Physics, Journal of,* vol. 127, pp. 363-379, 1996.

[12]   S. D. Gedney, "An anisotropic perfectly matched layer-absorbing medium for the truncation of FDTD lattices," *Antennas and Propagation, IEEE Transactions on,* vol. 44, pp. 1630-1639, 1996.

[13]   J. A. Roden and S. Gedney, "An efficient FDTD implementation of the PML with CFS in general media," *Antennas and Propagation Society International Symposium, 2000. IEEE,* vol.3., pp. 1362-1365, 2000.

[14]   J.-P. Berenger, "Improved PML for the FDTD solution of wave-structure interaction problems," *Antennas and Propagation, IEEE Transactions on,* vol. 45, pp. 466-473, 1997.

[15]   J.-P. Berenger, "Evanescent waves in PML's: origin of the numerical reflection in wave-structure interaction problems," *Antennas and Propagation, IEEE Transactions on,* vol. 47, pp. 1497-1503, 1999.

[16]   M.-S. Tong, M. Kuzuoglu, and R. A. J. Mittra, "A new anisotropic perfectly matched layer medium for mesh truncation in finite difference time domain analysis," *International Journal of Electronics,* vol. 86, pp. 1085-1091, 1999.

[17]   J. A. Roden and S. D. Gedney, "Convolution PML (CPML): An efficient FDTD implementation of the CFS–PML for arbitrary media," *Microwave and Optical Technology Letters,* vol. 27, pp. 334-339, 2000.

[18]   A. Z. Elsherbeni and V. Demir, *The finite-difference time-domain method for electromagnetics with MATLAB simulations.* Raleigh, NC: SciTech Pub., 2009.

[19]   M. Kuzuoglu and R. Mittra, "Frequency dependence of the constitutive parameters of causal perfectly matched anisotropic absorbers," *Microwave and Guided Wave Letters, IEEE,* vol. 6, pp. 447-449, 1996.

[20]   J.-P. Berenger, "Numerical reflection from FDTD-PMLs: a comparison of the split PML with the unsplit and CFS PMLs," *Antennas and Propagation, IEEE Transactions on,* vol. 50, pp. 258-265, 2002.

Chapter 3

FDTD Modelling and
Numerical Results

Following the theory of the Finite Differences and the derivation of explicit updating Maxwell's equations, the FDTD method has been implemented in MATLAB™. The explicit equations and the FDTD algorithms given in the previous chapter have been applied to model 1D, 2D and 3D FDTD electromagnetic problems with a variety of media and Absorbing Boundary Conditions (ABCs). In this chapter the FDTD method has been applied to a set of problems and the results are presented. The results are consistent with numerical electromagnetic problems presented in various publications given in the literature.

3.1 One-dimensional plane wave propagation

A simple 1D FDTD method has been implemented in order to verify the discrete equations for the updating coefficients, and the calculation of the electric and magnetic field in the leapfrog algorithm as derived in Chapter 2. The following results illustrate the propagation of the Electric and Magnetic field at different time steps. An x-directed Gaussian pulse with unit amplitude, width of 10 grid cells, and $1/e$ temporal half-width of $\tau = 100\,\mathrm{ps}$ is launched from the far-left side of the grid travelling along 0.6 m distance in free space with grid resolution of $\Delta_x = 6\,\mathrm{mm}$. The 1D FDTD simulation is using a Courant factor of 1.0 which is equivalent to the *magic time-step* $(c\Delta t = \Delta x)$. A Perfect Electric Conductor (PEC) sheet is used to simulate the boundary condition at the far-right of the FDTD grid.

The results presented below in Figure 3.1 illustrate the propagation of the wave, before and after it reaches the far-right grid boundary.
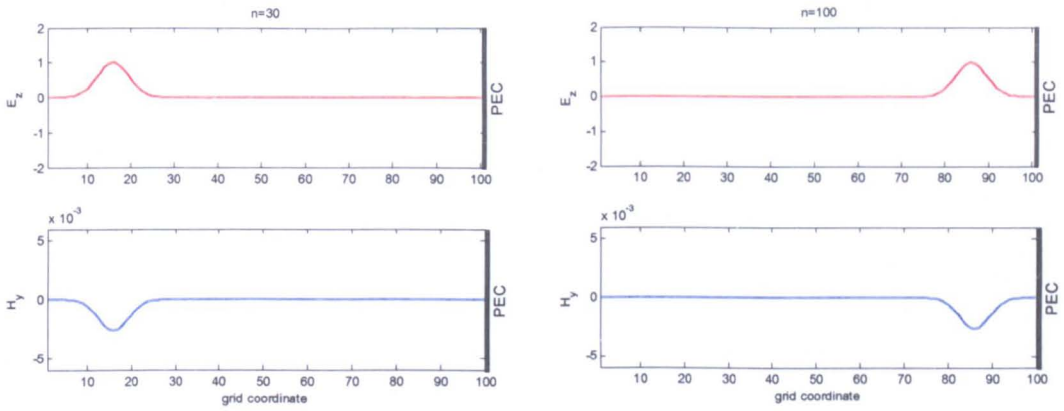
(a) At time step $n = 30$ the Gaussian pulse is propagating to the $x+$ direction.

(b) At time step $n = 100$ the pulse is approaching the far-right grid boundary.
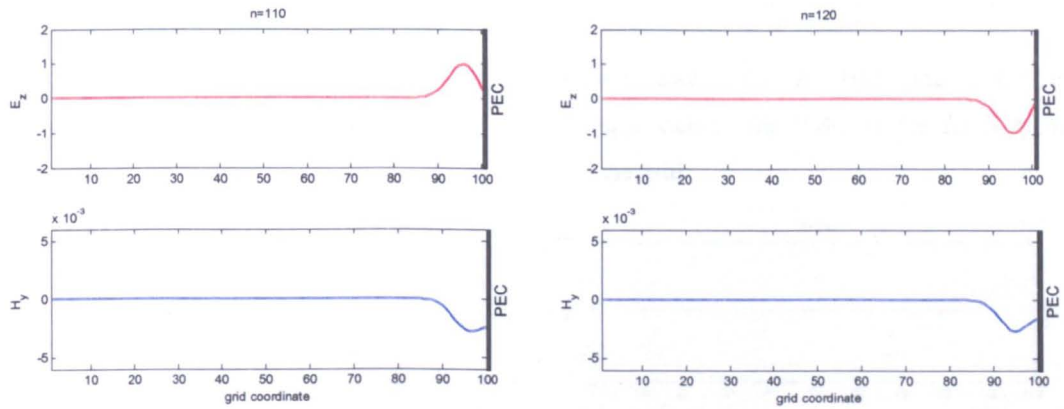
(c) The PEC acts as a mirror and reflects the incident wave at time step $n = 110$.

(d) The wave is reflected and continues to propagate along the $-x$-direction at time step $n = 120$.

Figure 3.1. One-dimensional plane wave propagation with PEC boundary.

The presence of the PEC enforces $E_z = 0$ at the boundary, thus the polarity of the electric field is reversed upon reflection, while the magnetic field H remains unchanged. After reflection, both the electric and magnetic field are propagating in the opposite direction. The direction of the power flow is given by the Poynting vector $(E \times H^*)$, which is the cross product of the electric field and the complex conjugate of the magnetic field. The Poynting vector in this case is consistent with plane wave propagation. Since the Courant factor is set to 1, the magnitudes of the reflected fields remain the same.

Similarly, the figures below in Figure 3.2 show a 1D FDTD simulation of the propagation of the electric and magnetic fields before and after the wave reaches the far-right grid boundary. The boundary condition in this simulation is a Perfect Magnetic Conductor (PMC). The 1D FDTD simulation settings remained unchanged for the source and the Courant factor.
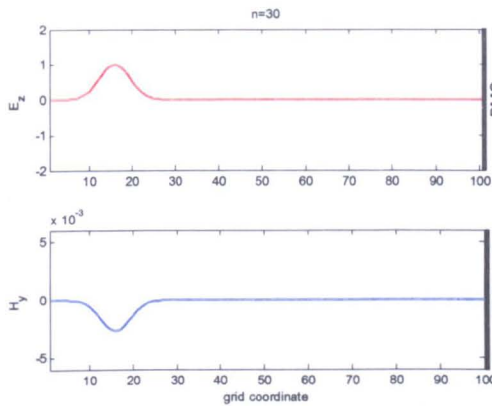
(a) At time step $n = 30$ the Gaussian pulse is propagating to the x+ direction.
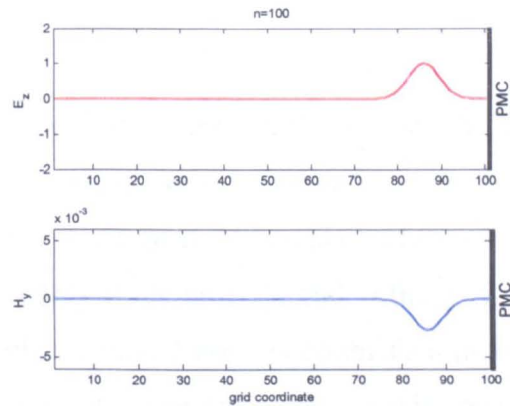
(b) At time step $n = 100$ the pulse is approaching the PMC at the far-right of the grid.
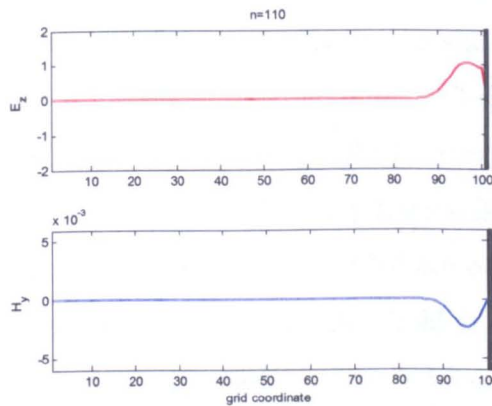
(c) The PMC acts as a mirror and reflects the incident wave at time step $n = 110$.
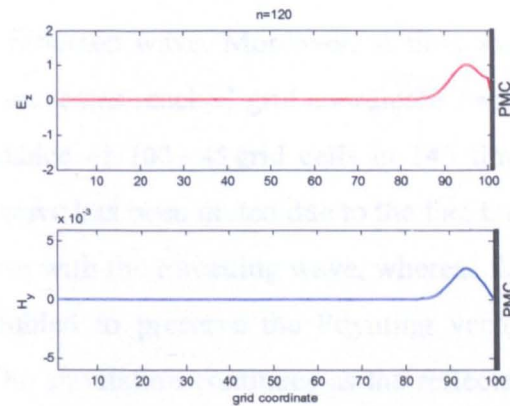
(d) The wave is reflected and continues to propagate along the $-x$-direction at time step $n = 120$.

Figure 3.2. One-dimensional plane wave propagation with PMC boundary.

Since the PMC enforces $H_y = 0$ at the boundary, the polarity of the magnetic field is reversed upon reflection. After reflection, both the electric and magnetic field are propagating in the opposite direction. Again, in this case the magnitudes of the electric and the magnetic fields remain the same since the Courant factor is set to 1.

A 1D FDTD grid was implemented of physical length 15 cm and grid spacing of $\Delta x = 1.5$ mm, with the electric-field hard source condition placed at the far-left grid boundary. The grid was sourced with 1.0 V/m amplitude of and a frequency of 10 GHz and the Courant factor was set to $S = 1.0$. A mirror modelled as a Perfect Electric Conductor (PEC) is placed at the far-right of the grid in order to demonstrate the retro-reflection artefact. The visualisations of the field distributions are shown below in Figure 3.3.

The incident sinusoidal wave from the hard source at the far-left of the grid is propagating in the $+x$ direction with amplitude of 1.0 V/m. At time step $n = 100$ the wave has reached the PEC mirror at the far-right boundary of the grid. As the wave is reflected from the PEC boundary at the far-right end of the grid, it propagates in the $-x$ direction and as a result a standing wave is established in the region of the grid where the reflected and incident waves are overlapping in space, as illustrated in Figure 3.3.(c). The amplitude of the standing wave is 2.0 V/m. The remainder of the grid contains only the incident travelling wave of amplitude 1.0 V/m. On the other hand, the magnetic field is distorted due to the destructive inference of the travelling wave and the reflected wave. Moreover, at time step $n = 145$, the leading edge of the reflected wave has reached grid coordinate $i = 55$ (i.e. the wave has propagated a total distance of $100 + 45$ grid cells in 145 time steps). During this time step the standing wave has been muted due to the fact that the reflected wave is now $180°$ out of phase with the travelling wave, whereas the magnitude of the magnetic field has doubled to preserve the Poynting vector product as illustrated in Figure 3.3.(d). The simulation continues as the reflected wave has reached the far-left boundary. At this time step ($n = 200$), as seen in Figure 3.3.(e) the standing wave covers the entire grid. Finally, if a mirror is modelled at the left-hand-side of the grid, then a retro-reflection effect creates a new standing wave with amplitude 3.0 V/m, where the retro-reflected, reflected and the incident wave are now counter-propagating as illustrated in Figure 3.3.(f). The simulation continues in a similar manner as before where the retro-reflection effects creates a new standing with higher amplitude at 4.0 V/m.
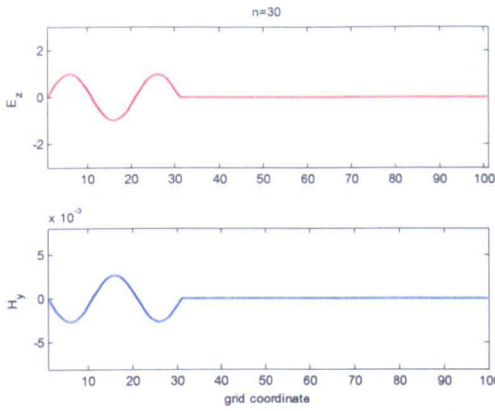
(a) The incident sinusoidal wave at time step $n = 30$.
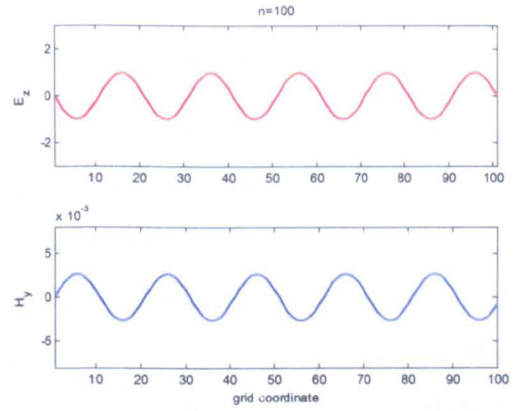
(b) The incident sinusoidal wave at time step $n = 100$ reaching the right end of the grid.
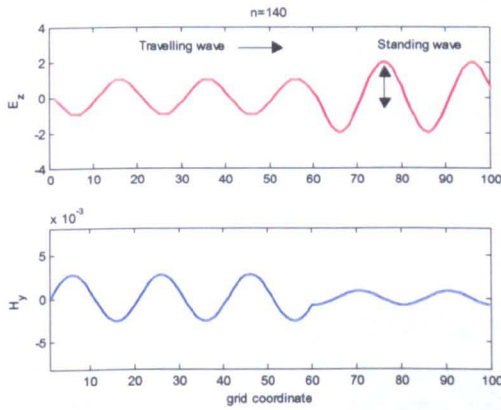
(c) Retro-reflection effect creating a standing wave at time-step $n = 140$.
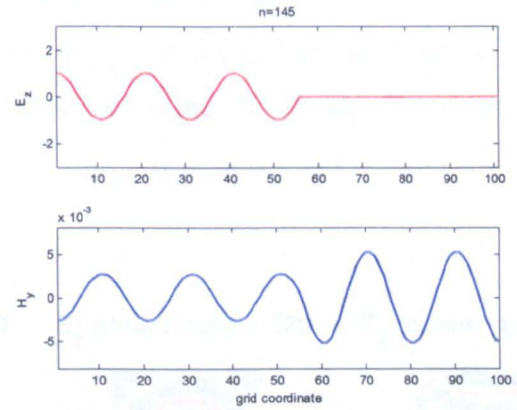
(d) Travelling and reflected wave propagation at time step $n = 145$.
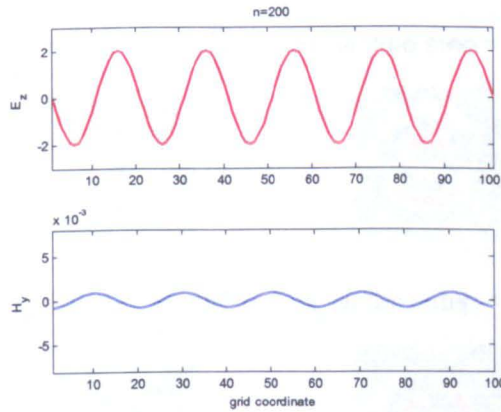
(e) Standing wave fills the entire grid at time step $n = 200$.
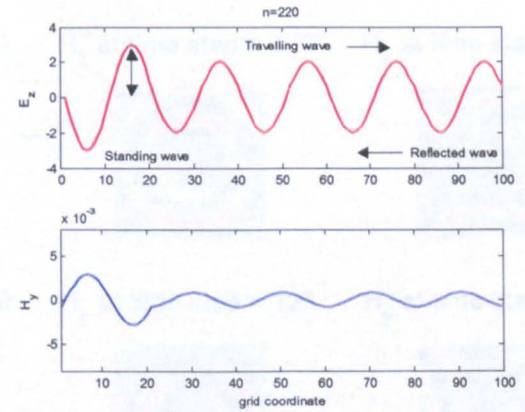
(f) Retro-reflection effect, a new standing wave at time-step $n = 220$.

Figure 3.3. One-dimensional plane wave propagation with PEC mirror.

3.2 Two-dimensional cylindrical wave propagation

The FDTD method formulation has been extended to the two-dimensional space (2D) and implemented in MATLAB™. The following diagrams in Figure 3.4 show the propagation of a sine-modulated Gaussian pulse cylindrical wave placed in the centre of the grid at a number of time snapshots, with carrier frequency 500 THz, and wavelength $\lambda = 0.5996$ µm. An electric field hard source is placed in the centre of 3 µm square grid propagating in the z-direction with grid resolution $\Delta x = \Delta y = \lambda/20$, and $c \cdot \Delta t = 1/\sqrt{2} \, \Delta x$. The horizontal axis indicate the propagation of the wave in the x-direction, the vertical axis show the propagation of the wave in the y-direction. The origin of the Cartesian system is located at the lower left hand corner, and for the two-dimensional TM_z case the fields required to be updated are E_z, H_x, and H_y (Units: $E_z = V/m$, H_y, $H_x = A/m$).

E_z at time step = 60	E_z at time step = 100	E_z at time step = 120	E_z at time step = 160
H_x at time step = 60	H_x at time step = 100	H_x at time step = 120	H_x at time step = 160
H_y at time step = 60	H_y at time step = 100	H_y at time step = 120	H_y at time step = 160
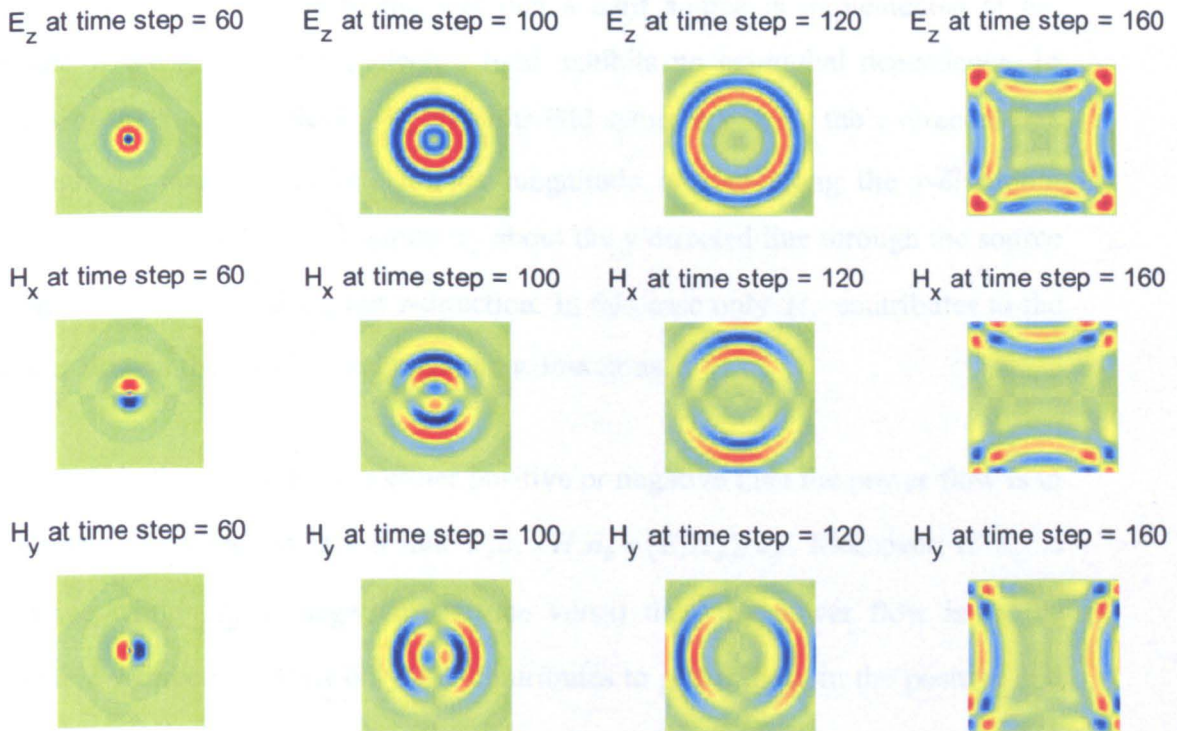
Figure 3.4. Two-dimensional TM_z cylindrical wave propagation.

In Figure 3.4, at time-step 60 the pulse is beginning to emerge from the source point at the center of the grid. Then at time-step 100 the pulse propagates radially outward from the source point. Moreover, at time-step 120 the leading edge of the pulse reaches the PEC boundary where $E_z = 0$. Finally, at time-step 160 the pulse is reflected and begins to propagate radially inward. Since the PEC boundary enforces $E_z = 0$, the polarity of the electric field is reversed upon reflection, while the magnetic fields H_x and H_y are propagating in the opposite direction.

The power flow or Poynting vector [1] is given by

$$S = \vec{E} \times \vec{H} \tag{3.1}$$

In this 2D FDTD simulation the electric field E_z exhibits complete rotational symmetry, due to the fact that a hard source is implemented at the center of the grid, thus the electric field exhibits no azimuthal dependence. In terms of the magnetic fields, H_x exhibits odd symmetry about the x-directed line through the source location, and its magnitude is zero along the x-direction. Similarly, H_y exhibits odd symmetry about the y-directed line through the source location, and is zero along the y-direction. In this case only H_x contributes to the power flow in the positive and negative y directions.

If both E_z and H_x are either positive or negative then the power flow is in the positive y-direction, given that $E_z \hat{a}_z \times H_x \hat{a}_x = (E_z H_x) \cdot \hat{a}_y$. Moreover, if E_z is positive while H_x is negative (or vice versa) then the power flow is in the negative y-direction. Thus only H_y contributes to power flow in the positive and negative x directions.

Also if E_z is positive while H_y is negative (or vice versa), then the power flow is in the positive x direction, given that $E_z \hat{a}_z \times H_y \hat{a}_y = -(E_z H_y) \cdot \hat{a}_x$. Furthermore, if both E_z and H_y are either positive or negative then the power

flow is in the negative y-direction. Thus only H_y contributes to power flow in the positive and negative y directions.

3.3 Numerical Stability and Dispersion

The numerical stability of the FDTD method is based on the Courant factor as discussed in Chapter 2, Section 2. The choice of the Courant factor requires that the time step Δt has a limit relative to the lattice space increments of the FDTD computational domain. A choice of the Courant factor greater than this limit exposes the FDTD simulation to the development of spurious fields in the FDTD space.

To illustrate the effects of the numerical stability and dispersion a Courant factor of 1.01 was chosen for 1D FDTD simulation. A Gaussian pulse was launched from the far-left side of the grid and a PMC sheet was used to terminate the FDTD grid, with grid resolution $\Delta x = 6$ mm and $c\Delta t = S \cdot \Delta x$. The results presented in Figure 3.5 show the propagation of the electric and magnetic field at different time steps, as the wave propagates towards the far-right grid boundary. At time step $n = 30$ the Gaussian pulse is propagating to the $x+$ direction. As the pulse propagates towards the far-right boundary, at time step $n = 40$, a noise component begins to emerge at the trailing edge of the Gaussian pulse. As the simulation continues, it becomes unstable as the trailing edge of the Gaussian pulse is contaminated by a rapidly oscillating and growing noise component (Figures 3.5.(b) – (e)) because the Courant number exceeds the stability limit. By time step $n = 100$, the Gaussian pulse is distorted to become a growing oscillating pulse that covers the entire grid (Figure 3.5.(f)).
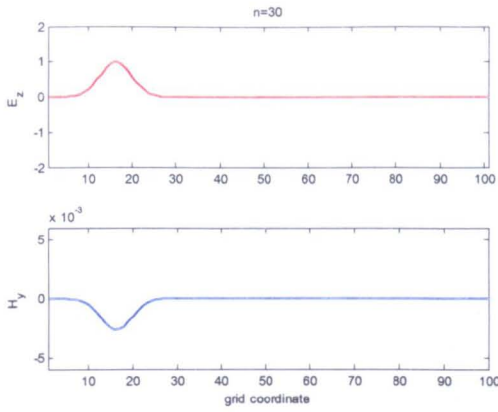
(a) Gaussian wave propagation at time step $n = 30$.
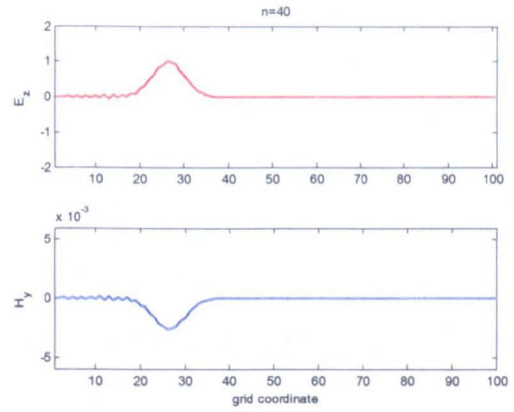
(b) Noise component begins to emerge at time step $n = 40$.
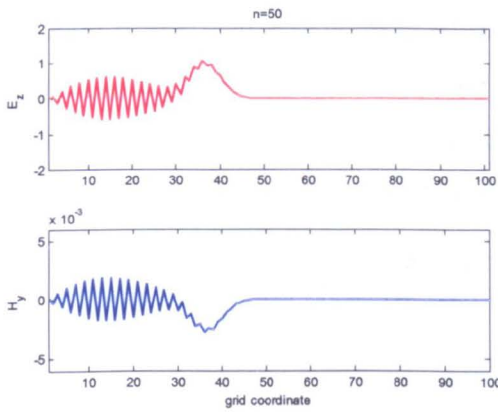
(c) Growing noise trailing edge at time-step $n = 50$.
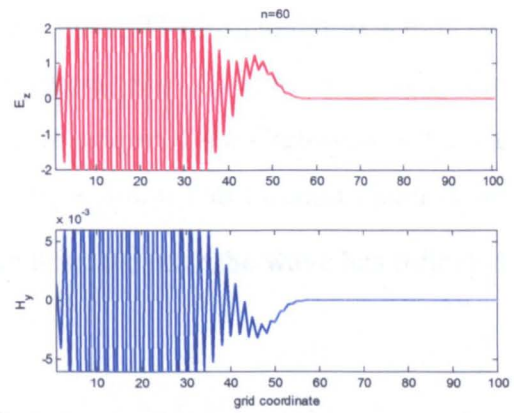
(d) Distorted Gaussian pulse at time step $n = 60$.
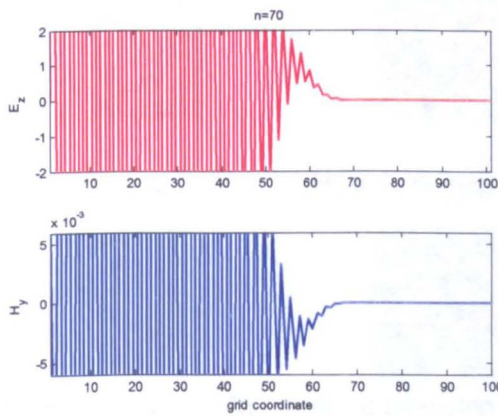
(e) Growing oscillating noise wave at time step $n = 70$.
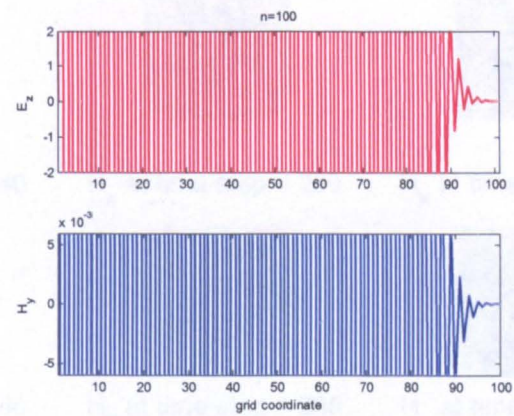
(f) Oscillating noise wave at time step $n = 100$.

Figure 3.5. One-dimensional plane wave propagation with Courant factor over the limit.

Based on the results in Figure 3.5, as the FDTD simulation progresses the magnitudes of the electric and the magnetic field begin to diverge, and the simulation becomes unstable. The Courant factor applies to inhomogeneous media as well. However, other factors can influence the numerical stability of the simulation, for example ABCs, nonuniform spatial grids, and nonlinear materials. Furthermore, it has been reported that the FDTD method can be extended to produce stable results for a choice of a Courant factor well above the FDTD limit using the Alternate Direction Implicit (ADI) method [2, 3].

The diagrams in Figure 3.6 show the propagation of a cylindrical wave in the centre of the grid at a number of time snapshots. The horizontal axis indicate the propagation of the wave in the x-direction, the vertical axis show the propagation of the wave in the y-direction. The origin of the Cartesian system is the lower left corner (Units: $E_z = V/m$, H_y, $H_x = A/m$). The Courant factor is set to 1.01, which causes the solution to become unstable after the wave has reflected of the boundary walls.
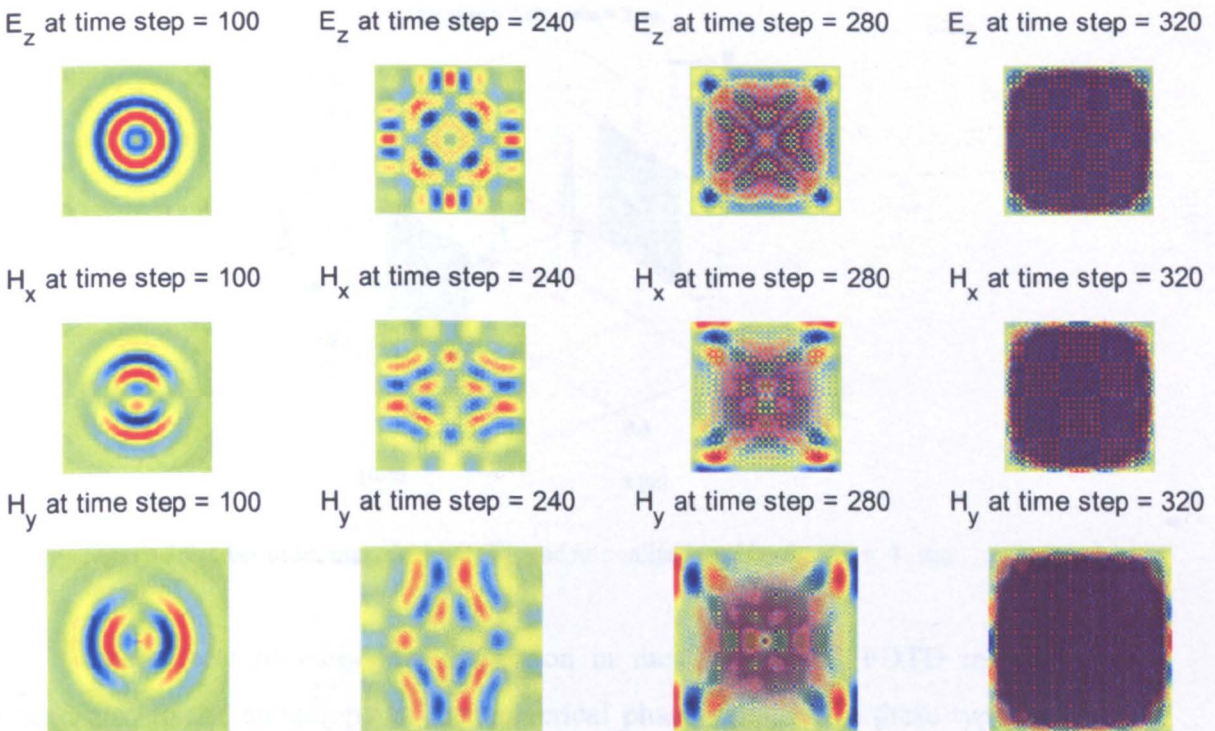
Figure 3.6. Two-dimensional TM_z cylindrical wave propagation with $\Delta t = 1.0005\Delta x/c\sqrt{2}$.

In this simulation, the time step $\Delta t = 1.0005\Delta x / c\sqrt{2}$ is slightly larger than the Courant stability limit for a 2-D square lattice. Therefore, as the time-stepping process continues, an unstable field pattern begins to emerge.

Moreover, the effects of numerical dispersion are not limited to the CFL limit. The following 1D FDTD simulation illustrates the effects of boundary conditions on the maximum field value and the field distribution. In this simulation the computational domain was 1 m wide, with cell size $\Delta x = 4$ mm, and time-step was set to $\Delta t = 3$ ps. A Gaussian pulse was launched in both directions from the centre of the FDTD grid, with magnitude 0.25 A/m². Two PEC plates were used to terminate the computational domain on either side of the FDTD grid. After 1000 time steps, the equivalent of 3 ns, Figure 3.7 shows the maximum magnitude of the electric field E_z and the magnetic field H_y normalised to the free space impedance $\eta_0 = \sqrt{\mu_0/\varepsilon_0}$. The effect of numerical dispersion is evident, as the reflected Gaussian pulse is distorted due to the size of the FDTD cell.
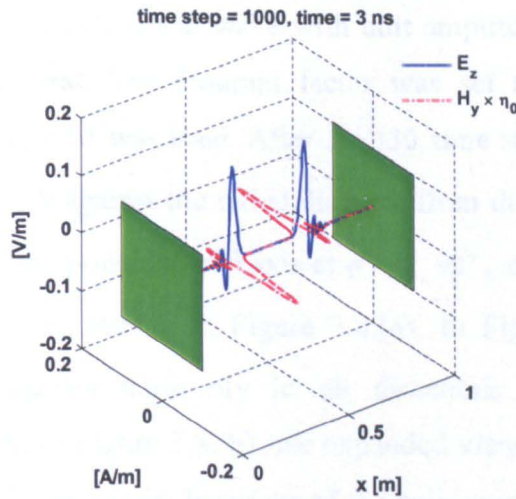
Figure 3.7. Maximum magnitude of E_z and normalised $\eta_0 H_y$ for $\Delta x = 4$ mm.

The effects of numerical dispersion in the 2D and 3D FDTD method extend also to the anisotropy of the numerical phase velocity. In these types of simulations the propagation velocity depends on the direction of wave propagation, thus it is important to take into consideration the effect on the value

of the numerical phase velocity $\tilde{v}_p$, given the angle of propagation ϕ [4]. The expression for the numerical wavevector along $\tilde{k}$ and numerical phase velocity $\tilde{v}_p = \omega / \tilde{k}$ along the principal axes of the grid at $\phi = 0°, 90°, 180°$, and $270°$ are given by

$$\tilde{k} = \frac{2}{\Delta} \sin^{-1} \left[\frac{1}{S} \sin \left(\frac{\pi S}{N_\lambda} \right) \right] \qquad (3.2)$$

$$\tilde{v}_p = \frac{\omega}{\tilde{k}} = \frac{\pi}{N_\lambda \sin^{-1} \left[\frac{1}{S} \sin \left(\frac{\pi S}{N_\lambda} \right) \right]} \qquad (3.3)$$

where Δ is the square-cell size, $S = c\Delta t / \Delta$ is the Courant factor, and $N_\lambda = \lambda_0 / \Delta$ is the grid sampling density or the number of cells per wavelength.

In the following simulation the theoretical anisotropy between oblique and along-axis numerical wave propagation is demonstrated. In this case, using the 2D FDTD TM$_z$, a sinusoidal cylindrical wave with unit amplitude was placed in the centre of a 360×360 grid. The Courant factor was set to $S = 0.5$ and a grid sampling density of $N_\lambda = 20$ was used. After $n = 330$ time steps, the electric field E_z distribution is plotted against the radial distance from the source at the centre of the grid, parallel to the principal grid axis at $\phi = 0°, 90°$, and parallel to the grid diagonal at $\phi = 45°$ as illustrated in Figure 3.8.(a). In Figure 3.8.(a) the field appears to be propagating uniformly in all directions with identical field distributions. However, in Figure 3.8.(b), the expanded view of the Figure 3.8.(a) between 63Δ and 64Δ, the spatial locations of the zero-crossing points show that the sinusoidal wave propagating along the grid diagonal at $\phi = 45°$ passes through zero at 63.618 cells, whereas the wave along the principal axis at $\phi = 0°, 90°$ passes through zero at 63.493 cells. This shows that the sinusoidal wave propagating along the principal axis is "leading" by 0.125 cells. This yields to the numerical phase anisotropy of a wave propagating along the grid at angle ϕ.
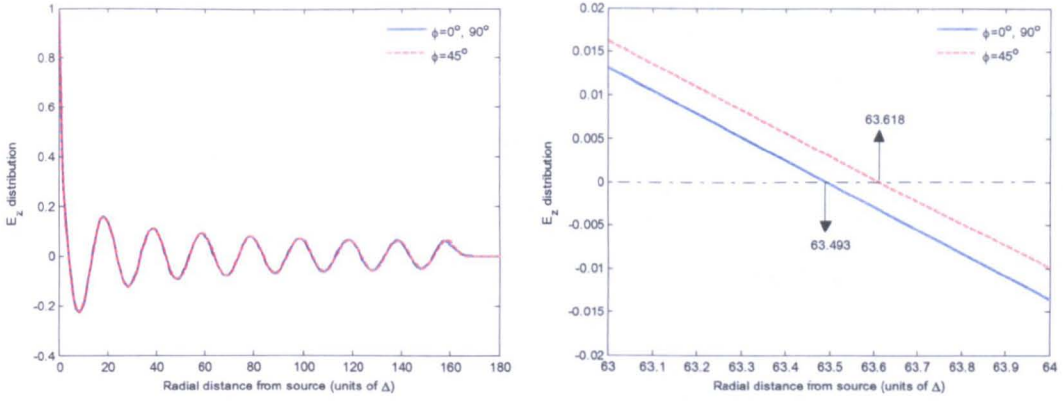
(a) Comparison of calculated wave propagation along the grid axes and along a grid diagonal.

(b) Expanded view of figure (a) at distances between 63 and 64 grid cells from the source.

Figure 3.8. Effect on numerical dispersion in two-dimensional TM_z propagation.

This effect of numerical phase anisotropy must be taken into consideration when developing FDTD simulations in 2D and 3D with an oblique angle of incidence of the source wave, particularly in the Total Field/Scattered Field formulation of the FDTD method. In this case, closed form expressions are required in order to determine the numerical phase velocity for any wave-propagation direction at angle ϕ [4]. Thus, the equation given in (3.2) for the numerical wavevector $\tilde{k}$, must be modified so it can be solved directly for propagation along the grid diagonals at $\phi = 45°, 135°, 225°,$ and $315°$

$$\tilde{k} = \frac{2\sqrt{2}}{\Delta} \sin^{-1} \left[\frac{1}{S\sqrt{2}} \sin \left(\frac{\pi S}{N_\lambda} \right) \right] \quad (3.4)$$

Given equation (3.4), the graphs in Figure 3.9 illustrate the normalized numerical phase velocity and the exponential attenuation constant as a function of the grid-sampling density N_λ. For the propagation along the principal axis at $\phi = 0°, 90°$, a minimum value of $\tilde{v}_p = (2/3)c$ is reached at $N_\lambda = 3$, and as the value of N_λ is reduced below 3, the phase velocity $\tilde{v}_p$ increases inversely with N_λ. Eventually, $\tilde{v}_p$ exceeds the value of c for $N_\lambda < 2$ and reaches a limiting velocity of $2c$ as N_λ approaches to 1. For propagation along the grid diagonal

at $\phi = 45°$, a minimum value of $\tilde{v}_p = \left(\sqrt{2}/2 \right) c$ is reached at $N_\lambda = 2$, which is also the point of the exponential attenuation. As N_λ is reduced below 2, the phase velocity $\tilde{v}_p$ increases inversely with N_λ. Furthermore, as $\tilde{v}_p$ exceeds the value of c for $N_\lambda < \sqrt{2}$, and reaches a limiting velocity of $\sqrt{2}c$ as N_λ approaches 1. In this case the attenuation constant approaches a value of 2.493 nepers/cell.
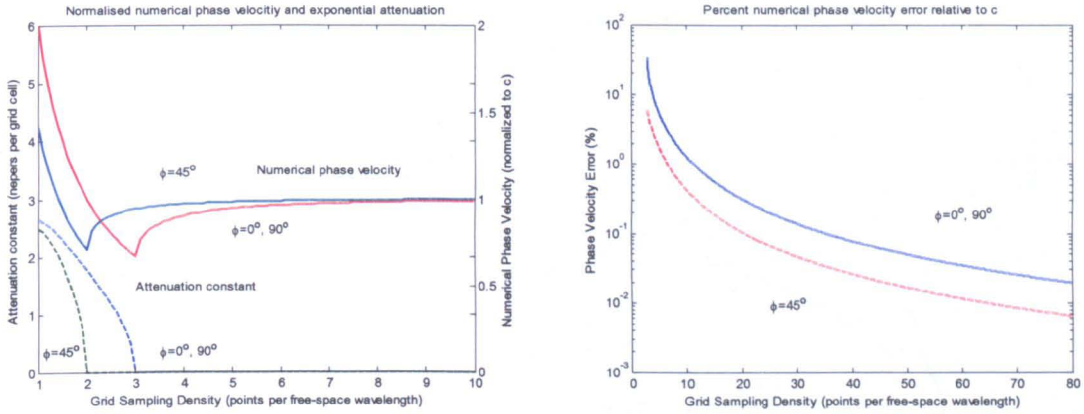
(a) Normalised numerical phase velocity and exponential attenuation constant per grid cell versus the grid-sampling density for on-axis and oblique wave propagation for a courant factor $S = 0.5$.

(b) Percent numerical phase-velocity error relative to the free-space speed of light as a function of the grid-sampling density for an on-axis and oblique wave propagation for a courant factor $S = 0.5$.

Figure 3.9. Numerical phase velocity and the numerical phase velocity error for $S = 0.5$.

In order to evaluate the calculation of wave propagation and the effects of numerical dispersion, a 2D FDTD simulation of a radially outward-propagating cylindrical wave, in a two-dimensional TM_z 360×360 - cell square Yee grid with $\Delta x = \Delta y = \Delta = 1.0$ is performed. The grid is excited at its centre point by applying a unit-step time-function to a single E_z field component and a Courant factor of $S = \sqrt{2}/2$. The E_z field distributions along the principal axis and grid diagonals at $\phi = 45°$ are plotted after $n = 232$ time steps. In Figure 3.10.(a) the numerical dispersion artefacts are displayed as the leading edge of the wave exhibits an oscillatory jitter on the propagation along the grid diagonal compared to the normal field falloff profile propagating along the principal axis. The expanded view of the Figure 3.10.(a) between the 120Δ and 180Δ points on the grid is shown in Figure 3.10.(b). In Figure 3.10.(b), the leading edge of the wave

propagating along the principal axis presents a superluminal artefact. The existence of this artefact is due to the poorly sampled short wavelength numerical modes that are generated by an abrupt field discontinuity, such as the one generated by a step-function [4]. An implication of this result is that attention must be paid in simulating plane-wave dispersion analysis for waves having curved fronts. However, if sampling is improved by increasing the mesh size and taking into account the numerical phase velocities of the incident plane wave propagating at an angle, the numerical dispersion artefact is reduced.
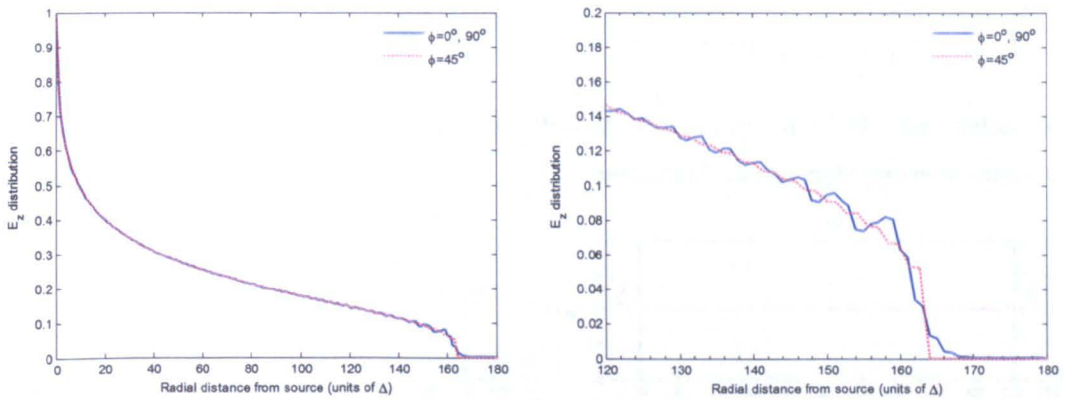
(a) Comparison of calculated wave propagation along the grid axes and along a grid diagonal.

(b) Expanded view of previous graph at distances between 120 and 180 grid cells from the source.

Figure 3.10. Effect of numerical dispersion in a two-dimensional grid upon a radially propagating cylindrical wave.

3.4 Modelling PML Absorbing Boundary Conditions

The PML technique introduced by Berenger in [5] has proven one of the most effective and robust methods of truncating the computational FDTD grid. The theory of the PML has been established in Chapter 2, Section 9. The following numerical results illustrate the implementation of the PML using the FDTD method according to the literature [4].

In order to demonstrate the effect of the PML absorbing boundary conditions (ABCs), a simple 1D FDTD method simulation with exactly the same parameters as in Figure 3.1 is used. An x-directed Gaussian pulse with unit amplitude, width of 10 grid cells, and $1/e$ temporal half-width of $\tau = 100\,\text{ps}$ is launched from the far-left side of the grid travelling along 0.6 m distance in free

space with grid resolution of $\Delta_x = 6\,\text{mm}$. The 1D FDTD simulation is using a Courant factor of 1.0 which is equivalent to the *magic time-step* $\left(c\Delta t = \Delta x\right)$.
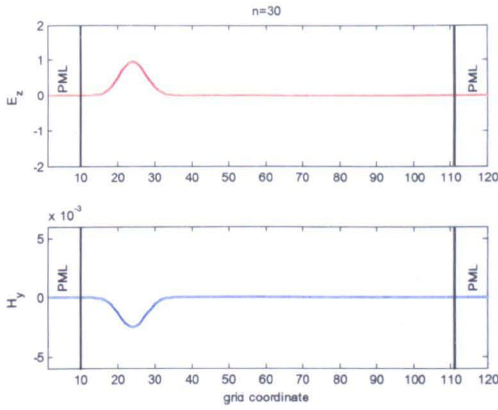
(a) At time step $n = 30$ the Gaussian pulse is propagating to the $x+$ direction.
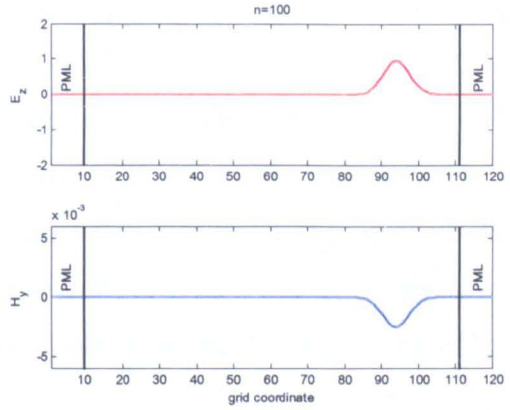
(b) At time step $n = 100$ the pulse is approaching the far-right grid boundary.
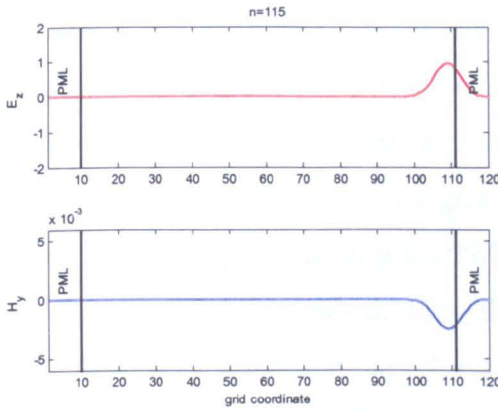
(c) The wave penetrates the PML ABCs.
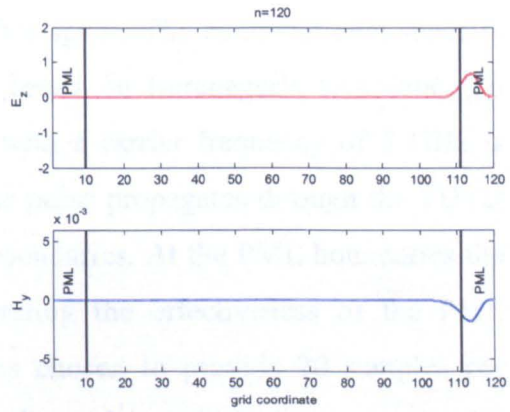
(d) The PML medium is acting as an absorber on the wave propagating.
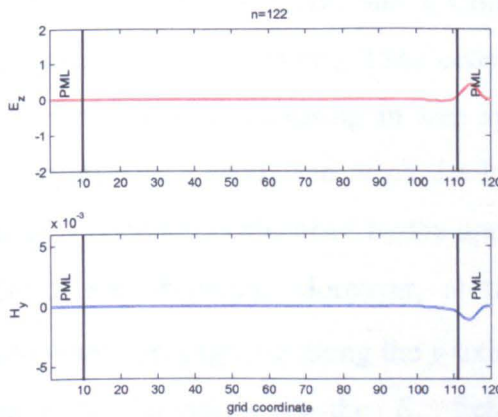
(e) The amplitude of the wave is considerably reduced by the PML.
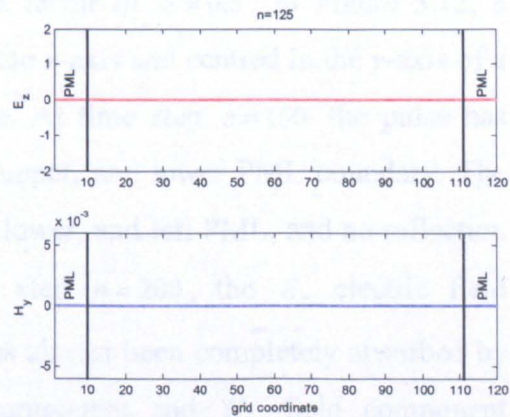
(f) By time step $n = 125$ the Gaussian pulse has been completely absorbed by the PML.

Figure 3.11. One-dimensional plane wave propagation with PML ABCs.

In this case, the PEC sheets on the left and on the far-right of the grid are replaced with PML ABCs. The thickness of the PML walls was set to 10 cells, with a reflection coefficient $R_0 = 1 \times 10^{-7}$, and PML order $n_{pml} = 2$ (parabolic). The results presented in Figure 3.11 illustrate the propagation of the wave, before and after it reaches the far-right grid boundary. The Gaussian pulse propagates in free space as in the previous simulation. When the pulse reaches the far-right grid boundary, the pulse penetrates the PML anistotropic medium. The PML matching condition embedded in the simulation is calculated based on the appropriate choice of the thickness of the PML walls and conductivity parameters given in equation 2.63. The incident plane wave is then totally attenuated within the PML region.

Similarly, for the 2D FDTD method with PML ABCs, the following plots show the propagation of a plane wave in free space. The computational space is truncated with the addition of split-PML based on Bereneger's technique. To illustrate the algorithm, a Gaussian pulse with a carrier frequency of 5 GHz is launched from the left side of the grid. The pulse propagates through the FDTD computational domain reaching the PML boundaries. At the PML boundaries the pulse is completely absorbed, thus illustrating the effectiveness of the PML ABCs. The grid resolution $\Delta x = 3$ mm was chosen to provide 20 samples per wavelength at the centre frequency of the pulse (which in turn provides approximately 10 samples per wavelength at the high end of the excitation spectrum, around 10 GHz) and a Courant factor of $S = 0.5$. In Figure 3.12, a cylindrical pulse, originating $15\Delta x$ cells in the x-axis and centred in the y-axis of a 100×50 grid, is propagating in free space. At time step $n = 150$ the pulse has propagated long enough to reach the left, upper, and lower PML boundary. The pulse is completely absorbed by the upper, lower, and left PML, and no reflection effects are observed. Moreover, at time step $n = 200$, the E_x electric field component propagating along the y-axis has almost been completely absorbed by the PML, leaving only the E_y field component and H_z field component propagating towards the far-right of the grid. At time step $n = 250$ the field components encounter the right PML boundary and by time step $n = 300$, all field components have been totally attenuated by the PML.
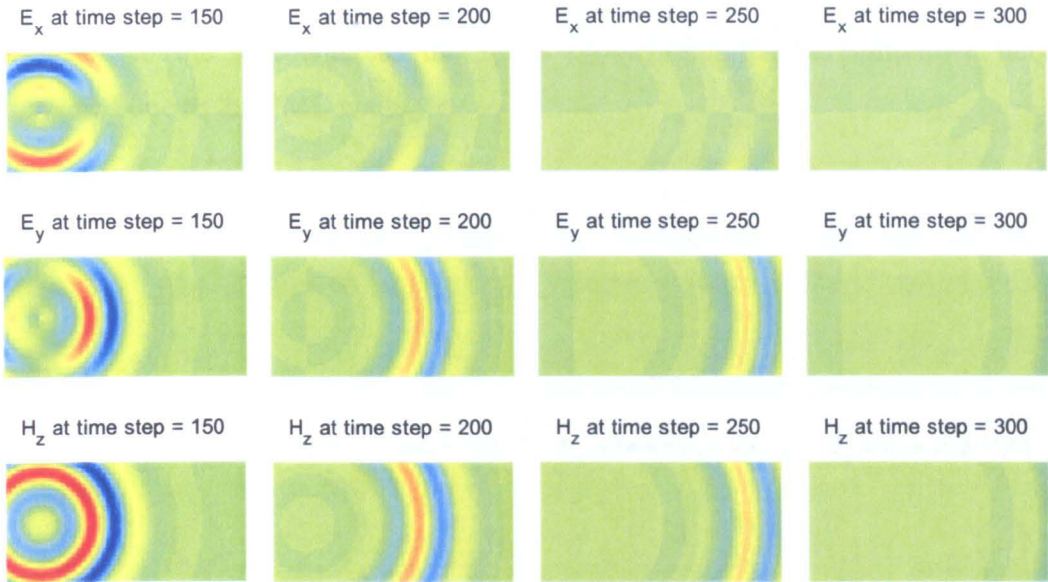
Figure 3.12. Two-dimensional Gaussian pulse propagation with
PML Absorbing Boundary Conditions.

Moreover, the following plots in Figure 3.13 show the propagation of a plane wave in free space with a metal cylinder placed at the far-right of the grid. The 100×50 grid cells computational space is truncated with the addition of an 8 cells-thick PML based on Bereneger's technique. To illustrate the algorithm, a 3-cm-radius metal cylinder is placed 80 cells in the x-axis and 25 cells in the y-axis of the grid, with relative permittivity $\varepsilon_r = 1$ and electric conductivity $\sigma = 1 \times 10^7$ S/m is depicted as a blue circle in the figure. The rest of the grid is modelled as free space. The source excitation is a Gaussian pulse with a carrier frequency of 5 GHz. A grid resolution of $\Delta x = 3$ mm was chosen to provide 20 samples per wavelength at the centre frequency of the pulse (which in turn provides approximately 10 samples per wavelength at the high end of the excitation spectrum, around 10 GHz). As the pulse propagates, at time step $n = 150$, the Gaussian pulse has not yet reached the metal cylinder, whereas it has propagated long enough to the left and to the vertical boundaries to reach the PML boundaries, where the electric and magnetic field components have been absorbed. At time step $n = 200$, the pulse has propagated to the right and it has already reached the metal cylinder. At the surface of the metal cylinder the electric field is very close to zero due to the high conductivity of the material. At the left boundary of the cylinder the electric and magnetic fields are reflected, whereas the pulse propagates to the right surrounding the metal cylinder on the

top and bottom boundaries. Finally, at time step $n = 300$, the reflected fields propagate to the left, whereas the fields propagating to the right have been attenuated due to the PML walls.
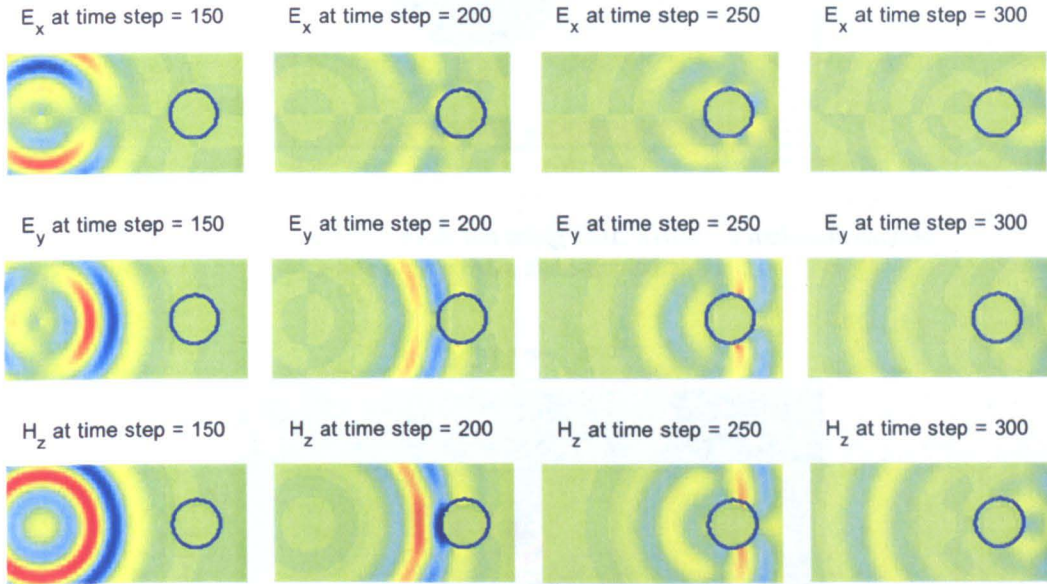
Figure 3.13. Two-dimensional Gaussian pulse propagation with PML ABCs and metal cylinder.

Furthermore, in Figure 3.14 a two-dimensional problem space including a dielectric scatterer sphere with $\varepsilon = 3.5$ and radius 20 cm is illustrated. The sphere is placed 40 cm in the x-axis and 50 cm in the y-axis in a 210×160 grid. A source (M_1) is placed 20 cm away from the sphere and the rest of the grid is initialised to free space. The grid is excited with a Gaussian pulse and the problem space is terminated with 10 cell-thick PML boundaries. The Yee-cell is set to $\Delta x = 5$ mm and the simulation is run for 8000 time steps with a Courant factor $S = 0.9$, just below the magic-step function. During the simulation the cylindrical wave is propagating in the FDTD grid in all directions. The wave propagating towards the PML boundaries is attenuated and completely absorbed by the PML. However, by monitoring the H_z magnetic field distribution during the simulation, as the Gaussian pulse has reached and propagated along the surface of the dielectric sphere, a magnetic field is formed encompassing the surface of the sphere.
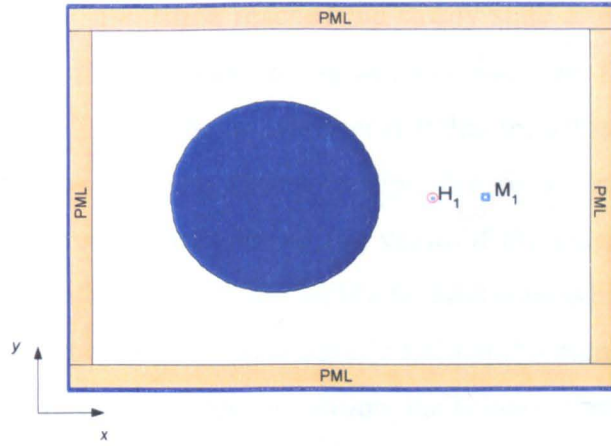
Figure 3.14. A 2D FDTD simulation using PML ABCs : A dielectric excited by a line source (M₁), and sampled at (H₁).
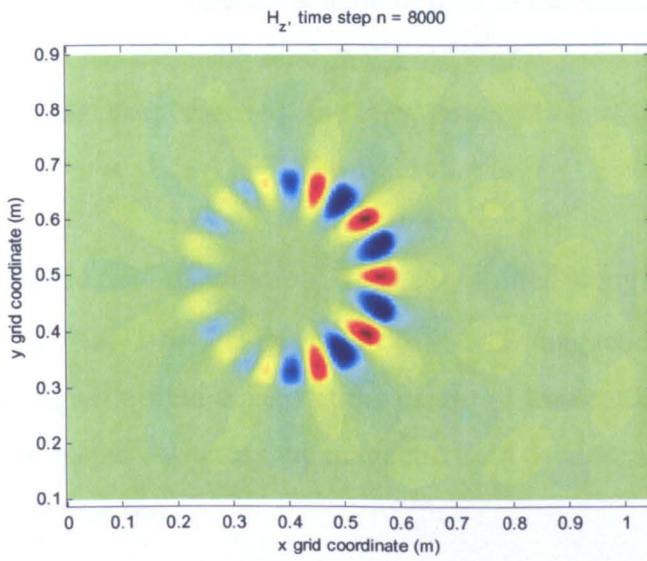
Figure 3.15. Sampled transient magnetic field H_z at time $n = 8000$.
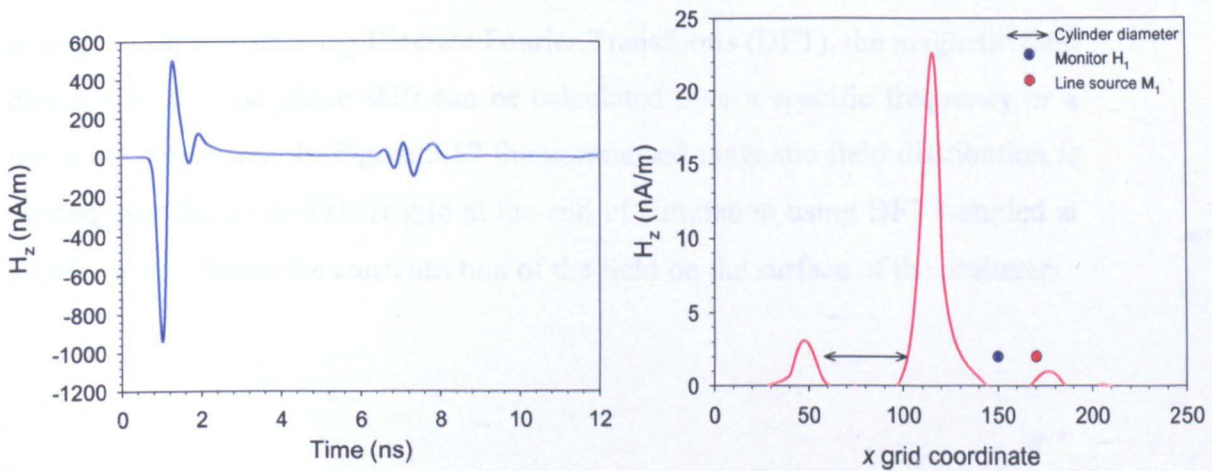
(a) Sampled magnetic field H_z at monitor H₁.

(b) Magnetic field H_z along the propagation direction

Figure 3.16. Sampled magnetic fields at time step 8000, across the centre of the FDTD grid.

The 2D FDTD simulation reached the steady state after 6000 time steps, where the magnetic field distribution is at maximum on the surface of the scatterer, without any reflections or evanescent fields from the boundaries of the FDTD grid. A monitor (H_1) was used to sample the magnetic field between the source and the scatterer. By monitoring the value of the magnetic field at each time step (Figure 3.16(a)), it is then possible to determine when the steady state has been reached, as the value of the magnetic field at the monitor becomes zero. Based on Figure 3.16(a), during the simulation, the Gaussian pulse has propagated past the monitor and towards the scatterer at time $t = 2$ ns. As the pulse has reached the surface of the scatterer, some of the magnetic field has been reflected back. At time $t = 6$ ns, the reflected magnetic field is travelling past the monitor. After time $t = 8$ ns, the magnetic field at the monitor is zero, thus indicating that the steady state has been reached and any propagating magnetic fields have decayed.

The magnetic field distribution H_z is also plotted along the y-coordinate at the centre of the FDTD grid (Figure 3.16(b)). The magnetic field distribution shows that the magnetic field is zero at the centre of the scatterer. The field is at maximum on the surface, whereas the magnetic field oscillates back-and-forth on the surface of the scatterer.

During the 2D FDTD simulation the maximum value of the magnetic field H_z across the entire FDTD computational domain is stored in memory. At the end of the simulation using Discrete Fourier Transforms (DFT), the magnetic field distribution and the phase shift can be calculated over a specific frequency or a range of frequencies. In Figure 3.17 the normalised magnetic field distribution is plotted over the entire FDTD grid at the end of simulation using DFT sampled at 1 GHz, which shows the concentration of the field on the surface of the scatterer.
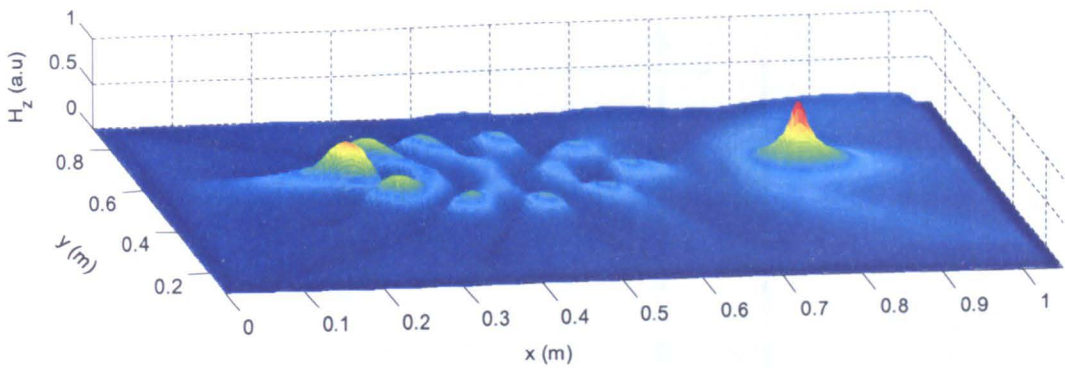
Figure 3.17. Magnetic field distribution sampled at 1 GHz.

Although, PML ABCs have been implemented and used, in order to evaluate the performance of the PML, and how PML parameters affect the performance of ABCs, the PML error function has been used for the following simulation and the results are presented. The relative error of the PML can be calculated based on the equation

$$\text{Rel. error} = 20 \times \log_{10} \frac{\left| E_{i,j}^{PML} - E_{i,j}^{ref} \right|}{\max\left(E_{i,j}^{ref} \right)} \tag{3.5}$$

where $E_{i,j}^{ref}$ is a reference field that is calculated without PML, but for a vast FDTD computational space and for the same time limit. The FDTD grid Δ was set to have 1 mm cells and $\Delta t = 0.98\,S$. The reference case was modelled for 1240×1240 –cell grid, where the monitors were placed at the same position relative to the source as in the test grid [4]. The reason for modelling $E_{i,j}^{ref}$ is to avoid any reflection effects from boundaries, as the field is propagating away from the source and the monitors. In order to evaluate the performance of the PML ABC, the following test structure in Figure 3.18 has been modelled.

74
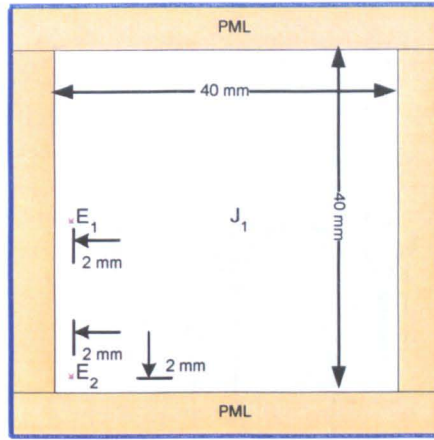
Figure 3.18. Two-dimensional FDTD grid with two sampled E-fields.

The PML test case was modelled for 60×60 –cell grid, where the monitors were placed at the same position relative to the source as in the reference grid. The grid was excited with a differentiated Gaussian pulse with temporal width of $t_w = 26.53$ ps and time-delay $t_0 = 4t_w$. The test structure was simulated for 1800 time steps for 5 PML cells and 10 PML cells, and the point of observation (A) was set at 2 mm away from the PML wall (E_1), and the second observation point (B) was set at the lower left-hand corner 2 mm from either side of the PML walls (E_2). For all the PML simulations the polynomial grading was $m = 4$ and the loss grading function was $R(0) = 10^{-7}$.

The values of the 2D FDTD simulations for the electric field for both the reference case and the test case have been recorded for 5 PML cells and 10 PML cells. The results presented in Figure 3.19 show the relative error calculation using equation (3.5). It is worth noting that the error for observation point A is almost always less than that of point B, due to the fact that the wave propagating towards A is nearly normally incident, whereas for point B, the wave is approaching in an oblique angle of 45°. Moreover, all results have localised minima, but overall the results for 10 PML cells present a smaller error. In this simulation, the results obtained indicate that errors can be reduced by using a larger number of PML cells, a better choice of the loss grading function, and polynomial grading. However, for a broad number of applications, the optimal choice is a 10-cell thick PML with a loss grading function of $R(0) = 10^{-7}$ [4].
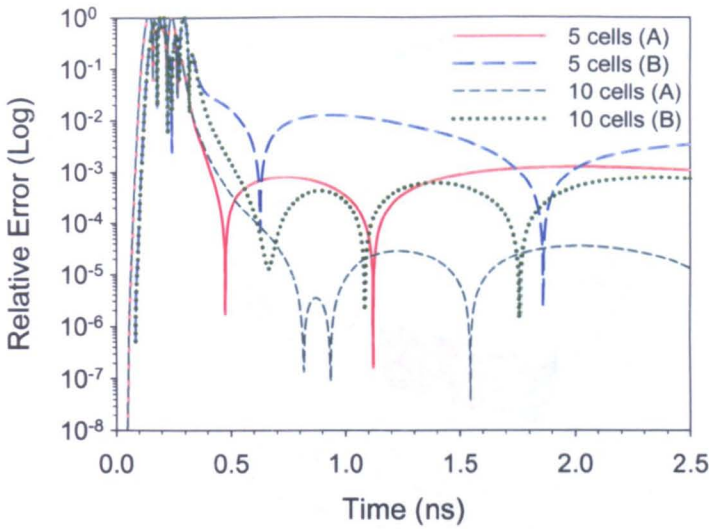
Figure 3.19. Relative error at points E_1 and E_2 over 1000 time-steps for 5 and 10 PML thick boundaries.

3.5 Modelling Lumped Elements

In some practical electromagnetic applications, the use of active and passive lumped elements is required. These elements could be active elements, such as voltage or current sources, or passive elements, such as resistors, capacitors, and inductors. In this case, for each of the elements listed above, Maxwell's curl equation is updated to include the relationship that ties the electric and magnetic field with those elements. Furthermore, the updating coefficients for the electric and the magnetic fields must be updated in order to take into account the parameters of the active and passive lumped elements.

The following diagram illustrates the simulation of active and passive lumped elements using a stripline structure. Specifically the structure has width/height ratio of 1.44 and is 60 mm in length. The stripline is suspended in air forming 50 Ω characteristic impedance with PEC boundaries. The stripline shown in Figure 3.20 is sourced using a voltage source and is excited by a unit step waveform with 1 volt magnitude that was turned on 50 time steps into the simulation. For the FDTD simulation a Courant factor of $S = 0.9$ is used with a grid resolution of $\Delta x = 0.72 \times 10^{-3}$ m and $\Delta y = \Delta z = 1.0 \times 10^{-3}$ m. The stripline and the two PEC plates' material properties were modelled with relative permittivity of

76

$\varepsilon_r = 1$ and electric conductivity of $\sigma = 1 \times 10^{10}$ S/m. A 50 Ω resistor is placed between the problem space and the PEC boundary.
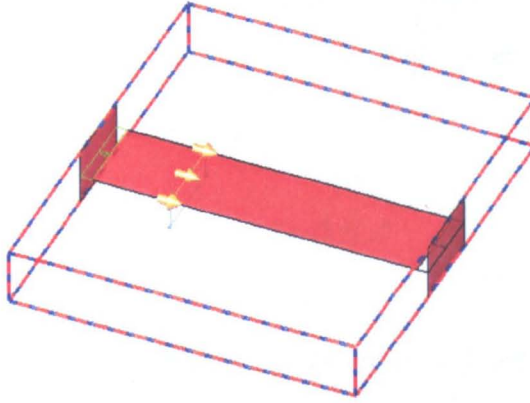
Figure 3.20. Stripline structure with 50 Ω characteristic impedance.

The voltage and current are sampled 32 cells away from the source in the y-direction. The voltage and current sampled values are plotted in Figure 3.21. The spikes appearing in the plot are largely the result of the PEC boundaries used, which make the FDTD simulation space into a cavity that resonates. For a unit step waveform, and 50 Ω characteristic impedance, the amplitude of the current passing through the monitor is approximately 0.02 A. As the unit pulse propagates through the FDTD grid at the monitor, the sampled voltage is a voltage pulse with 0.5 volts in amplitude.
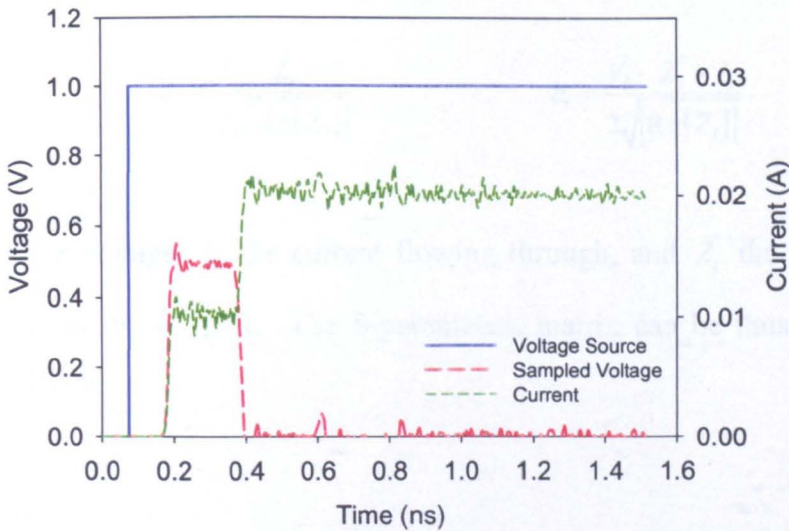
Figure 3.21. Stripline voltage source and sampled parameters.

In each time step during the FDTD simulation following the electric and magnetic field updating equations, the voltage or current sources are updated. The sampled current values at each observation point are calculated after the magnetic field equation has been updated. In this case the current value is the sum of the magnetic fields that surround the sampled current, at each observation point, given by

$$I = \oint \vec{H}.dl \tag{3.6}$$

Similarly, the sampled voltage values are calculated based on the sum of the electric fields that surround the sampled voltage, at each observation point, given by

$$V = -\int \vec{E}.dl \tag{3.7}$$

3.6 Scattering Parameters

Scattering parameters (S-parameters) are based on the power waves concept. They are used to describe the response of microwave circuits specifically when measuring at high frequencies [6]. The incident a_i and reflected waves b_i are calculated by

$$a_i = \frac{V_i + Z_i \times I_i}{2\sqrt{|Re\{Z_i\}|}}, \qquad b_i = \frac{V_i - Z_i^* \times I_i}{2\sqrt{|Re\{Z_i\}|}} \tag{3.8}$$

where V_i is the voltage, I_i the current flowing through, and Z_i the impedance looking out from the ith port. The S-parameters matrix can be thus expressed according to [6] as

$$
\begin{bmatrix} b_1 \\ b_2 \\ \vdots \\ b_n \end{bmatrix} = \begin{bmatrix} S_{11} & S_{12} & \cdots & S_{1n} \\ S_{21} & S_{22} & \cdots & S_{2n} \\ \vdots & \vdots & \ddots & \vdots \\ S_{n1} & S_{2n} & \cdots & S_{nn} \end{bmatrix} \times \begin{bmatrix} a_1 \\ a_2 \\ \vdots \\ a_n \end{bmatrix} \qquad (3.9)
$$

where the subscripts indicate the output port number (row) and the input port number (column). Using simple matrices, the S-parameters can be calculated for a multiport circuit where all ports are terminated with equivalent loads and one port is used as the source port by recording the values of the voltages and currents at each port. The S-parameters can be calculated for the reference port (m,n) using the equation

$$
S_{mn} = \frac{b_{mn}}{a_{mn}} \qquad (3.10)
$$

Furthermore, at the end of the FDTD simulation, since the S-parameters are complex quantities, their magnitude and phase can be plotted using DFT over a range of frequencies set at the beginning of the simulation using

$$
|S_{mn}|_{dB} = 20 \log_{10} \left(|S_{mn}| \right) \qquad (3.11)
$$

In order to evaluate the S-parameter formulation, a microstrip low-pass filter was simulated using the FDTD method. A voltage source with internal resistance of 50 Ω was used to terminate the microstrip at one end, whereas a 50 Ω resistor was used to terminate the other end of the microstrip [7]. Two current monitors were placed on each port to record the current over time. The following diagram illustrates the FDTD problem space. The FDTD space is composed of cells having $\Delta x = 0.4064$ mm, $\Delta y = 0.4233$ mm, and $\Delta z = 0.265$ mm. A gap of 5 cells is left between the structure and the PEC boundaries. The substrate of the structure is $3 \times \Delta z$ and has a dielectric constant $\varepsilon_r = 2.2$.
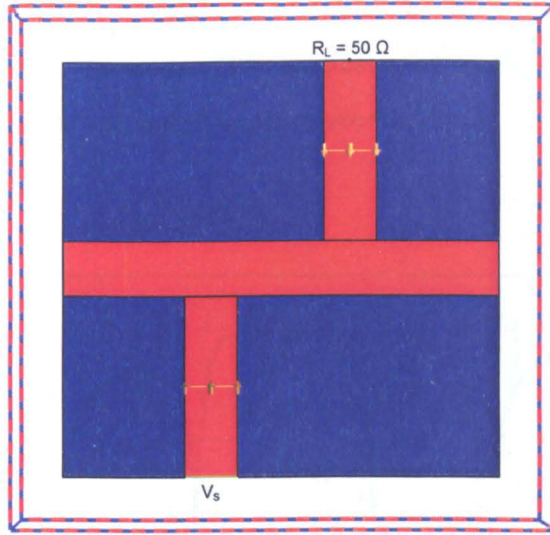
Figure 3.22. Microstrip low-pass filter terminated by a voltage source and a resistor.

The microstrip was excited with a Gaussian pulse for 3500 time steps. At the end of the FDTD simulation the voltage and current sampled values were used to calculate the S-parameters for each port using equation (3.10). Finally, the frequency domain S-parameter values were calculated using DFT. The S-parameter magnitudes in decibels are thus calculated using (3.11).

The FDTD simulation for the low-pass microstrip filter was repeated using a set of absorbers with Benzocyclobutene (BCB) $\varepsilon_r = 2.57$ placed around the problem space, and using CPML boundary conditions in order to eliminate the resonant cavity effect that PEC ABCs produce. The following diagrams illustrate the return loss $|S_{11}|_{dB}$ and the insertion loss $|S_{21}|_{dB}$ of the microstrip low-pass filter.

The S-Parameters obtained from the FDTD simulation are plotted in Figures 3.23 and 3.24. The figures show for the PEC boundary condition used initially, that although the simulation has produced results similar to [7], at certain frequencies the PEC boundaries make the FDTD simulation behave like a cavity that resonates. Similarly, the polymer absorber at frequencies higher than 10 GHz also produces undesired results, as spikes appear in the S-Parameters. This is due to the absorber material that allows the electric and magnetic fields to be reflected back, instead of being absorbed. Finally, the CPML boundary conditions produce almost identical results to these calculated in [7]. The CPML boundary conditions

80

successfully absorb the electromagnetic fields as they propagate towards the boundary without any reflections. This is illustrated in Figures 3.23 and 3.24 as there are no spikes appearing in the S-parameters plotted.
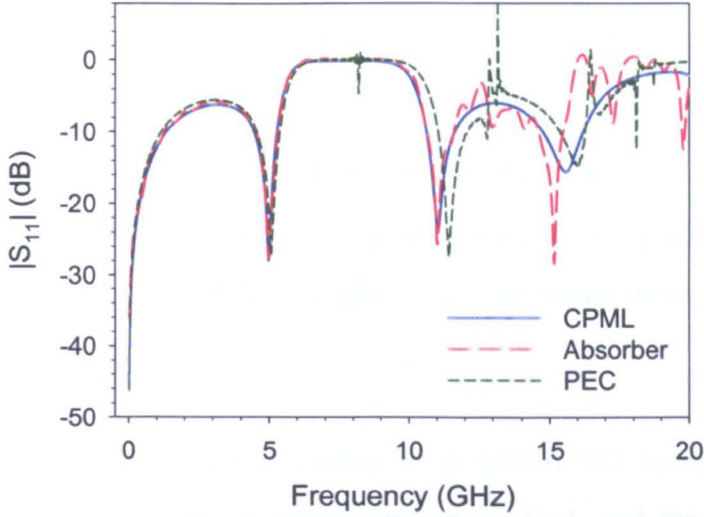
Figure 3.23. Return loss magnitude $\left|S_{11}\right|_{dB}$ of the microstrip low-pass filter.
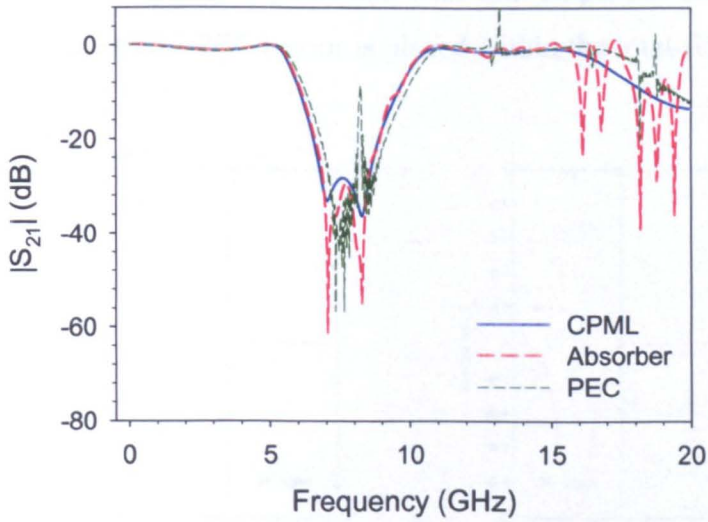
Figure 3.24. Insertion loss magnitude $\left|S_{21}\right|_{dB}$ of the microstrip low-pass filter.

Moreover, based on Figure 3.24, the performance of the microstrip low pass filter can be observed in the insertion loss $\left|S_{21}\right|_{dB}$. The circuit acts as a stop-band filter for frequencies up to 5.5 GHz just before the steep curve occurs, with some shift appearing near the high end of the frequency range.

3.7 Total-Field/Scattered Field

The *total-field/scattered-field* (TF/SF) is based on Maxwell's equations and assumes the physical total electric field and total magnetic field can be decomposed into

$$\vec{E}_{total} = \vec{E}_{inc} + \vec{E}_{scat} \qquad\qquad \vec{H}_{total} = \vec{H}_{inc} + \vec{H}_{scat} \qquad (3.12)$$

where $\vec{E}_{inc}$ and $\vec{H}_{inc}$ are the incident electric and magnetic fields, and $\vec{E}_{scat}$ and $\vec{H}_{scat}$ are the scattered fields. The formulation resulted from an attempt to create a plane-wave source that avoids the obstacles caused by using either hard source or initial conditions [8, 9].

A 1D FDTD simulation was setup for a grid of 400 cells, with $\Delta x = 1.0$. The Courant factor for this simulation was set to $S = 1$ and the time-step was selected to $c \cdot \Delta t = S \cdot \Delta x$. The overall effect of implementing the TF/SF formulation is illustrated in the Figure 3.25 below. In the one-dimensional grid, a Gaussian-pulse like behaviour is generated with unit amplitude and as the wave propagates within the grid a PEC mirror is placed within the total-field region.
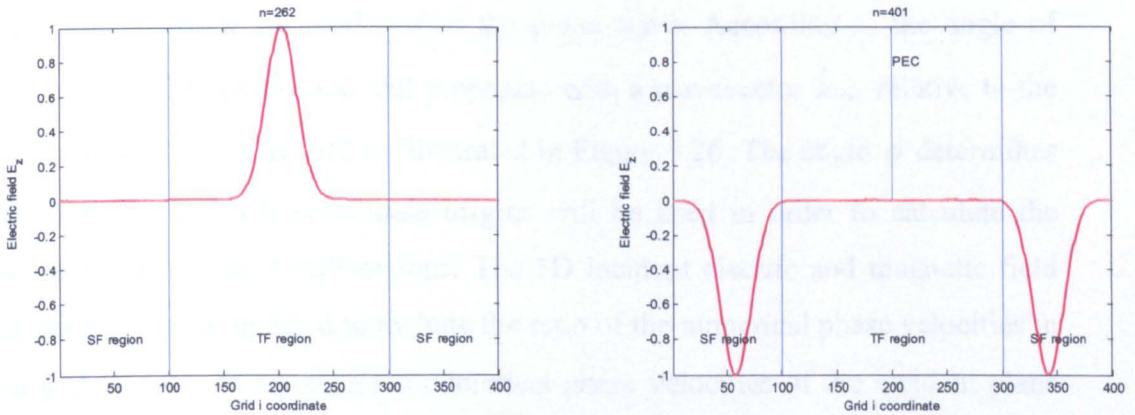
(a) Gaussian pulse propagating in free-space.   (b) PEC mirror placed within the TF region and resulting wave in SF regions.

Figure 3.25. Total-field/Scattered-field for one-dimensional FDTD grid.

The PEC sheet mirror forces $E_z = 0$ at the centre of the TF region. The PEC mirror generates a retroreflection effect, a negative x-directed reflection of the Gaussian pulse continuing well in to the SF to the left of the grid. At the same time the field behind the mirror in the TF region is at all time negative. Eventually in the SF region an x-directed wave appears propagating. This is not an error, but due to the equation (3.12), as the field in the TF region is zero, then the total field must be equal to the field in the SF region.

The TF/SF technique can be extended for the two dimensional FDTD case. The two-dimensional formulation allows the generation and propagation of an incident plane wave at any given angle of incidence. The formulation in this case becomes more complex than the one-dimensional formulation. The updating equations for the electric and magnetic fields in the TF/SF region have to be modified based on a set of consistency conditions [4]. The generic 2D FDTD electric and magnetic field updating equations are implemented as usual in the time-stepping algorithm, but in this case a set of incident-wave correction terms are added for each updating equation.

Furthermore, the calculation of the 1D incident field is updated to include the angle of incidence. For the 2D formulation a position vector is calculated based on the angle of incidence of the plane-wave. According to the angle of incidence φ the plane-wave will propagate with a wavevector $\hat{k}_{inc}$ relative to the x-axis of the 2D FDTD grid as illustrated in Figure 3.26. The angle φ determines which of the four (4) coordinate origins will be used in order to calculate the incident field in the TF/SF regions. The 1D incident electric and magnetic field equations are now updated to include the ratio of the numerical phase velocities in the grid in order to equalize the numerical phase velocities of the incident plane wave propagating at an angle φ and the wave in the source grid [4]. The diagram shown in Figure 3.26 illustrates the calculation of the 2D FDTD TF/SF incident plane-wave field calculation for an angle $0° \le \varphi \le 90°$, where $d = \hat{k}_{inc} \cdot r_{comp}$ is the distance from the origin to a perpendicular dropped to the wavevector from the location of the field. The numerical phase velocity and the numerical wave

propagation for a wave travelling at an angle φ is derived in Appendix A – C. For the TM_z case the TF/SF formulation is thus illustrated:
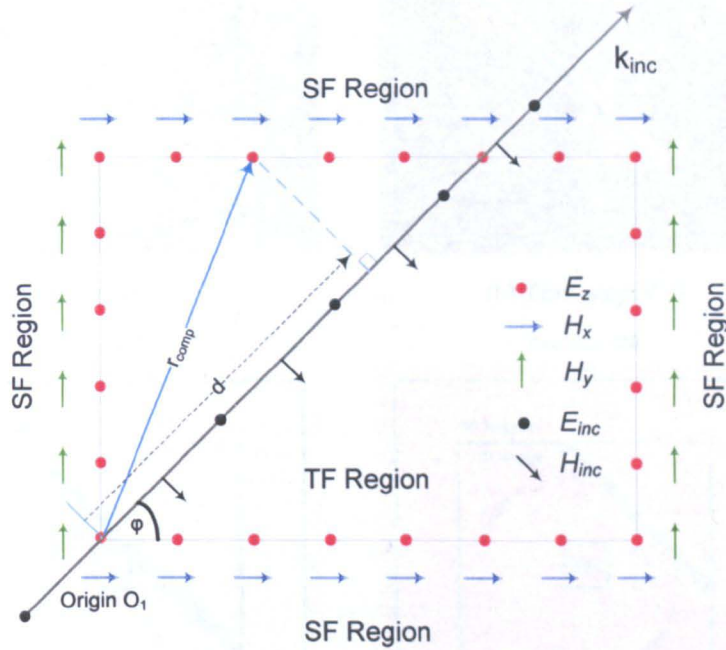
Figure 3.26. Incident plane-wave calculation for the 2D TF/SF FDTD formulation (TM_z).

The 2D TF/SF formulation has been implemented for both the TE_z and the TM_z case. A PEC square reflector ($\varepsilon_r = 1$ and $\sigma_e = 1 \times 10^6 \, S/m$) with width 70 cells has been placed in the middle of a 400×400 2D FDTD grid. The scattered-field region is set to 100 cells. The FDTD computational domain is terminated using 30 cells of PML ABCs. A Gaussian pulse has been used to source the incident plane wave conditions of the TF/SF formulation propagating at an angle $\varphi = 45°$. The following plots in Figure 3.27 illustrate the plane-wave propagation of the magnetic field H_z through the total-field zone at different time-steps for the TE_z case. The 2D FDTD parameters were set for a time-step $\Delta t = \Delta/2c$, where $\Delta = 5$ mm and a courant factor S of 0.5. The simulation was allowed to run for $n = 1400$ time steps.

(a) Time step: 750   (b) Time step: 910

(c) Time step: 1100   (d) Time step: 1250
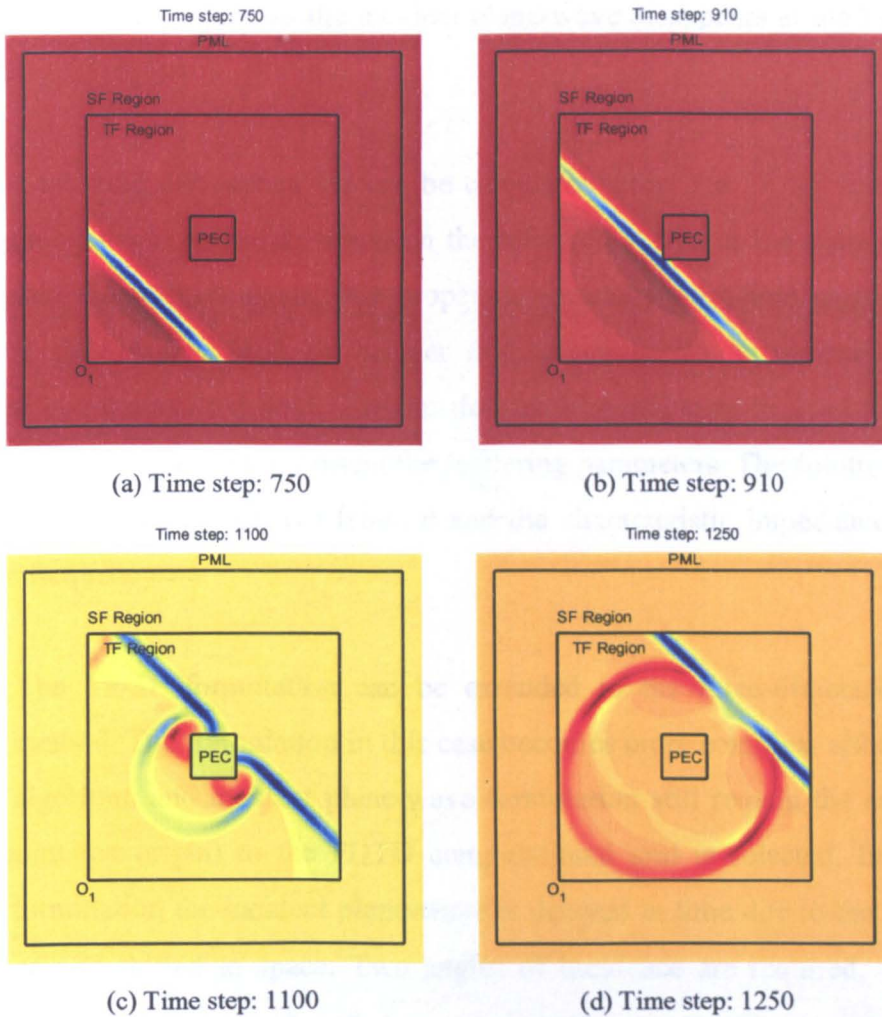
Figure 3.27. Incident plane-wave visualizations (H_z) for the 2D TF/SF FDTD formulation (TE$_z$) at different time steps.

In Figure 3.27, the incident plane wave is propagating through the total-field zone with an angle of incidence of 45° at time step $n = 120$. At 45° the origin of entry of the plane wave is O_1. As the wave propagates and interacts with the PEC reflector placed in the middle of the FDTD grid at time step $n = 910$. The wave eventually is reflected around the sides of the PEC object. As the incident plane wave is now partially reflected and partially propagating along the diagonal, two separate waves begin to emerge at either side of the PEC reflector at time step $n = 1100$. As the incident plane wave encountered the PEC object, the reflected waves still appearing in the total-field zone are now propagating towards the origin O_1, whereas the incident plane-wave continues to travel along the diagonal away from the origin O_1. Moreover, the reflected fields will reach the scattered-field region due to the angle of incidence of the plane wave and the scattering

effects of the PEC object, as the incident plane-wave disappears at the far end of the total-field region.

Scattering parameters (S) can be calculated using the TF/SF formulation for inhomogeneous materials based on the reflected waves in the scattered-field region and transmitted waves that propagate from the total-field region to the scattered field region [10]. A transfer matrix can be obtained based on the reflected and transmitted field. The transfer matrix could then be used to solve a linear set of equations that represent the scattering parameters. The solution can be used to calculate the effective index n and the characteristic impedance z for a specific frequency.

The TF/SF formulation can be extended to the three-dimensional 3D FDTD method. The formulation in this case becomes more complex, although the TF/SF algorithm and incident plane-wave formulation still remain the same. An entry point (an origin) to the FDTD computational grid is selected. In the 3D TF/SF formulation the incident plane-wave is delayed in time due to the angle of incidence and shifted in space. Two angles of incidence are required, θ_{inc} and φ_{inc}, to determine the waveform's entry point in the FDTD 3D space [4, 6]. The complex frequency analysis for a wave travelling at an angle θ_{inc} and φ_{inc} is presented in Appendix D.

A 3D FDTD numerical analysis of a 20 cm dielectric slab ($\varepsilon_r = 4$) was implemented to obtain the reflection and transmission coefficients using the TF/SF formulation [11]. The dielectric slab was placed in the middle of the FDTD grid with grid resolution of $\Delta = 5\ mm$. Two monitors were placed 10 cells above and below the dielectric slab, Monitor 1 was placed 25 mm below the dielectric slab, and Monitor 2 was placed 25 mm above the dielectric slab in order to monitor the sampled electric fields (incident and scattered) based on the TF/SF formulation. An x-polarised incident plane-wave travelling along the z-direction of the 3D space was used to source the FDTD grid, as illustrated in Figure 3.28. The FDTD computational domain was terminated using 10 cells of CPML ABCs

on the x and y axis, whereas on the z-axis 10 cells of free-space were added before the CPML boundary conditions.
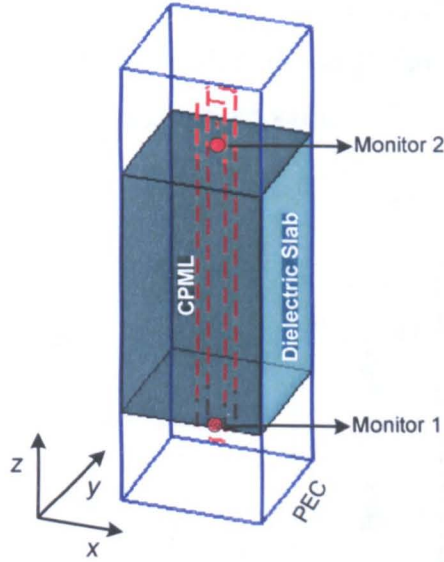
Figure 3.28. A 3D TF/SF FDTD simulation of a dielectric slab.

The 3D FDTD parameters were set for a time-step $\Delta t = 1 / c \cdot \sqrt{1/\Delta x^2 + 1/\Delta y^2 + 1/\Delta z^2}$, where $\Delta = 5$ mm and a courant factor S of 0.9. The FDTD simulation was allowed to run for 2000 time steps and the sampled electric fields were stored during the simulation along the direction of propagation. At the end of the simulation, the DFT of the sampled electric fields were calculated for $0.2 - 2.0$ GHz. Using equation (3.12) the transmission (T) and reflection (Γ) coefficients for the dielectric slab can be calculated based on [4] and are given by

$$|\Gamma| = \frac{|\vec{E}_{scat}|}{|\vec{E}_{inc}|} \tag{3.13}$$

$$|T| = \frac{|\vec{E}_{total}|}{|\vec{E}_{inc}|} = \frac{|\vec{E}_{scat} + \vec{E}_{inc}|}{|\vec{E}_{inc}|} \tag{3.14}$$

where $\vec{E}_{inc}$ is the incident electric field at the position of the monitor, $\vec{E}_{scat}$ is the scattered electric, and $\vec{E}_{total}$ is the total electric field at the same position. For this

simulation the incident and scattered fields are captured at two points above (Monitor 2) and below (Monitor 1) the dielectric slab. The sampled electric fields $\vec{E}_{inc}$ and $\vec{E}_{scat}$ are transformed to frequency domain, and $\vec{E}_{total}$ is calculated as the sum of the two fields. The frequency domain values are plotted in Figure 3.29. Based on the results plotted below when the scattered field value is equal to zero the total field is equal to the incident field value.
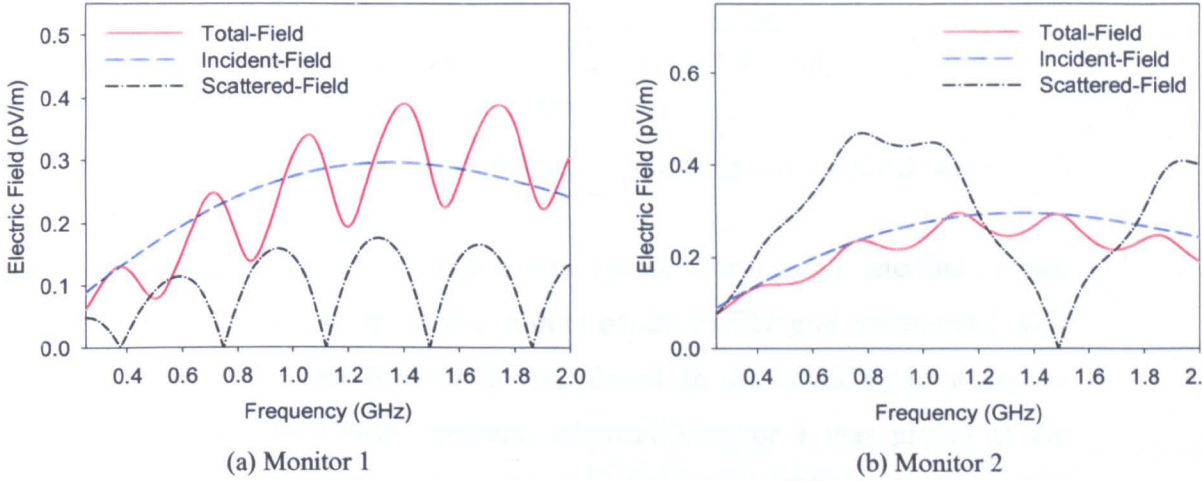
Figure 3.29. Incident field, scattered field and total field sampled at 2 monitors.

The sampled electric field parameters extracted from the 3D FDTD numerical analysis of the dielectric slab were then used in (3.13) and (3.14) to obtain the transmission and reflection coefficients. The transmission $|T|$ and reflection $|\Gamma|$ coefficients are plotted in Figure 3.30 and the results are in good agreement with [6] and the exact solution of the same problem was obtained from [11]. Based on the results plotted in Figure 3.30, the transmission coefficient is at maximum when the reflection coefficient is at zero, at frequencies 0.38, 0.75, 1.12, 1.50, and 1.86 GHz.
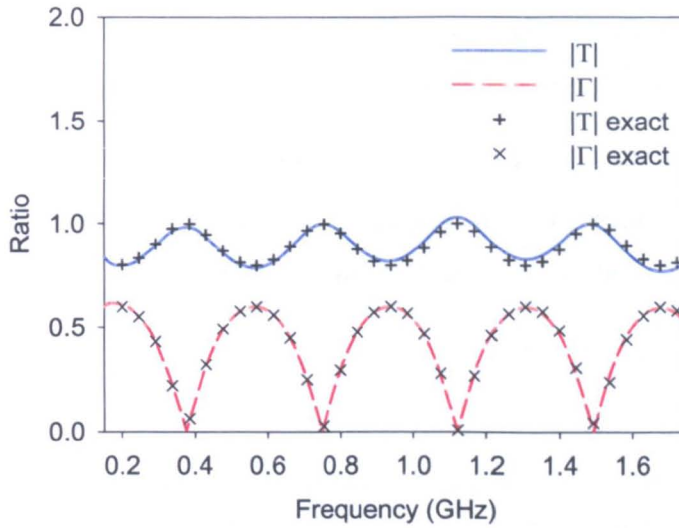
Figure 3.30. Transmission $|T|$ and reflection $|\Gamma|$ coefficients of a dielectric slab.

The same 3D FDTD simulation was repeated for a single interface, where the dielectric slab was placed in the middle of the FDTD grid surrounded with CPML ABCs. In this case Monitor 2 was placed on the boundary between the dielectric slab and the CPML medium, whereas Monitor 1 was placed at the boundary of 10 cells of free space the -x-axis and the CPML medium. The simulation was set to the same parameters as previously described and it was allowed to run for the same number of time steps. The following diagram in Figure 3.31 illustrates the modified setup of Figure 3.28 for a single interface.
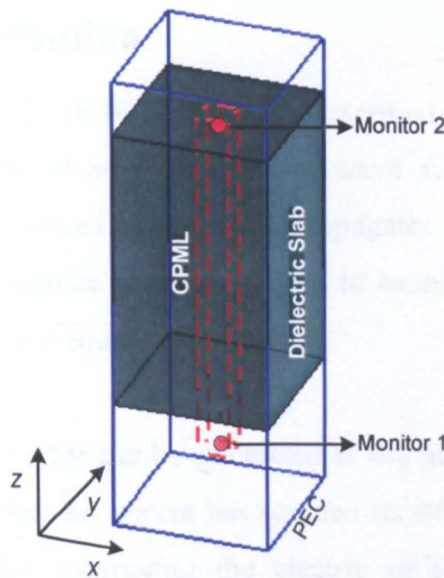
Figure 3.31. A 3D TF/SF FDTD single interface simulation of a dielectric slab.

The sampled electric field parameters extracted from the 3D FDTD numerical analysis of the dielectric slab for the single interface are then used to obtain the transmission and reflection coefficients. The transmission $|T|$ and reflection $|\Gamma|$ coefficients are plotted in Figure 3.32 and the results are almost identical to the results of Figure 3.30. Similarly, the transmission coefficient is at maximum when the reflection coefficient is at zero, at frequencies 0.38, 0.75, 1.12, and 1.50, and 1.86 GHz.
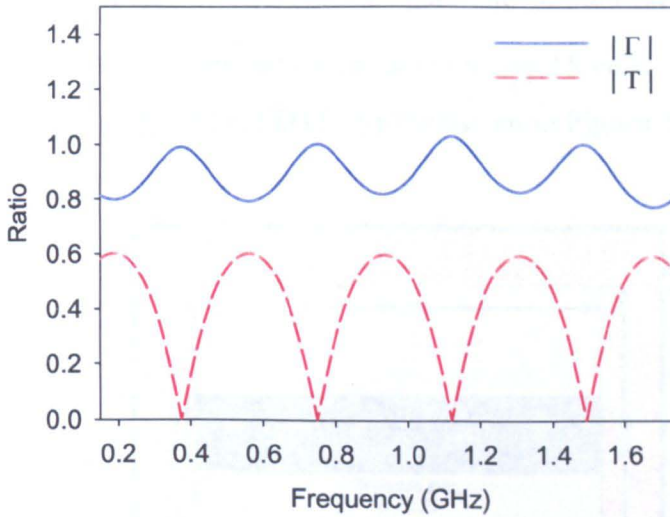
Figure 3.32. Transmission $|T|$ and reflection $|\Gamma|$ coefficients of a dielectric slab for single interface.

3.8 Power Distribution

Following the 2D FDTD TF/SF formulation described in the previous section that allows the propagation of an incident plane-wave at an oblique angle and the reduction of parasitic waves as the wave propagates in the total-field region, a TF/SF 2D FDTD simulation was carried out to examine the power distribution using the Poynting vector equation (3.1).

The Poynting vector can be calculated at any given time step in the FDTD simulation provided that the system has reached its steady-state. The steady-state can be determined by monitoring the electric or the magnetic field values, depending if it is TE_z or a TM_z simulation along the axis of propagation [12]. In

each time-step the maximum and minimum values are recorded and the peak-to-peak amplitudes are evaluated. As the incident plane-wave propagates through the total-field zone and the peak-to-peak values are calculated for each time-step the simulation continues until the steady-state has been reached. In this case the peak-to-peak values calculated are constant with each time-step.

A 2D FDTD simulation of a plane-wave propagating through a dielectric slab is considered for calculating the Poynting vector. The dielectric slab is placed in the middle of the FDTD grid with 100 cells in the x-direction and 80 cells in the y-direction with a cell size of $\Delta_x = \Delta_y = 0.5\ \mu m$. The courant factor was set at 0.9, and the computational domain was terminated using 15 cells of PML boundary conditions. The geometry of the FDTD grid is shown in Figure 3.33 below [12].
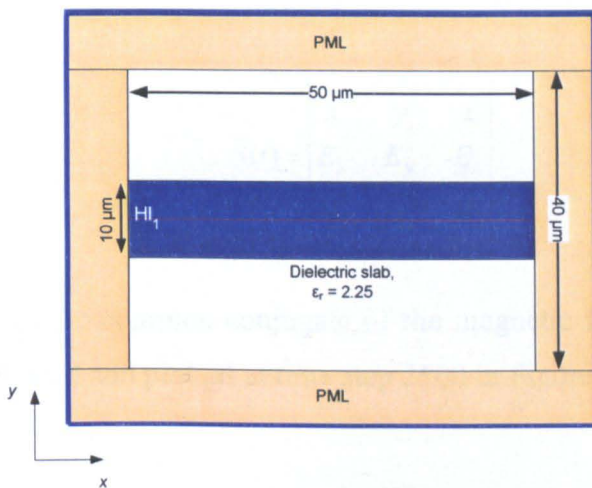
Figure 3.33. Dielectric slab waveguide structure.

A 20 THz sinusoidal plane-wave was launched at 15 cells in the x-direction of the FDTD grid covering the dielectric slab from grid coordinate 45 to 65 in the y-direction. The field values of the H_z magnetic field were monitored in the centre of the dielectric slab, along the line of propagation (H_{l1} indicated by the red line) until the peak-to-peak values remained constant through the time-stepping algorithm. After 2100 time steps the 2D FDTD simulation has reached its steady-state and the steady-state value of H_z is plotted in Figure 3.34.
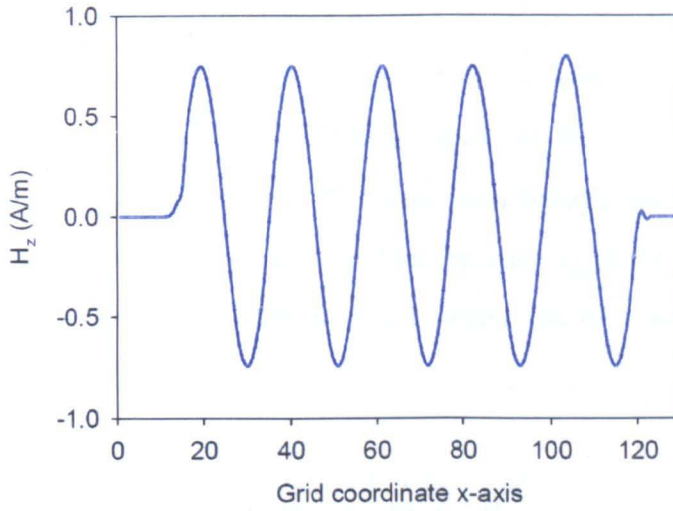
Figure 3.34. Sampled magnetic field H_z reaching steady-state.

The field distributions of the electric field E_y and the magnetic field H_z are used to calculate the Poynting vector for x-direction of propagation based on

$$\vec{S}(t) = \begin{vmatrix} \vec{x} & \vec{y} & \vec{z} \\ E_x & E_y & E_z \\ H_x^* & H_y^* & H_z^* \end{vmatrix} \tag{3.15}$$

where the * denotes the complex conjugate of the magnetic field. The Poynting vector is thus calculated and plotted at time step 2100 in Figure 3.35.
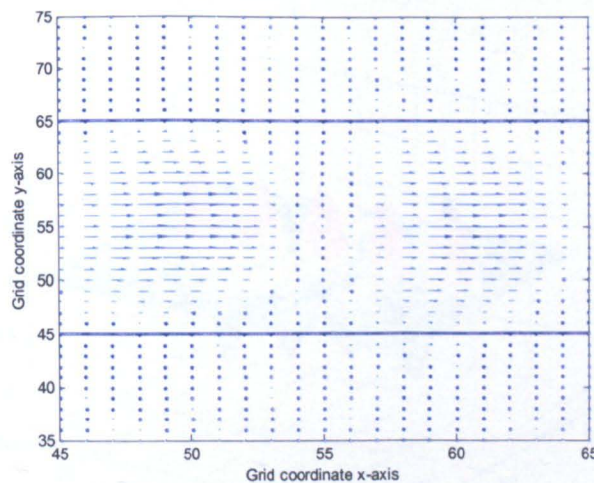
Figure 3.35. Poynting vector S after 2100 time steps.

The electric field E_y and magnetic field H_z were used for the calculation of the Poynting vector S along the x-axis of propagation, and the results are consistent with [12]. For the 2D FDTD formulation of the TE_z case the value of the electric field E_z becomes zero. The field distributions of the electric and magnetic field are plotted in Figure 3.36. The time-averaged Poynting vector at any given time-step, provided the steady-state amplitude for each field has been calculated, is given by [12]

$$\vec{S}_{ave} = \frac{1}{2}\mathrm{Re}\left\{\vec{E} \times \vec{H}^*\right\} \tag{3.16}$$
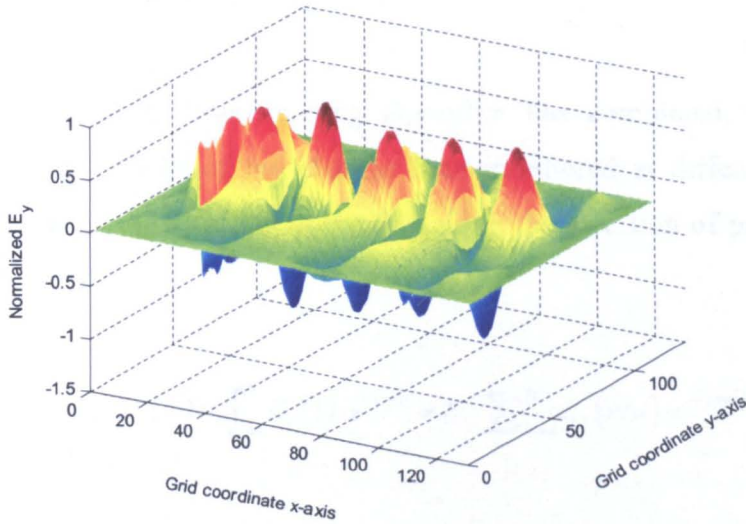
(a) Normalized electric field E_y distribution.
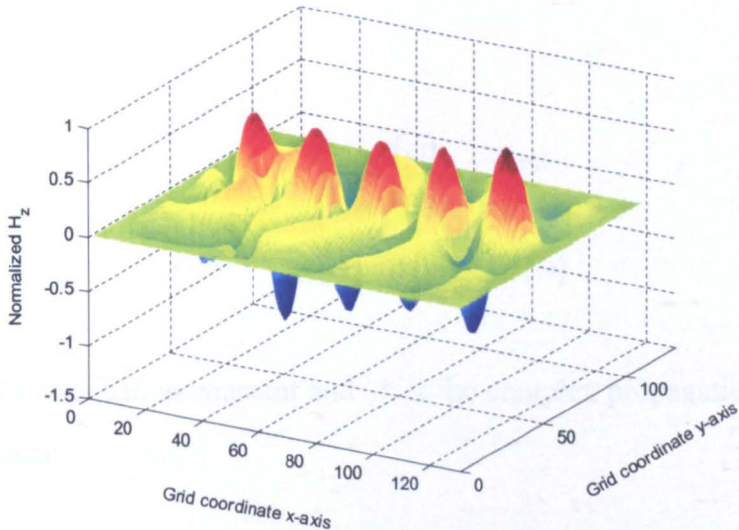
(b) Normalized Magnetic field H_z distribution
Figure 3.36. Electric and magnetic field distributions after 2100 time steps.

3.9 Dispersion Characteristics

Although the properties and analytical dispersion parameters for microstrip lines have been extensively studied [13, 14], in this section the application of the FDTD method as a numerical analysis tool to determine the dispersive characteristics of microstrips is discussed. The application of the FDTD time for investigating and extracting dispersion characteristics of microstrips has been studied extensively for a wide range of frequencies and using different formulations [15-18]. The FDTD method is extended to calculate the dispersion parameters for microstrip lines with use of CPML ABCs. During the FDTD time-stepping algorithm the electric fields are monitored at different locations along the axis of propagation of the microstrip. The dispersion characteristics and the effective dielectric constant can be calculated as follows [18-20].

After the FDTD time-stepping algorithm has completed, the Discrete Fourier Transform (DFT) of the electric field monitored at different locations underneath the centre [18] of the microstrip along the direction of propagation is calculated:

$$E_z(\omega) = \int_{-\infty}^{\infty} E_z(t) \cdot e^{-j\omega t} = \Delta t \cdot \sum_{n=1}^{N} E_z(n\Delta t) \cdot e^{-j\omega n\Delta t} \qquad (3.17)$$

The ratio of the DFT of the electric field at different locations with separation L yields the transfer function of that section of the microstrip, which is calculated by:

$$\frac{E_{z,x=L}(\omega)}{E_{z,x=0}(\omega)} = e^{-\gamma(\omega)L} \qquad (3.18)$$

$$\gamma(\omega) = \alpha(\omega) + j\beta(\omega) \qquad (3.19)$$

where α is the attenuation constant and β is the complex propagation constant at angular frequency $\omega = 2\pi f$.

The effective permittivity ε_{reff} at angular frequency ω is thus calculated based on the propagation constant β

$$\varepsilon_{reff}(\omega) = \frac{\beta^2(\omega)}{\omega^2 \varepsilon_0 \mu_0} \qquad (3.20)$$

Using the 3D FDTD method a typical microstrip structure on a dielectric substrate has been simulated. The microstrip structure is illustrated in Figure 3.37, where a PEC microstrip line of 0.6875 mm width and 100 μm thickness of GaAs substrate ($\varepsilon_r = 13.0$) with width/height ratio of 0.75, is simulated using the FDTD method [18]. The length of the microstrip was set to 1 mm and CPML boundary conditions have been used to simulate the microstrip extending to infinity.
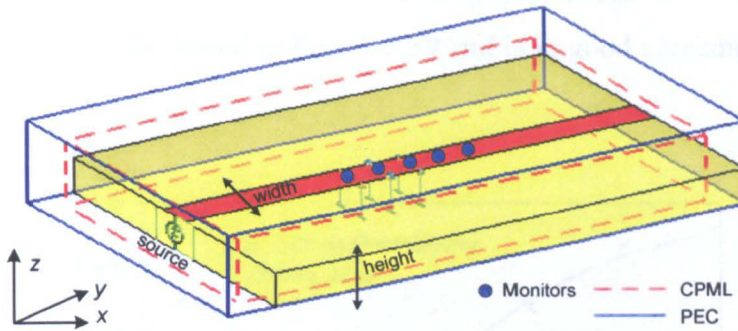
Figure 3.37. Microstrip structure modelled in 3D FDTD using CPML ABCs.

The FDTD grid parameters were set to $\Delta_x = \Delta_y = \Delta_z = 6.25$ μm, with grid resolution set to 20 cells per wavelength and the simulation was run for 2500 time steps with $\Delta t = 1.0833 \times 10^{-14}$ s. A Gaussian pulse with E_z component and spot size $20 \times \Delta x$ was launched at the front surface of the microstrip. In each time-step in the FDTD algorithm the electric field was monitor along the direction of propagation of the microstrip. At the end of the simulation the DFT of the sampled electric fields at each monitor was calculated using equation (3.17). The time variations of the z-directed electric field at different positions along the axis of propagation and the dispersive properties of the microstrip are illustrated in Figure 3.38.
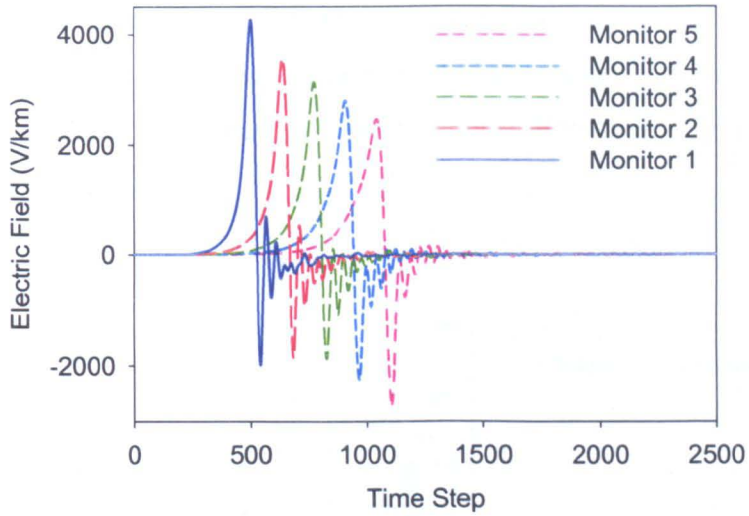
Figure 3.38. Time variations of sampled electric fields monitored along the axis of propagation.

The DFT of the sampled electric fields were used to calculate the effective permittivity using equations (3.20) over a frequency range 10 – 300 GHz. The effective permittivity is plotted in Figure 3.39 and is in good agreement with [18].
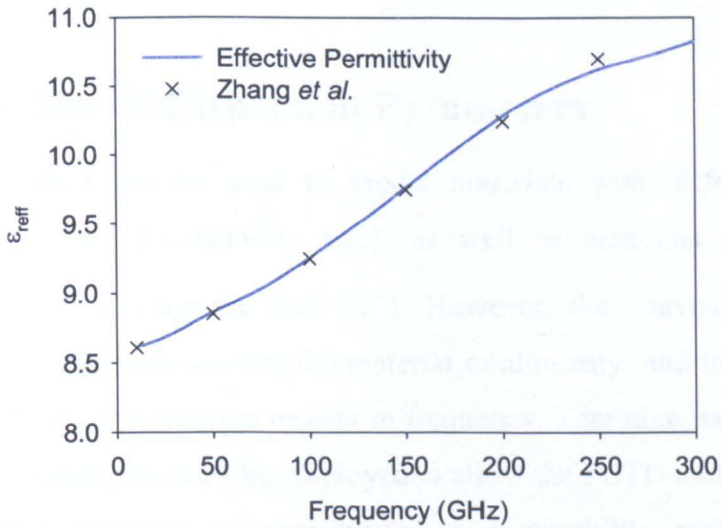
Figure 3.39. Effective dielectric constant calculated using frequency-domain electric fields.

The characteristic impedance and the propagation constant are calculated using (3.19) again using the DFT of the sampled electric fields. The results in Figure 3.40 illustrate how the characteristic impedance and the propagation constant change over the frequency range of $10 - 300$ GHz. The results are in good agreement with [18, 19].

(a) Characteristic impedance   (b) Propagation constant
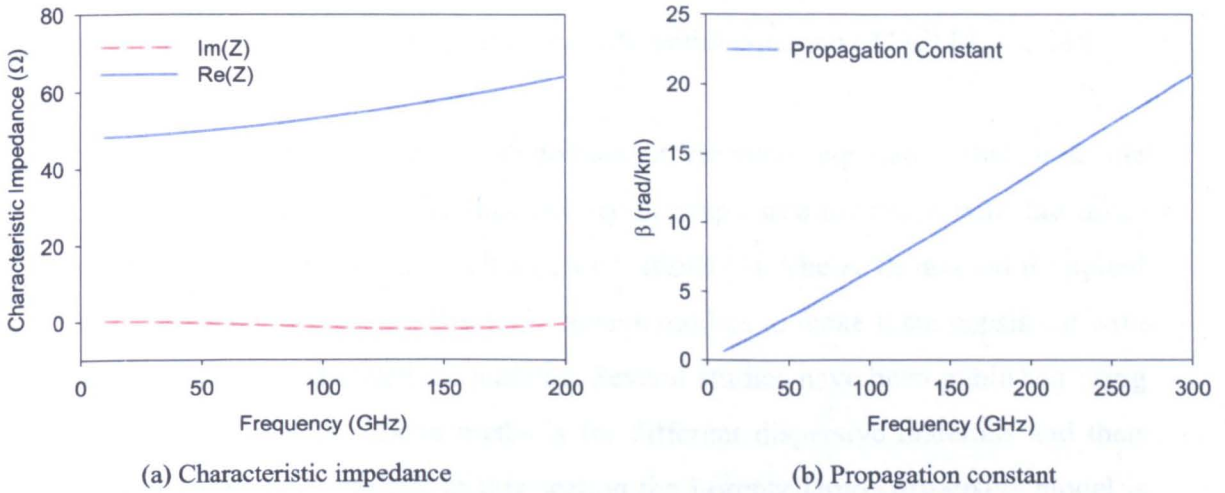
Figure 3.40. Frequency dependence of characteristic impedance and propagation constant for microstrip structure.

3.10 Drude Model Dispersion Parameters

The FDTD method can be used to model materials with different relative permittivity (ε_r) and permeability (μ_r), as well as materials with electric conductivity (σ) and magnetic loss (σ^*). However, the conventional FDTD method does not take into account the material nonlinearity, and the changes of the material's behaviour with the respect to frequency. Therefore, new dispersive FDTD method techniques must be employed to allow the FDTD method to model linear dispersion (changes in permittivity or permeability with respect to frequency), nonlinearity (changes in permittivity or permeability with respect to the electric and magnetic field), and nonlinear dispersion (changes in permittivity or permeability with respect to a single frequency wave) [4].

Dispersive materials with frequency dependent parameters have been modelled using the FDTD method for the calculation of scattering parameters using a number of approaches [21, 22]. Most of the available dispersive models are in the frequency domain, thus an approach is required to make these models consistent with the time-domain updating equations. Several approaches have emerged for converting the frequency domain dispersion equations to time domain such as the recursive convolution (RC), the piecewise linear recursive convolution (PLRC), and the auxiliary differential equation (ADE) [4, 23, 24].

The ADE employs time-domain differential equations that link the polarization and the electric flux density of dispersive materials with the time-stepping algorithm and Maxwell's curl equations [4]. The ADE method is applied to the Debye, Lorentz and Drude dispersive models to make them consistent with the time domain Maxwell's equations. Several studies have been published using a combination of the above methods for different dispersive materials and their respective parameters [25]. In this section the Lorentz-Drude dispersive model is derived, using the ADE approach and the FDTD ADE algorithm for the time-stepping equations is presented. The Lorentz-Drude (LD) model can be expressed as

$$\varepsilon_r(\omega) = \varepsilon_\infty - \frac{\omega_{pD}^2}{\omega^2 + j\Gamma_D\omega} - \frac{\Delta\varepsilon_L\omega_{pL}^2}{\omega^2 + j\omega\Gamma_L + \omega_L^2} \tag{3.21}$$

where ε_∞ is the permittivity of the material at infinite frequency, ω_{pD} is the Drude angular frequency, Γ_D is the collision frequency for the Drude pole relaxation, $\Delta\varepsilon_L$ is the change in relative permittivity due to the Lorentz pole, ω_{pL} is the angular resonance Lorentz pole frequency, Γ_L is the Lorentz pole damping coefficient, and ω_L is its oscillation frequency [26]. Although a greater number of poles can be used to increase the accuracy of the model at the cost of computational resources and time, a single pole for this case is sufficient to model the required response over the terahertz range of frequencies.

Given Maxwell's frequency equations in Section 2.4, the LD model in (3.21) can be used to express the relative permittivity of the material in the frequency domain. The electric field curl equation thus becomes

$$\nabla \times \overline{H} = j\omega\varepsilon_0\left(\varepsilon_\infty + \frac{\omega_{pD}^2}{j^2\omega^2 + j\Gamma_D\omega} + \frac{\Delta\varepsilon_L\omega_{pL}^2}{j^2\omega^2 + j\omega\Gamma_L + \omega_L^2}\right)\cdot\overline{E} \quad (3.22)$$

Using the ADE approach, the LD model equations can now be expressed in curl equation form. The LD model partial differential equations in scalar form can be found in [27]. The magnetic field equations for the LD model for electrically dispersive material remain unchanged, and the electric field for the x-direction is thus expressed as [28]:

$$E_x\Big|_{i,j+1/2,k+1/2}^{n+1/2} = \frac{1}{\Omega_x}\cdot E_x\Big|_{i,j+1/2,k+1/2}^{n+1/2} + \frac{1}{\Omega_x}C_b(m)\cdot\Big[H_z\Big|_{i,j+1,k+1/2}^{n} -$$

$$H_z\Big|_{i,j,k+1/2}^{n} + H_y\Big|_{i,j+1/2,k}^{n} - H_y\Big|_{i,j+1/2,k+1}^{n}\Big] -$$

$$\frac{1}{2\Omega_x}C_b(m)\begin{bmatrix}\alpha_x\cdot J_x\Big|_{i,j+1/2,k+1/2}^{n} + \beta_x E_x\Big|_{i,j+1/2,k+1/2}^{n+1/2} \\ + J_x\Big|_{i,j+1/2,k+1/2}^{n}\end{bmatrix} \quad (3.23)$$

$$-\frac{1}{2\Omega_x\varepsilon_r}\begin{bmatrix}\zeta_x\cdot E_x\Big|_{i,j+1/2,k+1/2}^{n+1/2} + \tau_x P_x\Big|_{i,j+1/2,k+1/2}^{n+1/2} - \\ \rho_x P_x\Big|_{i,j+1/2,k+1/2}^{n-1} - P_x\Big|_{i,j+1/2,k+1/2}^{n}\end{bmatrix}$$

where the Drude model coefficients are

$$J_x\Big|_{i,j+1/2,k+1/2}^{n+1/2} = \alpha_x\cdot J_x\Big|_{i,j+1/2,k+1/2}^{n} + \beta_x\cdot\Big[E_x\Big|_{i,j+1/2,k+1/2}^{n+1} + E_x\Big|_{i,j+1/2,k+1/2}^{n}\Big] \quad (3.24)$$

and the Lorentz model coefficients are

$$P_x\Big|_{i,j+1/2,k+1/2}^{n+1/2} = \zeta_x\cdot\Big[E_x\Big|_{i,j+1/2,k+1/2}^{n+1} + E_x\Big|_{i,j+1/2,k+1/2}^{n}\Big]$$

$$+\tau_x P_x\Big|_{i,j+1/2,k+1/2}^{n+1/2} - \rho_x P_x\Big|_{i,j+1/2,k+1/2}^{n-1} \quad (3.25)$$

where

$$\alpha_x = \frac{\left(1 - \frac{\Delta_t \Gamma_D}{2}\right)}{\left(1 + \frac{\Delta_t \Gamma_D}{2}\right)}, \quad \beta_x = \frac{\left(\frac{\Delta_t \omega_{pD} \varepsilon_0}{2}\right)}{\left(1 + \frac{\Delta_t \Gamma_D}{2}\right)}, \quad \Omega_x = \left(\frac{\zeta_x}{\varepsilon_r} + 1 + \frac{\Delta_t \beta_x}{2 \varepsilon_0 \varepsilon_r}\right), \quad \zeta_x = \frac{\frac{\Delta_t^2 \Delta \varepsilon_L \omega_{pL}}{2}}{\left(1 - \Delta_t \Gamma_L + \frac{\Delta_t^2}{2} \omega_L^2\right)},$$

$$\tau_x = \frac{2 + \Delta_t \Gamma_L - \frac{\Delta_t^2}{2} \omega_L^2}{\left(1 + \Delta_t \Gamma_L + \frac{\Delta_t^2}{2} \omega_L^2\right)}, \quad \rho_x = \frac{1}{\left(1 + \Delta_t \Gamma_L + \frac{\Delta_t^2}{2} \omega_L^2\right)}$$

Using equations (3.23) – (3.25) it is straightforward to derive equations for y, and z-direction electric fields for the 3D FDTD method. Although an ADE formulation of the CPML ABC has been reported [29], it is possible to use the conventional CPML formulation, provided that the LD model is only applied to the structure modelled and ABCs are placed sufficiently far away.

The LD model has been implemented in the 3D FDTD leapfrog algorithm. The FDTD algorithm is updated to include the updating coefficients of the LD model in the x, y, and z components of the electric fields, whereas the updating coefficients of the magnetic fields remain unchanged. The algorithm for the LD model evaluates the magnetic field updating equations as previously described in Section 2.11, including the CPML ABCs updating equations. The electric field updating equations are then evaluated using equation (3.23). However, the previous value ($E|^n$) and the current value ($E|^{n+1}$) of the electric fields are stored in memory. These values are then used to calculate the updating equations of the LD model parameters using equations (3.24) and (3.25), directly after the electric field updating equations have been evaluated.

The most important aspect of any model describing dispersive materials is the choice of parameters based on the wavelength range that will be used in the numerical analysis. Several studies have been published using one specific model or a combination of the three with a number of Lorentz or Drude terms over a broad spectrum of frequencies [30-32].

In order to validate and check the Drude model implementation of the 3D FDTD method, the microstrip structure presented in Section 3.9 has been simulated. The Drude model parameters for the microstrip line (Au) were set to $\omega_{pD} = 2.7 \times 10^{14}$ Hz, $\Gamma_D = 1.4 \times 10^{11}$ Hz, and dc conductivity variance $\sigma_0 = 7.34 \times 10^6$ Sm^{-1} [33]. The effective permittivity of the microstrip was then calculated using equation (3.19), by taking the ratio of the DFT of the electric field at different locations with separation L. The effective permittivity is then plotted in Figure 3.41 and the results are consistent with Zhang *et al.* [18].
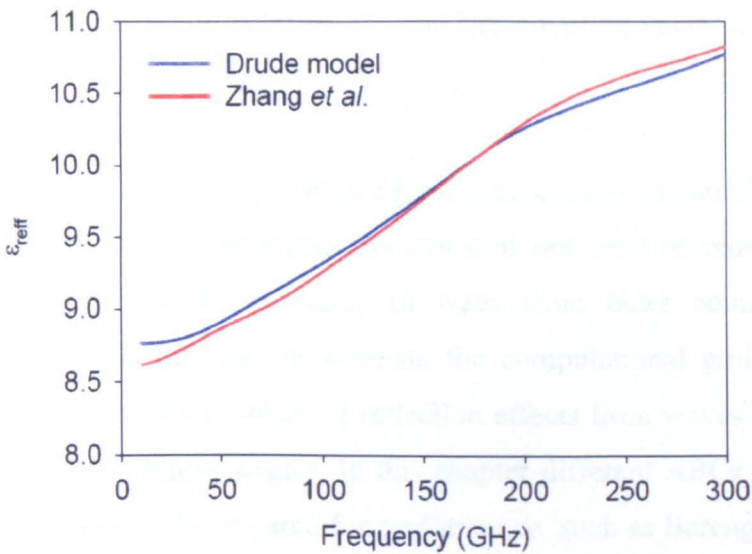
Figure 3.41. Effective permittivity of microstrip using the Drude model.

3.11 Summary

This chapter considered the numerical implementation of the FDTD solution using various formulations and ABCs to illustrate the fundamental concepts of the FDTD numerical solution to Maxwell's equations presented in Chapter 2. To begin with, the 1D FDTD wave propagation for the electric and the magnetic field has been presented and calculations of practical examples were provided. The FDTD computational solution has been extended to the two-dimensional formulation where examples of wave propagation and parameter extraction have been presented for both the TE and the TM modes. Also the three-dimensional implementation of the FDTD method has been presented with numerical analysis

of various structures with distinct properties and using a number of ABCs to terminate the FDTD computational domain.

Moreover in this chapter numerical dispersion and stability conditions have been presented that should be taken into consideration when modelling using the FDTD method. Specifically the effect of numerical dispersion has been studied compared with the ideal dispersion case, and how the numerical phase velocity changes with an oblique angle of incidence of a plane wave. In this context the TF/SF formulation has been presented with numerical analysis and simulated examples of structures, as well as parameter extraction such as transmission and reflection coefficients, and the Poynting vector calculation, for the 2D and the 3D FDTD method.

Absorbing Boundary Conditions have been extensively studied to enhance the FDTD method as a numerical analysis tool not only to reduce numerical dispersion artefacts or the reflection of wave from outer boundaries to the computational space, but also to simulate the computational grid extending to infinity and eliminate the problem of reflection effects from waves impinging the outer boundaries at oblique angles. In this chapter different ABCs and absorbers have been simulated and compared for performance, such as Berenger's PML and Mittra's CPML.

Furthermore, the FDTD method formulation has been extended to model other types of structures such as linear and nonlinear electronic circuits. Also lumped elements have been introduced in the FDTD method such as resistors, capacitors, and diodes. Finally, using the FDTD method as a simulation tool, electronic-circuit models of stripline and microstrip have been presented. Scattering and dispersion parameters have been calculated and plotted and numerical examples of parameter extraction and have been illustrated.

Finally, in order to obtain results for dispersion parameters and taking into account the dispersive nature of the materials used and specifically the microstrip line, the Lorentz-Drude model was implemented in the FDTD method using the ADE to transform the frequency domain curl equations to time-domain finite-difference equations. The method was used to model the microstrip structure using Drude parameters from published results. The Drude results were used to obtain dispersion parameters, such as the effective permittivity, attenuation constant and characteristic impedance of a microstrip.

In the next chapter, a rigorous numerical analysis of microstrip structures at Terahertz frequencies is presented, using the underlying theory presented in Chapter 2 and the simulation techniques and parameter extraction and calculation presented in this chapter.

References

[1]   R. F. Harrington, *Time-harmonic electromagnetic fields*. New York: IEEE Press : Wiley-Interscience, 2001.

[2]   T. Namiki and K. Ito, "A new FDTD algorithm free from the CFL condition restraint for a 2D-TE wave," *Antennas and Propagation Society International Symposium, 1999. IEEE*, vol.1., pp. 192-195, 1999.

[3]   M. Unno, S. Aono, and H. Asai, "A new FDTD algorithm based on alternating-direction explicit method," in *Electrical Design of Advanced Packaging & Systems Symposium, 2009. (EDAPS 2009). IEEE*, pp. 1-4, 2009.

[4]   A. Taflove and S. C. Hagness, *Computational Electrodynamics: The Finite-Difference Time-Domain Method*, 3rd ed.: Artech House Publishers, 2005.

[5]   J.-P. Berenger, "A perfectly matched layer for the absorption of electromagnetic waves," *Computational Physics, Journal of*, vol. 114, pp. 185-200, 1994.

[6]   A. Z. Elsherbeni and V. Demir, *The finite-difference time-domain method for electromagnetics with MATLAB simulations*. Raleigh, NC: SciTech Pub., 2009.

[7]   D. M. Sheen, S. M. Ali, M. D. Abouzahra, and J.-A. Kong, "Application of the three-dimensional finite-difference time-domain method to the analysis of planar microstrip circuits," *Microwave Theory and Techniques, IEEE Transactions on*, vol. 38, pp. 849-857, 1990.

[8]   G. Mur, "Absorbing Boundary Conditions for the Finite-Difference Approximation of the Time-Domain Electromagnetic-Field Equations," *Electromagnetic Compatibility, IEEE Transactions on*, vol. EMC-23, pp. 377-382, 1981.

[9]   K. Umashankar and A. Taflove, "A Novel Method to Analyze Electromagnetic Scattering of Complex Objects," *Electromagnetic Compatibility, IEEE Transactions on*, vol. EMC-24, pp. 397-405, 1982.

[10]   D. R. Smith, D. C. Vier, T. Koschny, and C. M. Soukoulis, "Electromagnetic parameter retrieval from inhomogeneous metamaterials," *Physical Review E, APS*, vol. 71, p. 036617, 2005.

[11]   V. Demir and A. Z. Elsherbeni, "A graphical user interface for calculation of the reflection and transmission coefficients of a layered medium," *Antennas and Propagation Magazine, IEEE*, vol. 48, pp. 113-119, 2006.

[12]   S. T. Chu and S. K. Chaudhuri, "Finite-Difference Time-Domain Method for Optical Waveguide Analysis," *Progress In Electromagnetics Research*, vol. 11, pp. 255-300, 1995.

[13]   E. H. Fooks and R. A. Zakarevicius, *Microwave engineering using microstrip circuits*. New York: Prentice Hall, 1990.

[14]   D. M. Pozar, *Microwave Engineering*, 3rd ed. Hoboken, NJ: J. Wiley, 2005.

[15]   J. M. Fernandez, M. Sierra-Castaner, and C. Caloz, "Metallic wire substrate (MWS) microstrip structure: Characterization and application to a patch antenna," *Antennas and Propagation, 2006. EuCAP 2006. First European Conference on*, pp. 1-5, 2006.

[16]   C. Hulse and A. Knoesen, "Dispersive models for the finite-difference time-domain method: design, analysis, and implementation," *Optical Society of America A, Journal of,* vol. 11, pp. 1802-1811, 1994.

[17]   E. I. Kirby, J. M. Hamm, K. L. Tsakmakidis, and O. Hess, "FDTD analysis of slow light propagation in negative-refractive-index metamaterial waveguides," *Optics A: Pure and Applied Optics, Journal of,* vol. 11, p. 114027, 2009.

[18]   X. Zhang, F. Jiayuan, K. K. Mei, and Y. Liu, "Calculations of the dispersive characteristics of microstrips by the time-domain finite difference method," *Microwave Theory and Techniques, IEEE Transactions on,* vol. 36, pp. 263-267, 1988.

[19]   J. Fang, X. Zhang, and K. K. Mei, "Dispersion characteristics of microstrip lines in the vicinity of a coplanar ground," *Electronics Letters,* vol. 23, pp. 1142-1143, 1987.

[20]   A. Krukonis and V. Urbanavicius, "Investigation of Microstrip Lines Dispersion by the FDTD Method," *High Frequency Technology, Microwaves,* vol. 115, no. 9, pp. 51-54, 2011.

[21]   O. P. Gandhi, B. Q. Gao, and J.-Y. Chen, "A frequency-dependent finite-difference time-domain formulation for general dispersive media," *Microwave Theory and Techniques, IEEE Transactions on,* vol. 41, pp. 658-665, 1993.

[22]   R. Luebbers, F. P. Hunsberger, K. S. Kunz, R. B. Standler, and M. Schneider, "A frequency-dependent finite-difference time-domain formulation for dispersive materials," *Electromagnetic Compatibility, IEEE Transactions on,* vol. 32, pp. 222-227, 1990.

[23]   D. F. Kelley and R. J. Luebbers, "Piecewise linear recursive convolution for dispersive media using FDTD," *Antennas and Propagation, IEEE Transactions on,* vol. 44, pp. 792-797, 1996.

[24]   M. Okoniewski, M. Mrozowski, and M. A. Stuchly, "Simple treatment of multi-term dispersion in FDTD," *Microwave and Guided Wave Letters, IEEE,* vol. 7, pp. 121-123, 1997.

[25]   A. Vial, "Implementation of the critical points model in the recursive convolution method for modelling dispersive media with the finite-difference time domain method," *Optics A: Pure and Applied Optics, Journal of,* vol. 9, p. 745, 2007.

[26]   K. Soon-Cheol, J. J. Simpson, and V. Backman, "ADE-FDTD Scattered-Field Formulation for Dispersive Materials," *Microwave and Wireless Components Letters, IEEE,* vol. 18, pp. 4-6, 2008.

[27]   I. Ahmed, E. H. Khoo, O. Kurniawan, and E. P. Li, "Modeling and simulation of active plasmonics with the FDTD method by using solid state and Lorentz-Drude dispersive model," *Optical Society of America B, Journal of,* vol. 28, pp. 352-359, 2011.

[28]   K. H. Lee, I. Ahmed, R. S. M. Goh, E. H. Khoo, E. P. Li, and T. G. G. Hung, "Implementation of the FDTD method based on Lorentz-Drude dispersive model on GPU for plasmonics applications," *Progress In Electromagnetics Research,* vol. 116, pp. 441-456, 2011.

[29]   S. D. Gedney and Z. Bo, "An Auxiliary Differential Equation Formulation for the Complex-Frequency Shifted PML," *Antennas and Propagation, IEEE Transactions on,* vol. 58, pp. 838-847, 2010.

[30]   P. B. Johnson and R. W. Christy, "Optical Constants of the Noble Metals," *Physical Review B,* vol. 6, pp. 4370-4379, 1972.

[31]   E. D. Palik and G. Ghosh, *Handbook of optical constants of solids.* San Diego: Academic Press, 1998.

[32]   A. D. Rakic, A. B. Djurisic, J. M. Elazar, and M. L. Majewski, "Optical Properties of Metallic Films for Vertical-Cavity Optoelectronic Devices," *Applied Optics,* vol. 37, pp. 5271-5283, 1998.

[33]   Y. Poo, R. Wu, X. Fan, and J. Q. Xiao, "Measurement of ac conductivity of gold nanofilms at microwave frequencies," *Review of Scientific Instruments,* vol. 81, pp. 064701-5, 2010.

Chapter 4

Microstrip at Terahertz Frequencies

Microstrip circuits and microstrip transmission lines have been used extensively for generating and processing of signals at microwave and millimetre wave frequencies. Traditionally microstrip circuits are constructed using a metal transmission line fabricated on a dielectric substrate. Although numerous designs on different dielectrics have been reported regarding the characteristics of microstrip band-stop filters at microwave frequencies, however, the field is relatively new at terahertz frequencies.

Although, the terahertz frequency range remained one of the least developed spectral regions, during the past decade a surge of activity has advanced its potential for a wide range of applications. The importance of terahertz radiation lies in the development of innovative sensing systems, ultrafast, wireless communications, scanning systems, and assay devices for medical applications to name just a few [1]. Remarkable progress in terahertz technology has led to the development of sensors particularly for biomedical applications [1]. Recently a number of terahertz frequency range band-stop filters have been reported [2-4]. The characterisation of terahertz filters is achieved by embedding the filter in a microstrip line and applying terahertz time-domain spectroscopy (TDS). TDS is widely used to obtain terahertz frequency-dependent properties, such as the refractive index and the transmission or reflection coefficients of materials loaded on the terahertz filters. The range of materials that

could be used to obtain their properties includes crystalline semiconductors, chemical compounds and biological materials such as hybridized and denaturised DNA, all of which exhibit different dielectric constants at terahertz frequencies [2, 5].

The Finite Difference Time Domain (FDTD) method has been regarded as a versatile, useful and widely used electromagnetic tool. The performance of the FDTD method is embellished with the development of new algorithms to cope with a wide variety of EM problems, as well as different boundary conditions, such as ABCs [6]. These algorithms have been presented in Chapter 3. In the following sections of this Chapter a rigorous analysis of microstrip structures at terahertz frequencies will be presented, taking into account a number of parameters and how these parameters affect the performance of the microstrip.

4.1 Microstrip with Polymer Dielectric

Thin-film microstrip lines (TFMS) with a polymer dielectric placed between the ground and the conductor (microstrip) or polymer-based sandwich microstrip lines have been investigated in the past for sub-millimetre and millimetre-wave interconnects for ultrafast microelectronic circuits. Devices of this type exhibit low dispersion properties and losses for frequencies up to 1.5 THz and are attractive as transmission line elements for GHz frequencies [7]. Recently these types of device have also been investigated for rapid terahertz sensing applications, such as genetic diagnostics [8] and detecting single stranded or hybridized DNA [9, 10].

Specifically, the geometry of the thin-film microstrip structure under consideration is a 30 μm-wide Au (gold) and 4 mm in length microstrip line. In terms of fabrication, a thin layer of 500 nm of Ti/Au is deposited onto a high conductivity (5 Ω cm) Si (silicon) wafer. A 6 μm-thick polymer substrate made of benzocyclobutene (BCB) is then spun-on. The BCB is an organic material showing stable permittivity values and low losses over a wide range of frequencies, with $\varepsilon_r = 2.57$ at 400 GHz, with little variation for the frequency

range between 10 GHz and 1.5 THz [11, 12] and with negligible modal dispersion within this frequency range [7]. The microstrip line and filters were deposited on the BCB by thermal evaporation. All metal layers are taken as 0.5 μm thick. Design and fabrication of these TFMS are explained in detail in [3, 11]. The following diagram illustrates the geometry of the structure under consideration:
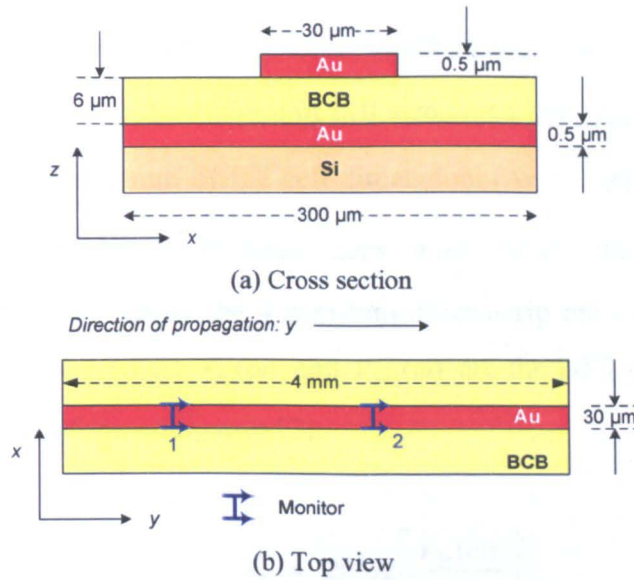
Figure 4.1. Geometry of the microstrip structure (not to scale).

The microstrip presented in Figure 4.1 has been simulated using the 3D FDTD method. The material parameters of the microstrip used in the simulation were for the BCB dielectric $\varepsilon_r = 2.57$, for gold (Au) the relative permittivity was set to $\varepsilon_r = 1$ and the electric conductivity was set to $\sigma = 7.34 \times 10^6$ S/m [13]. The width of the structure (300 μm) was selected in order to accommodate the filter stubs that could be loaded on the microstrip, as described in Section 4.2, as well as restricting the size of the computational window. The silicon (Si) cladding has been modelled using CPML ABCs. The microstrip is surrounded by 8 CPML thick cells in all directions. The microstrip is extended into the CPML walls in both the x-direction and y-direction, to simulate an infinitely wider BCB substrate and an infinitely long microstrip line respectively. In the z^+-direction 40 cells of free space were used above the microstrip, with relative permittivity $\varepsilon_r = 1$ and permeability $\mu = 1$, and the computational domain was terminated with CPML ABCs. In the z^--direction the lower gold (Au) metal layer is used as a ground plate, and the silicon wafer (Si) is simulated by extending the layer in the CPML

boundary conditions. The CPML conductivity profile factor was set to $\sigma_{factor} = 1.3$, and the PML order was set to $n_{pml} = 3$. The inner-domain CPML interface parameters were set to $\kappa_{max} = 10$, and $\alpha_{max} = 0.05$, the theory of which was presented in Section 2.11. The parameters used for the FDTD grid were set to $\Delta x = 1\ \mu m$, $\Delta y = 2\ \mu m$, and $\Delta z = 0.5\ \mu m$, and a CFL factor of $S = 0.9$. A Gaussian pulse was used to source the FDTD grid over the $30\ \mu m$-width microstrip, with number of cells per wavelength $n_{c\lambda} = 20$, which denotes the proportion of the highest frequency wavelength to the unit cell size, such that $f_{max} = c/(n_{c\lambda}.\Delta s_{max})$, where Δs_{max} is the maximum of the cell dimensions $(\Delta x, \Delta y, \Delta z)$. The simulation was allowed to run for 6000 time steps with $\Delta t = 1.3102 \times 10^{-3}\ ps$. The transmission parameters across the 4 mm-long microstrip are calculated and the insertion loss is plotted, where $V_{in}(\omega)$ and $V_{out}(\omega)$ are the DFT of the voltages at the input and output of the microstrip [2]:

$$S_{21} = -20 \log \left[\frac{V_{in}(\omega)}{V_{out}(\omega)} \right] \qquad (4.1)$$

The following figures present the transmission parameters and the dispersion parameters of the microstrip structure. The calculation of microstrip dispersive characteristics and parameters has been discussed in Section 3.9. The time variations of the z-directed electric field at six different positions, between $160\,\Delta y$ and $260\,\Delta y$ with $20\,\Delta y$ spacing, along the axis of propagation and the dispersive properties of the microstrip are illustrated in Figure 4.2. The electric fields illustrated in Figure 4.2 indicate that the pulses decrease in amplitude and increase in pulse width, with increasing propagation length, as a result of the attenuation and dispersion.
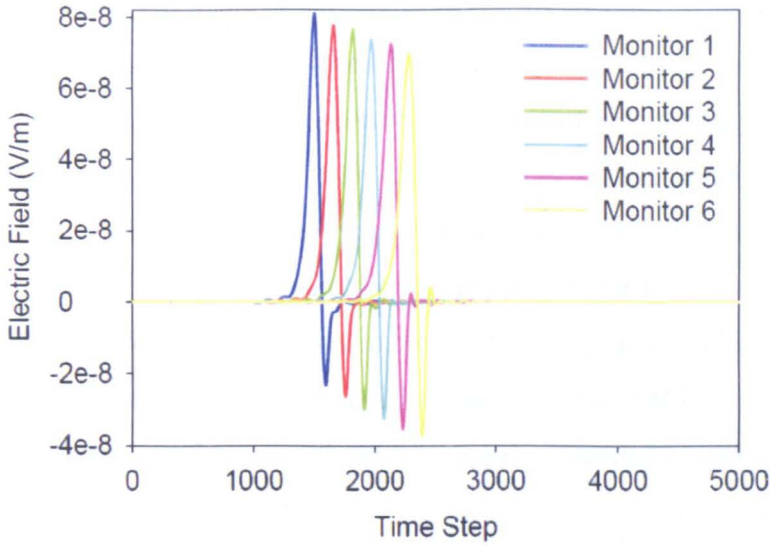
Figure 4.2. Time variations of sampled electric fields monitored along the axis of propagation.

The DFT of the electric fields have been used to calculate the transfer function of the microstrip based on the theory developed in section 3.20, where the effective permittivity is given by equation (3.20). The effective permittivity calculated here is plotted in Figure 4.3. It can be observed that as the frequency increased the effective permittivity also slightly increased in almost linear manner. The trend is similar in nature to the effective permittivity of BCB reported in [8].
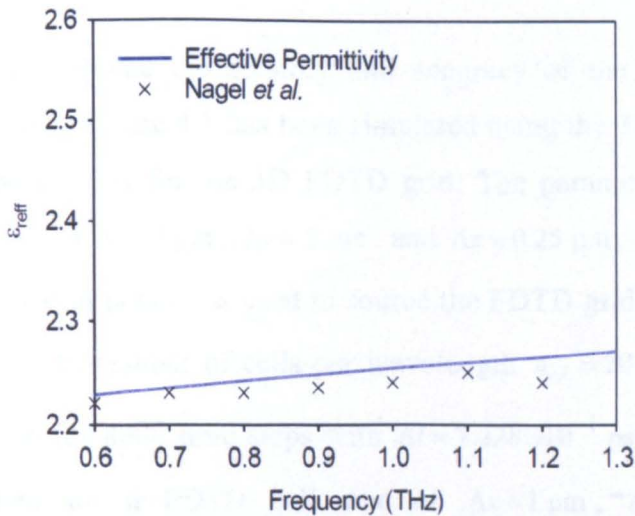
Figure 4.3. Effective permittivity calculated using frequency-domain electric fields at terahertz frequencies.

The characteristic impedance and the propagation constant are thus calculated by using the DFT of the sampled electric fields. The following figure illustrates how the characteristic impedance and the complex propagation constant change over the frequency range of 0.6 – 1.3 THz. The characteristic impedance is calculated by monitoring the voltage across the monitor and the current flowing through the monitor along the axis of propagation of the microstrip during the time-stepping algorithm as described in Section 3.5. The complex propagation constant is calculated by using the DFT of the electric fields at two different locations with separation distance 20 μm, using equations (3.17) and (3.18).

| (a) Characteristic Impedance | (b) Propagation Constant |
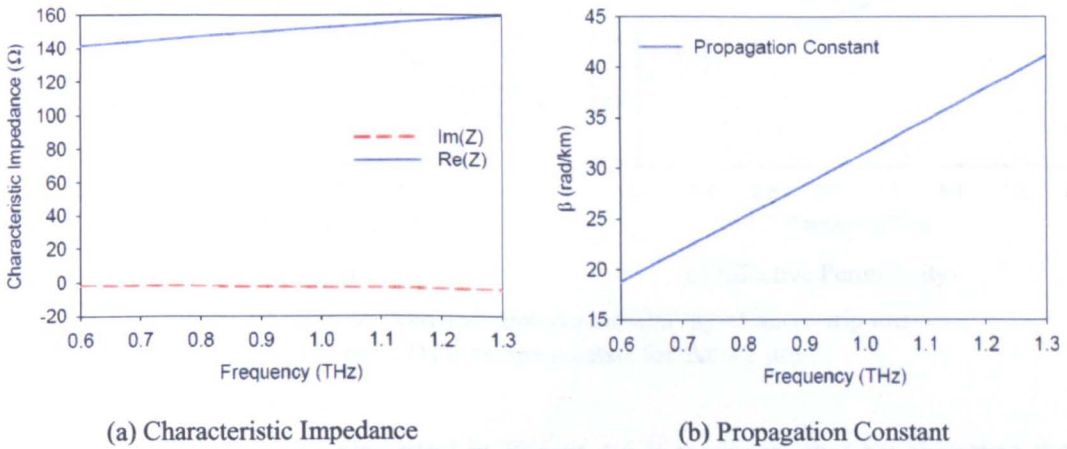
Figure 4.4. Frequency dependence of characteristic and propagation constant for microstrip structure at terahertz frequencies.

In order to validate the stability and accuracy of the simulations, the structure illustrated in Figure 4.1 has been simulated using the 3D FDTD method using different parameters for the 3D FDTD grid. The parameters used for the FDTD grid were set to $\Delta x = 1 \, \mu m$, $\Delta y = 2 \, \mu m$, and $\Delta z = 0.25 \, \mu m$, and a CFL factor of $S = 0.9$. A Gaussian pulse was used to source the FDTD grid over the 30 μm-width microstrip, with number of cells per wavelength $n_{c\lambda} = 20$. The simulation was allowed to run for 8000 time steps with $\Delta t = 7.228 \times 10^{-4}$ ps. The simulation was also repeated for a FDTD cell size of $\Delta x = 1 \, \mu m$, $\Delta y = 2.5 \, \mu m$, and $\Delta z = 0.25 \, \mu m$. The simulation was allowed to run for 8000 time steps with $\Delta t = 7.247 \times 10^{-4}$ ps. The transmission parameters across the microstrip line have been calculated using equation (4.1). The insertion loss for the different FDTD grid parameters is plotted in Figure 4.5(a) below. The insertion loss presented in

Figure 4.5(a) is the result of the finite propagation velocity, attenuation, and dispersion of the Gaussian pulse propagating along the microstrip line. Also, the DFT of the electric fields sampled at six different positions between $160\,\Delta y$ and $260\,\Delta y$ with $20\,\Delta y$ spacing along the axis of propagation have been used to calculate the effective permittivity of the microstrip. The effective permittivity is plotted in Figure 4.5(b) for the different FDTD grid parameters.

(a) Insertion Loss   (b) Effective Permittivity
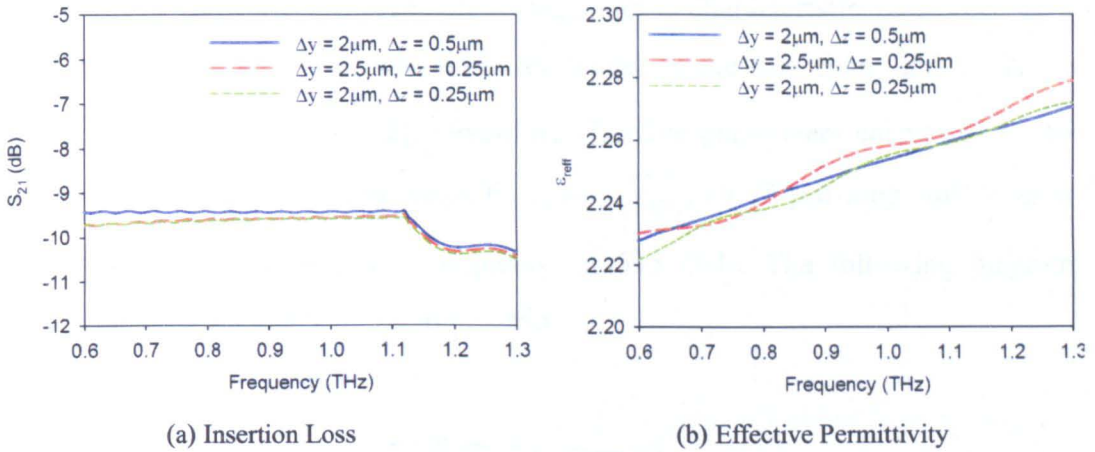
Figure 4.5. Insertion loss and effective permittivity of microstrip line for different FDTD cell parameters for $\Delta x = 1\ \mu m$.

Given the results presented in Figure 4.5 it is shown that by changing the FDTD cell parameters in order to obtain a finer mesh for metal layers, in this case can have a small effect in the calculation of different transmission and dispersion parameters. However, the differences are minute with maximum error 0.85%, thus the stability and accuracy of the FDTD simulation results is ensured. It should be noted, that by decreasing the size of the Yee cell, the size of the mesh is also increasing, thus allowing more FDTD grid cells to be allocated for layers that would have been sampled with one cell thickness, at the cost of computational resources and in particular memory, as well as total simulation time.

4.2 Microstrip Band-stop Filters

Terahertz band-stop filters embedded in a microstrip line have been employed for sensing and detection applications. The filter design under consideration allows cascading filters to be employed on the same microstrip line. In this section a set

of frequency range filters are presented with their respective properties at terahertz frequencies [2, 3].

The microstrip structure presented in the previous section is used to demonstrate the effect of terahertz band-stop filters on the characteristic properties of the microstrip. Initially a stub filter has been placed in the centre of the microstrip structure, 2 mm away from the source. The stub filter designed for operation at the terahertz frequency range has a characteristic resonance at a frequency given by $v_p/4l$, where l is the length of the stub filter, and v_p is the phase velocity of the filter [2]. Given the effective parameters calculated in the previous section as the phase velocity $v_p = c/\sqrt{\varepsilon_{eff}}$, an 83 µm-long stub filter is expected to yield a resonance frequency of 595 GHz. The following diagram shows the new geometry of the microstrip.

(a) Cross section

(b) Top view
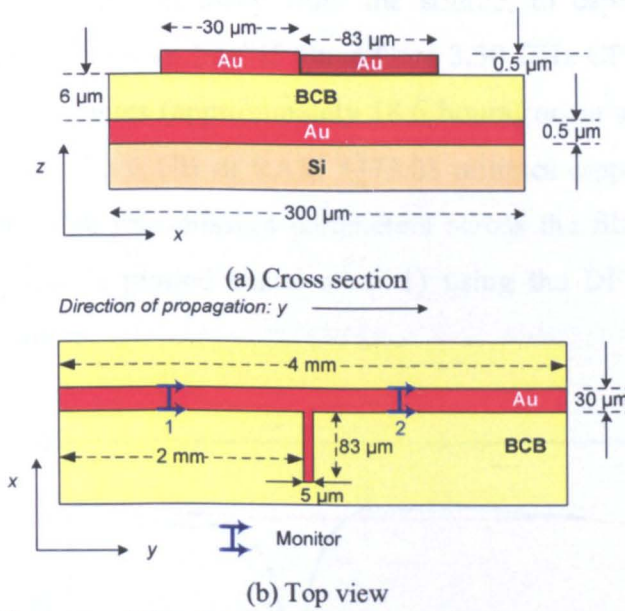
Figure 4.6. Geometry of the microstrip structure and band-stop filter (not to scale).

The microstrip structure with the terahertz filter illustrated in Figure 4.6 has been simulated using the 3D FDTD method. The material parameters of the microstrip and the ABCs used in the simulation were exactly the same as previously described, where the BCB dielectric relative permittivity is set $\varepsilon_r = 2.57$, for gold (Au) the relative permittivity was set to $\varepsilon_r = 1$, the electric conductivity was set to $\sigma = 7.34 \times 10^6$ S/m, and for free space the material

parameters were set to $\varepsilon_r = 1$ and $\mu = 1$. The CPML conductivity profile factor was set to $\sigma_{factor} = 1.3$, and the PML order was set to $n_{pml} = 3$. The inner-domain CPML interface parameters were set to $\kappa_{max} = 10$, and $\alpha_{max} = 0.05$. In this case the microstrip line is shifted towards the x^+-direction in order to accommodate the 83 µm filter stub on the BCB substrate as shown in the Figure 4.6. The parameters used for the FDTD grid were modified to model the 5 µm width of filter, such that $\Delta x = 1$ µm, $\Delta y = 5$ µm, and $\Delta z = 0.5$ µm, and a Courant factor of $S = 0.9$. A Gaussian pulse was used to source the FDTD grid over the 30 µm-width microstrip, with number of cells per wavelength $n_{c\lambda} = 20$, which denotes the proportion of the highest frequency wavelength to the unit cell size, such that $f_{max} = c/(n_{c\lambda}.\Delta s_{max})$, where Δs_{max} is the maximum of the cell dimensions $(\Delta x, \Delta y, \Delta z)$. The simulation was allowed to run for 13 000 time steps with $\Delta t = 1.0007 \times 10^{-3}$ ps. Two monitors were placed before and after the filter stub at 1.5 mm and 2.5 mm away from the source, to capture the sampled voltages. The simulation on an Intel i5 Quad Core 3.30 GHz CPU with 16 GB of RAM took 1118.26 minutes (approximately 18.6 hours) or on an AMD Opteron 250 Dual Core CPU with 6 GB of RAM 3373.03 minutes (approximately 56.21 hours) to complete. The transmission parameters across the filter are calculated and the insertion loss is plotted based on (4.1) using the DFT of the voltage sampled at the monitors.
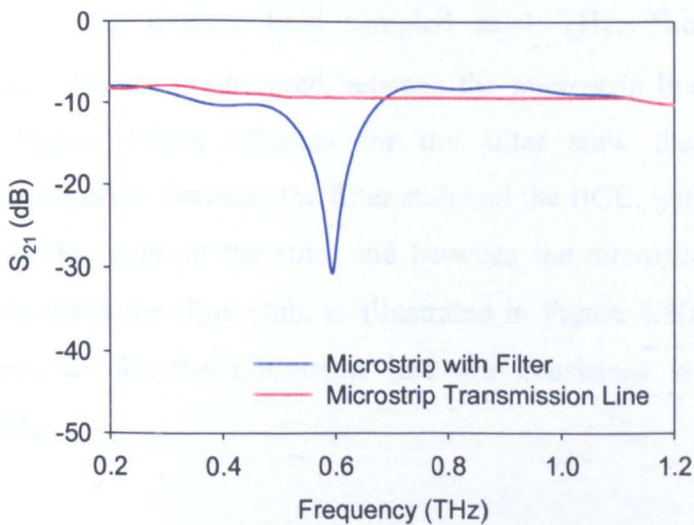
Figure 4.7. Insertion loss of the microstrip transmission line and microstrip loaded with filter structure.

The result plotted in Figure 4.7 shows the average loss of the microstrip line without the filter over the frequency range between 0.2 THz and 1.2 THz. Also, the figure clearly indicates a peak loss of -30 dB at 595 GHz for the 83 μm long stub for the terahertz filter. These results are in good agreement with measured results reported in [2], although at lower frequencies the insertion loss in the FDTD simulation is slightly higher than the measured values. This difference is a likely consequence of not taking into consideration to the frequency dependent parameters of the metal (Drude model).

Furthermore, the electric field distributions have been sampled at 1 THz for the single filter stub at various points along the direction of propagation. The sampled electric fields are presented in Figure 4.8 below, where the insets illustrate the position of the electric field monitor along the microstrip line. In Figure 4.8(a) the electric field distribution E_x is illustrated for the microstrip line sampled at 1 THz, before the filter stub 1 mm away from the source. The white lines illustrate the microstrip line and the filter stub, as well the BCB substrate, the red lines indicate the CPML boundary conditions. The figure shows that the electric field concentration is observed on the left and right edge of the microstrip line. In Figure 4.8(b), the electric field distribution E_x is illustrated for the filter stub and the microstrip line sampled at 1 THz. In this case, the figure shows that the electric field concentration is observed on the edge of the filter stub and the right edge of the microstrip line. Similarly, the electric field distributions are presented for the E_z electric field sampled at 1 THz. The electric field concentration in this case is observed between the microstrip line and the BCB substrate, in Figure 4.8(c), whereas for the filter stub, the electric field concentration is observed between the filter stub and the BCB, with stronger field concentration on the edge of the stub, and between the microstrip line and the BCB flowing towards the filter stub, as illustrated in Figure 4.8(d). The electric field concentrations for the microstrip line are consistent with the results presented in [14].
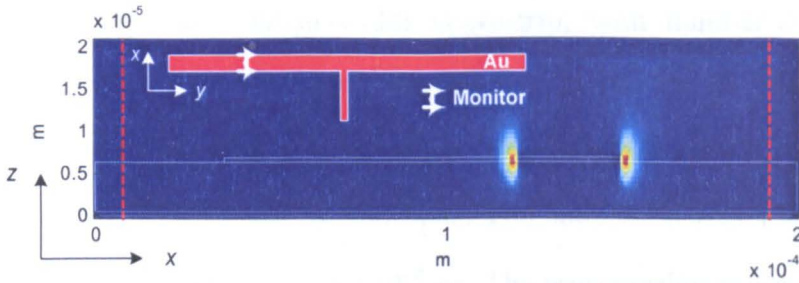
(a) Sampled electric field E_x at 1 THz for the microstrip line.
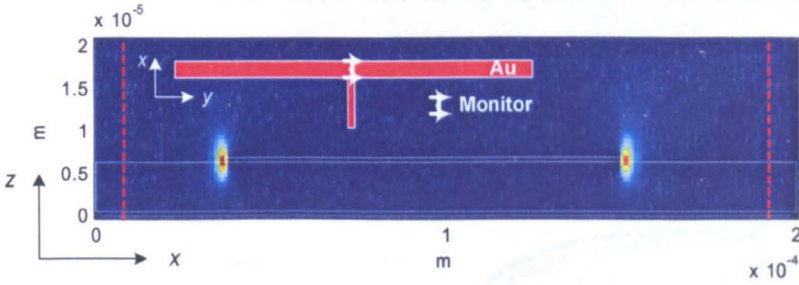
(b) Sampled electric field E_x at 1 THz for the filter stub and microstrip line.
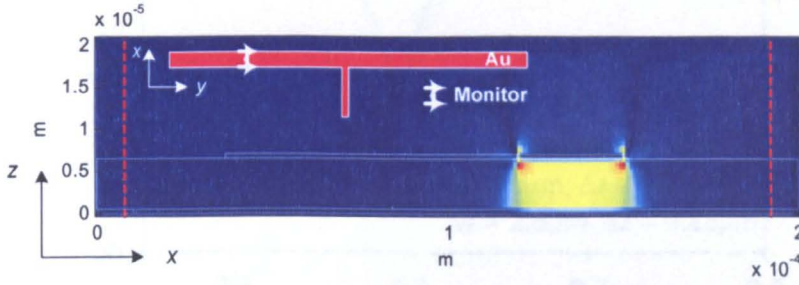
(c) Sampled electric field E_z at 1 THz for the microstrip line.
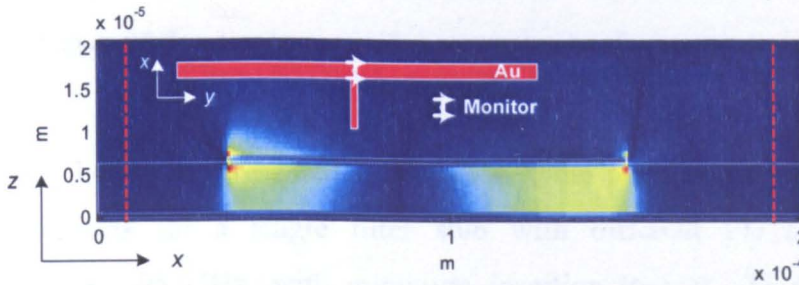
(d) Sampled electric field E_z at 1 THz for the filter stub and microstrip line.

Figure 4.8. Electric field distributions sampled at 1 THz for
the microstrip line and the filter stub.

The 3D FDTD simulation for the structure illustrated in Figure 4.6 has been simulated using the 3D FDTD method with grid cell parameters $\Delta x = 1\ \mu m$, $\Delta y = 5\ \mu m$, and $\Delta z = 0.5\ \mu m$. To ensure the stability and accuracy of the results, the simulation has been repeated for different parameters for the 3D FDTD grid. The parameters used for the FDTD grid were set to $\Delta x = 1\ \mu m$, $\Delta y = 5\ \mu m$, and $\Delta z = 0.25\ \mu m$, and a CFL factor of $S = 0.9$. A Gaussian pulse was used to source

the FDTD grid over the $30\,\mu m$-width microstrip, with number of cells per wavelength $n_{c\lambda} = 20$. The simulation was allowed to run for 26 185 time steps with $\Delta t = 7.247 \times 10^{-4}$ ps. The simulation was also repeated for a FDTD cell size of $\Delta x = 1\,\mu m$, $\Delta y = 2.5\,\mu m$, and $\Delta z = 0.25\,\mu m$. The simulation was allowed to run for 26 300 time steps with $\Delta t = 7.276 \times 10^{-4}$ ps. The transmission parameters across the microstrip line have been calculated using equation (4.1). The insertion loss for the different FDTD grid parameters is plotted in Figure 4.9.
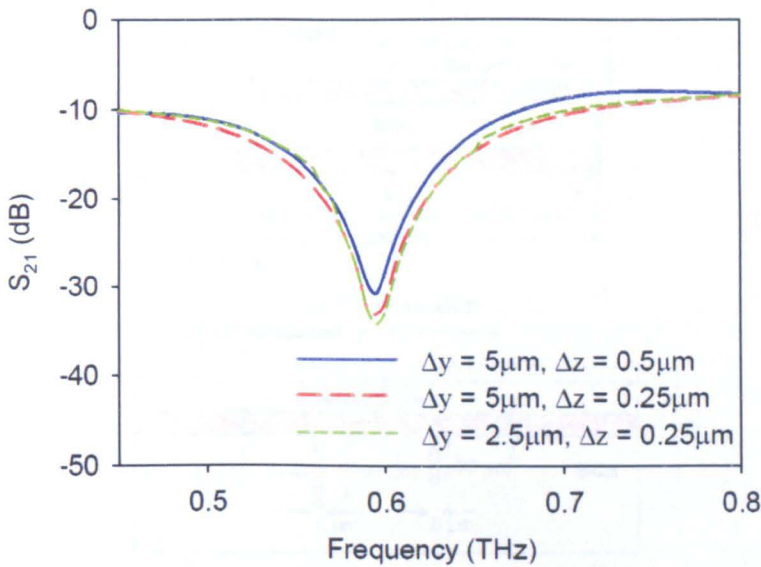
Figure 4.9. Insertion loss and effective permittivity of microstrip line
for different FDTD cell parameters for $\Delta x = 1\,\mu m$.

Given the results presented in Figure 4.9, the peak insertion loss of the FDTD simulations for a single filter stub with different FDTD grid cell dimensions is at 595 GHz, with minimum insertion loss at –31 dB and the maximum insertion loss observed is –33 dB. The differences between the different FDTD grid parameters simulations are again small, thus the stability and accuracy of the FDTD simulation results is ensured.

Several band-stop filters can be loaded on the same microstrip line, each with a different centre frequency. For sensing applications the resonance frequency of each stub should be sufficiently separated across the terahertz frequency range. It has been reported that cascaded filters have been fabricated and loaded with dielectric material to model sensing and detection applications at

terahertz frequencies [3]. A set of cascaded filters have been modelled using the 3D FDTD method. Each stub is embedded on the microstrip line previously described. In this case the length of each filter has been chosen to give significantly different centre frequencies. The length of the stubs have been set to 194 µm and 82 µm with the fundamental centre frequencies at 260 GHz and 600 GHz respectively, given by $v_p/4l$, and as presented in [3]. The stubs have been placed at the centre of the microstrip with 400 µm spacing. The geometry of the new structure is illustrated in Figure 4.10.

(a) Cross section

(b) Top view
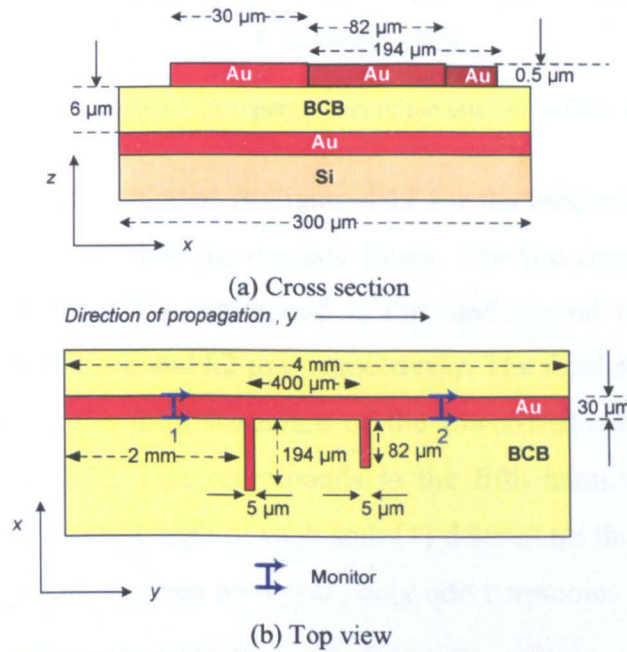
Figure 4.10. Geometry of the microstrip structure and band-stop filters cascade (not to scale).

The microstrip structure with the terahertz filter illustrated in Figure 4.10 has been simulated using the 3D FDTD method. The material parameters of the microstrip and the ABCs used in the simulation were exactly the same as previously described. The microstrip line is shifted towards the x^+-direction in order to accommodate the 194 µm filter stub on the BCB substrate as shown in Figure 4.10. The simulation parameters used for the FDTD computational grid remained the same as in the previous simulation. Two monitors were placed before and after the filter stubs to capture the sampled voltages. The transmission parameters across the filter are calculated and the insertion loss is plotted.
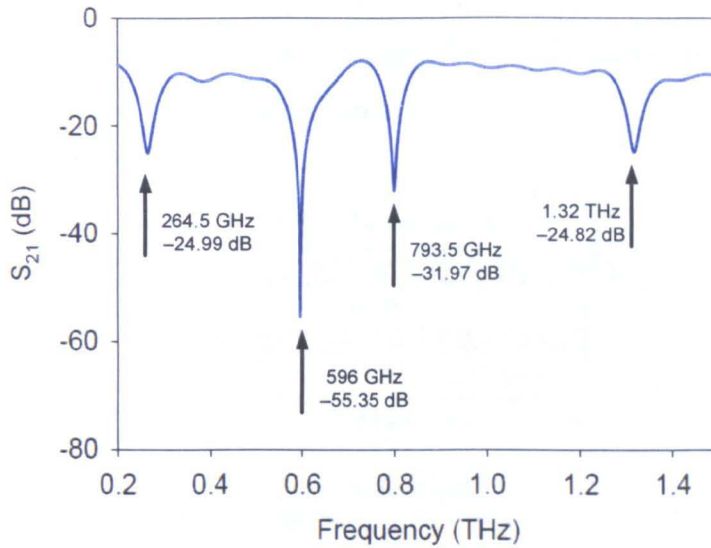
Figure 4.11. Transmission parameters of the microstrip/filter array.

The insertion loss plotted in Figure 4.11 for the terahertz filters show the terahertz transmission through the cascade filters. The two resonances appearing at 264.5 GHz and 596 GHz correspond to the fundamental modes of the two filters, with length 192 μm and 82 μm, respectively. The third resonance at 793.5 GHz corresponds to the third harmonic of the lower-frequency filter, and the fourth resonance at 1.32 THz corresponds to the fifth harmonic of the lower-frequency filter. Since the length of each stub (l) determines the centre frequency of its resonance, which is given by $v_p/4l$, only odd harmonics resonate, whereas even harmonics will not, because this will change the centre resonating frequency of the stubs. In addition, the 82-μm filter now presents an insertion loss peak value of –55 dB, as opposed to its previous value of –30 dB, when the simulation was carried out for a microstrip with only one filter. The 3D FDTD numerical simulation results are in good agreement with measured results in [3].

Given the microstrip structure with the array of stubs shown in Figure 4.10, the first stub (194 μm) has been replaced with a filter of length 82 μm, identical to the second stub as illustrated in Figure 4.12. The new microstrip structure simulated using the 3D FDTD method. The material parameters of the microstrip and the ABCs used in the simulation were exactly the same as previously described. The simulation parameters used for the FDTD computational grid remained the same as in the previous simulation, as well as the

position of the microstrip line. Two monitors were placed before and after the filter stubs to capture the sampled voltages. The transmission parameters across the filter are calculated and the insertion loss is plotted.

(a) Cross section

(b) Top view
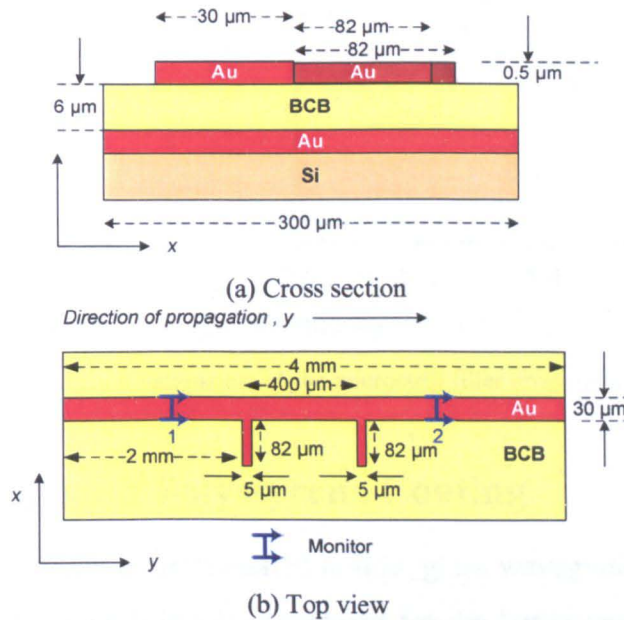
Figure 4.12. Geometry of the microstrip structure and band-stop filters cascade (not to scale).

The insertion loss plotted in Figure 4.13 for the identical terahertz filters show the terahertz transmission through the cascade filters. Instead of two resonances appearing, in this case a sharper resonance peak appears at 600 GHz with an insertion loss value of –69.90 dB, and without the appearance of other harmonics. The full-width half-maximum (FWHM) for the two identical filter stubs is 91 GHz, whereas the FWHM value of the microstrip line loaded with a single filter (83 µm) is 87 GHz.
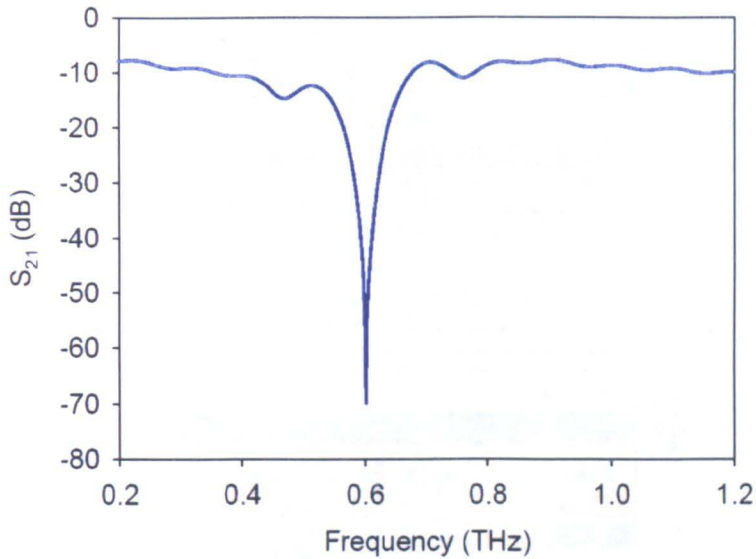
Figure 4.13. Transmission parameters of the microstrip filter array with identical filters.

4.3 Microstrip with Polystyrene Coating

It has been reported that a metal-coated hollow glass waveguide (HGW) with an inner silver/polystyrene-coating is considered for the better understanding of the various loss mechanisms and subsequently design optimization of a low-loss THz waveguide [15]. The deposition of low-loss material, such as polystyrene on the metal surface of hollow-core metallic waveguides for THz radiation, reduces effectively the attenuation. In this section, the effect of the presence of the above material, along the metal surface of the microstrip line, on the propagation, attenuation characteristics and frequency response in band-stop filter design, is investigated, and the results are presented. Furthermore, the effect of polystyrene coating in different geometries of the microstrip line and filters is also presented, such as variation of the width of the microstrip, the thickness of the BCB substrate, and the thickness of the polystyrene coating. The microstrip geometry under consideration is illustrated below for a single stub.

(a) Cross section

(b) Top view
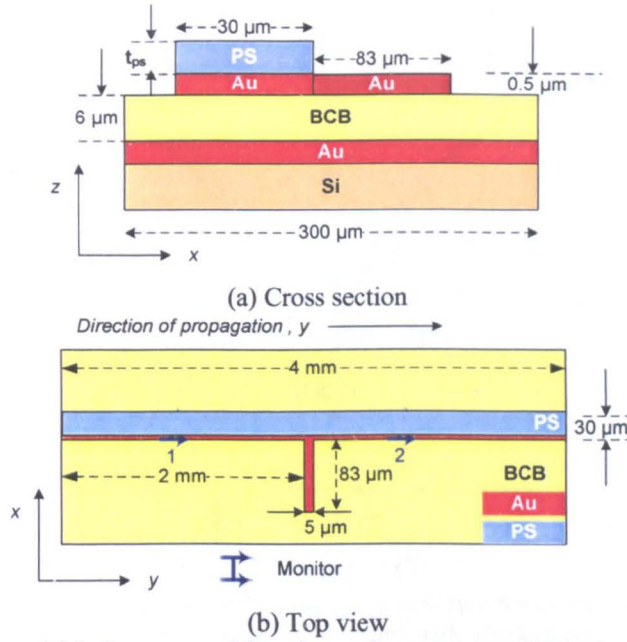
Figure 4.14. Geometry of the microstrip structure with single filter, and polystyrene coating (not to scale).

The microstrip structure with the polystyrene coating illustrated in Figure 4.14 has been simulated using the 3D FDTD method with CPML ABCs. The material parameters of the microstrip and the ABCs used in the simulation were exactly the same as described in the previous section. The microstrip line has been coated with polystyrene with relative permittivity $\varepsilon_r = 2.4967$ with small losses of less than 1.5 cm^{-1} for frequencies less than 4 THz [16]. The parameters used for the FDTD grid were modified to model the thickness t_{ps} of the polystyrene coating with 1 μm increments, such that $\Delta x = 1$ μm, $\Delta y = 5$ μm, and $\Delta z = 0.25$ μm, and a Courant factor of $S = 0.9$. A Gaussian pulse was used to source the FDTD grid over the 30 μm -width microstrip. The simulation was allowed to run for 20 000 time steps with $\Delta t = 1.0007 \times 10^{-3}$ ps. Two monitors were placed before and after the filter stub to capture the sampled voltage.

The transmission parameters across the filters and under the polystyrene coating have been calculated using the method described in Section 4.1. The microstrip structure has been modelled for a range of polystyrene thickness (0 – 15 μm) without changing the length of the filter attached to the microstrip line. The insertion loss S_{21} for the coated microstrip with single filter has been evaluated and plotted in the figure below.
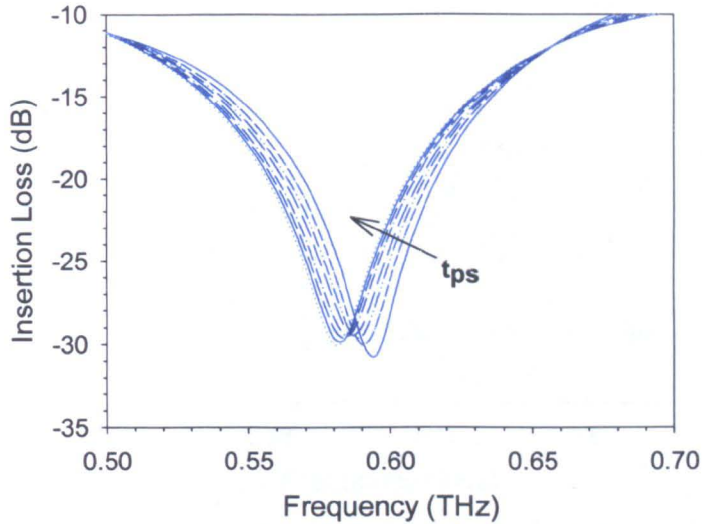
Figure 4.15. Insertion loss of the microstrip structure for different values of polystyrene thickness (0 – 15μm) with single filter.

In Figure 4.15, the insertion loss is plotted against the PS coating thickness for the 600 GHz filter [17]. As the value of the polystyrene thickness increases there is slight shift in the resonance frequency of the filter from 600 GHz to 580 GHz. The interaction of the electric field with the deposited dielectric material leads to the observed change in the filter resonant frequency and insertion loss. The electric field s almost fully enclosed within the dielectric layer causing the addition of PS coating to have incrementing less impact on the resonant frequency. The insertion loss peak value is also affected with the deposition of polystyrene coating. The effect of polystyrene coating on the microstrip, regarding the shift in frequency and the slight change in the insertion loss peak values, is illustrated in the expanded view of Figure 4.15 in Figure 4.16 below. As the polystyrene coating is increasing, the insertion loss peak values are decreasing towards –29 dB at ~586 GHz. After that threshold, the insertion loss peak values are increasing for higher values of polystyrene coating thickness reaching –30 dB at 580 GHz for 15 μm of polystyrene coating.
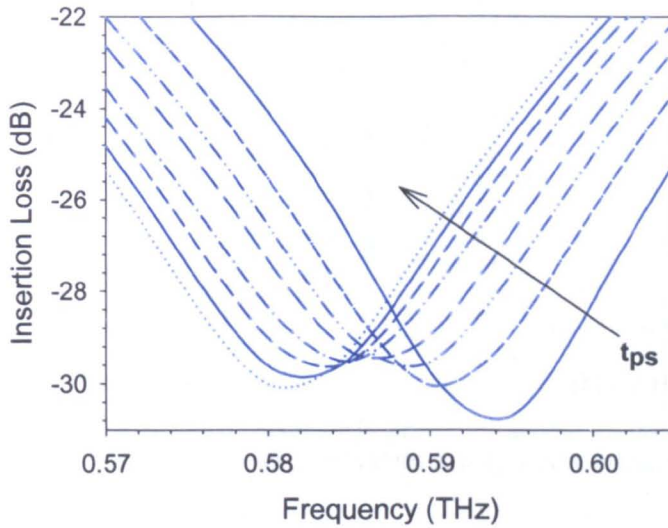
Figure 4.16. Effect of polystyrene coating on microstrip with single filter.

Furthermore, the relationship between the maximum insertion loss observed by simulating the microstrip structure with different thickness of PS coating and the full-width half-power (FWHP) bandwidth for a sinusoidal pulse with frequency 1 THz, is illustrated in Figure 4.17. As the PS coating increases the maximum insertion loss is observed at 5 μm of PS coating, whereas the resonance frequency of the 600 GHz filter is almost linearly decreasing as the PS coating thickness is increasing. In terms of the FWHP bandwidth, as the PS coating is increasing, the FWHP bandwidth follows a similar trend as the maximum insertion loss, with local minima at 5 μm. Also, the FWHP bandwidth for a sinusoidal pulse is increasing for a PS coating of up to 8 μm, and after that it is gradually decreasing. As the PS coating is increasing the electric field is confined in the dielectric layer. The addition of PS coating is causing a shift in the insertion loss and the FWHP bandwidth due to the confinement of the electric field. The deposition of more PS coating is causing the electric field to be almost fully enclosed in the dielectric layer, leading to a decrease in the maximum insertion loss. In terms of the FWHP bandwidth, the addition of PS coating is causing a shift in the FWHP bandwidth up to 8 μm. Further deposition of PS coating is having an incrementally less effect on the FWHP.
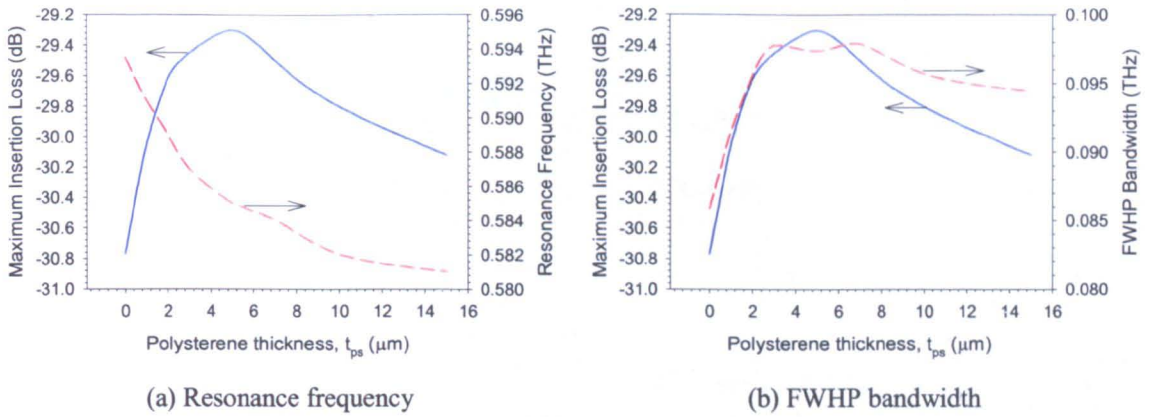
Figure 4.17. Relationship between maximum insertion loss and (a) resonance frequency, and (b) FWHP power bandwidth, for different values of polystyrene thickness (0 – 15μm).

The microstrip structure with the polystyrene coating illustrated in Figure 4.18 has been simulated using the 3D FDTD method with CPML ABCs. In this case two filters of different length, 194 μm and 82 μm respectively, were attached at the centre of the microstrip line, in a distance of 400 μm from each other. The material parameters of the microstrip and the ABCs used in the simulation were exactly the same as previously described. The microstrip line has been coated with polystyrene with relative permittivity $\varepsilon_r = 2.4967$. The parameters used for the FDTD grid were modified to model the thickness t_{ps} of the polystyrene coating with 1 μm increments, such that $\Delta x = 1$ μm, $\Delta y = 5$ μm, and $\Delta z = 0.5$ μm, and a Courant factor of $S = 0.9$. A Gaussian pulse, 30 μm wide, was used to source the FDTD grid with number of cells per wavelength $n_{c\lambda} = 20$. The simulation was allowed to run for 20 000 time steps with $\Delta t = 1.0007 \times 10^{-3}$ ps. Two monitors were placed before and after the filter stubs to capture the sampled voltages.

The transmission parameters across the filters and under the polystyrene coating have been calculated using the method described in Section 4.1 using the DFT of the sampled voltages over a frequency of 200 – 1500 GHz. The microstrip structure has been modelled for a range of microstrip widths (16 – 30μm) without changing the length of the filters attached to the microstrip line. The insertion loss S_{21} for the filter cascade has been evaluated for each microstrip width.

(a) Cross section

(b) Top view
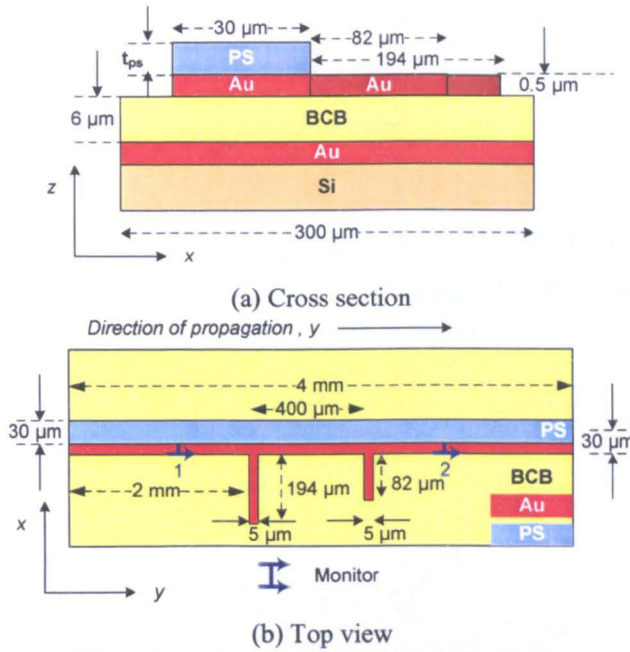
Figure 4.18. Geometry of the microstrip structure, filters, and polystyrene coating (not to scale).

In Figure 4.19 the insertion loss of the microstrip loaded with PS coating clearly shows a change in the value of the insertion loss. As the PS coating is increased the insertion loss peak value for the 600 GHz filter decreases for the microstrip line with 30 μm width. In order to observe the shifts in frequency as the PS coating is increased, in Figure 4.20 an expanded view of the 600 GHz filter is plotted.
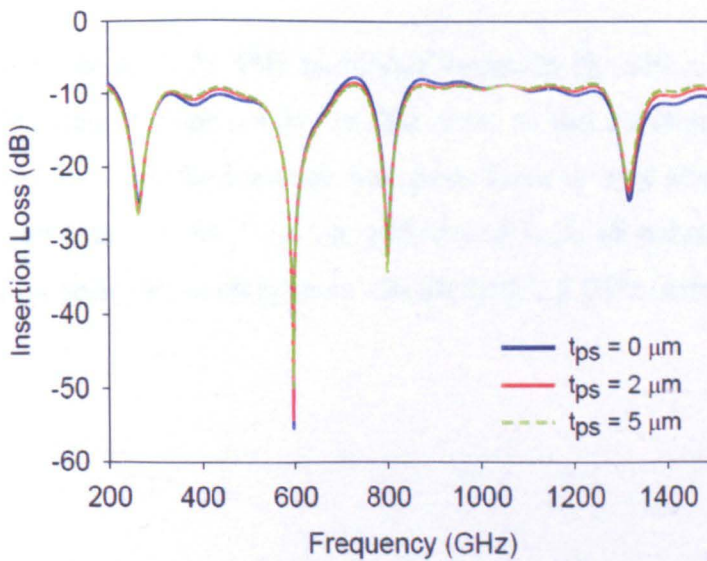
Figure 4.19. Insertion loss of the microstrip ($W = 30$ μm) for different values of polystyrene coating.

The effect of polystyrene coating on the microstrip and specifically on the 600 GHz filter, regarding the shift in frequency and the slight change in the insertion loss peak values, is illustrated in Figure 4.20. As the polystyrene coating is increasing towards 2 μm, the insertion loss peak value is only slightly decreased towards −54 dB at 596 GHz. With a thickness of 5 μm of polystyrene coating, the insertion loss peak values change rapidly, reaching −49 dB with 0.5 GHz shift in frequency.
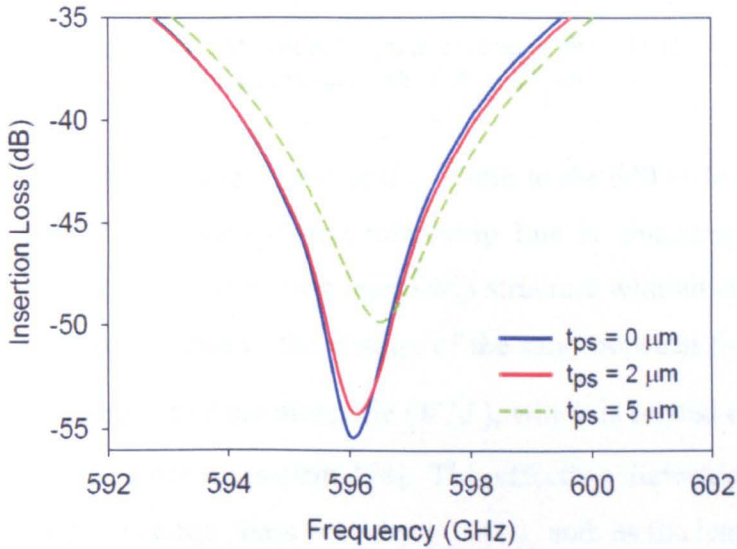
Figure 4.20. Effect of polystyrene coating on the 600 GHz filter for a microstrip width of $W = 30$ μm .

Similarly, for the 1.32 THz harmonic frequency the effect of polystyrene coating is illustrated in Figure 4.21. In this case, as the polystyrene coating is increasing towards 2 μm, the insertion loss peak value is only slightly decreased from −25 dB towards −23 dB. With the addition of 5 μm of polystyrene coating, the insertion loss peak values changes to −22 dB with 2.5 GHz shift in frequency.
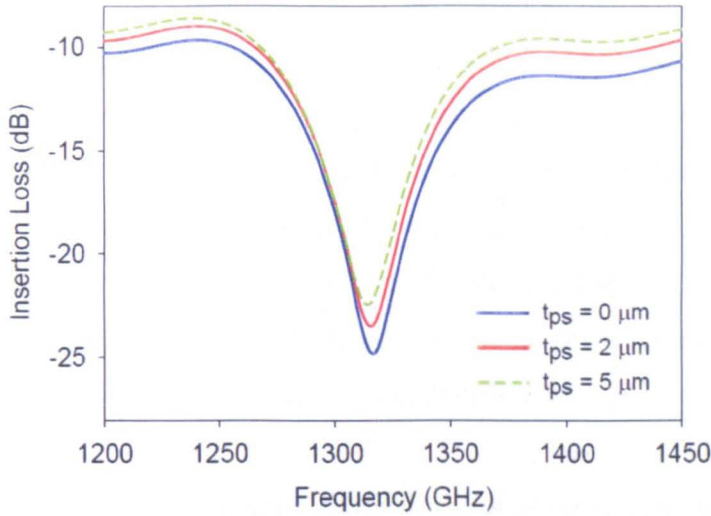
Figure 4.21. Effect of polystyrene coating on the 1.32 THz harmonic
for a microstrip width of $W = 30$ μm .

The effect of changing the microstrip width to the 600 GHz filter is shown in Figure 4.22. As the width of the microstrip line is changing, the resonant frequency of the filter is shifted for a microstrip structure without any polystyrene coating ($t_{ps} = 0$). This is due to the change of the ratio between the width of the microstrip and the height of the dielectric (W/d), which is related to the effective dielectric constant of the microstrip [18]. The effective dielectric constant can then be used to evaluate the phase velocity $v_{p=\sqrt{\varepsilon_{\it eff}}/c}$ and, as the length of the stub resonates at a frequency given by $v_p/4l$, a change in phase velocity would result in a frequency shift.
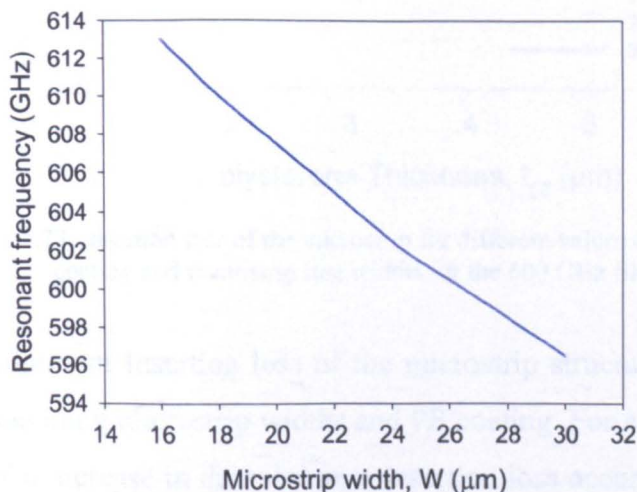
Figure 4.22. Frequency shift of the 600 GHz filter for different values of
microstrip width ($16 - 30$ μm) for $t_{ps} = 0$.

Moreover, the microstrip structure has been modelled using PS coating on the microstrip line. The following results in Figure 4.23 illustrate the effects of the thickness of PS coating on the filter array. For each case of microstrip width (16 – 30 μm) the thickness of PS coating has been varied from 1 μm to 10 μm. The results of the insertion loss calculated, using (4.1), of the filter cascade over the 200-1500 GHz frequency spectrum is plotted for different values of PS coating in Figure 4.24. The frequency shift observed due to the presence of PS coating is also consistent with loading the filters with dielectric coating [3].

The effect on the propagation characteristics of the device of a polystyrene layer along the top of the metal layer for the 600 GHz filter is illustrated in Figure 4.23. In this case, as the polystyrene thickness increases for the different values of width (16 – 30 μm) of the microstrip, the insertion loss peak values are reduced reaching a threshold after the deposition of 6 μm of polystyrene coating. As the thickness of the PS coating increases above 3 μm, the electric field confinement in the dielectric layer is causing a decrease in the minimum insertion loss.
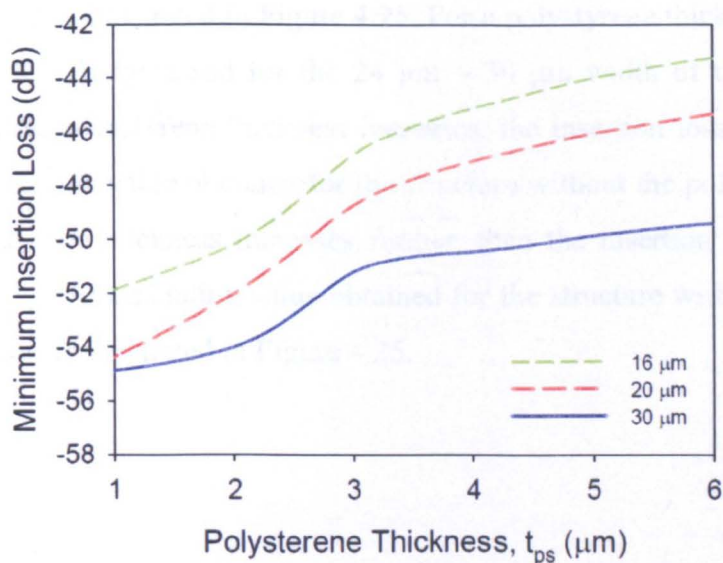
Figure 4.23. Insertion loss of the microstrip for different values of polystyrene coating and microstrip line widths for the 600 GHz filter.

The minimum insertion loss of the microstrip structure is also evaluated for the corresponding microstrip widths and PS coating. For a microstrip width of 28 μm a sudden increase in the minimum insertion loss occurs, with little change on the deposition of PS film on the microstrip line, whereas for 25 μm the

minimum insertion loss is recorded for the 600 GHz filter. The results are illustrated in Figure 4.24.
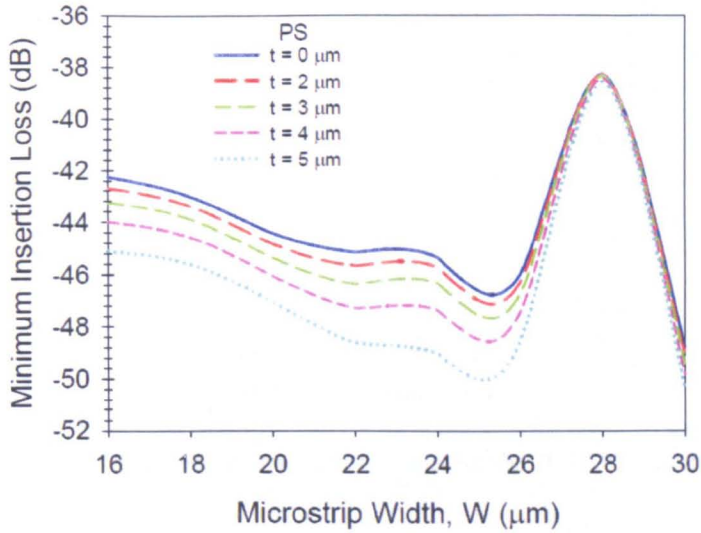
Figure 4.24. Minimum insertion loss of the microstrip for different values of polystyrene coating and microstrip line widths for the 600 GHz filter.

Similarly, for the 800 GHz resonance, the effect on the propagation characteristics of the device of a polystyrene layer along the top of the metal layer using the FDTD is illustrated in Figure 4.25. For a polystyrene thickness of 2 μm, the insertion loss is increased for the 24 μm – 30 μm width of the microstrip. However, as the polystyrene thickness increases, the insertion loss of the above material reaches the value obtained for the structure without the polystyrene film. As the polystyrene thickness increases further, then the insertion loss increases much above the corresponding value obtained for the structure without the above film deposition, as illustrated in Figure 4.25.
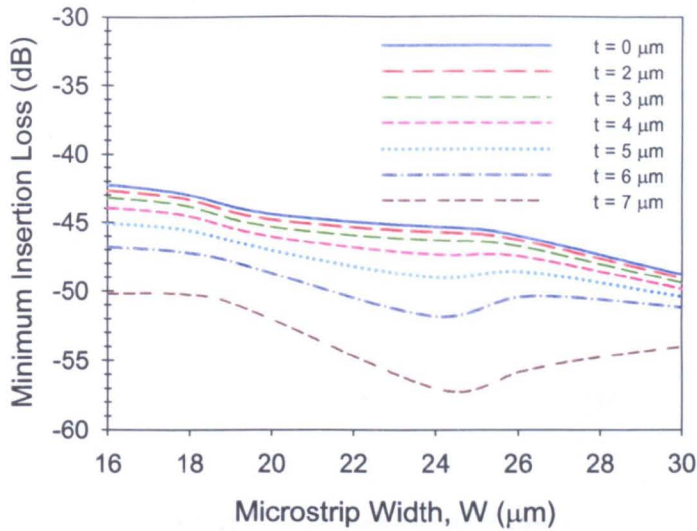
Figure 4.25. Minimum insertion loss of the microstrip for different values of polystyrene coating and microstrip line widths for the 800 GHz resonance.

Finally, the effect of varying the height of the dielectric substrate (BCB) is studied with respect to the change in insertion loss and shift of the resonance frequency for the 600 GHz filter. The results are plotted below in Figure 4.26 as the height of the BCB substrate increases, the insertion loss remains relatively the same, whereas a sudden increase occurs at 8.5 μm, after which the insertion loss is rapidly decreasing as the BCB height reaches 10 μm. As the height of the BCB substrate increases at 8.5 μm, the electric field confinement in the dielectric layer is reduced, causing an increase in the minimum insertion loss. Regarding the frequency shift of the 600 GHz filter, as the BCB height increases there is a constant shift in frequency, which is related to the change of the ratio between the width of the microstrip and the height of the dielectric (W/d) [18].
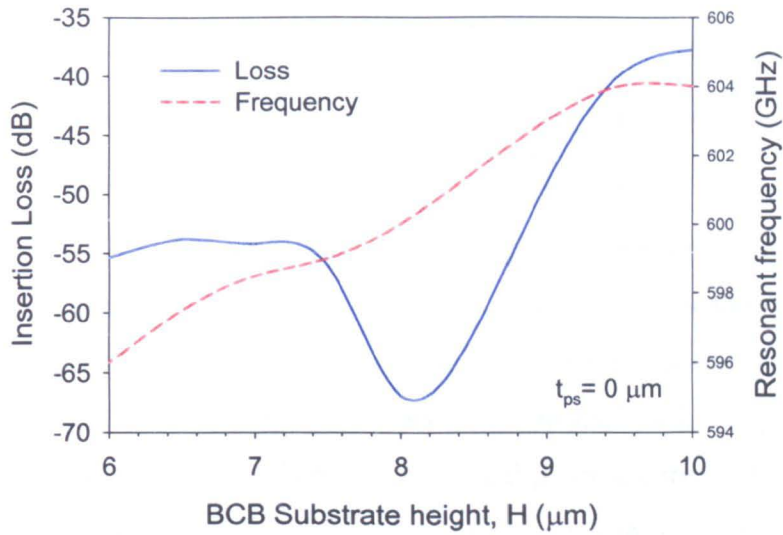
Figure 4.26. Insertion loss of the microstrip structure and resonant frequency of the 600 GHz filter for different values of BCB height (6 – 10 μm).

4.4 Drude Model Dispersion Parameters

The Drude model has been used to model the microstrip structure presented in Section 3.10 using the 3D FDTD method. The microstrip structure has been modelled without attaching any filters to the microstrip line. The microstrip line has been simulated using a polystyrene coating and varying thickness (t_{ps}) from 0 – 1 μm. The structure of the microstrip is illustrated in Figure 4.28.

(a) Cross section   (b) Top view
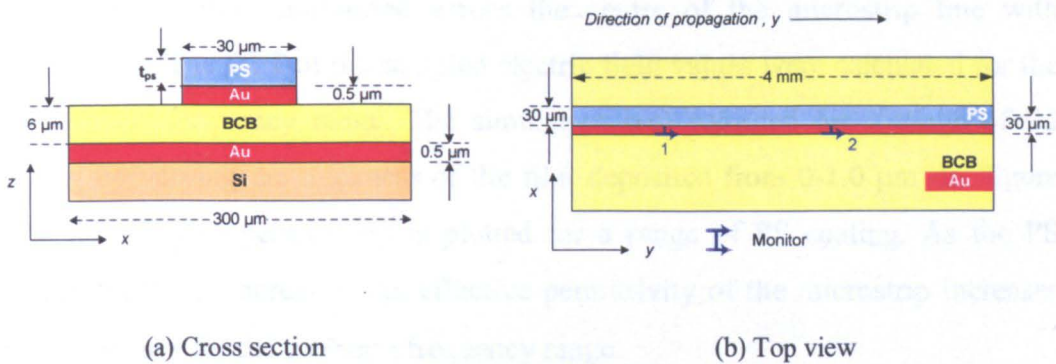
Figure 4.27. Microstrip with PS coating (not to scale).

The material parameters of the microstrip used in the simulation were for the BCB dielectric $\varepsilon_r = 2.57$. The values of the Drude model parameters for gold (Au) were selected as follows: the relative permittivity was set to $\varepsilon_r = 9.07$, the

133

Drude plasma frequency was set to $\omega_{pD} = 1.2 \times 10^6$ rad/s, the Drude damping coefficient was set to $\Gamma_D = 1.2 \times 10^{14}$ rad/s, and the electric conductivity was set to $\sigma = 7.34 \times 10^6$ S/m [19, 20]. The silicon (Si) cladding has been modelled using CPML ABCs. The PS coating relative permittivity was set to $\varepsilon_r = 2.9$ with absorption loss 4 cm^{-1} for the Drude model [21]. The microstrip is surrounded by 15 CPML thick cells in all directions. The microstrip penetrates the CPML walls in the x-direction and y-direction, to simulate an infinitely wide BCB substrate and an infinitely long microstrip line respectively. In the z^+-direction 40 cells of air were used, with relative permittivity $\varepsilon_r = 1$ and permeability $\mu = 1$. The CPML conductivity profile factor was to $\sigma_{factor} = 1.3$, and the PML order was set to $n_{pml} = 3$. The inner-domain CPML interface parameters were set to $\kappa_{max} = 10$, and $\alpha_{max} = 0.05$, the theory of which was presented in Section 2.11. The parameters used for the FDTD grid were set to $\Delta x = 1$ μm, $\Delta y = 2$ μm, $\Delta z = 0.1$ μm, and a CFL factor of $S = 0.9$. A Gaussian pulse was used to source the FDTD grid over the 30 μm-width microstrip. The simulation was allowed to run for 20 000 time steps with $\Delta t = 1 / c\sqrt{1/\Delta x^2 + 1/\Delta y^2 + 1/\Delta z^2}$. The dispersion parameters of the 4 mm-long microstrip are calculated and the results are presented.

The effective permittivity of the microstrip is calculated using the sampled electric field values monitored across the centre of the microstrip line with separation L. The DFT of the sampled electric field values were calculated for the 0.6-1.3 THz frequency range. The simulation was repeated for a range of PS coating by varying the thickness of the film deposited from 0-1.0 μm. In Figure 4.29 the effective permittivity is plotted for a range of PS coating. As the PS coating thickness increases, the effective permittivity of the microstrip increases almost linearly for the terahertz frequency range.
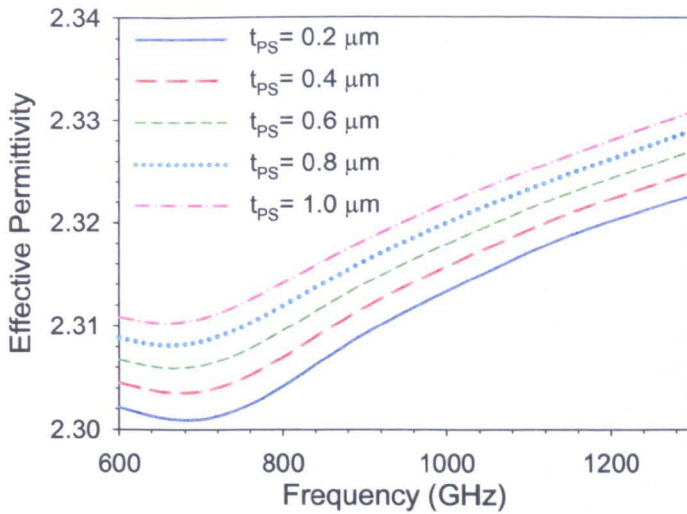
Figure 4.28. Effective permittivity of the microstrip structure for different values of polystyrene thickness (0 – 1.0 μm).

Furthermore, the characteristic impedance of the microstrip is calculated for the same set of results. The characteristic impedance of the microstrip for the terahertz frequency range is decreasing with frequency, as the deposition of PS coating reduces slightly the value of the characteristic impedance (characteristic impedance of free space is $Z_o = 377\ \Omega$). The results are presented in Figure 4.30.
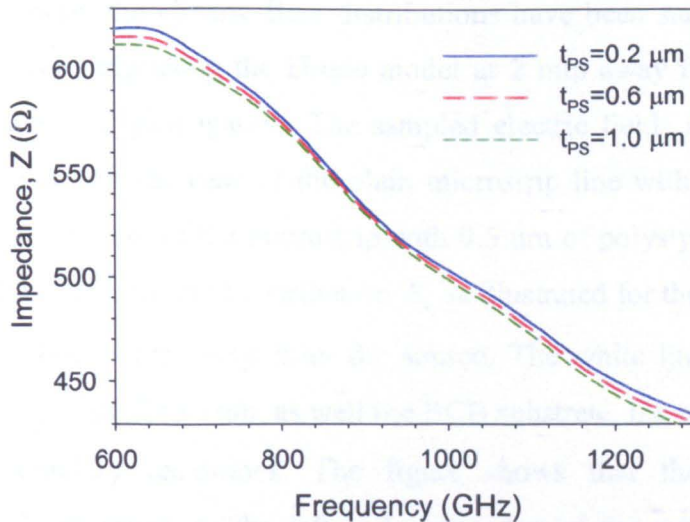
Figure 4.29. Characteristic impedance of the microstrip structure for different values of polystyrene thickness (0 – 1.0 μm).

The effect on the attenuation constant of the device of a polystyrene layer along the top of the metal layer is illustrated in Figure 4.31. The attenuation constant is increasing over the terahertz frequency range, while the PS coating thickness only causes slight changes in the increase of the attenuation of the microstrip structure.
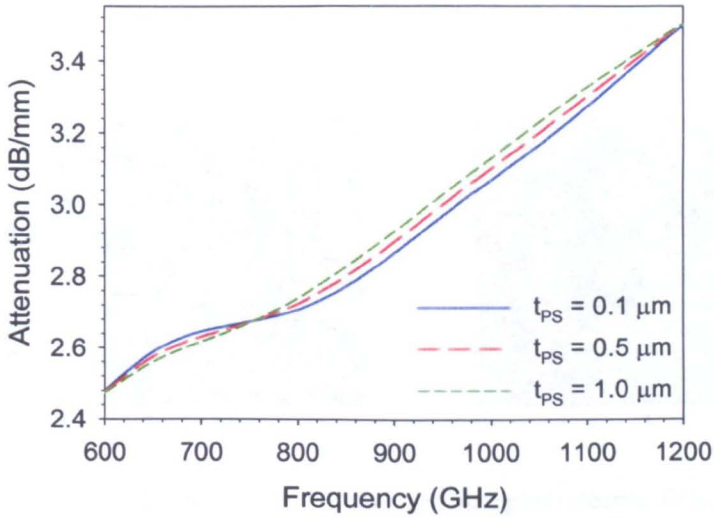
Figure 4.30. Insertion loss of the microstrip structure for different values of polystyrene thickness (0 – 1.0 μm).

Furthermore, the electric field distributions have been sampled at 1 THz for the plain microstrip using the Drude model at 2 mm away from the source, along the direction of propagation. The sampled electric fields are presented in Figure 4.32 below for the case of the plain microstrip line with no polystyrene coating, and for the case of the microstrip with 0.5 μm of polystyrene coating. In Figure 4.32(a) the electric field distribution E_x is illustrated for the microstrip line sampled at 1 THz, 2 mm away from the source. The white lines illustrate the microstrip line and the filter stub, as well the BCB substrate, the red lines indicate the CPML boundary conditions. The figure shows that the electric field concentration is observed on the left and right edge of the microstrip line. In Figure 4.32(b), the electric field distribution is presented for the E_z electric field sampled at 1 THz. The electric field concentration in this case is observed between the microstrip line and the BCB substrate, with some field concentration on the left and right edge of the microstrip. The results are consistent with the

electric field distributions presented earlier in Figure 4.8. In Figure 4.32(c) and 4.32(d) the electric field distribution are presented for the plain microstrip with 0.5 μm of polystyrene coating. In this case, the electric field E_x concentration in Figure 4.32(c) is observed on the left and right edge of the microstrip line, as well as on left and right edge of the polystyrene coating. In Figure 4.32(d), the electric field E_z concentration is observed between the filter stub and the BCB, with some field concentration on the left and right edge of the polystyrene coating.
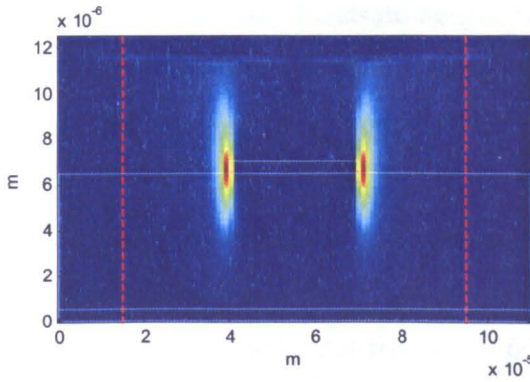
(a) Sampled electric field E_x at 1 THz for the microstrip line with no PS coating.
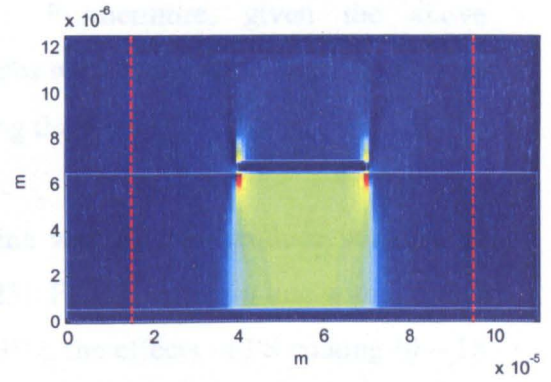
(b) Sampled electric field E_z at 1 THz for the microstrip line with no PS coating.
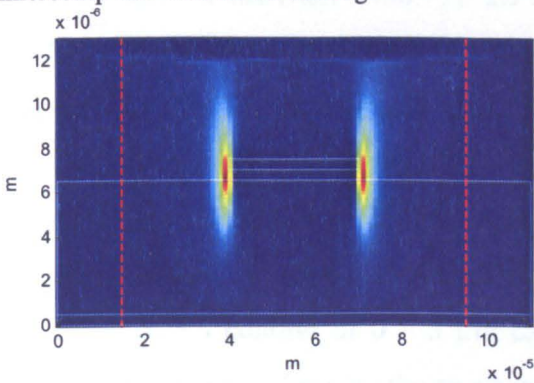
(c) Sampled electric field E_x at 1 THz for the microstrip line with 0.5 μm PS coating.
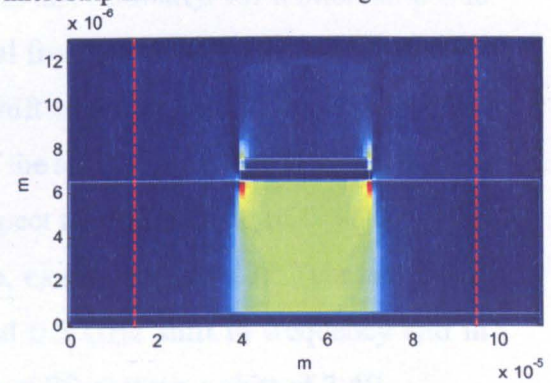
(d) Sampled electric field E_z at 1 THz for the microstrip line with 0.5 μm PS coating.

Figure 4.31. Electric field distributions sampled at 1 THz for the microstrip line with no PS coating (a – b), and with 0.5 μm of PS coating (c – d).

4.5 Summary

In this chapter a rigorous analysis of a microstrip structure at terahertz frequencies is presented. The 3D FDTD method with ABCs was used to validate the method as well as the implementation against known results from the literature. Moreover in this analysis PS coating deposition was considered for minimising losses of the microstrip at terahertz frequencies. Also the effects of PS deposition on the microstrip line were studied in conjunction with the effect of changing the microstrip-width to substrate-height ratio. Furthermore, given the above parameters the frequency shift of the filter stubs was also studied as the microstrip parameters changed over a range of PS coating thickness.

The PS coating on the microstrip line was able to produce some good results over a very thin-film deposition [22, 23]. For a microstrip line with a single filter stub with fundamental frequency 600 GHz, the effects of PS coating (0 – 15 μm), caused a shift in frequency of 16 GHz. The PS coating also caused a shift in insertion loss for the filter from –32 dB to –29dB. Similarly, for a microstrip line loaded with two filter stubs with fundamental frequencies 295 GHz and 600 GHz respectively, the PS coating also caused a shift in frequency. In this case for the 600 GHz filter and a PS coating of 0 – 5 μm, the shift was limited to 0.5 GHz. The insertion loss for the 600 GHz filter with respect to a PS coating of 0 – 5 μm, also caused a shift from –55 dB to –50 dB. Also, examining the 1.32 THz harmonic, the effect of PS coating of 0 – 5 μm caused 0.5 GHz shift in frequency and in terms of the insertion loss for the same range of PS coating, a shift of 2 dB.

Moreover, examining the effect of the microstrip width from 16 μm to 30 μm, for a microstrip line loaded with a two filter stubs with fundamental frequencies 295 GHz and 600 GHz respectively, caused an almost linear trend where the fundamental frequency of the 600 GHz filter shifted from 613 GHz to 596 GHz. The effect of PS coating on the microstrip line with the two filter stubs, by varying the width of the microstrip, was also examined. In this case, the insertion loss for a PS coating of 0 – 3 μm and a microstrip width 16 – 30 μm caused a shift of 5 dB for the 600 GHz filter. By increasing the PS coating from 4 – 6 μm, the effect on the insertion loss begins to have less impact on the 600 GHz

filter. Also, for a microstrip width of 28 μm, the effect of PS coating of 0 – 5 μm appears to have negligible effect on the insertion loss of the 600 GHz filter. The insertion loss of the microstrip for different values of PS coating and microstrip widths for the 800 GHz resonance was also examined. For the 800 GHz resonance, a PS coating of 0 – 7 μm caused an increase in insertion loss for a microstrip width between 16 μm and 30 μm, with a maximum insertion loss of -57 dB for a microstrip width of 25 μm and 7 μm of PS coating.

Furthermore, the effect of varying the BCB substrate height was also examined for a microstrip line loaded with a single filter stub with resonant frequency 600 GHz, without PS coating. The effect of the BCB substrate height of 6 – 10 μm caused an almost linear trend in the resonant frequency shift, with a maximum frequency shift of 8 GHz at 10 μm of BCB substrate. In terms of the insertion loss, as the BCB substrate height increased from 6 μm to 7.5 μm, the value remained constant –55 dB. As the substrate height increased to 8 μm, the insertion loss was increased to –67 dB. By increasing the BCB substrate height from 8 μm to 10 μm, the insertion loss was decreased to –37 dB.

Finally, the Drude model implementation was also used to model the microstrip structure with and without one filter stub over a range of PS coating thickness as previously described. Similarly, the Drude model indicated that losses were able to be minimised over a thin layer of PS coating. The Drude model results also showed that a frequency shift was observed for the filter stub, over a limit of very thin layer of PS coating, after this limit the frequency shift was declining.

In the next chapter, a novel low-loss multimode interference device is introduced. The theory behind MMI structures is presented and the low-loss MMI coupler is modelled using the FDTD method. The numerical analysis results are used for parameter extraction and characterisation of the MMI device.

References

[1]   P. H. Siegel, "Terahertz technology in biology and medicine," in *Microwave Symposium Digest, 2004 IEEE MTT-S International*, vol. 3, pp. 1575-1578, Pasadena, USA, 2004.

[2]   J. Cunningham, C. Wood, A. G. Davies, I. Hunter, E. H. Linfield, and H. E. Beere, "Terahertz frequency range band-stop filters," *Applied Physics Letters*, vol. 86, pp. 213503-213503-3, 2005.

[3]   J. Cunningham, C. Wood, A. G. Davies, C. K. Tiang, P. Tosch, D. A. Evans, E. H. Linfield, I. C. Hunter, and M. Missous, "Multiple-frequency terahertz pulsed sensing of dielectric films," *Applied Physics Letters*, vol. 88, pp. 071112-3, 2006.

[4]   C. K. Tiang, J. Cunningham, C. Wood, I. C. Hunter, and A. G. Davies, "Electromagnetic simulation of terahertz frequency range filters for genetic sensing," *Applied Physics, Journal of,* vol. 100, pp. 066105-3, 2006.

[5]   H. Heiliger, M. Nagel, H. G. Roskos, H. Kurz, F. Schnieder, and W. Heinrich, "Thin-film microstrip lines for MM and sub-MM/wave on-chip interconnects," in *Microwave Symposium Digest, 1997., IEEE MTT-S International*, pp. 421-424 vol.2., Denver, USA, 1997

[6]   A. Taflove and S. C. Hagness, *Computational Electrodynamics: The Finite-Difference Time-Domain Method*, 3 ed.: Artech House Publishers, 2005.

[7]   H. M. Heiliger, M. Nagel, H. G. Roskos, and H. Kurz, "Low-dispersion thin-film microstrip lines with cyclotene (benzocyclobutene) as dielectric medium," *Applied Physics Letters*, vol. 70, p. 2233, 1997.

[8]   H. M. Heiliger, M. Nagel, H. G. Roskos, R. Hey, and H. Kurz, "Sandwich microstrip lines with polymer dielectric for high-speed on-chip interconnects," in *Ultrafast Electronics and Optoelectronics*, p. UC7, Nevada, 1997.

[9]   G. Klatt, M. Nagel, T. Dekorsy, and A. Bartels, "Rapid and precise readout of terahertz sensor by high-speed asynchronous optical sampling," *Electronics Letters*, vol. 45, pp. 310-311, 2009.

[10]   M. Nagel, T. Dekorsy, M. Brucherseifer, P. Haring Bolívar, and H. Kurz, "Characterization of polypropylene thin-film microstrip lines at millimeter and submillimeter wavelengths," *Microwave and Optical Technology Letters*, vol. 29, pp. 97-100, 2001.

[11]   D. Burdeaux, P. Townsend, J. Carr, and P. Garrou, "Benzocyclobutene (BCB) dielectrics for the fabrication of high density, thin film multichip modules," *Journal of Electronic Materials*, vol. 19, pp. 1357-1366, 1990.

[12]   S. Costanzo, I. Venneri, G. Massa, and A. Borgia, "Benzocyclobutene as substrate material for planar millimeter-wave structures: Dielectric characterization and application," *Journal of Infrared, Millimeter, and Terahertz Waves*, vol. 31, pp. 66-77, 2009.

[13]   Y. Poo, R. Wu, X. Fan, and J. Q. Xiao, "Measurement of ac conductivity of gold nanofilms at microwave frequencies," *Review of Scientific Instruments*, vol. 81, pp. 064701-5, 2010.

[14] S. K. Sable and P. Gour, "Dispersion analysis of a microstrip line at higher frequencies by using Sonnet and Matlab," in *Communication Systems and Network Technologies (CSNT), 2011 International Conference on*, pp. 211-215, India, 2011.

[15] C. Themistos, B. M. A. Rahman, M. Rajarajan, K. T. V. Grattan, B. Bowden, and J. A. Harrington, "Characterization of silver/polystyrene (PS)-coated hollow glass waveguides at THz Frequency," *Lightwave Technology, Journal of,* vol. 25, pp. 2456-2462, 2007.

[16] G. Zhao, M. Mors, T. Wenckebach, and P. C. M. Planken, "Terahertz dielectric properties of polystyrene foam," *Optical Society of America B, Journal of,* vol. 19, pp. 1476-1479, 2002.

[17] C. Themistos, C. Markides, B. M. A. Rahman, and K. T. V. Grattan, "Characterization of microstrips for THz waves," in *Electron Devices and Solid State Circuit (EDSSC), 2012 IEEE International Conference on*, pp. 1-4, Bangok, Thailand, 2012.

[18] D. M. Pozar, *Microwave Engineering*, 3rd ed. Hoboken, NJ: J. Wiley, 2005.

[19] E. D. Palik, *Handbook of optical constants of solids*. Orlando: Academic Press, 1985.

[20] A. Vial, A.-S. Grimault, D. Macias, D. Barchiesi, and M. L. de la Chapelle, "Improved analytical fit of gold dispersion: Application to the modeling of extinction spectra with a finite-difference time-domain method," *Physical Review B,* vol. 71, p. 085416, 2005.

[21] P. Dean, M. U. Shaukat, S. P. Khanna, S. Chakraborty, M. Lachab, A. Burnett, G. Davies, and E. H. Linfield, "Absorption-sensitive diffuse reflection imaging of concealed powders using a terahertz quantum cascade laser," *Optics Express,* vol. 16, pp. 5997-6007, 2008.

[22] B. M. A. Rahman, K. T. V. Grattan, C. Themistos, and C. Markides, "Design optimization of low-loss waveguides and devices for THz systems," in *International Conference on Fibre Optics and Photonics*, p. M1A.1, Chennai, India, 2012.

[23] B. M. A. Rahman, C. Themistos, A. Quadir, C. Markides, H. Tanvir, and K. T. V. Grattan, "Design of low-loss THz waveguides and guided-wave devices by using the finite element method," in *MIOMD-XI Infrared Optoelectronics: Materials and Devices*, Chicago, USA, 2012.

Chapter 5

Low-loss Multimode Interference Devices for Terahertz Frequencies

Multimode interference (MMI) couplers have been widely used in the design of optoelectronic systems and optical communication networks, as well as building blocks for cascaded integration [1]. The unique characteristics of MMI coupler devices make them an attractive choice for several wavelength-division multiplexing (WDM) systems. In this Chapter, the MMI coupler based on the self-image principle, a well-established device in the optical spectrum, has been implemented successfully on a hollow-core polystyrene coated plasmonic waveguide structure for THz wave transmission. The attractive properties of the proposed scheme demonstrated here, such as low loss, small polarization dependence, and wide bandwidth, makes it attractive for further developments of THz guided-wave devices, such as directional couplers/polarizers and interferometers in the THz frequency band.

5.1 Multimode Interference Couplers

MMI devices have been used to replace directional couplers due to the ease of fabrication, their advantages of being very compact, large fabrication tolerance, wide bandwidth, excellent splitting ratio, as well as low-loss and polarization independence [2]. The properties of MMI coupler devices are based on the self-imaging principle, where the input field profile is reproduced at periodic intervals [2]. These properties spawned a wide range of applications for WDM systems using MMI devices. Among a few are power splitters [3], arrayed waveguide

filters (AWG) [4], MMI-AWG-based multiwavelength lasers [5] and Mach-Zehnder Interferometric switches [6].

MMI devices are based on the self-imaging property [2], where the guided modes of a multimode waveguide are excited and interfere constructively to produce single or multiple images of an input field launched usually via single mode optical waveguides at the one end of the structure, at periodic intervals along the direction of propagation. The number of the modes excited in each MMI structure and consequently the position of the images along the direction of propagation are dependent on the position of the input waveguides in the lateral x-direction, called the interference mechanism [2]. Thus, the self-imaging is a property of multimode waveguides by which an input field profile is reproduced in single or multiple or images at periodic intervals along the direction of propagation of the waveguide [2].

In terms of the guided-mode propagation analysis [2], given a step-index multimode waveguide, the shape of the input field, and consequently the types of images formed at a distance $z = L$ can be determined by the modal excitation, and the properties of the mode phase factor with respect to the mode number v given by

$$\exp\left[j\frac{v(v+2)\pi}{3L_\pi}L \right] \tag{7.1}$$

where L_π is the beat length of the two lowest-order modes. In this case, under certain circumstances, the input field can be reproduced (self-imaging) at a distance L. A set of mechanisms exist that allow the self-imaging of the input field, which are independent of the modal excitation, or the self-imaging of the input field is obtained only when exciting certain modes.

The General Interference (GI) mechanism is independent of the modal excitation. Under this mechanism the single and multiple images are obtained at specific multiples of the beat length. Under the GI mechanism, direct and mirror

images of the input field can be formed by general interferences at intervals of odd and even multiples of the length ($3L_\pi$) in the direction of propagation, where L_π is the beat length of the two lowest-order modes [2]. The GI mechanism principle is illustrated in Figure 5.1, where W_M is the width of the waveguide, n_r is the effective refractive index of the ridge, and n_c is the effective refractive index of the cladding. However, under the Restrictive Interference (RI) mechanism single and multiple images are obtained provided that certain modes are excited alone. On the other hand, the selective modal excitation of the RI mechanism yields to a set of new interference mechanisms the Paired Interference (PI) and the Symmetric interference (SI) mechanism.
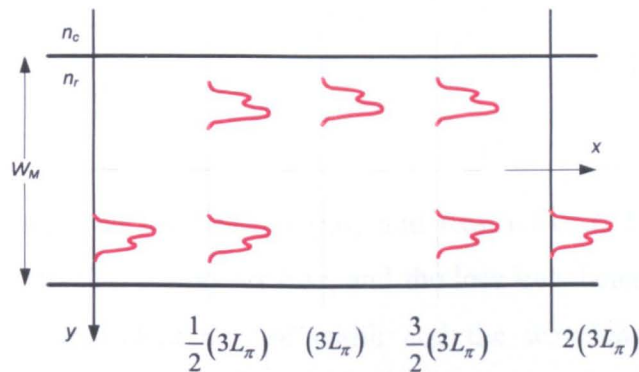
Figure 5.1. MMI waveguide with single image at ($3L_\pi$), direct single image at $2(3L_\pi)$, and two-fold images at $\frac{1}{2}(3L_\pi)$ and at $\frac{3}{2}(3L_\pi)$.

Under the symmetric interference (SI) mechanism, the first image of an input field launched via an input waveguide placed in the centre of the MMI width, is obtained at a self image length of $L_i = 3L_\pi/4$, along the direction of propagation.

The principle of self-imaging in MMI devices in which guided modes of a multimode waveguide (typically ≥ 3) are excited and interfere constructively to reproduce single or multiple images of the input field is central to the waveguide design. Selective excitation of the modes in an MMI structure and consequently the position of the images in the direction of propagation are subject to a set of self-imaging mechanisms [2]. Under the self-imaging mechanism the periodicity of single or multiple images is based on a set of interference mechanisms. The

effects of the width and the size of the input field can yield $l \times N$ or $N \times M$ beam splitters, where N and M are the number of input and output waveguides respectively. The Symmetric Interference (SI) mechanism is the result of combining the even (symmetric) modes. Based on the SI mechanism single images of the input field launched inside the waveguide can be obtained at a self image length, L_i, defined by:

$$L_i = \frac{3L_\pi}{4} = \frac{3\pi}{4(\beta_0 - \beta_1)} \qquad (7.2)$$

where L_π, is the coupling length, β_0 and β_1 are the propagation constants of the fundamental and the first higher order mode respectively.

$$L_\pi = \frac{1}{\beta_0 - \beta_1} \qquad (7.3)$$

Related works [7] on the General (GI) and Restrictive (RI) interference mechanisms have shown that the power loss, and the loss imbalance of an MMI-based 3dB splitter is dependent on the width and the wavelength variation. Furthermore the effects of the fabrication parameters and a comparison of the SI, GI and RI have been presented elsewhere [8]. In the following sections a detailed study of a novel MMI-based 3dB THz wave coupler/splitter implemented using Gold/polystyrene (PS) coated hollow glass rectangular waveguides is presented, including the performance and the effects of the SI scheme using the Finite Difference Time Domain method.

5.2 MMI-based 3dB THz Splitter

A thin metallic hollow core rectangular waveguide with silica cladding was considered as the waveguide structure of the MMI device, where the interior of the metal-cladding is coated with dielectric material to reduce the modal loss. A thin layer of polystyrene is deposited at the inner surface of the metal cladding.

The height H_{MMI}, and the width, W_{MMI}, of the MMI structure were considered to be 1 mm and 3 mm, respectively and the position of the input and output ports, spaced by a distance of half the MMI width along the horizontal direction, according to the self imaging principle, are also pointed in Figure 5.2.
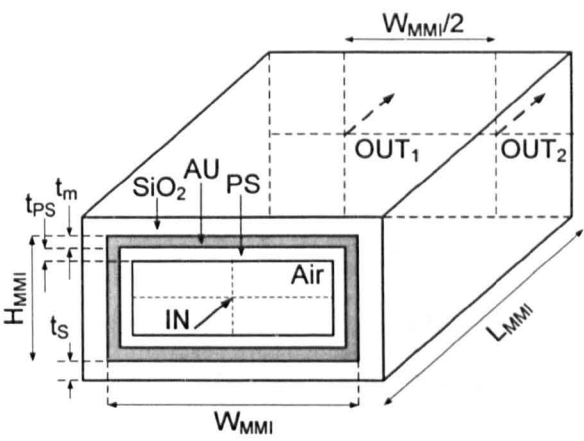
Figure 5.2. Hollow-core polystyrene coated Terahertz Multimode Interference device.

The cross section of the structure is presented in Figure 5.3 and the MMI device layout in Figure 5.4. The metal thickness was considered to be 0.5 μm and the polystyrene thickness was varied to achieve minimum modal loss. It should be noted that the MMI height has been designed to be 1 mm to ensure single-mode behaviour along the vertical dimension. Polymer materials, such as polystyrene, which was used in this study to reduce attenuation, exhibit low absorption coefficient at the THz range [9]. In the present study only the coupler section has been examined.
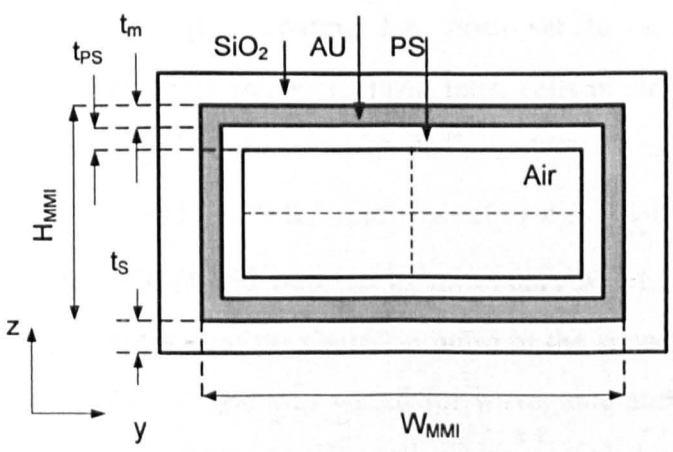
Figure 5.3. Cross section of the metallic hollow core polystyrene coated waveguide.
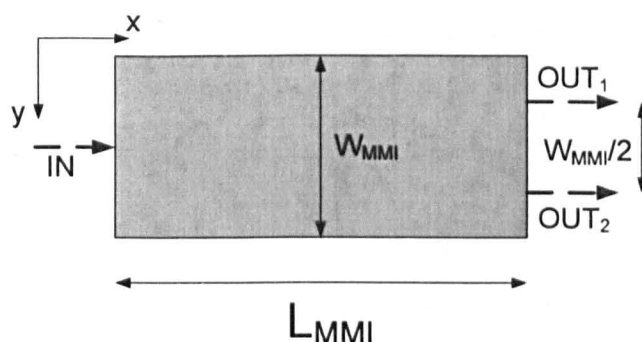
Figure 5.4. MMI device layout.

5.3 Low-Loss MMI FDTD Analysis

In simulating the multimode interference waveguide using the 2D FDTD method Perfectly Matched Layer (PML) [10] absorbing boundary conditions (ABC) are applied to terminate the problem space.

Given the structure presented in Figures 5.2 – 5.4, the metal thickness of the metal-clad silica rectangular waveguide with an air core and polystyrene coating was considered to be 0.5 µm. In this case, the 3D FDTD simulation would require a minimum of $\Delta z = 0.5$ µm. Due to the computational resources required in terms of memory this was not feasible. Thus, the MMI coupler presented in Figures 5.2 – 5.4 has been simulated using the 2D FDTD method. The material parameters of the MMI waveguide used in the simulation were for the silica clad (SiO$_2$) dielectric $\varepsilon_r = 3.8416$, for gold (Au) the relative permittivity was set to $\varepsilon_r = 1$ and the electric conductivity was set to $\sigma = 7.34 \times 10^6$ S/m [11]. The permittivity of polystyrene (PS) coating has been set to $\varepsilon_r = 2.4964$. The rectangular waveguide is surrounded by 12 PML thick cells in all directions. The PML reflection coefficient of the finite-width PML medium at normal incidence was set to $R(0) = 1 \times 10^{-15}$, and the PML order was set to $n_{pml} = 2$ (parabolic). The parameters used for the FDTD grid were set to $\Delta x = 1$ µm, $\Delta y = 1$ µm, and a CFL factor of $S = 0.9$. The spot size of the Gaussian pulse or the sinusoidal wave that was used to source the FDTD grid was varied for waveguide analysis, which is described next. The source at any given simulation was centred along the y-axis of the MMI coupler with number of cells per wavelength $N_\lambda = 20$. The simulation

was allowed to run for 4000 to 7500 time steps with $\Delta t = 1.3102 \times 10^{-3}$ ns depending on the length of the MMI coupler in order to allow for the pulse to propagate through the waveguide along the x direction.

The performance of the MMI device in the time domain has been examined using the FDTD approach. Initially, a sinusoidal wave at 2.5 THz has been launched to demonstrate the performance of the device for a monochromatic source and the field evolution from a horizontal plane at the centre of the waveguide is presented in Figure 5.6. The electric field distribution illustrated in the Figure 5.5 is obtained as the FDTD algorithm is executed, and during the calculation of the electric fields, using DFT at a specified frequency, 2.5THz in this case. The view generated in Figure 5.5 is based on the MMI device layout in Figure 5.3.
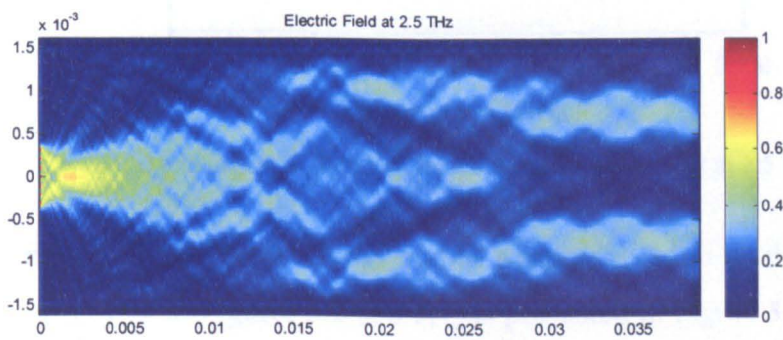
Figure 5.5. FDTD simulation of the MMI for a sinusoidal wave input at 2.5 THz.

In the aforementioned simulation, 4000 time steps have been used and by launching a sinusoidal wave with a spot-size diameter of 0.76 mm, the length of the device was found to be 38.8 mm, therefore, in fine agreement with the designed MMI length obtained using the modal solution of the FEM approach [12]. The fundamental and the first order higher TM modes of the MMI cross section, have been obtained using the full vectorial H-field FEM [12] and the propagation constants were found to be $\beta_0 = 52.2424 \text{ mm}^{-1}$ and $\beta_1 = 52.2120 \text{ mm}^{-1}$, respectively, thus giving a self image length, L_i of 77.51 mm and consequently a half power length corresponding to the length of the MMI of $L_{MMI} = 38.76 \text{ mm}$.

The frequency spectrum of the output sinusoidal wave at the left port (assigned as port OUT_1 in Figures 5.2 and 5.4) is presented in Figure 5.6, where it can be seen that the maximum frequency is located at 2.5 THz as expected. The sinusoidal wave evolution along the direction of propagation is also shown as inset in the time domain.
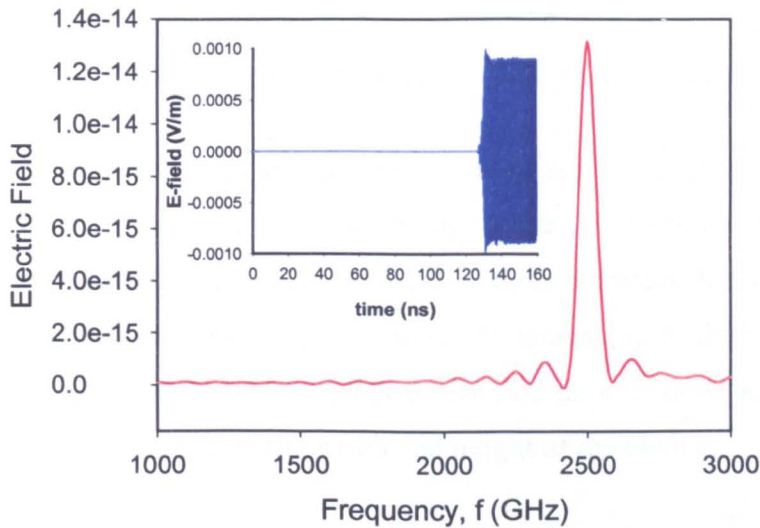
Figure 5.6. FDTD simulation of the MMI for a sinusoidal wave input at 2.5 THz.

The frequency spectrum of the output sinusoidal wave at the left port (assigned as port OUT_1 in Figures 5.2 and 5.4) is presented in Figure 5.6, where it can be seen that the maximum frequency is located at 2.5 THz as expected. The sinusoidal wave evolution along the direction of propagation is also shown as inset.

Moreover, a Gaussian beam of spot-size diameter of 0.76 mm, launched the input of the MMI device has been simulated using the FDTD approach and the field evolution from a horizontal plane at the centre of the device, along the direction of propagation is presented in Figure 5.7. The length of the device for the above spot-size diameter was found to be about 38.82 mm, in fine agreement with the length obtained from the FEM modal solution [12].
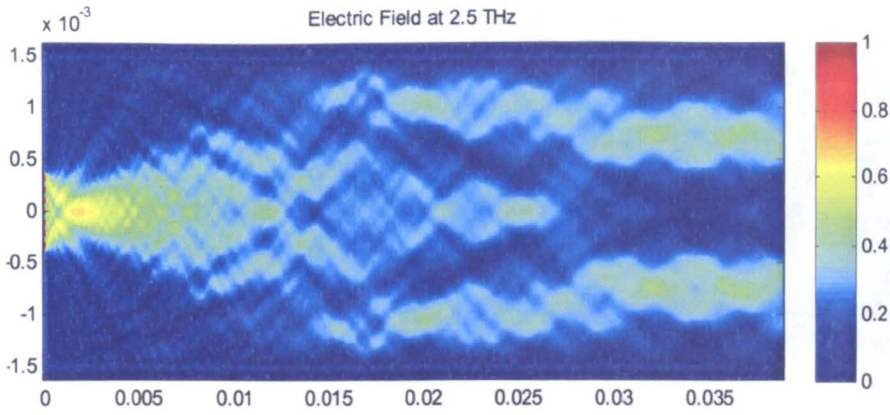
Figure 5.7. FDTD simulation of the MMI 3dB coupler for a Gaussian input.

Furthermore, the MMI length can be optimized by varying the spot-size diameter of the beam source, as presented in Figure 5.8. In the aforementioned characteristics, it can be seen that the MMI length increases linearly with the source spot-size diameter, for a certain range. By increasing further the spot-size diameter, the images at the output ports deteriorate as illustrated in Figure 5.9, since the spot-size is limited by the width and height of the device.
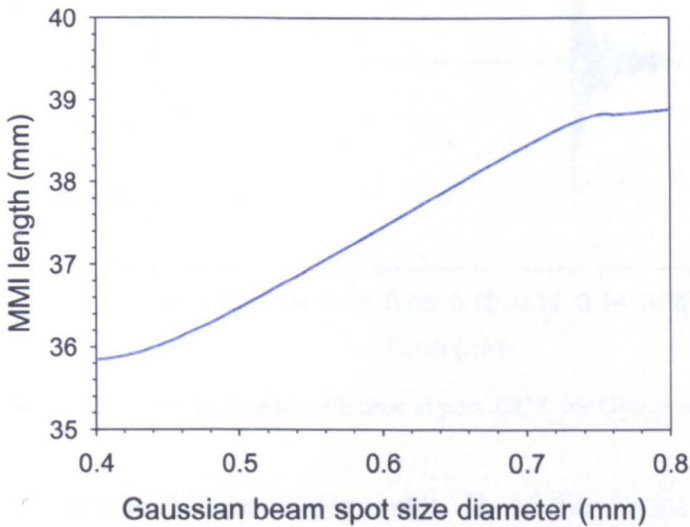
Figure 5.8. MMI length with Gaussian input spot-size diameter.

In Figure 5.9, the FDTD simulation for a spot size of 0.9 mm, over limit, indicates that the output signal deteriorates over distance for the specific frequency.
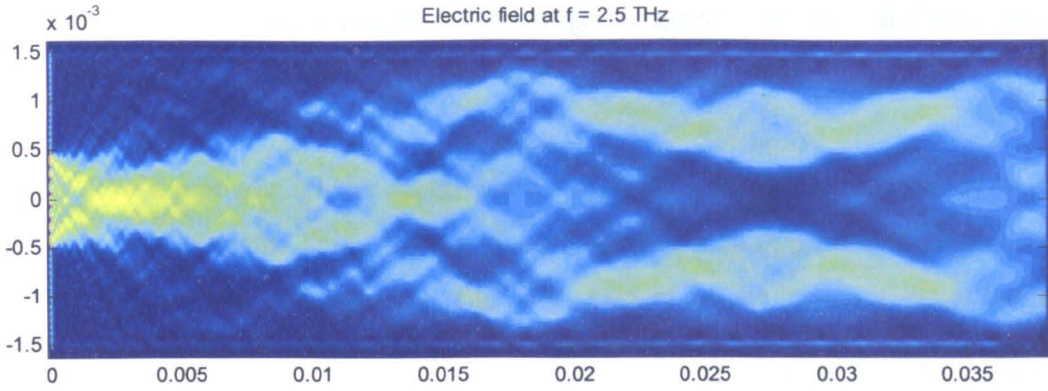
Figure 5.9. FDTD simulation of the MMI for a sinusoidal wave input at 2.5 THz, spot size over the limit (deterioration of output).

The electric field, obtained from the monitor of the left port output of the MMI device, from the Gaussian input beam of spot size diameter of 0.76 mm, is presented in Figure 5.10.
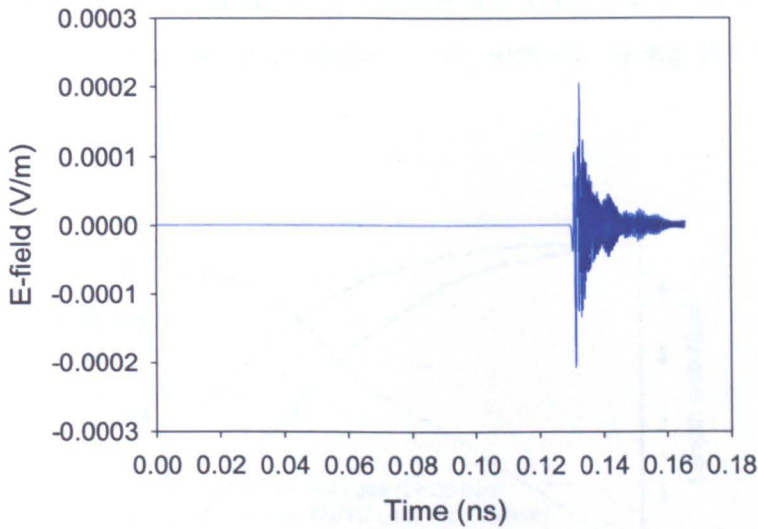
Figure 5.10. Output E-field with time at port OUT_1 for Gaussian input.

The waveguide dispersion parameter, D, of the device at 2.5 THz was estimated to be about 0.1 ps/(μm $\times$ m), by measuring the pulse spread along the direction of propagation. This corresponds to pulse broadening of about 0.85 ps for a 38 mm long waveguide and a bandwidth of 1.4 THz. The dispersion levels of the device are relatively small because the propagation is performed inside the air core and the mode is fairly isolated from the surface modes propagating along the metal-dielectric interfaces of the structure due to the polystyrene coating. The

dispersion level is also found to be in good agreement with the dispersion presented in [13] for a structure with circular geometry.

For the power splitter design shown here, the device length depends on the operating wavelength. Thus, for any given wavelength an optimized design can be achieved. However, for a given design with a fixed device length if the operating wavelength is varied, the performance would deteriorate as the device length would not conform to the design requirement. Figure 5.11 shows performance of the 3-dB power splitter designed, at the length of the TM polarization and the average TM/TE length, of 37.2 mm and 36.126 mm, respectively where the frequency is varied. This shows the performance deteriorating with the frequency variation, however, for a smaller frequency change, the performance can be considered satisfactory. The actual bandwidth of the device was estimated to be about 0.8 THz. The image quality of the replicas of the input field deteriorates dramatically when the frequency drops below 2.1 THz, due to the change of the position ($L_i/2$) where the two replicas are formed, along the direction of propagation.
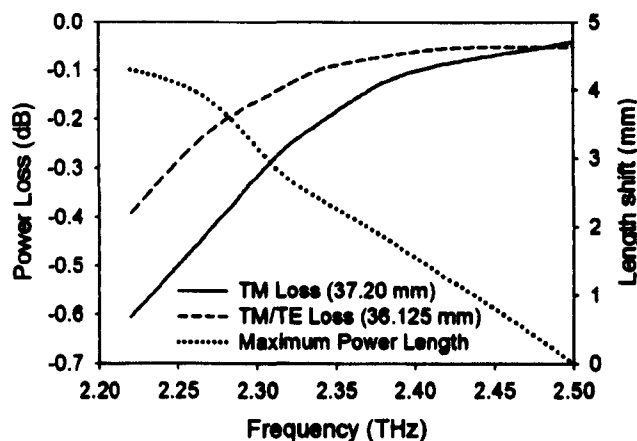
Figure 5.11. Variation of the output power loss at the TM length and the average TM/TE length and shift of the maximum output power position along the length, with the frequency variation.

The variation of the position of the maximum power at the output ports, corresponding to the device length, with the variation of the frequency has also been examined and presented in Figure 5.11, where it can be seen the device length changes linearly with the decrease of the frequency at a rate of about 15 μm/GHz.

5.4 Summary

In this chapter the 2D FDTD method has been applied in the analysis of a low-loss MMI coupler at THz wavelengths. The aim was the development of an MMI-based device that would exhibit low-loss at THz frequencies. Significant research has been carried out over the recent years on dielectric-lined hollow waveguides with metal cladding. This work has been applied in the design of an MMI device with minimum loss and optimal configuration for first higher order modes. A suitable choice of a low-loss dielectric coating, such as Polystyrene coating, Au metal cladding, its thickness and geometry can yield minimum loss. Furthermore, the 2D FDTD has been used to examine and study the propagation, attenuation and losses both in time and space. The proposed MMI design shows significantly low loss and dispersion levels when excited with a Gaussian-shaped beam.

In the next chapter the underlying theory of surface plasmon and surface plasmon polaritons is presented. The FDTD method is used as a numerical analysis tool for the simulation and the evaluation of a low-loss plasmonic waveguide in terms of losses and dispersion characteristics.

References

[1]   T. Trung Le and L. W. Cahill, "The modeling of MMI structures for signal processing applications," in *Integrated Optics: Devices, Materials, and Technologies XII*, San Jose, pp. 68961G-7, CA, USA, 2008,.

[2]   L. B. Soldano and E. C. M. Pennings, "Optical multi-mode interference devices based on self-imaging: principles and applications," *Lightwave Technology, Journal of*, vol. 13, pp. 615-627, 1995.

[3]   T. Rasmussen, J. K. Rasmussen, and J. H. Povlsen, "Design and performance evaluation of 1-by-64 multimode interference power splitter for optical communications," *Lightwave Technology, Journal of*, vol. 13, pp. 2069-2074, 1995.

[4]   M. R. Amersfoort, J. B. D. Soole, H. P. LeBlanc, N. C. Andreadakis, A. Rajhel, and C. Caneau, "Passband broadening of integrated arrayed waveguide filters using multimode interference couplers," *Electronics Letters*, vol. 32, p. 449, 1996.

[5]   C. G. P. Herben, C. G. M. Vreeburg, X. J. M. Leijtens, H. Blok, F. H. Groen, I. Moerman, J. W. Pedersen, and M. K. Smit, "Chirping of an MMI-PHASAR demultiplexer for application in multiwavelength lasers," *Photonics Technology Letters, IEEE*, vol. 9, pp. 1116-1118, 1997.

[6]   N. Yoshimoto, Y. Shibata, S. Oku, S. Kondo, and Y. Noguchi, "High-input-power saturation properties of a polarization-insensitive semiconductor Mach-Zehnder interferometer gate switch for WDM applications," *Photonics Technology Letters, IEEE*, vol. 10, pp. 531-533, 1998.

[7]   C. Themistos, M. Rajarajan, B. M. A. Rahman, S. S. A. Obayya, and K. T. V. Grattan, "Rigorous Comparison of Parabolically Tapered and Conventional Multimode-Interference-Based 3-dB Power Splitters in InGaAsP/InP Waveguides," *Appl. Opt.*, vol. 43, pp. 5228-5235, 2004.

[8]   C. Themistos and B. M. A. Rahman, "Design issues of a multimode interference-based 3-dB splitter," *Appied. Optics*, vol. 41, pp. 7037-7044, 2002.

[9]   G. Zhao, M. Mors, T. Wenckebach, and P. C. M. Planken, "Terahertz dielectric properties of polystyrene foam," *Optical Society of America B, Journal of*, vol. 19, pp. 1476-1479, 2002.

[10]   J.-P. Berenger, "A perfectly matched layer for the absorption of electromagnetic waves," *J. Comput. Phys.*, vol. 114, pp. 185-200, 1994.

[11]   Y. Poo, R. Wu, X. Fan, and J. Q. Xiao, "Measurement of ac conductivity of gold nanofilms at microwave frequencies," *Review of Scientific Instruments*, vol. 81, pp. 064701-5, 2010.

[12]   C. Markides, C. Themistos, H. Tanvir, B. M. A. Rahman, and K. T. V. Grattan, "Multimode Interference 3dB splitters in hollow core metallic waveguides for low loss THz wave transmission," *Selected Topics in Quantum Electronics, IEEE Journal of*, vol. 19, p. 8500606, 2012.

[13]   O. Mitrofanov and J. A. Harrington, "Dielectric-lined cylindrical metallic THz waveguides: mode structure and dispersion," *Optics Express*, vol. 18, pp. 1898-1903, 2010.

Chapter 6

Numerical Dispersion for Plasmonic Waveguides

Today, there is an increasing interest in Surface Plasmon based research and recent studies have shown that a wide range of plasmon-based optical elements and techniques have led to the development of a variety of active switches, passive waveguides, biosensors, lithography masks, to name just a few. In this chapter the underlying theory of surface plasmons will be introduced with emphasis on the application of surface plasmons to the terahertz frequency range. Furthermore, the FDTD method will be used as a numerical analysis tool for the calculation of the dispersion parameters and the propagation loss of a low-loss plasmonic rectangular waveguide at terahertz frequencies.

6.1 Surface Plasmons

Surface plasmons are electromagnetic fields that are formed due to the coupling of free electrons in the interface between a dielectric medium and a conductor. These electron charges can perform coherent fluctuations called surface plasmon oscillations, which are a combination of propagating electromagnetic field and charge density oscillations [1]. A surface plasmon mode may be defined as the fundamental electromagnetic mode at the interface between a material with negative permittivity and a material with positive permittivity, where at a specific frequency electron surface-charge oscillations occur. Surface plasmon modes are confined to surfaces where there is a strong interaction of the electromagnetic waves at the interface of the bounding materials. Surface plasmon modes couple

with the free charge carriers along the interface between a metal and a dielectric. The interaction of the free electrons with the electromagnetic field causes surface plasmon polaritons that propagate along the interface of the materials and decay evanescently on both sides of the material [2].

The nature of surface plasmons (SP) can be expressed in terms of their respective field distributions, wavevectors, and the key characteristic of the electric field propagation along the interface and decaying away from both the conducting and dielectric media. The surface plasmon condition for a metal-dielectric interface for the 2D x-directed wavevector (k_{sp}) of the surface mode propagating along an optically thick conducting sheet is given by

$$k_{sp}(\omega) = k_o \sqrt{\frac{\varepsilon_m \cdot \varepsilon_d}{\varepsilon_m + \varepsilon_d}} \qquad (6.1)$$

in which the wavevector is determined by the permittivity of the conducting sheet (ε_m) and the dielectric coating (ε_d), where k_o is the free space wavevector (ω/c). Given the SP dispersion relation (6.1), for materials such as metals with complex dielectric functions (Drude model), the SP wavevector will in turn also become complex. Thus, the magnitude of the SP wavevector (k_{sp}) will be greater than the free-space wavevector (k_o), which means that the orthogonal to the surface wavevector (k_z) must be imaginary.

The following diagram in Figure 6.1 illustrates the SP wavevector (k_{sp}) propagating along the interface of a metal conductor and a dielectric, the surface-normal wavevector (k_z), and the electric field (E_z). The diagram shows the exponential decay of the electric field of the surface mode in both the metal conductor and the dielectric, which depends on the imaginary surface-normal wavevector.
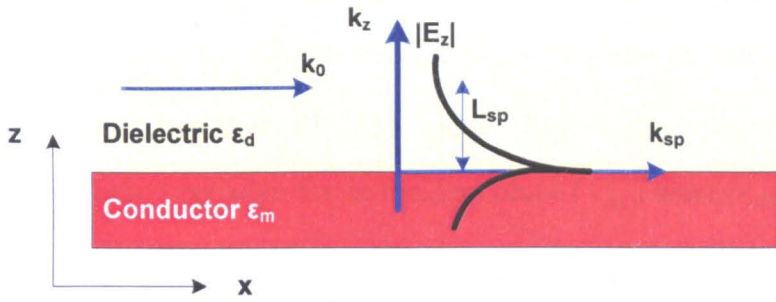
Figure 6.1. Illustrating the SP wavevector k_{sp} propagating along the surface of the conductor, with
decaying electric field E_z, the imaginary surface-normal wavevector k_z, SP attenuation length
(L_{sp}), and free space wavevector (k_0).

Moreover, in Figure 6.1 the attenuation length or decay length (L_{sp}) of the
SP electric field, perpendicular to the surface is shown. The spatial extension of
the SP electromagnetic field perpendicular to the interface is given by the inverse
of the evanescent surface normal wavevector (k_z)

$$k_z = \sqrt{\varepsilon_d \cdot k_0 - k_{sp}^2} \tag{6.2}$$

$$L_{sp} = \frac{1}{|k_z|} = \frac{\lambda}{2\pi} \cdot \left| \frac{\varepsilon_m + \varepsilon_d}{\varepsilon_m \cdot \varepsilon_d} \right|^{\frac{1}{2}} \tag{6.3}$$

Given the x-direction SP wavevector (k_{sp}) from equation (6.1), the
propagation distance (δ_{sp}) after which the intensity decreases $1/e$ of the SP mode
propagating along the interface of the metal and the dielectric can be determined
by

$$\delta_{sp} = \frac{1}{2 \, \text{Im}(k_{sp})} \tag{6.4}$$

For optical excitation of a SP, a photon must be coupled with a surface
charge oscillation. Nonradiative SPs do not directly couple to an incident plane
wave due to the momentum required of the incident photon to match that of the
SP [2]. In this case, excitation techniques of SP have been reported that enhance

157

the momentum of the incident light [3]. For nonradiative SPs, the free space wavevector ratio (k_o) to the SP wavevector (k_{sp}) is given as the propagation constant for a single-interface SP TM mode $\beta_{TM} = \sqrt{\varepsilon_m \cdot \varepsilon_d / \varepsilon_m + \varepsilon_d}$. The momentum conservation equation for an incident plane (k_{inc}) wave is given by

$$k_{inc} = k_0 \sqrt{\varepsilon_d} \tag{6.5}$$

6.2 Surface Plasmon Dispersion

Given the SP wavevector equations in the previous section, the frequency dependent properties may be obtained. In order to determine the frequency dependent electric permittivity of a metal conductor, the Drude model dielectric function can be used. The Drude model was introduced in Section 4.4, and is presented here for clarity

$$\varepsilon_r(\omega) = \varepsilon_\infty - \frac{\omega_{pD}^2}{\omega^2 + j\omega\Gamma_D} \tag{6.6}$$

where ε_∞ is the permittivity of the material at infinite frequency, ω_{pD} is the Drude angular frequency, and Γ_D is the collision frequency for the Drude pole relaxation [4]. The Drude model parameters may be obtained from various sources [5, 6], and here the Drude parameters for gold (Au) were taken from [4], as the permittivity of the material $\varepsilon_\infty = 9.1$, the Drude angular frequency $\omega_{pD} = 1.2 \times 10^{16}$ rad/s, and the collision frequency $\Gamma_D = 1.2 \times 10^{14}$ rad/s. Although the Drude model can provide reliable results over a range of frequencies, however, there are limitations. In this case, the frequency spectrum is split into zones where different parameters should be used for each frequency range in order to get the best fit [7]. The real and imaginary parts of the frequency dependent relative permittivity $\varepsilon_r(\omega)$ are plotted for a range of frequencies from 300 THz up to 600 THz, for benchmarking purposes in Figure 6.2.
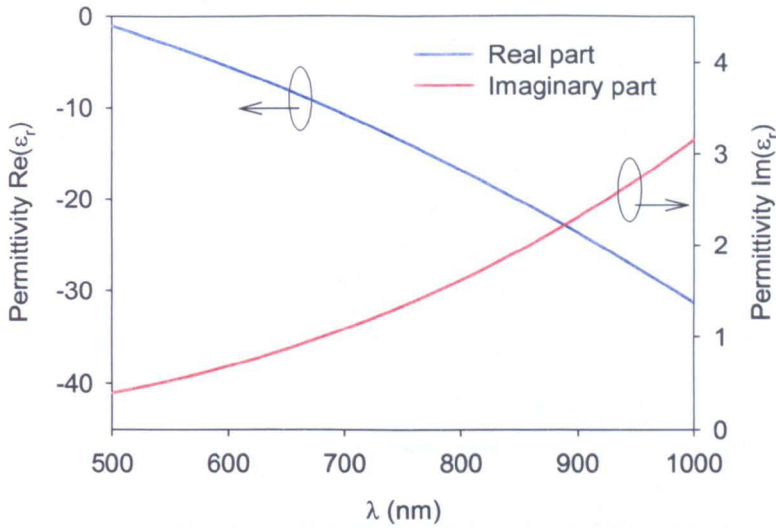
Figure 6.2. Gold (Au) permittivity (real and imaginary part)
calculated with the single Drude model.

With the Drude model frequency dependent permittivity values now available, it is now possible to model the wavevector, field profile, and propagation length of a SP over a gold-air interface for a wide range of frequencies. The equations required for obtaining results were presented in the previous section. The following figures (6.3, 6.4) illustrate the properties of a SP over a gold-air interface for a range of frequencies from 1 GHz up to 1 PHz, outlining a spectrum of frequencies from the microwave region to the ultraviolet.

In Figure 6.3, the real (red line) and imaginary (blue line) parts of the SP wavevector (k_{sp}) are plotted for a range of frequencies up to 1 PHz. The free-space wavevector (k_o) is also plotted for the same range of frequencies. In the figure, the asymptote in the SP wavevector indicates the surface plasma frequency (ω_{sp}). At this frequency the permittivity of the gold becomes equal to –1, and the surface plasmon no longer propagates at frequencies higher than the value of ω_{sp}. Moreover, at this frequency the imaginary part of the SP wavevector is also at maximum.

ω_{sp}
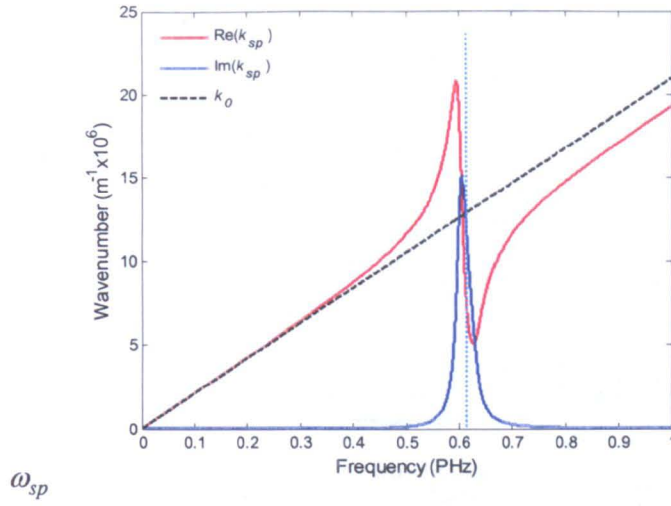
Figure 6.3. SP wavevector k_{sp} (blue: imaginary part, red: real part) for gold-air interface, free space wave vector k_o (black), and ω_{sp} is the surface plasma frequency.

Using the SP wavevector (k_{sp}) calculated values, the propagation length (δ_{sp}) and field confinement (L_{sp}) can be determined using equations (6.4) and (6.3) respectively for the gold-air interface. The propagation length values were normalised to the freespace wavelength (λ), such that $\delta_{spn} = \delta_{sp}/\lambda$. Similarly, the field confinement was also normalised to $L_{spn} = (\lambda - L_{sp})/\lambda$. The normalised values were plotted in logarithmic scale and are illustrated in Figure 6.4 below.

As shown in Figure 6.4a, the propagation length of the SP is greatly reduced at frequencies near the surface plasma frequency (ω_{sp}). Moreover, at frequencies just above 550 THz the SP propagates for less than one wavelength. At the same region of frequencies, and above the surface plasma frequency (ω_{sp}) the field confinement as shown in Figure 6.4b is at maximum all the way up to the ultraviolet region. However, at the lower frequency spectrum at infrared and terahertz frequencies, the threshold is reached and the SP field is greater than the freespace wavelength (λ), as the field confinement drops below zero. More importantly, at the THz region the SP wavevector (k_{sp}) is almost equal to the freespace wavevector (k_o) (Figure 6.3), thus the SP mode propagates along the gold-air interface behaving like a photon [2].

Propagation Length
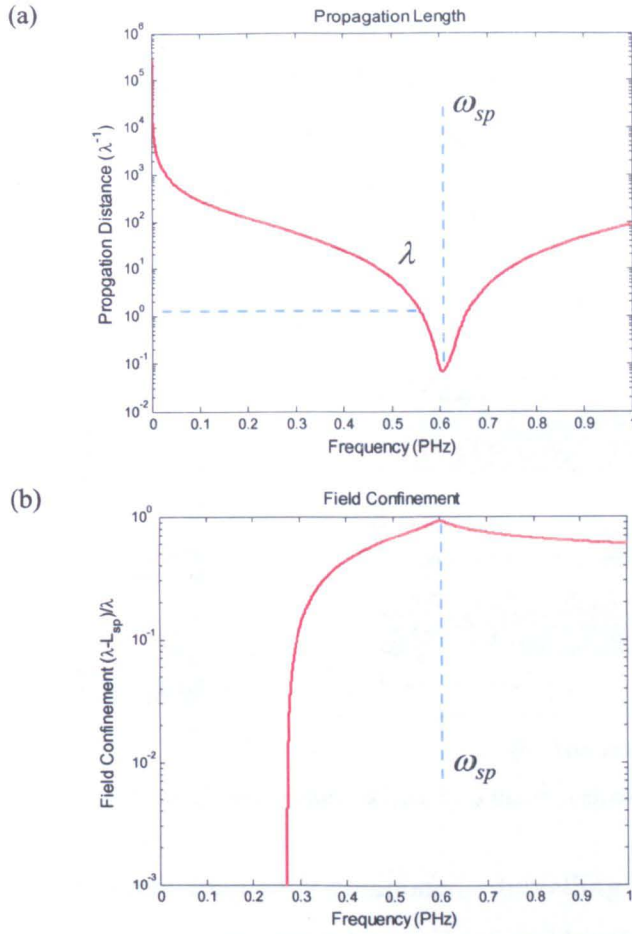
Field Confinement

Figure 6.4. (a) Normalised propagation length δ_{spn}, λ is the freespace wavelength, (b) normalised field confinement L_{spn}, and ω_{sp} is the surface plasma frequency.

6.3 Dispersion of Low-Loss Rectangular Waveguide

At terahertz frequencies most systems and applications utilise free-space propagation due to the lack of low-loss waveguides. However, the optimization of a metal-clad circular hollow waveguide by adjusting the polystyrene (PS) coating to achieve minimum loss has been reported [8]. Similarly, a hollow core rectangular waveguide for terahertz propagation is considered for measuring dispersion parameters [9, 10]. Similar to PS coating, Teflon has also been reported as a lower-loss dielectric medium at terahertz frequencies [11].

The structure illustrated in Figure 6.5, is composed of a thin gold clad (t_m) silicon waveguide with air core. The dimensions of the rectangular waveguide are set to 1 mm width, and the length (L) is set to 4.3 mm. The thickness of the thin gold cladding (t_m) was set to 1 µm. A thin layer of 1 µm of Teflon (t_d) with a

relative permittivity of $\varepsilon_r = 2.21$ and loss $\tan\delta$ 0.01 at 2.5 THz [12], was deposited in the inner surface of the cladding. Although the structure of the waveguide supports many modes, only the profile of the fundamental mode is considered, with low loss of 10.22 dB/m at 2.5 THz, for 1 μm of Teflon coating [11].

(a) Cross section view   (b) Top view
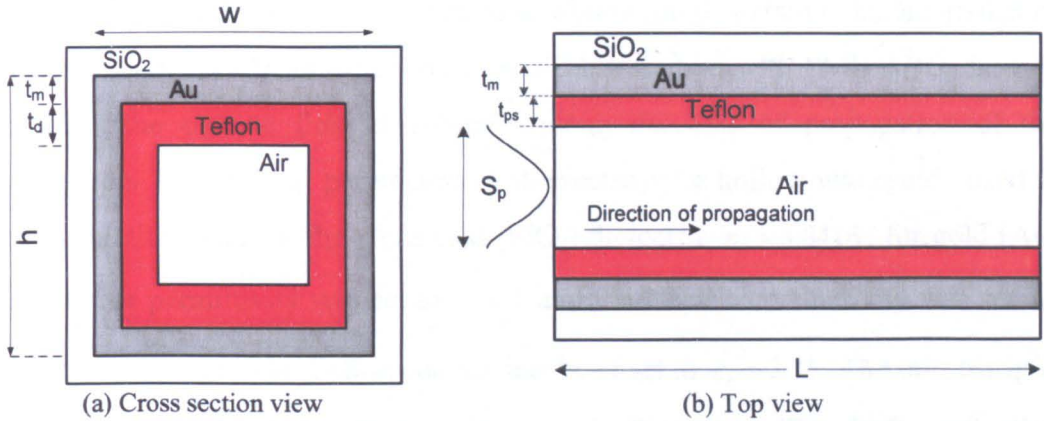
Figure 6.5. Plasmonic Waveguide structure, where S_p is the spot size of the input pulse.

Due to the different frequency components travelling in the medium, the material dispersion properties are also taken under consideration. In this case, the group velocity dispersion parameter [13] (GVD) is expressed as the temporal spread (ps) per unit propagation distance (km), per unit pulse spectral width (nm) and it is measured in ps/nm-km. The GVD parameter is associated with the second derivative of the propagation constant β [13] , thus:

$$D = \frac{2\pi c}{v_g^2 \lambda^2} \cdot \frac{dv_g}{d\omega} \tag{6.7}$$

where λ is the free space wavelength, v_g is the group velocity, and $dv_g/d\omega$ is the rate of change of the group velocity with respect to the angular frequency ω. Moreover, the group and phase velocities associated with planar surfaces waves are determined by

$$v_{ph} = \frac{c}{n'} \tag{6.8}$$

$$v_g = \left(\frac{d\omega}{dk}\right)_{\bar{k}} = \left(\frac{c}{n' + \omega\dfrac{dn'}{d\omega}}\right)_{\bar{k}} \qquad (6.9)$$

where $c = 1/\sqrt{\varepsilon_0\mu_0}$ is the speed of light in free space, n' is the real part of the effective index, and $\bar{k}$ is the angular frequency dependant wavevector [2].

The FDTD method can be used to obtain the dispersion characteristics of the waveguide. A 2D formulation of the FDTD method with PML ABCs is used to study the electric field distribution along the axis of propagation of the waveguide. The material parameters of the rectangular hollow waveguide used in the simulation were for the silica clad (SiO$_2$) dielectric $\varepsilon_r = 3.8416$, for gold (Au) the relative permittivity was set to $\varepsilon_r = 1$ and the electric conductivity was set to $\sigma = 7.34 \times 10^6$ S/m. The Teflon coating has been set to $\varepsilon_r = 2.21$. The microstrip is surrounded by 12 PML thick cells in all directions. The PML reflection coefficient of the finite-width PML medium at normal incidence was set to $R(0) = 1 \times 10^{-15}$, and the PML order was set to $n_{pml} = 2$ (parabolic). The parameters used for the FDTD grid were set to $\Delta x = 1$ μm, $\Delta y = 1$ μm, and a CFL factor of $S = 0.9$. The spot size of the Gaussian pulse or the sinusoidal wave that was used to source the FDTD grid was varied for waveguide analysis, which is described next. The source at any given simulation was centred along the y-axis of the rectangular waveguide with number of cells per wavelength $N_\lambda = 20$. The simulation was allowed to run for 6000 to 6500 time steps with $\Delta t = 2.1228 \times 10^{-3}$ ns. A Gaussian pulse was launched into the waveguide and the electric field at various points along the direction of propagation was monitored. During the FDTD time-stepping algorithm the maximum value of the electric field passing through the monitor was recorded in each time step. The electric field distribution for a spot size of 80% and 90% of the width of the rectangular waveguide is illustrated in Figure 6.6, sampled at 2.5 THz using DFT for waveguide width of 900 μm.

(a) 80% input pulse spot size.

(b) 90% input pulse spot size.
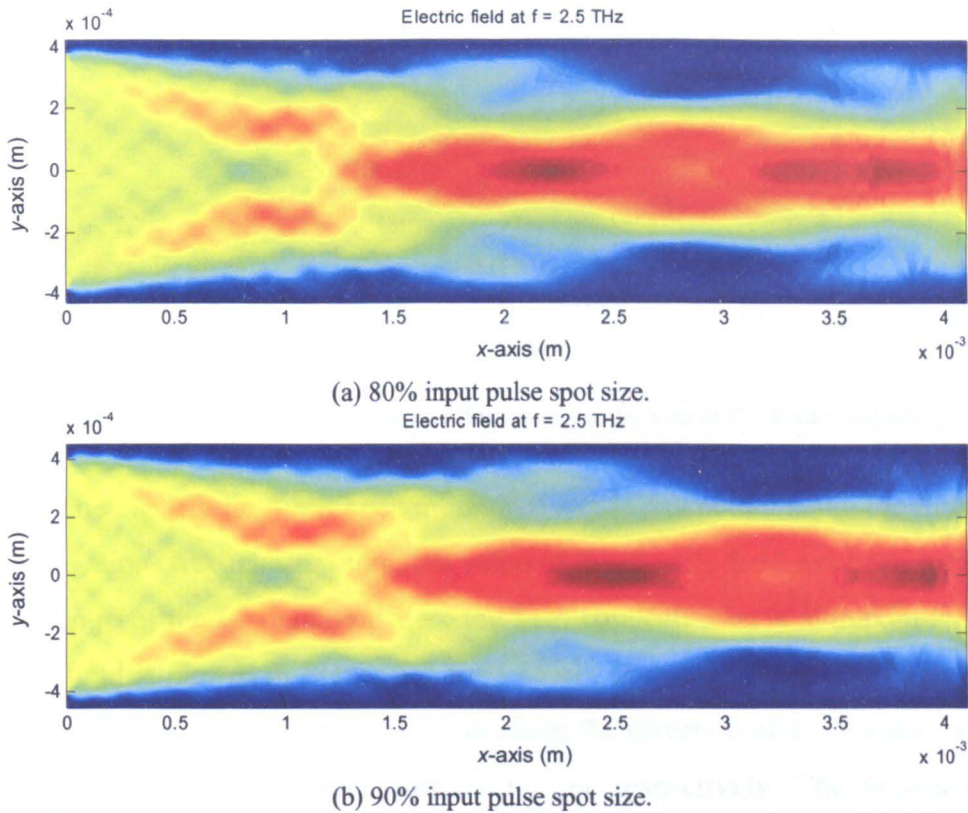
Figure 6.6. Electric field intensity distribution along the direction of propagation.

The waveguide supports a propagating fundamental mode along the centre of the waveguide with high field concentration, based on the electric field distribution. The propagating fundamental mode can be supported with small losses as the spot size of the input pulse is decreased to 90% and 80% of the width of the waveguide. After that threshold, as the spot size decreases there is a rapid decay in the electric field with significant losses and the plasmonic behaviour of the waveguide rapidly deteriorates. If the spot size remains relatively small compared to the width of the waveguide, then the waveguide behaves more like an MMI device if the pulse is allowed to propagate long enough, as illustrated in Figure 6.7. A set of simulations have been carried out by varying the waveguide width and length in order to establish the minimum length and width that the fundamental mode will propagate in the waveguide. In Figure 6.7, the electric field distribution for a spot size of 100 μm rapidly deteriorates over a relatively small length (2.15 mm) of the waveguide. The width of the waveguide was set to 1 mm and the electric field distribution was obtained using DFT at 2.5 THz.
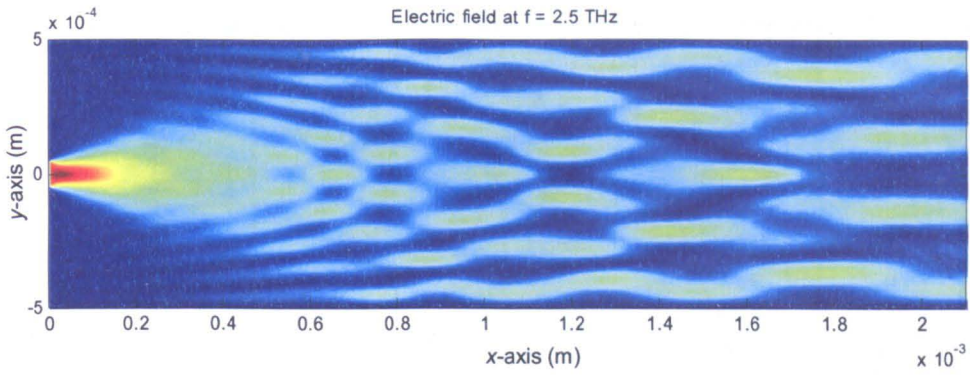
Figure 6.7. Electric field intensity distribution along the *x* direction with rapid decay.

The electric field has been monitored at various points along the direction of propagation. At each time step, the value of the electric field has been recorded at the centre of the waveguide, where the field concentration is at maximum. The electric field is plotted in Figure 6.8 for a source spot size (Sz) of 90% the width of the waveguide (W) was set at 0.9 mm along the direction of propagation at two different points, at $x = 2.0$ mm and $x = 3.0$ mm respectively. The difference in amplitude of the electric field with respect to the position of the monitor along the *x* direction of propagation represents the attenuation of the pulse, which is calculated to 0.012 dB/mm.
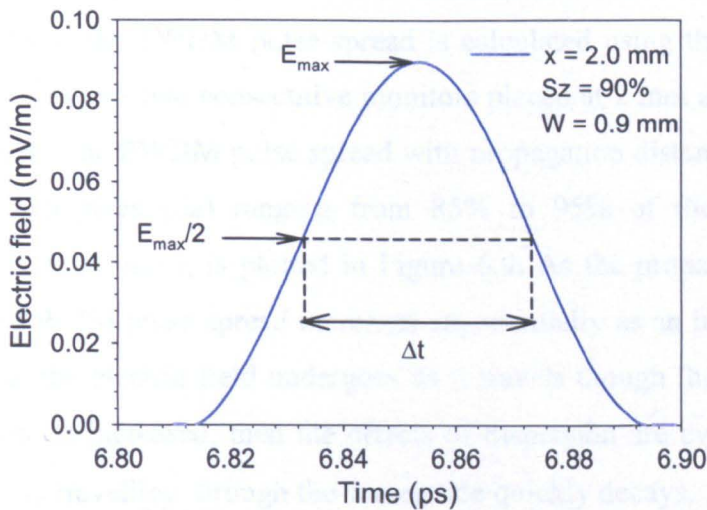
(a) Electric field monitored at $x = 2$ mm.
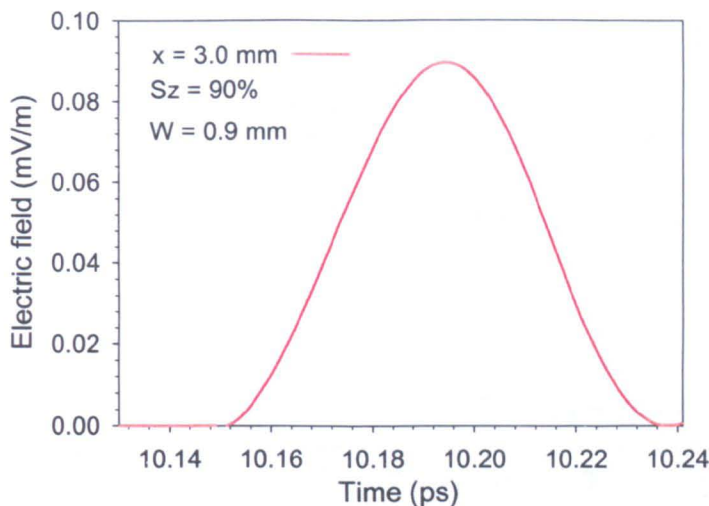
(b) Electric field monitored at $x = 0.3$ mm .

Figure 6.8. Electric field along the x direction of propagation.

The dispersion parameters of the plasmonic waveguide can be calculated based on the GVD equation given earlier. Given the time-domain values of the electric fields monitored along the direction of propagation in the middle of the waveguide, where the electric field concentration is observed, the full-width half-maximum (FWHM) pulse width in ps for each of the monitors can be determined. Based on Figure 6.8(a), the maximum value of the electric field is determined (E_{max}) at the monitor. At half-maximum ($E_{max}/2$), the pulse spread (Δt) is determined. Thus, the FWHM pulse spread is calculated using the difference of FWHM pulse between two consecutive monitors placed at 2 mm and 3 mm away from the source. The FWHM pulse spread with propagation distance for different input pulse spot sizes (Sz) ranging from 85% to 95% of the width of the waveguide ($W = 0.95$ mm), is plotted in Figure 6.9. As the propagation distance increases the FWHM pulse spread increases exponentially as an indication of the dispersion that the electric field undergoes as it travels though the waveguide. If the pulse width is increased, then the effects of dispersion are even greater, and the electric field travelling through the waveguide quickly decays.
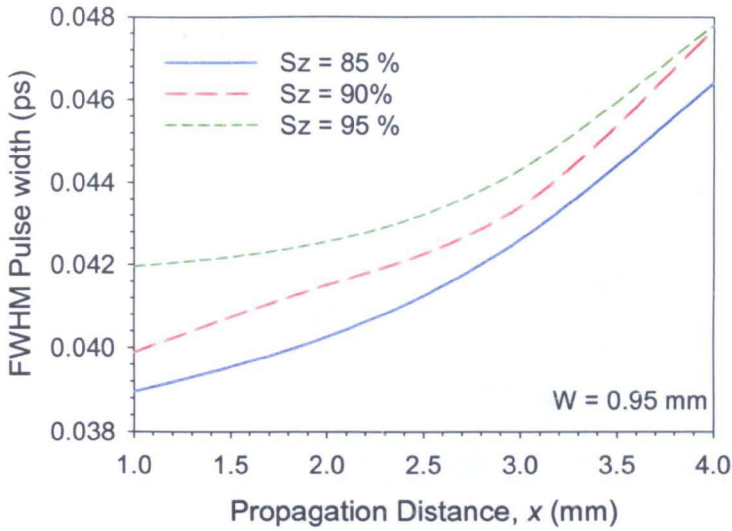
Figure 6.9. Full-wave half-maximum pulse spread with propagation distance for different input pulse spot size.

The FWHM pulse spread is plotted in Figure 6.10 for different widths (W) of the waveguide and for a spot size (Sz) of 90% the width of the waveguide. As the waveguide width decreases from 0.85 mm to 0.7 mm, the FWHM pulse spread increases. Whereas the plasmonic waveguide behaviour in terms of the FWHM pulse spread changes in the case of 0.9 mm and 0.95 mm where the FWHM pulse spread significantly decreases compared to the other values, indicating that for these values the waveguide dispersion is significantly lower. At 2.15 mm the FWHM pulse spread value for the 0.80 mm and 0.70 mm case is the same. Similarly, at 2.2 mm the FWHM pulse spread value for the 0.95 mm, 0.9 mm, and 0.85 mm case is the same, however, as the propagation distance increases the effects of dispersion for the 0.70 mm, 0.80 mm, and 0.85 mm case are significantly greater, compared to the 0.90 mm and 0.95 mm case.
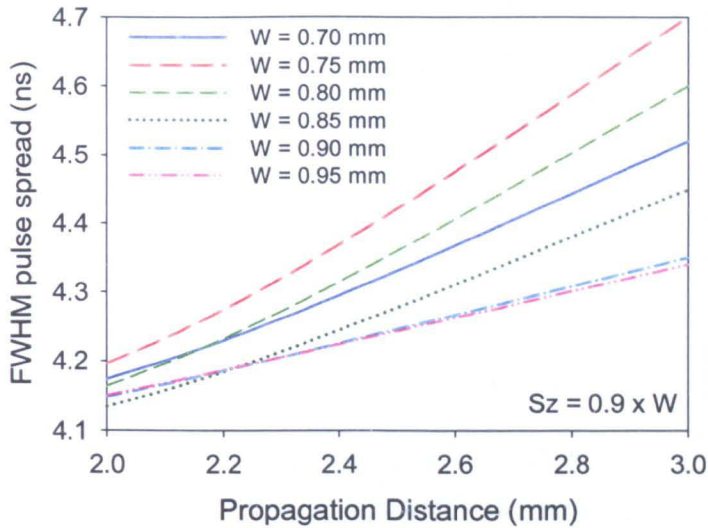
Figure 6.10. Full-wave half-maximum pulse spread with propagation distance for different waveguide width at 90% input pulse spot size.

The plasmonic waveguide dispersion per unit length (ps/mm) is illustrated in Figure 6.11 for various widths of the waveguide and for spot sizes of 90% and 95% of the width. As the waveguide width is decreased the dispersion per unit length is increased reaching a maximum for a waveguide width of 0.75 mm and a spot size of 95% of the width of the waveguide. Similarly, the waveguide dispersion is reaching a maximum for a waveguide width of 0.76 mm for a spot size of 90% of the width. As the width is decreased further down to 0.7 mm the waveguide dispersion is also decreasing but at a much lower rate, compared with the minimum waveguide dispersion values obtained for a 0.9 mm waveguide width and spot size 90% and 95% of the width.
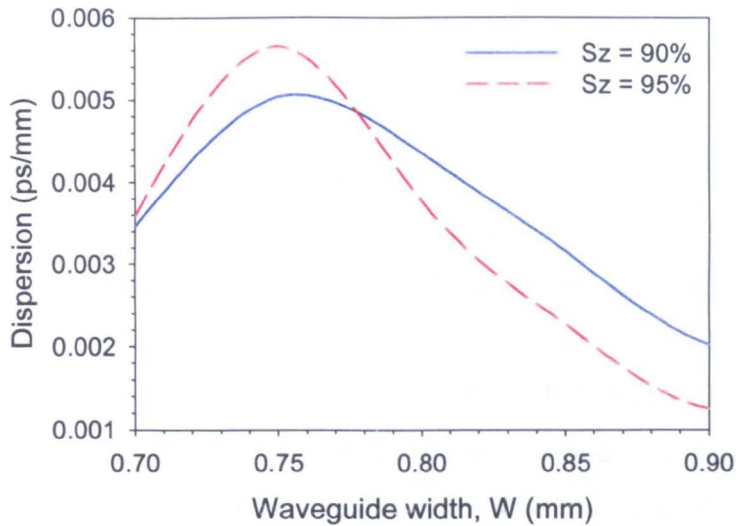
Figure 6.11. Dispersion per unit length with propagation distance for different input pulse spot size.

6.4 Surface Plasmon Analysis

It has been reported that surface plasmon analysis to determine the terahertz optical properties of a waveguide could be achieved by employing a scattering technique which involves the placement of sharp apertures (coupling blade) just above the conducting surface [14]. The technique could be used both experimentally and in numerical simulations, where a Gaussian pulse is launched near the surface of the plasmonic waveguide. An aperture is placed near the source and just above the conducting surface. The aperture scatters the Gaussian pulse over the surface of the plasmonic waveguide and into free space. A second scattering aperture (a coupling blade) is placed at a distance l, after the pulse has propagated along the waveguide, and the surface plasmon is coupled back in to free space. A monitor is placed after the second aperture just above the conducting surface and the electric field is sampled over time. This geometry ensures that any electric or magnetic fields propagating in parallel will be reflected from the coupling blade and only the surface plasmon propagating along the surface of the waveguide will be sampled.

Given the geometry described above, the FDTD method and the Drude model could be used to simulate such a geometry using the plasmonic waveguide structure described in Section 6.3 in order to obtain time-domain numerical results

for the propagation of surface plasmons along the surface of the waveguide. Using a cross-section of the plasmonic waveguide and in this case polystyrene coating (PS) instead of Teflon as a dielectric for coating the conducting surface of the waveguide, numerical analysis is performed. In this simulation, the geometry of the waveguide is changed as the metal thickness (t_m) is taken as 300 μm, and the length of the waveguide to 5.6 mm. The left steel blade was placed at 100 μm above the inner surface of the waveguide and 600 μm away from the source. The right blade was placed 4.3 mm away from the first blade and 100 μm above the inner surface of the waveguide. In order to obtain the time-domain values for the electric field surface plasmon propagation, a monitor was placed 400 μm away from the second aperture and 600 μm above the inner surface of the waveguide. The above geometry is illustrated in Figure 6.12.
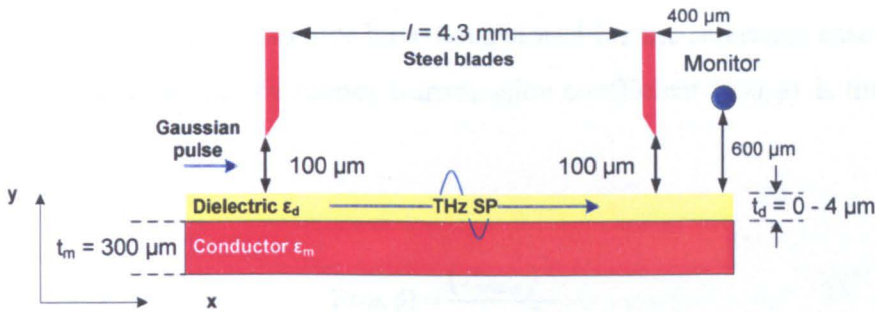
Figure 6.12. Geometry of plasmonic waveguide cross-section for surface plasmon analysis.

The 2D FDTD method has been used with the Drude model to simulate the geometry presented in Figure 6.12. The values of the Drude model parameters for gold (Au) were selected as follows: the relative permittivity was set to $\varepsilon_r = 9.07$, the Drude plasma frequency was set to $\omega_{pD} = 1.2 \times 10^6$ rad/s, the Drude damping coefficient was set to $\Gamma_D = 1.2 \times 10^{14}$ rad/s, and the electric conductivity was set to $\sigma = 7.34 \times 10^6$ S/m [4, 15]. The polystyrene (PS) coating has been set to $\varepsilon_r = 2.4964$ [16] and the silica clad (SiO$_2$) dielectric has been modelled using PML ABCs. The waveguide is surrounded by 15 PML thick cells in all directions. The PML reflection coefficient of the finite-width PML medium at normal incidence was set to $R(0) = 1 \times 10^{-15}$, and the PML order was set to $n_{pml} = 2$ (parabolic). The parameters used for the FDTD grid were set to $\Delta x = 1$ μm,

$\Delta y = 1 \ \mu m$, and a CFL factor of $S = 0.9$. A Gaussian pulse was used to source the FDTD grid with number of cells per wavelength $n_{c\lambda} = 20$. The simulation was allowed to run for 11500 time steps with $\Delta t = 1.6678 \times 10^{-3}$ ns. In order to obtain the time-domain parameters and the transmission properties of the plasmonic waveguide during the simulation, a monitor was placed after the right aperture to sample the electric field as the surface plasmon propagates along the interface of the waveguide and it is coupled back into free space after reaching the right aperture.

The transmission properties of the plasmonic waveguide were calculated based on the reference case. The reference case is the simulation of the waveguide without any PS coating ($t_d = 0$). The simulation was repeated for a thickness of 1 μm, 2 μm, and 4 μm of PS coating. In every simulation the DFT of the sampled electric field values at the monitor have been stored for the reference case and the case with PS coating. The frequency transmission coefficient $T(\omega,\phi)$ is thus given by [17]

$$T(\omega,\phi) = \frac{\left(A_{trans}\right)^2}{\left(A_{ref}\right)^2} \tag{6.10}$$

where A_{ref} is the amplitude of the DFT of the electric field for the reference case, and A_{trans} for the transmission case (with PS coating) respectively. Given that l is the propagation length between the two apertures, the change in wavenumber corresponds to

$$\Delta k = \frac{\Delta\phi}{l} \tag{6.11}$$

where $\Delta\phi$ is the change in phase across the surface of the waveguide, which is obtained by normalising the transmission spectra against the reference case and extracting the phase as

$$T(\omega,\phi) = A(\omega) \cdot e^{j\phi(\omega)} \qquad (6.12)$$

It is also possible to calculate the effective refractive index of the waveguide using the phase shift between the reference case and the sample case with PS coating [17] given by

$$n_{eff} = n_0 + \frac{\Delta\phi \cdot c}{\omega \cdot l} \qquad (6.13)$$

where n_0 is the index of the reference medium (air in this case, $n_0 = 1$) and l is the distance between the two apertures.

The FDTD simulation results have used to obtain the transmission properties of the plasmonic waveguide based on the surface plasmon analysis theory described above. In Figure 6.13, the electric field distribution for a frequency of 2.5 THz is presented. In the figure, as the Gaussian pulse propagates along the surface of the waveguide and in free space, it reaches the second aperture where it is reflected (ripple-like pattern). The surface plasmon propagates along the inner surface of the waveguide, under the second aperture, and coupled in free space where the monitor is placed.
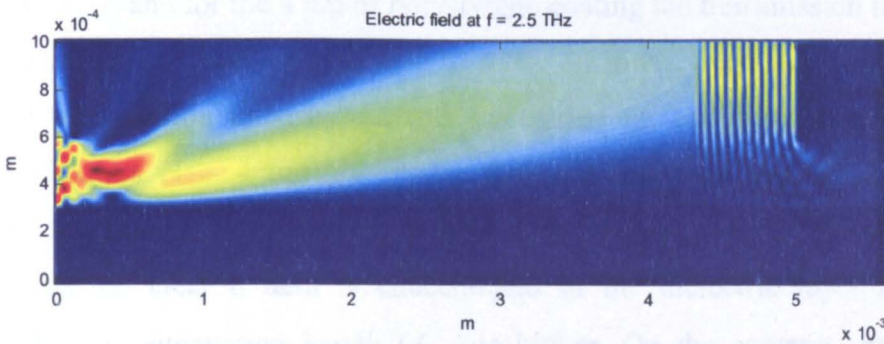
Figure 6.13. Electric field distribution of the plasmonic waveguide cross-section for surface plasmon analysis.

The sampled electric field magnitude over a frequency range of $0.2 - 3$ THz for the reference case ($t_d = 0$) is shown in Figure 6.14. The surface plasmon propagating beyond the second aperture appears to have maximum magnitude over 1.6 THz.
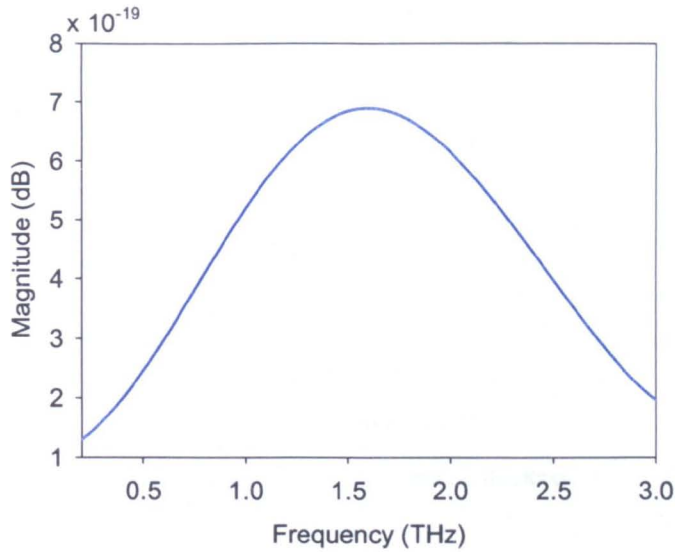
Figure 6.14. Electric field magnitude of the plasmonic waveguide cross-section for surface plasmon analysis for the reference case.

The transmission intensity of the various thicknesses of polystyrene coating normalised against the reference case (without coating) is presented in Figure 6.15. The transmission intensity ($T(\omega)$) is changing rapidly as the frequency approaches 2.5 THz. The transmission intensity reaches a minimum value at ~2.8 THz. Specifically for the 1 μm of polystyrene coating the transmission intensity reaches a minimum value of 0.9482 at 2.87 THz, for the 2 μm of polystyrene coating the transmission intensity reaches a minimum value of 0.9 at 2.85 THz, and for the 4 μm of polystyrene coating the transmission intensity reached a minimum value of 0.82 at 2.83 THz. At lower frequencies (0.5 – 1.5 THz) the transmission intensity for the waveguide for the given range of PS coating thickness (1 – 4 μm) is greater than the reference case (without PS coating), indicating that at these frequencies with the presence of PS coating the surface plasmon electric field is concentrated in the dielectric layer and the surface plasmon attenuation length (L_{sp}) is higher. On the contrary, at higher frequencies (2.8 THz), the transmission intensity for the given range of PS coating is significantly less than the reference, indicating that the surface plasmon is attenuated as it propagates beyond the second aperture, thus causing a minimum in the transmission intensity.
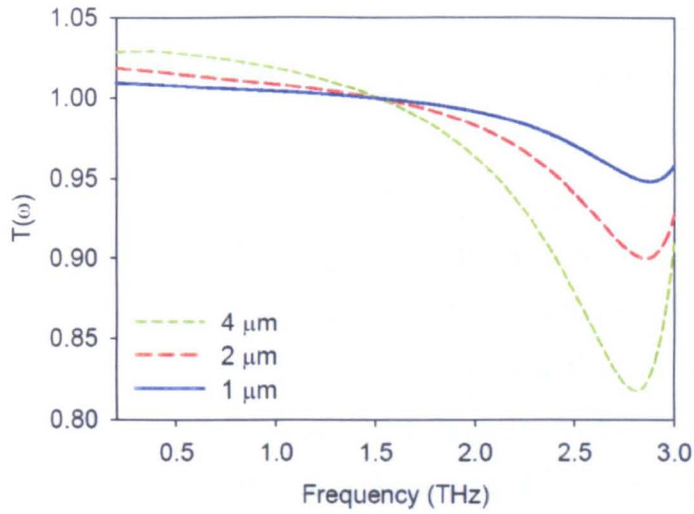
Figure 6.15. Transmission intensity ($T(\omega)$) for various thicknesses of polystyrene coating.

In terms of the simulated change in dispersion of the surface plasmon induced by the various thicknesses of polystyrene coating, at 0.2 – 3 THz frequency range the relative permittivity of gold (Au) is very large and predominantly imaginary based on the Drude model. At 1.6 THz the permittivity of gold is calculated as $\varepsilon_{rD} = -1.367 \times 10^4 + j1.57 \times 10^5$, so that the surface plasmon mode is weakly bound on the surface [14]. In Figure 6.16, the change in wavenumber (Δk) is illustrated for a polystyrene thickness of 1 μm, 2 μm, and 4 μm. Based on the results of Figure 6.16, the dispersion shift rapidly increases as the excitation frequency reaches 2.5 THz and the phase shifts are larger as the thickness of the polystyrene coating increases.
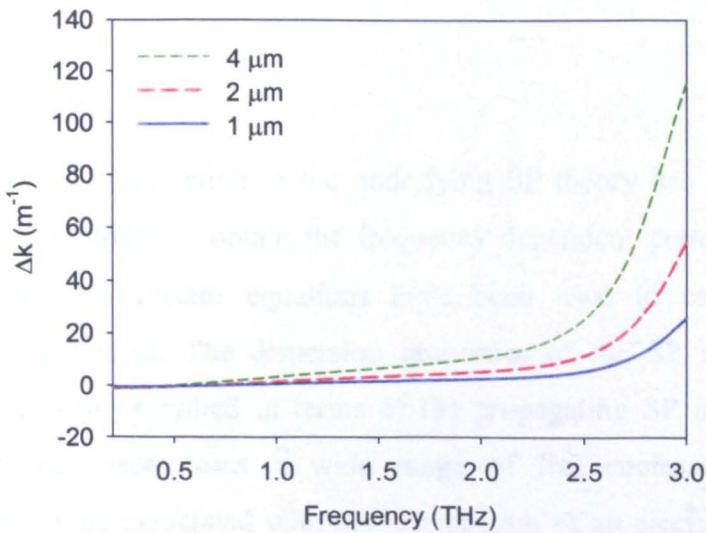
Figure 6.16. Change in dispersion (Δk) for various thicknesses of polystyrene coating.

Furthermore, using the phase shift between the reference and sample numerical results obtained using the FDTD method, the effective refractive index (n_{eff}) can be calculated for the various thicknesses of polystyrene coating using equation (6.13). The real part of the effective index for the three cases of polystyrene coating is illustrated in Figure 6.17 for a frequency range of 0.2 – 3 THz. Given the results presented in Figure 6.17, the effective index for the various thicknesses of polystyrene coating appears to be less than air ($n_0 = 1$) for a frequency range less than 0.5 THz. As the frequency reaches 2.5 THz, the real part of the effective index for the three cases of polystyrene coating begins to increase rapidly.
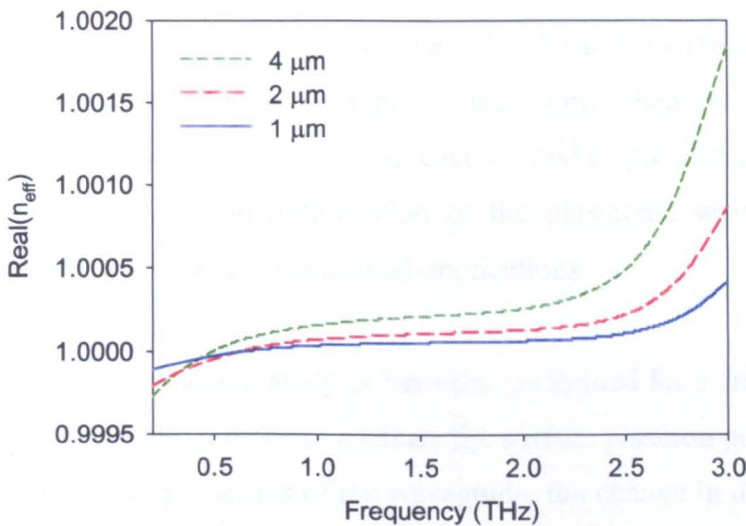
Figure 6.17. Real part of the effective index (n_{eff}) for various thicknesses of polystyrene coating.

6.5 Summary

In this chapter an introduction to the underlying SP theory has been presented. Using the Drude model to obtain the frequency dependent permittivity of gold (Au), the basic wavevector equations have been used to calculate the SP characteristic properties. The dispersion properties of the SP for the gold-air interface have been described in terms of the propagating SP modes, the field confinement, and decay over a wide range of frequencies. Moreover, the dispersion equations associated with the propagation of an electromagnetic field

inside a waveguide at terahertz frequencies have been used to obtain the attenuation and dispersion characteristics using the FDTD method.

Furthermore, a low-loss hollow-core rectangular plasmonic waveguide structure has been presented with Teflon dielectric coating for terahertz propagation. The plasmonic behaviour of the waveguide is analyzed using the full vectorial FEM and the modal properties of the waveguide with emphasis on the surface plasmon mode (SPM). Moreover, the FDTD method has been used as a numerical analysis tool for evaluating the electric field distribution and determining the dispersion characteristics of the plasmonic waveguide.

The parameters that have been taken into consideration are the width of the waveguide, and the spot size of the source. It has been shown that the structure of the waveguide is at optimum (minimum dispersion) when the width of the waveguide is 0.9 mm with 1 μm of Teflon coating, and a spot size of 95% of the width of the waveguide. The optimisation of the plasmonic waveguide is an important feature for terahertz wave guided-applications.

Finally surface plasmon analysis has been performed for a cross section of the plasmonic waveguide in order to evaluate the surface plasmon parameters and obtain the transmission properties of the waveguide, the change in dispersion and the effective index of the structure.

In the next chapter, concluding remarks and an evaluation regarding the outcomes of this thesis are presented. Finally, an outline of future research that may be carried out is also provided, regarding applications of numerical analysis of structures at terahertz frequencies.

References

[1]   H. Raether, *Surface plasmons on smooth and rough surfaces and on gratings*. Berlin ; New York: Springer-Verlag, 1988.

[2]   D. Sarid and W. A. Challener, *Modern introduction to surface plasmons : theory, Mathematica modeling, and applications*. Cambridge ; New York: Cambridge University Press, 2010.

[3]   J. M. Pitarke, V. M. Silkin, E. V. Chulkov, and P. M. Echenique, "Theory of surface plasmons and surface-plasmon polaritons," *Reports on Progress in Physics*, vol. 70, p. 1, 2007.

[4]   A. Vial, A.-S. Grimault, D. Macias, D. Barchiesi, and M. L. de la Chapelle, "Improved analytical fit of gold dispersion: Application to the modeling of extinction spectra with a finite-difference time-domain method," *Physical Review B*, vol. 71, p. 085416, 2005.

[5]   P. B. Johnson and R. W. Christy, "Optical Constants of the Noble Metals," *Physical Review B*, vol. 6, pp. 4370-4379, 1972.

[6]   E. D. Palik and G. Ghosh, *Handbook of optical constants of solids*. San Diego: Academic Press, 1998.

[7]   A. Vial, "Implementation of the critical points model in the recursive convolution method for modelling dispersive media with the finite-difference time domain method," *Optics A: Pure and Applied Optics, Journal of*, vol. 9, p. 745, 2007.

[8]   C. Themistos, B. M. A. Rahman, M. Rajarajan, K. T. V. Grattan, B. Bowden, and J. A. Harrington, "Characterization of Silver/Polystyrene (PS)-Coated Hollow Glass Waveguides at THz Frequency," *Lightwave Technology, Journal of*, vol. 25, pp. 2456-2462, 2007.

[9]   C. Markides, C. Viphavakit, C. Themistos, M. Komodromos, K. Kalli, A. Quadir, and B. M. A. Rahman, "Dispersion characteristics of plasmonic waveguides for THz waves," in *Proc. SPIE Optics and Optoelectronics*, Prague, 2013.

[10]   B. M. A. Rahman, C. Markides, M. Uthman, A. Quadir, N. Kejalakshmy, and C. Themistos, "Characterization of low-loss waveguides and devices for terahertz radiation," *Optical Engineering*, vol. 53, pp. 031210-031210, 2014.

[11]   B. M. A. Rahman, A. Quadir, H. Tanvir, and K. T. V. Grattan, "Characterization of Plasmonic Modes in a Low-Loss Dielectric-Coated Hollow Core Rectangular Waveguide at Terahertz Frequency," *Photonics Journal, IEEE*, vol. 3, pp. 1054-1066, 2011.

[12]   Y. S. Jin, G. J. Kim, and S. G. Jeon, "THz spectroscopy of polymer materials," in *Infrared Millimeter Waves and 14th International Conference on Teraherz Electronics, 2006. IRMMW-THz 2006. Joint 31st International Conference on*, pp. 475-475, Shanghai, 2006.

[13]   R. Ramaswami, K. Sivarajan, and G. Sasaki, *Optical Networks: A Practical Perspective*, 3rd Edition ed.: Morgan Kaufmann, 2009.

[14]   T. H. Isaac, W. L. Barnes, and E. Hendry, "Determining the terahertz optical properties of subwavelength films using semiconductor surface plasmons," *Applied Physics Letters,* vol. 93, pp. 241115-3, 2008.

[15]   E. D. Palik, *Handbook of optical constants of solids.* Orlando: Academic Press, 1985.

[16]   P. Dean, M. U. Shaukat, S. P. Khanna, S. Chakraborty, M. Lachab, A. Burnett, G. Davies, and E. H. Linfield, "Absorption-sensitive diffuse reflection imaging of concealed powders using a terahertz quantum cascade laser," *Optics Express,* vol. 16, pp. 5997-6007, 2008.

[17]   T. H. Isaac, J. Gomez Rivas, J. R. Sambles, W. L. Barnes, and E. Hendry, "Surface plasmon mediated transmission of subwavelength slits at THz frequencies," *Physical Review B,* vol. 77, p. 113411, 2008.

Chapter 7

Conclusions

7.1 Conclusions and Evaluations

A remarkable expansion of technology to a wide range of components, instruments and applications, carried out in the terahertz portion of the electromagnetic spectrum (loosely defined as the frequencies from 0.3 THz to 10 THz), has been witnesses in recent years. These advances in terahertz applications depend on the transmission properties of terahertz sources, the penetration of terahertz radiation through dielectric materials and the high sensitivity of terahertz sensors. The unique properties of terahertz radiation and spectroscopic sensing have lead to new fields of interest and significant advances in astrophysics and atmospheric science, biological and medical sciences, security screening and illicit material detection, non-destructive evaluation (NDE), communications technology, and ultrafast spectroscopy. Terahertz radiation exhibits good balance between good resolution and penetration as well as good selectivity (fingerprint) in many materials.

At present the techniques for generating terahertz radiation are based on optically pumped lasers (OPTL), time-domain system sources, backward wave oscillators, direct multiplied sources, and frequency mixing. The introduction of quantum-cascade lasers (QCL) has proved more successful for terahertz generation and recently new techniques have revealed that that the performance of

terahertz QCLs can be greatly improved by the use of spoof surface plasmon (SP) for active photonic devices.

Moreover significant research is carried out on the development of terahertz waveguides in order to expand on current applications. Due to the absorption of THz radiation of dielectrics and metals, an outstanding problem has been the development of efficient waveguide structures with minimal transmission loss and minimal dispersion. Several waveguide designs have been proposed, including photonic crystal fibres, cylindrical hollow waveguides with dielectric coating, on-chip terahertz circuits, metallic slit, and microstrip circuits [1-4].

The Finite Difference Time Domain method (FDTD) has been regarded as a versatile, useful and widely used electromagnetic tool. The performance of the FDTD is embellished with the development of new algorithms to cope with a wide variety of EM problems as well as ABCs. Specifically, the FDTD method has been presented from first principles with the application of the finite-difference method to Maxwell's curl equations, in order to obtain the discrete spatially and time-varying equations.

Moreover, the FDTD method formulation has been implemented using MATLAB^{TM} in 1D, 2D and 3D. The FDTD implementations have been benchmarked using examples from the literature. A wide range of applications and results have been presented, where the FDTD method has been used as a numerical analysis tool. The range of formulations consisted 1D, 2D, and 3D formulations, extending the FDTD implementation using PML, and CPML absorbing boundary conditions (ABCs) for both 2D, and 3D formulations. Also the limitations of the FDTD method have been indicated.

Furthermore, it has been illustrated how the FDTD method can be used to model, and obtain results for a wide range of problems, for example modelling 2D propagation of electromagnetic fields, lumped elements in 3D formulations with ABCs, and obtaining scattering parameters. Also, other formulations illustrated in

this thesis the application of the FDTD method in the Total Field/Scattered Field (TF/SF) in 1D, 2D, and 3D grids.

Finally, the FDTD method has been applied to obtain the Poynting vector in 2D as well as obtaining dispersion parameters for 2D, and 3D grids, and the Auxiliary Differential Equation (ADE) has been presented with the implementation of the Drude model for the 2D and the 3D FDTD method.

The FDTD method has been used for the rigorous analysis of a microstrip at terahertz frequencies. The microstrip was simulated using polystyrene (PS) coating that has proved to exhibit low-loss at terahertz frequencies. The PS coating was able to produce a low-loss microstrip at terahertz frequencies with the deposition of a very-thin film. With the deposition of PS coating there was some shift in the insertion-loss frequency of the microstrip, whereas the insertion loss was also decreased. When the deposition of PS coating was increased the insertion loss also increased. Similarly, with the deposition of PS coating over a limit, the frequency shift became saturated since the electric field is mostly confined within the PS coating layer.

The Drude model FDTD formulation was used to obtain results for the dispersion parameters of the microstrip. The simulation results from the Drude model implementation were to obtain dispersion parameters, such as the effective permittivity, attenuation constant and characteristic impedance of the microstrip. In addition, the Drude model implementation was used to model the microstrip structure with and without one filter stub over a range of PS coating thickness. The characteristic impedance, attenuation and effective permittivity were obtained using the Drude model, and were in good agreement with previously obtained results.

In this thesis, the 2D FDTD method has been applied to examine and study the propagation, attenuation and losses both in time and space of a low-loss MMI coupler at THz wavelengths. The aim was the development of an MMI device that would exhibit low-loss at THz frequencies. This work has been applied in the design of an MMI device with minimum loss and optimal configuration for first

higher order modes. A suitable choice of a low-loss dielectric coating, such as polystyrene (PS) coating, gold (Au) metal cladding, its thickness and geometry can yield minimum loss. The characteristics of the MMI coupler have been obtained by simulating the MMI device using both Gaussian and sinusoidal sources, and monitoring the output of the coupler in order to obtain dispersion parameter results. The proposed MMI design shows significantly low loss when excited with a Gaussian-shaped beam.

Next, in this thesis the underlying theory of surface plasmons (SP) is presented. Significant research has been carried out in the field of SP with numerous applications. Here, a low-loss plasmonic waveguide for terahertz frequencies has been studied in order to obtain dispersion parameters. In this case, the FDTD method has been used as a numerical analysis tool for evaluating the electric field distribution and determining the dispersion characteristics of the plasmonic waveguide. The proposed waveguide is a low-loss Teflon-coated hollow-core rectangular waveguide that is able to support Surface Plasmon Modes (SPMs). The waveguide structural parameters (width, height, and length) have been taken under consideration in order to optimise the waveguide for terahertz guiding applications.

7.2 Future Research

Throughout this thesis it is evident that research at terahertz frequencies will be advancing at an increasing rate, with new applications for terahertz sources, sensors, and waveguiding. In this case, there will be a constant demand for low-loss waveguides at this frequency spectrum.

Moreover, the FDTD method has emerged as a robust and versatile numerical simulation tool that can be used to accurately simulate a number of elements, structures, and sources, taking into account the frequency dependent dispersion properties of materials. For future work, the current FDTD formulation can be extended to take into account other dispersion properties of materials, such as the critical point model of dispersion, which aims to highlight the influence of localized surface plasmon resonances.

Furthermore, as the FDTD method is computationally expensive and access to cloud computing is more accessible now than in the past, a parallel FDTD method implementation could take advantage of the computational resources available. There have been numerous reports on parallel FDTD method algorithms, and the implementations extend not only towards taking advantage of the multi-core CPU architectures, but also extending the implementation in the GPU for considerable computational speed.

In addition, as there is an increased interest in research in SP and surface plasmon polaritons (SPP) at terahertz frequencies, the existing FDTD formulations could be extended to model a wider range of metal-based structures, as well as integrating the Lorentz, and the Debye model for taking into account the frequency behaviour of semiconductors and dielectrics. Finally, the FDTD method could be used for the analysis and modelling of plasmonic nano-antennas [5], in terms of obtaining transmission spectra.

References

[1]   J. Cunningham, C. Wood, A. G. Davies, C. K. Tiang, P. Tosch, D. A. Evans, E. H. Linfield, I. C. Hunter, and M. Missous, "Multiple-frequency terahertz pulsed sensing of dielectric films," *Applied Physics Letters,* vol. 88, pp. 071112-3, 2006.

[2]   O. Mitrofanov, R. James, F. A. Fernandez, T. K. Mavrogordatos, and J. A. Harrington, "Reducing Transmission Losses in Hollow THz Waveguides," *Terahertz Science and Technology, IEEE Transactions on,* vol. 1, pp. 124-132, 2011.

[3]   B. M. A. Rahman, A. Quadir, H. Tanvir, and K. T. V. Grattan, "Characterization of Plasmonic Modes in a Low-Loss Dielectric-Coated Hollow Core Rectangular Waveguide at Terahertz Frequency," *Photonics Journal, IEEE,* vol. 3, pp. 1054-1066, 2011.

[4]   L. B. Soldano and E. C. M. Pennings, "Optical multi-mode interference devices based on self-imaging: principles and applications," *Lightwave Technology, Journal of,* vol. 13, pp. 615-627, 1995.

[5]   N. Berkovitch, P. Ginzburg, and M. Orenstein, "Nano-plasmonic antennas in the near infrared regime," *Journal of Physics: Condensed Matter,* vol. 24, p. 073202, 2012.

Appendix A

Numerical Phase Velocity

Solving the dispersion relation directly for $\tilde{k}$ propagation along the major axes of the grid at $\phi = 0°, 90°, 180°, 270°$:

$$\frac{1}{S^2} \sin^2\left(\frac{\pi S}{N_\lambda}\right) = \sin^2\left(\frac{\Delta \cdot \tilde{k} \cos\phi}{2}\right) + \sin^2\left(\frac{\Delta \cdot \tilde{k} \sin\phi}{2}\right) \qquad (A.1)$$

For $\phi = 0°$, equation (A.1) simplifies to

$$\frac{1}{S^2} \sin^2\left(\frac{\pi S}{N_\lambda}\right) = \sin^2\left(\frac{\Delta \cdot \tilde{k}}{2}\right)$$

$$\frac{1}{S} \sin\left(\frac{\pi S}{N_\lambda}\right) = \sin\left(\frac{\Delta \cdot \tilde{k}}{2}\right) \qquad (A.2)$$

Equivalently equation (A.2) becomes

$$\tilde{k} = \frac{2}{\Delta} \sin^{-1}\left[\frac{1}{S} \sin\left(\frac{\pi S}{N_\lambda}\right)\right] \qquad (A.3)$$

Substituting equation (A.3) into the numerical phase velocity given by

$$\tilde{v}_p = \frac{\omega}{\tilde{k}} = \frac{2\pi f}{\frac{2}{\Delta} \sin^{-1}\left[\frac{1}{S} \sin\left(\frac{\pi S}{N_\lambda}\right)\right]} = \frac{2\pi(c/\lambda)}{\frac{2}{\Delta} \sin^{-1}\left[\frac{1}{S} \sin\left(\frac{\pi S}{N_\lambda}\right)\right]} \qquad (A.4)$$

If $N_\lambda = \lambda/\Delta$, then

$$\tilde{v}_p = \cfrac{2\pi(c/\lambda)}{\cfrac{2}{\Delta}\sin^{-1}\left[\cfrac{1}{S}\sin\left(\cfrac{\pi S}{N_\lambda}\right)\right]} = \cfrac{\pi c}{\cfrac{\lambda}{\Delta}\sin^{-1}\left[\cfrac{1}{S}\sin\left(\cfrac{\pi S}{N_\lambda}\right)\right]}$$

$$= \cfrac{\pi}{N_\lambda \sin^{-1}\left[\cfrac{1}{S}\sin\left(\cfrac{\pi S}{N_\lambda}\right)\right]}c \qquad (A.5)$$

The dispersion relation (A.1) can also be solved for $\tilde{k}$ for a wave propagating along the grid diagonals at $\phi = 45°, 135°, 225°, 315°$ or $2/\sqrt{2}$ yielding

$$\tilde{k} = \frac{\sqrt{2}}{\Delta}\sin^{-1}\left[\frac{1}{S\sqrt{2}}\sin\left(\frac{\pi S}{N_\lambda}\right)\right] \qquad (A.6)$$

The corresponding phase velocity for propagation along the grid diagonals becomes

$$\tilde{v}_p = \cfrac{\pi}{N_\lambda \sqrt{2}\sin^{-1}\left[\cfrac{1}{S\sqrt{2}}\sin\left(\cfrac{\pi S}{N_\lambda}\right)\right]}c \qquad (A.7)$$

Appendix B

Numerical Wave Propagation Along the Principal Axis

The following analysis investigates the possibility of complex-valued numerical wavenumbers existing for the FDTD solution of Maxwell's equations. Consider the numerical wave propagation along the major axes of a Yee space grid:

$$\tilde{k} = \frac{2}{\Delta} \sin^{-1}\left[\frac{1}{S}\sin\left(\frac{\pi S}{N_\lambda}\right)\right] \equiv \frac{2}{\Delta}\sin^{-1}(\zeta) \qquad (B.1)$$

Where

$$\zeta = \frac{1}{S}\sin\left(\frac{\pi S}{N_\lambda}\right) \qquad (B.2)$$

In the complex numerical wavenumber regime for $N_\lambda < N_\lambda\big|_{transition}$, we observe that $\zeta > 1$ in (B.2). The following relation for the complex-value arc-sine function becomes useful:

$$\sin^{-1}(\zeta) = -j\ln\left(j\zeta + \sqrt{1-\zeta^2}\right) \qquad (B.3)$$

Substituting equation (B.3) into the equation given below, using the sum of simpler logarithms yields:

$$\tilde{k} = \frac{2}{\Delta}\left[-j\ln\left(j\zeta + \sqrt{1-\zeta^2}\right)\right] = -\frac{2j}{\Delta}\cdot\ln\left(j\zeta + j\sqrt{\zeta^2-1}\right) \qquad (B.4)$$

Using Euler's formula the above can be written in complex form

$$\tilde{k} = -\frac{2j}{\Delta}\cdot\ln\left[\left(\zeta + j\sqrt{\zeta^2-1}\right)\cdot e^{+j\pi/2}\right] \qquad (B.5)$$

Equation (B.5) simplifies further to:

$$\tilde{k} = \frac{\pi}{\Delta} - j\frac{2}{\Delta} \cdot \ln\left(\zeta + \sqrt{\zeta^2 - 1}\right) \qquad (B.6)$$

Separating real and complex arguments from equation (B.6) yields to

$$\tilde{k}_{real} = \frac{\pi}{\Delta}, \qquad\qquad \tilde{k}_{img} = -j\frac{2}{\Delta} \cdot \ln\left(\zeta + \sqrt{\zeta^2 - 1}\right) \qquad (B.7)$$

Let the numeric phase velocity $\tilde{c} = \omega/\Re\left(\tilde{k}\right)$, where $\Re(\cdot)$ represents the real part of the wavenumber $\tilde{k}$. If $c = \omega/k$ where $k = 2\pi/\lambda = 2\pi/\Delta N_\lambda$, by taking the ratio of the numeric phase velocity to the exact phase velocity yields

$$\tilde{v}_p = \frac{\omega}{\tilde{k}_{real}} = \frac{\omega}{\left(\pi/\Delta\right)} = \frac{2\pi f\Delta}{\pi} = \frac{2f\lambda_0}{N_\lambda} = \frac{2}{N_\lambda}c \qquad (B.8)$$

The wave-amplitude multiplier per grid cell of propagation is

$$e^{\tilde{k}_{img}\Delta} \equiv e^{-a\Delta} = e^{-2\ln\left(\zeta+\sqrt{\zeta^2-1}\right)} = \frac{1}{\left(\zeta + \sqrt{\zeta^2-1}\right)^2} \qquad (B.9)$$

Since $\zeta > 1$, the numerical wave amplitude decays exponentially with spatial position.

Appendix C

Numerical Wave Propagation Along a Grid Diagonal

The following analysis explores the possibility of complex-valued wavenumbers arising for oblique numerical wave propagation in a square-cell grid. Consider the corresponding numerical dispersion relation:

$$\tilde{k} = \frac{2\sqrt{2}}{\Delta}\sin^{-1}\left[\frac{1}{S\sqrt{2}}\sin\left(\frac{\pi S}{N_\lambda}\right)\right] \equiv \frac{2\sqrt{2}}{\Delta}\sin^{-1}(\zeta) \qquad (C.1)$$

Where

$$\zeta = \frac{1}{S\sqrt{2}}\sin\left(\frac{\pi S}{N_\lambda}\right) \qquad (C.2)$$

The transition between real and complex values of $\tilde{k}$ occurs when $\zeta = 1$.

In the complex-numerical wavenumber regime for $N_\lambda < N_\lambda\big|_{transition}$ we observe that $\zeta > 1$ in (C.2). The following relation for the complex-value arc-sine function becomes useful:

$$\sin^{-1}(\zeta) = -j\ln\left(j\zeta + \sqrt{1-\zeta^2}\right) \qquad (C.3)$$

Substituting equation (C.3) into the equation given below, using the sum of simpler logarithms yields:

$$\tilde{k} = \frac{2\sqrt{2}}{\Delta}\left[-j\ln\left(j\zeta + \sqrt{1-\zeta^2}\right)\right] = -\frac{2\sqrt{2}j}{\Delta}\cdot\ln\left(j\zeta + j\sqrt{\zeta^2-1}\right) \qquad (C.4)$$

Using Euler's formula the above can be written in complex form

$$\tilde{k} = -\frac{2\sqrt{2}j}{\Delta} \cdot \ln\left[\left(\zeta + j\sqrt{\zeta^2 - 1}\right) \cdot e^{+j\pi/2}\right] \tag{C.5}$$

Equation (C.5) simplifies further to:

$$\tilde{k} = \frac{\pi\sqrt{2}}{\Delta} - j\frac{2\sqrt{2}}{\Delta} \cdot \ln\left(\zeta + \sqrt{\zeta^2 - 1}\right) \tag{C.6}$$

Separating real and complex arguments from equation (C.6) yields

$$\tilde{k}_{real} = \frac{\pi\sqrt{2}}{\Delta}, \qquad \tilde{k}_{img} = -j\frac{2\sqrt{2}}{\Delta} \cdot \ln\left(\zeta + \sqrt{\zeta^2 - 1}\right) \tag{C.7}$$

The numerical phase velocity to the exact phase velocity yields

$$\tilde{v}_p = \frac{\omega}{\tilde{k}_{real}} = \frac{\omega}{\left(\pi\sqrt{2}/\Delta\right)} = \frac{2\pi f \Delta}{\pi\sqrt{2}} = \frac{\sqrt{2}f\lambda_0}{N_\lambda} = \frac{\sqrt{2}}{N_\lambda}c \tag{C.8}$$

The wave-amplitude multiplier per grid cell of propagation is

$$e^{\tilde{k}_{img}\Delta} \equiv e^{-a\Delta} = e^{-2\sqrt{2}\ln\left(\zeta+\sqrt{\zeta^2-1}\right)} = \frac{1}{\left(\zeta + \sqrt{\zeta^2 - 1}\right)^{2\sqrt{2}}} \tag{C.9}$$

Since $\zeta > 1$, the numerical wave amplitude decays exponentially with spatial position.

Appendix D

Complex Frequency Analysis

Assuming a sinusoidal travelling wave present in a three-dimensional FDTD space lattice discretely sampled at (x_I, y_J, z_K, t_n). By allowing the possibility of complex angular frequency, $\tilde{\omega} = \tilde{\omega}_{real} + j\tilde{\omega}_{imag}$, a field vector in this wave can be expressed as:

$$\vec{V}\Big|_{I,J,K}^{n} = \vec{v}_0 e^{j\left[\left(\tilde{\omega}_{real} + j\omega_{imag}\right)n\Delta t - \tilde{k}_x I \Delta x - \tilde{k}_y J \Delta y - \tilde{k}_z K \Delta z\right]}$$

$$= \vec{V}_0 e^{-\omega_{imag} n\Delta t} e^{j\left(\omega_{real} n\Delta t - \tilde{k}_x I \Delta x - \tilde{k}_y J \Delta y - \tilde{k}_z K \Delta z\right)} \quad (D.1)$$

The numerical dispersion relation allowing for a complex-valued angular frequency is given by:

$$\left[\frac{1}{c\Delta t}\sin\left(\frac{\omega\Delta t}{2}\right)\right]^2 = \left[\frac{1}{\Delta x}\sin\left(\frac{\hat{k}_x \Delta x}{2}\right)\right]^2 + \left[\frac{1}{\Delta y}\sin\left(\frac{\hat{k}_y \Delta y}{2}\right)\right]^2 + \left[\frac{1}{\Delta z}\sin\left(\frac{\hat{k}_z \Delta z}{2}\right)\right]^2 \quad (D.2)$$

Taking equation (D.2) and solving for $\tilde{\omega}$ yields

$$\tilde{\omega} = \frac{2}{\Delta t}\sin^{-1}(\xi) \quad (D.3)$$

where

$$\xi = c\Delta t \sqrt{\frac{1}{(\Delta x)^2}\sin^2\left(\frac{\tilde{k}_x \Delta x}{2}\right) + \frac{1}{(\Delta y)^2}\sin^2\left(\frac{\tilde{k}_y \Delta y}{2}\right) + \frac{1}{(\Delta z)^2}\sin^2\left(\frac{\tilde{k}_z \Delta z}{2}\right)} \quad (D.4)$$

In the unstable range of $1 < \xi < \xi_{upper\ bound}$ where

$$0 \leq \xi \leq c\Delta t \sqrt{\frac{1}{\left(\Delta x\right)^2} + \frac{1}{\left(\Delta y\right)^2} + \frac{1}{\left(\Delta z\right)^2}} \equiv \xi_{\text{upper bound}} \tag{D.5}$$

and exists only if

$$\xi_{\text{upper bound}} = c\Delta t \sqrt{\frac{1}{\left(\Delta x\right)^2} + \frac{1}{\left(\Delta y\right)^2} + \frac{1}{\left(\Delta z\right)^2}} > 1 \tag{D.6}$$

The unstable range is defined by

$$\Delta t = \frac{1}{c\sqrt{\dfrac{1}{\left(\Delta x\right)^2} + \dfrac{1}{\left(\Delta y\right)^2} + \dfrac{1}{\left(\Delta z\right)^2}}} \equiv \Delta t_{\substack{\text{stable} \\ \text{limit-3D}}} \tag{D.7}$$

To prove the claim for instability for the range $\xi > 1$, the complex-valued $\sin^{-1}\left(\xi\right)$ is given by

$$\sin^{-1}\left(\xi\right) = -j\ln\left(j\xi + \sqrt{1-\xi^2}\right) \tag{D.8}$$

Substituting equation (D.8) into equation (D.3) and solving for $\tilde{\omega}$ yields

$$\tilde{\omega} = \frac{2}{\Delta t}\sin^{-1}\left(\xi\right) = -\frac{2j}{\Delta t}\ln\left(j\xi + \sqrt{1-\xi^2}\right) \tag{D.9}$$

Factoring out $j = e^{+j\pi/2}$ in the argument of the natural logarithm

$$\tilde{\omega} = -\frac{2j}{\Delta t}\ln\left(j\xi + \sqrt{1-\xi^2}\right) = -\frac{2j}{\Delta t}\ln\left[\left(\xi + \sqrt{\xi^2-1}\right)e^{+j\pi/2}\right] \tag{D.10}$$

Taking the natural logarithm of equation (D.10) yields

$$\begin{aligned}
\tilde{\omega} &= -\frac{2j}{\Delta t}\ln\left[\left(\xi + \sqrt{\xi^2-1}\right)e^{+j\pi/2}\right] \\
&= \frac{\pi}{\Delta t} - \frac{2j}{\Delta t}\ln\left(\xi + \sqrt{\xi^2-1}\right)
\end{aligned} \tag{D.11}$$

Separating the real and imaginary parts of ω from equation (D.11)

$$\tilde{\omega}_{real} = \frac{\pi}{\Delta t} \qquad \text{and} \qquad \tilde{\omega}_{imag} = -\frac{2}{\Delta t}\ln\left(\xi + \sqrt{\xi^2 - 1}\right) \qquad \text{(D.12)}$$

Substituting equation (D.12) into equation (D.1) the following equation is obtained

$$
\begin{aligned}
\vec{V}\Big|_{I,J,K}^{n} &= \vec{V}_0 e^{-\omega_{imag}n\Delta t} e^{j\left(\omega_{real}n\Delta t - \tilde{k}_x I\Delta x - \tilde{k}_y J\Delta y - \tilde{k}_z K\Delta z\right)} \\
&= \vec{V}_0 e^{2/\Delta t \ln\left(\xi + \sqrt{\xi^2-1}\right)n\Delta t} e^{j\left(\omega_{real}\pi/\Delta t\, n\Delta t - \tilde{k}_x I\Delta x - \tilde{k}_y J\Delta y - \tilde{k}_z K\Delta z\right)}
\end{aligned}
\qquad \text{(D.13)}
$$

In the unstable range of $1 < \xi < \xi_{\text{upper bound}}$ and using the identity $e^{\ln(x)} = x$, equation (D.13) becomes

$$
\begin{aligned}
\vec{V}\Big|_{I,J,K}^{n} &= \vec{V}_0 e^{2/\Delta t \ln\left(\xi + \sqrt{\xi^2-1}\right)n\Delta t} e^{j\left(\omega_{real}\pi/\Delta t\, n\Delta t - \tilde{k}_x I\Delta x - \tilde{k}_y J\Delta y - \tilde{k}_z K\Delta z\right)} \\
&= \left(\xi + \sqrt{\xi^2 - 1}\right)^{**2n} e^{j\left(\omega_{real}\pi/\Delta t\, n\Delta t - \tilde{k}_x I\Delta x - \tilde{k}_y J\Delta y - \tilde{k}_z K\Delta z\right)}
\end{aligned}
\qquad \text{(D.14)}
$$

where $**2n$ denotes the $2n$-th power. Based on equation (D.14) the following multiplicative factor greater than 1, amplifies the numerical wave every time-step:

$$q_{growth} \equiv \left(\xi + \sqrt{\xi^2 - 1}\right)^2 \qquad \text{(D.15)}$$